Forcing of globally unstable jets and flames

Larry K.B. Li

Emmanuel College

University of Cambridge

A thesis submitted for the degree of

Doctor of Philosophy

2011

Declaration

This dissertation is the result of my own work and includes nothing that is the outcome of work done in collaboration except where specifically indicated in the text. No part of this dissertation has already been, or is concurrently being, submitted for any other degree, diploma or qualification. This dissertation contains approximately 50000 words and 100 figures.

Larry Li
31 August 2011

To Villian and Mini Roar!

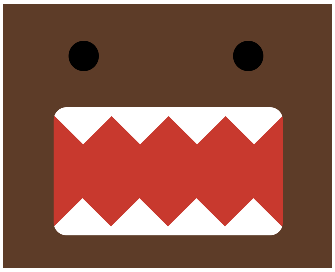

Acknowledgements

I would first and foremost like to express my gratitude for the guidance and support of my supervisor, Dr. Matthew Juniper. Without his perspicacity and pertinacity, I would probably still be in the laboratory – or in front of my computer, fiddling with commas.

Others to whom I owe a debt of gratitude include Professor Simone Hochgreb, Professor Nondas Mastorakos, Dr. Tim Nickels, Dr. James Dawson, Dr. Martin Davy (Loughborough), and Professor Sheldon Green (UBC).

I would also like to thank my friends and colleagues, both here in Cambridge and back home in Vancouver, for their personal support.

Funding for this research was generously provided by Emmanuel College, Trinity College, and the Bill & Melinda Gates Foundation through the Gates Cambridge Trust.

Abstract

In the analysis of thermoacoustic systems, a flame is usually characterised by the way its heat release responds to acoustic forcing. This response depends on the hydrodynamic stability of the flame. Some flames, such as a premixed bunsen flame, are hydrodynamically globally stable. They respond only at the forcing frequency. Other flames, such as a jet diffusion flame, are hydrodynamically globally unstable. They oscillate at their own natural frequencies and are often assumed to be insensitive to low-amplitude forcing at other frequencies.

If a hydrodynamically globally unstable flame really is insensitive to forcing at other frequencies, then it should be possible to weaken thermoacoustic oscillations by detuning the frequency of the natural hydrodynamic mode from that of the natural acoustic modes. This would be very beneficial for industrial combustors.

In this thesis, that assumption of insensitivity to forcing is tested experimentally. This is done by acoustically forcing two different self-excited flows: a non-reacting jet and a reacting jet. Both jets have regions of absolute instability at their base and this causes them to exhibit varicose oscillations at discrete natural frequencies. The forcing is applied around these frequencies, at varying amplitudes, and the response examined over a range of frequencies (not just at the forcing frequency). The overall system is then modelled as a forced van der Pol oscillator.

The results show that, contrary to some expectations, a hydrodynamically self-excited jet oscillating at one frequency is sensitive to forcing at other frequencies. When forced at low amplitudes, the jet

responds at both frequencies as well as at several nearby frequencies, and there is beating, indicating quasiperiodicity. When forced at high amplitudes, however, it locks into the forcing. The critical forcing amplitude required for lock-in increases with the deviation of the forcing frequency from the natural frequency. This increase is linear, indicating a Hopf bifurcation to a global mode.

The lock-in curve has a characteristic $\vee$ shape, but with two subtle asymmetries about the natural frequency. The first asymmetry concerns the forcing amplitude required for lock-in. In the non-reacting jet, higher amplitudes are required when the forcing frequency is above the natural frequency. In the reacting jet, lower amplitudes are required when the forcing frequency is above the natural frequency. The second asymmetry concerns the broadband response at lock-in. In the non-reacting jet, this response is always weaker than the unforced response, regardless of whether the forcing frequency is above or below the natural frequency. In the reacting jet, that response is weaker than the unforced response when the forcing frequency is above the natural frequency, but is stronger than it when the forcing frequency is below the natural frequency.

In the reacting jet, weakening the global instability – by adding coflow or by diluting the fuel mixture – causes the flame to lock in at lower forcing amplitudes. This finding, however, cannot be detected in the flame describing function. That is because the flame describing function captures the response at only the forcing frequency and ignores all other frequencies, most notably those arising from the natural mode and from its interactions with the forcing. Nevertheless, the flame describing function does show a rise in gain below the natural frequency and a drop above it, consistent with the broadband response.

Many of these features can be predicted by the forced van der Pol oscillator. They include (i) the coexistence of the natural and forcing frequencies before lock-in; (ii) the presence of multiple spectral peaks around these competing frequencies, indicating quasiperiodicity; (iii) the occurrence of lock-in above a critical forcing amplitude; (iv) the $\vee$-shaped lock-in curve; and (v) the reduced broadband response at lock-in. There are, however, some features that cannot be predicted. They include (i) the asymmetry of the forcing amplitude required for lock-in, found in both jets; (ii) the asymmetry of the response at lock-in, found in the reacting jet; and (iii) the interactions between the fundamental and harmonics of both the natural and forcing frequencies, found in both jets.

Contents

List of Figures

Nomenclature

Roman Symbols

A	Forcing amplitude
B	Pressure amplitude
b	Damping coefficient
C	Coupling function
c	Speed of sound
D	Dispersion relation
d	Diameter or characteristic dimension
F	External forcing function
f	Frequency
FDF	Flame describing function
G	Green's function
g	Gravitational acceleration
He	Helmholtz number, $\equiv fL/c$
I	Local pixel intensity
k	Axial wavenumber or spring constant

L	Characteristic dimension
l	Nonlinear coefficient in Stuart–Landau equation
M	Mach number, $\equiv U/c$
m	Mass or azimuthal wavenumber or embedding dimension
N	Image height or degrees of freedom
p	Pressure
PSD	Power spectral density
q	Heat release
R	Control parameter
r	Radial coordinate
Re	Reynolds number, $\equiv \rho U d/\mu$
Ri	Richardson number, $\equiv g d_j(\rho_\infty - \rho_j)/\rho_j U_j^2$
S	Integration surface
s	Density ratio, $\equiv \rho_{in}/\rho_{out}$
SNR	Signal-to-noise ratio
SPL	Sound pressure level
St	Strouhal number, $\equiv fd/U$
T	Temperature
t	Temporal variable
U	Bulk velocity or characteristic velocity
u	Local velocity in streamwise direction
V	Integration volume or voltage

x	Spatial variable or streamwise coordinate
y	Spatial variable or cross-stream coordinate
Z	Mixture fraction (by mass)

Greek Symbols

β	Open area ratio
δ^*	Displacement thickness
ϵ	Control parameter in van der Pol equation
γ	Specific heat ratio
Λ	Shear ratio, $\equiv (U_{in} - U_{out})/(U_{in} + U_{out})$
μ	Dynamic viscosity
ν	Kinematic viscosity
ω	Angular frequency
ϕ	Perturbation eigenfunction or phase
ψ	Perturbation part of stream function or phase
ρ	Density
Σ	Alignment integral
σ	Linear coefficient in Stuart–Landau equation
τ	Oscillation period or embedded time delay
Θ	Angular position of pendulum
θ	Phase difference or momentum thickness

Subscripts

0	Zero group velocity

ad	Adiabatic
bif	Onset of bifurcation
d	Cylinder
f	Forced mode
for	With forcing
g	Global, for the entire field of view
i	Imaginary component
in	Inner fluid stream
∞	Freestream
j	Jet outlet
l	Local, at a particular x/d_1
loc	Onset of lock-in
$-$	Backward propagation
n	Natural mode (fundamental)
1	Central flow
out	Outer fluid stream
$+$	Forward propagation
pp	Peak to peak
qp	Between heat release and pressure
r	Real component
rms	Root-mean-square
sat	Saturation

st	Stoichiometric
2	Annular coflow
unf	Without forcing
$u\rho$	Between velocity and density
vdp	Van der Pol

Other Symbols

$\bar{\ }$	Time average
$\dot{\ }$	Time derivative
$\hat{\ }$	Fourier transform
$'$	Fluctuating component
[ ]	Concentration (by volume)

Acronyms

AI	Analogue input
AU	Absolutely unstable
CAEP	Committee on Aviation Environmental Protection
CMOS	Complementary metal oxide semiconductor
CU	Convectively unstable
DAQ	Data acquisition system
DC	Direct current (zero-frequency component)
DI	Digital input
DNS	Direct numerical simulation
DO	Digital output

DOF	Degree of freedom
FFT	Fast Fourier transform
FS	Full scale
GU	Globally unstable
HWA	Hot-wire anemometry
IP	Inflexion point
KH	Kelvin–Helmholtz
LDV	Laser Doppler velocimetry
MGS	Marginally globally stable
NIST	National Institute of Standards and Technology
NO_x	Nitrogen oxides
RMS	Root-mean-square
STP	Standard temperature and pressure, NIST: 293.15 K and 101.325 kPa
TMM	Two-microphone method
TTL	Transistor–transistor logic
VDP	Van der Pol

Chapter 1

Introduction

In many combustion systems, high-amplitude pressure oscillations can develop at frequencies close to one or more of the acoustic modes of the combustor. Known as thermoacoustic instabilities[1], such oscillations arise when local fluctuations in heat release and pressure couple together in positive feedback, enabling energy to be transferred from the flame to its surrounding acoustic field. Thermoacoustic instability is a serious problem because it is difficult to predict and control. If left unchecked it can induce flame blowoff or flashback, trigger thrust and power variations, and enhance heat transfer to the combustor walls. Over time it can even impart sufficient cyclic loading to structural components to cause catastrophic fatigue failure.

One of the most important factors determining the stability and amplitude of thermoacoustic oscillations is the design of the fuel injector. Although certain injector designs have been found to be less prone to instability than others, the underlying reasons for this are not well understood. Nevertheless, by making small incremental changes to previously proven designs, engineers have managed to stabilise current combustion systems to tolerable levels. Future efficiency and pollutant targets, however, may only be met with new designs, some of which can turn out to be prone to thermoacoustic instability. Thus, without a bet-

---

[1] Also known as combustion instabilities or pulsating combustion. In industry, the oscillations can be further classified according to their frequencies (Krebs et al., 2005): chugging/rumble for low frequencies, $\mathcal{O}(10)$ Hz; buzzing for intermediate frequencies, $\mathcal{O}(100)$ Hz; and screeching/screaming/squealing for high frequencies, $\mathcal{O}(1000)$ Hz.

ter understanding of why some injector designs perform better than others, the incremental improvement process would have to begin over again.

This thesis is part of an overall research effort to investigate how hydrodynamic[1] oscillations interact with thermoacoustic[2] oscillations, and whether the former can be used to weaken the latter. The aim of this thesis in particular is to examine the forced response of flames that have different strengths of hydrodynamic global instability (or simply 'global instability'). Previous work has suggested that flows with global instability are universally characterised by self-excited oscillations at discrete natural frequencies and by insensitivity to external disturbances imposed at other frequencies. On first sight, these instability characteristics appear to have the potential to reduce the receptivity of a flame to incident flow perturbations, and may therefore be useful for disrupting the energy coupling that gives rise to thermoacoustic instability. This thesis, however, will show that the dynamics of globally unstable flames is richer than that, resembling instead the dynamics of nonlinear oscillators.

1.1 Thermoacoustic instability

It has been known for over two centuries that sound can be generated by a flame when it is enclosed in a combustion chamber (Higgins, 1802). Back then, though, it was merely a novelty phenomenon, used occasionally to entertain guests at musical parties – as Le Conte did in 1858. Thermoacoustic instability, as the phenomenon later became known, was not considered a serious problem until the late 1930s, when it began appearing in high-performance combustion devices such as the gas turbine and the rocket engine[3]. Since that time, researchers from both academia and industry have been trying to discover the dominant physical mechanisms that govern how a flame responds to incident flow perturbations. Although many such mechanisms have now been identified, most of them are

---

[1] The term 'hydrodynamic' refers to instabilities caused by fluid mechanics for which compressibility effects are negligible. Its usage is therefore not restricted to water.

[2] The term 'thermoacoustic' refers to instabilities caused by heat release and acoustics.

[3] A notable example is the F-1 engine of the Saturn V rockets used in the Apollo space missions. Overcoming instability required an extensive trial-and-error program involving nearly 2000 full-scale tests. One of the eventual solutions was a modification to the fuel injector design.

still not fully understood. Worse still, the problem is exacerbated if the flow perturbations are large[1], because then the nonlinear dynamics of heat release, about which little is known, becomes important. As Peracchio and Proscia (1999) and Zinn and Lieuwen (2005) have noted, this lack of understanding, particularly concerning nonlinear combustion processes, is what makes it difficult to predict the onset[2] and saturation of thermoacoustic oscillations without costly and often prohibitive full-scale testing.

In recent years, thermoacoustic instability has been a growing concern for developers of gas turbines. New environmental legislations[3] calling for lower emissions of nitrogen oxides (NO_x) have led to a technological shift from diffusion to lean-premixed combustors. Although lean-premixed operation can indeed reduce flame temperatures and hence thermal NO_x production[4], it also tends to make the overall system more thermoacoustically unstable. This is due partly to the nature of the flame stabilisation mechanism but mostly to the increased sensitivity of heat release to equivalence ratio fluctuations[5], Keller (1995) and Lieuwen et al. (2001) have shown.

Other combustion devices in which thermoacoustic instability can arise include aeroengine afterburners (Langhorne, 1988; Macquisten and Dowling, 1995; Schadow et al., 1987), industrial furnaces (Correa, 1998), ramjet missiles (Crump et al., 1986), and both solid- and liquid-fuelled rockets (Blomshield, 2001; Crocco and Cheng, 1956; Harrje and Reardon, 1972). Referring to liquid-fuelled rockets

---

[1] Typically if the oscillation amplitude grows to $\mathcal{O}$(mean), for pressure or velocity.

[2] Even in a 'stable' combustor, there is always some degree of unsteadiness in the flow. What demarcates the onset of thermoacoustic instability, according to Huang and Yang (2009), is when the pressure amplitude becomes greater than about 5% of the mean chamber pressure.

[3] One example is the recommendation made by the United Nations Committee on Aviation Environmental Protection (CAEP) at the 37th Session of the International Civil Aviation Organisation Assembly held in Montreal, October 2010. At the Assembly, CAEP recommended "NO_x standards up to 15 percent more stringent than current levels, applicable to new aircraft engines certified after 31 December 2013." It also recommended that "engines not be produced under existing NO_x standards after 31 December 2012."

[4] Via the mechanism of Zel'dovich et al. (1985), which operates through high-temperature (>1400 K) oxidation of the diatomic nitrogen present in atmospheric air. The extended version of this mechanism has three principal reactions: (i) $N_2 + O \rightleftharpoons NO + N$; (ii) $N + O_2 \rightleftharpoons NO + O$; and (iii) $N + OH \rightleftharpoons NO + H$.

[5] In lean-premixed combustion, the rate of heat release increases as the equivalence ratio increases. Consequently, a significant drop in the equivalence ratio causes local extinction, and any rise causes the flame to become richer, releasing significantly more heat.

in particular, Yang and Anderson (1995) remarked that the high density of heat release[1] occurring in a chamber with little damping sets up conditions that are ideal for self-excitation and sustenance of high-amplitude pressure oscillations. But while thermoacoustic instability is detrimental to continuous combustion devices, it is the principle on which pulsed combustors operate (Zinn, 1996).

1.1.1 Basic theory

The cause of thermoacoustic instability is the resonant interaction that occurs between unsteady combustion and acoustics. According to Dowling and Ffowcs-Williams (1983), even infinitesimal fluctuations in heat release from a flame can cause the reacting gases to expand and contract cyclically, propagating initially weak acoustic waves to the surroundings. On interacting with the combustor, these waves may partially reflect back to perturb the flame. If the flame is perturbed such that moments and locations of high heat release coincide with moments and locations of high pressure, it will transfer some of its thermal energy to the acoustic modes of the combustor, thereby amplifying them over time.

Rayleigh (1878) was the first to scientifically explain the physical mechanism by which a heat source can transfer energy to an acoustic field. In what is now one of the most widely quoted passages in the field of combustion, he established the basic criterion for the onset of thermoacoustic instability:

> “If heat be periodically communicated to, and abstracted from, a mass of air vibrating in a cylinder bounded by a piston, the effect produced will depend upon the phase of the vibration at which the transfer of heat takes place. If heat be given to the air at the moment of greatest condensation or be taken from it at the moment of greatest rarefaction, the vibration is encouraged. On the other hand, if heat be given at the moment of greatest rarefaction, or abstracted at the moment of greatest condensation, the vibration is discouraged.”

---

[1] For example, the power density of the F-1 rocket engine is 22 GW m^{-3} and that of the Space Shuttle main engine is 35 GW m^{-3}. By comparison, the figure for solid-fuelled rockets rarely exceeds 1 GW m^{-3} and for aeroengine afterburners is 0.3–0.4 GW m^{-3} (Culick, 2006).

This mechanism is analogous to the thermodynamic Carnot cycle, except that work is done on the acoustic field rather than against a piston. Almost a century later, Putnam (1971) reformulated Rayleigh's criterion into a more useful form:

$$\int_{\tau} \int_{V} q'(x,t)\ p'(x,t)\ \mathrm{d}^3x\ \mathrm{d}t > 0, \tag{1.1}$$

where $q'(x,t)$ is the fluctuating heat release, $p'(x,t)$ is the fluctuating pressure, and x and t are spatial and temporal variables, respectively. Known as the Rayleigh integral, (1.1) is meant to be evaluated over an oscillation period, τ, and a control volume, V, that encompasses the entire thermal source.

If the Rayleigh integral is positive, an acoustic wave gains energy from the flame, becoming excited. If it is negative, the acoustic wave loses energy to the flame, becoming damped. If it is zero, no net energy is exchanged over a full oscillation period. In theory, the sign of the Rayleigh integral is influenced by both the spatial and temporal correlations between heat release and pressure, as (1.1) explicitly shows. In practice, however, the spatial correlation is only mildly influential because most industrial flames are acoustically compact[1]. At any moment in time, every location on the flame surface experiences the same acoustic pressure: $p'(x,t) \to p'(t)$ within the flame boundary. For a given flame size and position, therefore, the spatial distribution of heat release is of secondary importance. Of primary importance is how the heat release fluctuates in time because that determines how well it is correlated temporally to the acoustics. For thermoacoustic instability to arise, that correlation must be strong enough to create a positive Rayleigh integral. This tends to occur if the dominant frequency of heat release is near one of the acoustic frequencies of the combustor, and if the phase difference between the heat release and pressure is $0^\circ \leq |\theta_{qp}| < 90^\circ$. If $90^\circ < |\theta_{qp}| \leq 180^\circ$, however, the Rayleigh integral becomes negative and the instability is damped. The Rayleigh integral is zero if $|\theta_{qp}| = 90^\circ$.

As written in (1.1), the Rayleigh integral applies only to periodic oscillations which, by definition, do not grow or decay over a period. A rigorous analysis must therefore separate the system into two timescales: a rapidly varying timescale and

---

[1] This means that the acoustic wavelength is much larger than the largest flame dimension.

a slowly varying timescale. From this point of view, Rayleigh's criterion applies to the system over a period of the rapidly varying timescale, but determines the change in amplitude on the slowly varying timescale (Culick, 1976).

In real combustors, inequality (1.1) is a necessary but insufficient condition for thermoacoustic instability because it does not account for energy dissipation. This is not to say, though, that damping is required to reach a limit cycle. Using a nonlinear analysis, Balasubramanian and Sujith (2008) showed that a thermoacoustic system can still saturate even without damping. Undamped saturation can occur, for example, if θ_{qp} varies with the amplitude as follows: (i) for initial growth, the system exhibits $0^\circ \leq |\theta_{qp}| < 90^\circ$ and thus has a positive Rayleigh integral; then (ii) as the oscillation grows, θ_{qp} approaches exactly 90°. The final state of such a system would be a finite-amplitude limit cycle in which no net energy is exchanged between the flame and its surrounding acoustic field.

Real combustors invariably have some degree of damping, however. To support a limit cycle, they must always exhibit $0^\circ \leq |\theta_{qp}| < 90^\circ$, as this ensures that at least some energy is supplied to the acoustic field to balance the damping. Recognising this, Chu (1964) generalised the Rayleigh criterion to include energy loss across boundaries. He noted that for an inviscid ideal gas, fluctuations in density can be caused by fluctuations in pressure or entropy (heat):

$$\frac{\partial \rho'}{\partial t} = \frac{1}{\overline{c}^2}\frac{\partial p'}{\partial t} - \frac{(\gamma - 1)q'}{\overline{c}^2}, \tag{1.2}$$

where ρ is the density, γ is the specific heat ratio, and c is the speed of sound. The overbars denote time-averaged quantities and the primes denote fluctuating quantities. Chu (1964) then combined (1.2) with the linearised continuity and momentum equations, and integrated the result over a combustor of volume V bounded by surface S, arriving at an equation for the acoustic energy:

$$\frac{\partial}{\partial t}\int_V \left(\frac{1}{2}\overline{\rho}u^2 + \frac{1}{2}\overline{\rho}\overline{c}^2\left(\frac{p'}{\overline{p}\gamma}\right)^2\right)\mathrm{d}V = \frac{\gamma - 1}{\overline{p}\gamma}\int_V q'p'\,\mathrm{d}V - \int_S p'u \cdot \mathrm{d}S, \tag{1.3}$$

where u is the local velocity. From left to right, the first term in (1.3) is the time rate of change of acoustic energy (both kinetic and potential) within the control volume; the amplitude of an acoustic mode grows if this term is positive over an oscillation period. The second term, equivalent to the Rayleigh integral, is the energy gained by acoustic waves as a result of heat addition. The last term is a general surface integral used to account for energy lost across boundary S; the major sources of this term, according to Zinn and Lieuwen (2005), are heat transfer through the combustor walls, viscous dissipation in the boundary layers, vorticity generation due to flow separation at sharp edges and sudden expansions, and radiation and advection of acoustic energy out of the system.

For thermoacoustic modes to grow, the energy gained from combustion must exceed the energy lost across boundaries:

$$\frac{\gamma - 1}{\overline{p}\gamma} \int_V q' p' \mathrm{d}V > \int_S p' u \cdot \mathrm{d}S, \tag{1.4}$$

where the overbar now denotes time averaging over one oscillation period. As the modes grow, though, they become increasingly nonlinear and this can affect the initial energy imbalance. For instance, the energy gain term could vary because the phase difference between heat release and pressure could vary, as in the analysis of Balasubramanian and Sujith (2008). The energy loss term probably increases because, as Zinn and Lieuwen (2005) have noted, damping mechanisms generally become more effective as the oscillation amplitude grows. The thermoacoustic modes will continue to grow until the two energy terms become equal. Once this occurs, the system saturates, eventually settling into a limit cycle (Dowling, 1997; Peracchio and Proscia, 1999). It should be noted that in most systems, the acoustic damping is small and increases only linearly with the pressure amplitude. Saturation therefore does not usually occur through increased damping, but through the nonlinear response of the flame. Further information on thermoacoustic theory is available in the books by Zinn (1996) and Poinsot and Veynante (2005), and in the articles by Culick (1987) and Nicoud and Poinsot (2005).

1.1.2 Driving mechanisms

Many physical mechanisms can cause a flame to release heat unsteadily. Some of the more notable ones were highlighted by Candel (1992, 2002) in his lectures at the 24th and 29th International Symposia on Combustion:

- **Flame-vortex interaction.** Shear flows – such as jets, wakes, and mixing layers – tend to be unstable and can develop large-scale coherent structures (Brown and Roshko, 1974). Known as vortices, such structures can be induced hydrodynamically, for example by the Kelvin–Helmholtz (KH) mechanism (Helmholtz, 1868; Kelvin, 1871) or by vortex breakdown if the flow is swirling (Leibovich, 1978). They can also be induced externally, for example by mechanical vibration or by acoustic waves impinging on the injector lip or the flame holder[1]. Regardless of the physical cause, the growth and development of such organised flow structures can have profound effects on combustion. Schadow et al. (1989), for example, showed that vortices can enhance local entrainment and mixing, creating spatially coherent pockets of high heat release. Rogers and Marble (1956) and Poinsot et al. (1987), moreover, showed that as vortices roll up and advect downstream, they can entrain and trap a combustible mixture of unburnt reactants and hot products. The mixture eventually ignites, but only after a time delay, resulting in heat being released periodically such that energy can be transferred to the acoustic modes of the combustor. Another way in which vortices can cause fluctuations in heat release is by physically distorting the flame and altering its surface area (Balachandran et al., 2005).

---

[1] In this mechanism, acoustic waves – travelling at the speed of sound – impinge on a solid surface and generate vorticity as a result of the no-slip condition. The vorticity is released periodically and then carried downstream at the mean advective velocity, forming a travelling vortical wave. On a related note, the presence of acoustic waves can also give rise to an instability driving mechanism that does not involve large-scale vortex generation. According to Howe (2008), this process starts with the acoustic waves impinging on the flame holder and causing periodic fluctuations in the flame anchoring point. This produces a travelling wave on the flame surface, which, as Boyer and Quinard (1990) have shown, propagates at a phase velocity equal to the component of the mean velocity that is locally tangent to the flame front. The result is that the flame stretch fluctuates in both space and time, causing fluctuations in the flame speed and hence in the burning rate.

- **Mixture-strength oscillation.** The pressure oscillations associated with thermoacoustic instability can cause modulations in pressure drop across any unchoked supplies of air, fuel, and premixed air–fuel, Zinn and Lieuwen (2005) have noted. If the supply of fuel or premixed air–fuel is unchoked, the amount of fuel entering the combustor could vary in time. By conservation of energy, this would induce direct fluctuations in heat release. Similar fluctuations in heat release can arise even if the fuel supply is choked. That is because, according to Lieuwen and Zinn (1998), if the air supply is not choked[1] or if the acoustics can propagate upstream to the premixer and affect air–fuel mixing, the pressure oscillations could induce fluctuations in the equivalence ratio of the reactants. When advected to the flame front, these would induce fluctuations in the heat of reaction and the flame speed, thereby causing fluctuations in the heat release.

- **Unsteady atomisation.** Pressure waves impinging on a developing fuel spray can aid the secondary breakup[2] of ligaments and droplets. The resultant increase in liquid surface area would cause an increase in the local rate of fuel evaporation and hence in the heat release (Tong and Sirignano, 1986a,b, 1987). Furthermore, even without pressure waves, atomisation is itself an unsteady process. In measurements on air-blast sprays, which are used in gas turbines and rocket engines, Faragó and Chigier (1992) and Batarseh et al. (2009) reported large spatial and temporal fluctuations in the size, shape, and number density of droplets – even for quiescent ambient conditions and nominally steady flow rates. Such fluctuations, Chigier (1976) and Lefebvre (1980) have shown, can lead to localised regions of high fuel concentration and high heat release, which, if phased properly, could cause thermal energy to be transferred to the combustor acoustics.

---

[1] Allowing for an instability driving mechanism known as air-side coupling.

[2] Secondary breakup, according to Lefebvre (1989), is a process involving the disintegration of the discrete ligaments and droplets formed during the earlier process of primary breakup. For most Newtonian liquids, it is driven by aerodynamic forces and opposed by capillary forces (Li et al., 2009). It is not to be confused with secondary instability, which, as Bayly et al. (1988) have explained, is determined by performing a stability analysis about a solution other than the laminar one. It is also not to be confused with secondary flow, a term reserved for the streamwise vortices produced by the centrifugal forces arising at the bends of pipe flow.

Other instability driving mechanisms include flame acceleration by shock waves (important for flames in ducts), flame interaction with solid boundaries, unsteady strain and curvature effects on flame structure and speed, and periodic flame extinction and ignition.

1.1.3 Control methods

Several methods are available for controlling thermoacoustic instability. They can be divided into two main categories: passive control and active control.

In passive control, the energy gain is decreased by modifying the injector design or the combustor geometry, so as to alter the frequency–phase relationship between heat release and pressure (Gutmark et al., 1995; Noiray et al., 2007; Richards and Janus, 1998; Steele et al., 2000). The energy loss is increased by deploying damping devices, such as Helmholtz resonators (Bellucci et al., 2004; Gysling et al., 2000) and acoustic liners (Eldredge and Dowling, 2003), which convert the acoustic energy of the oscillations into vorticity.

Passive control faces two problems, however. First, it is expensive and time consuming to implement, requiring careful modification of the combustion system, often at late stages of the development program. Second, it tends to be effective over only a limited range of operating conditions. The reason for this, Straub and Richards (1998) and Yang and Anderson (1995) have argued, is that most combustors are highly resonant systems containing a multitude of acoustic modes, whose characteristics (e.g. spectrum and saturation amplitude) and mutual interactions (e.g. nonlinear energy transfer) may change depending on the actual operating condition. In fact, according to Dowling and Morgans (2005), current methods of passive control tend to be ineffective at low frequencies, where thermoacoustic instability can cause the most damage.

In active control, the energy gain is decreased by adjusting, via feedback, the fuel flow rate such that heat is released more out of phase with pressure (Neumeier and Zinn, 1996; Sattinger et al., 2000). The energy loss is increased by modifying the downstream pressure conditions with loudspeakers (Annaswamy et al., 2000; Blonbou et al., 2000; Dines, 1983). Further information on active control can be found in the reviews by McManus et al. (1993) and Dowling and Morgans (2005).

1.2 Hydrodynamic instability

Thermoacoustic instability is not the only type of instability that can arise in the flows within a combustion chamber: hydrodynamic instability can arise as well. As noted in §1, this thesis concerns the effect that thermoacoustics can have on the behaviour of globally unstable flows. A necessary condition for global instability, though, is the presence of a finite region of absolute instability. It is therefore instructive to explain the concepts of absolute and convective instability[1]. As will be discussed, the term ‘global’ describes the instability of an entire flow field, whereas the terms ‘absolute’ and ‘convective’ describe the instability of the velocity profile at a particular streamwise location.

The following discussion will focus on open shear flows because this is the type of flow found in most fuel injectors. A shear flow is simply one in which the velocity varies principally in a direction perpendicular to the mean flow. The term ‘open’ implies that the fluid particles enter and exit the domain of interest (e.g. a combustor) without recirculating. This is in contrast to ‘closed’ flows, such as Rayleigh–Bénard convection cells (Getling, 1997) and Taylor–Couette flow between concentric rotating cylinders (Taylor, 1923), where the fluid particles, along with the instabilities they support, recirculate in a periodic manner.

1.2.1 Spatiotemporal theory

Determining whether a shear flow is absolutely or convectively unstable requires an inspection of its impulse response. Such an inspection, Huerre (2000) has shown, must be done with a spatiotemporal analysis. This is because distinguishing between absolute and convective instability necessarily involves tracking infinitesimal perturbations, applied to the basic laminar flow, as they develop in both space and time. Classical theories of hydrodynamic instability, which rely on either a spatial or temporal approach, are incapable of such tracking.

A two-dimensional baseflow[2], with streamwise and cross-stream coordinates

---

[1] Originated in the field of plasma physics (Briggs, 1964), the concepts of absolute and convective instability are used in this thesis to describe instabilities due to hydrodynamics.

[2] It is not necessary to consider more than two dimensions because the theorem of Squire (1933) states that if a three-dimensional instability exists it will always be less unstable than a

x and y respectively, is assumed to be locally parallel[1] but may vary with a control parameter such as the Reynolds number[2]. The stability of this baseflow is determined by separating its total stream function into basic and perturbation (ψ) components. After linearisation[3] around the base state, a normal mode decomposition is applied to give elementary solutions of the form:

$$\psi(x, y, t) = \mathrm{Re}\{\phi(y)e^{i(kx-\omega t)}\}, \tag{1.5}$$

where k is the axial wavenumber, ω is the angular frequency, and ϕ is the eigenfunction that describes the cross-stream distribution of perturbations; all three of these quantities are complex. Equation (1.5) satisfies an ordinary differential equation of the Orr-Sommerfeld type. Enforcement of appropriate boundary conditions leads to an eigenvalue problem wherein non-trivial solutions for $\phi(y)$ exist if and only if k and ω satisfy a dispersion relation of the form:

$$D(k, \omega, R) = 0, \tag{1.6}$$

where R denotes all generalised control parameters. Each complex pair of k and ω that satisfies (1.6) has a corresponding eigenfunction $\phi(y)$. The distinction between absolute and convective instability is finally made by examining the Green's function, $G(x, t)$: the linear response of the flow to an applied impulse fixed in both space and time, say at $(x, t) = (0, 0)$. If that response decays in

---

corresponding two-dimensional instability.

[1] This assumes that in the streamwise direction, the baseflow is constant over a lengthscale comparable to the most unstable wavelength. In the analysis, therefore, the velocity profile can be extracted at a given streamwise location and replicated indefinitely both upstream and downstream, creating a 'doubly infinite domain'.

[2] For instabilities not driven by shear, other control parameters may be more important. If the instability is driven by thermal convection – as it is in the Rayleigh–Bénard instability – the key control parameter is the Rayleigh number: a ratio of the buoyancy force, from an applied thermal gradient, to the momentum and thermal diffusivities. If the instability is driven by centrifugal forces – as it is in the Taylor–Couette instability – the key control parameter is the Taylor number: a ratio of the centrifugal force, from an applied rotational rate, to the momentum diffusivity.

[3] Linearisation involves neglecting the terms that contain products of perturbations, on the basis that if the perturbations themselves are small then their products will be even smaller.

time everywhere in space, the flow is linearly stable:

$$\lim_{t\to\infty} G(x,t) = 0 \quad \text{along all rays of } x/t = \text{constant}. \tag{1.7}$$

If it grows in time anywhere in space, however, the flow is linearly unstable:

$$\lim_{t\to\infty} G(x,t) = \infty \quad \text{along at least one ray of } x/t = \text{constant}. \tag{1.8}$$

Only for unstable flows can the distinction between absolute and convective instability be made. The procedure involves examining, in the complex k–ω plane, how the response at the impulsive source ($x = 0$) evolves with time. This is equivalent to tracking the temporal evolution of the mode that has a group velocity[1] of zero: $\partial\omega/\partial k = 0$. If this stationary mode has wavenumber k_0 (called the 'absolute wavenumber'), its temporal growth rate is the imaginary part of the corresponding angular frequency or $\omega_{0,i} = \mathrm{Im}\{\omega(k_0)\}$.

Three different types of impulse response can arise in an unstable flow. Shown in figure 1.1, they are best described on spatiotemporal diagrams of $G(x,t)$. If $\omega_{0,i} < 0$ (figure 1.1a), the response at $x = 0$ decays in time, eventually leaving the flow in its undisturbed state. Such a flow is termed convectively unstable because kinetic energy is convected[2] downstream at a higher rate than it is supplied to the stationary mode. If, however, $\omega_{0,i} > 0$ (figure 1.1c), the response at $x = 0$ grows exponentially in time, propagating both upstream and downstream to contaminate the entire domain. Such a flow is termed absolutely unstable because kinetic energy is convected downstream at a lower rate than it is supplied to the stationary mode. If, moreover, $\omega_{0,i} = 0$ (figure 1.1b), the trailing edge of the wavepacket stays precisely at $x = 0$, leading to marginal instability.

---

[1] The group velocity is the velocity at which an entire wavepacket propagates. It is not to be confused with the phase velocity, which is the velocity at which an individual frequency component propagates. Physically, the group velocity can be thought of as being the speed at which the kinetic energy of perturbations is advected downstream.

[2] Here the term 'convect' is used by convention only. Nowadays it is interchangeable with the term 'advect', although some researchers still prefer to define convection as strictly the advection of heat by bulk fluid motion.

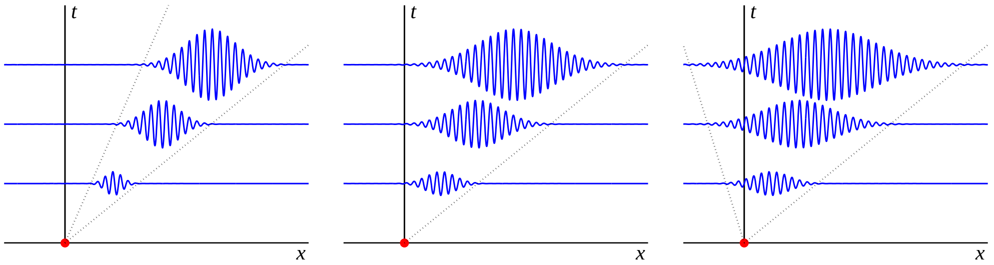

(a) Convective (b) Marginal (c) Absolute

Figure 1.1: Linear impulse response of an unstable parallel shear flow: (a) convectively unstable, (b) marginally unstable, and (c) absolutely unstable. The impulse is fixed in both space and time at $(x, t) = (0, 0)$, as indicated by the red circular markers. The black dotted lines delineate the leading and trailing edges of the growing wavepacket.

1.2.2 Amplifiers and oscillators

The key concept is that absolute instability enables perturbations to grow both upstream and downstream, whereas convective instability enables perturbations to grow downstream only. A flow that is convectively unstable everywhere, therefore, acts as a spatial amplifier of external perturbations. A flow that is absolutely unstable over a sufficient region, by contrast, acts as an oscillator. In hydrodynamics, this conceptual distinction has several implications:

- **Hydrodynamic amplifier.** This class of flow exhibits extrinsic dynamics as a result of being strongly sensitive to external disturbances such as background noise and intentional forcing. As its name suggests, an amplifier spatially amplifies incoming disturbances[1], typically over a broad frequency range – although certain frequencies may be amplified more than others, leading to a preferred wavelength for fastest instability growth. The strong receptivity of amplifiers to external disturbances makes them well suited for achieving specific control goals. Examples of amplifiers include coflowing mixing layers, constant-density jets, wakes at Reynolds numbers below the onset of von Kármán vortex shedding, and boundary layers on a flat plate.

---

[1] In a perfectly noiseless system, an amplifier would have nothing to amplify and the flow would thus be steady (but unstable). Perfectly noiseless systems do not exist in reality.

- **Hydrodynamic oscillator.** This class of flow exhibits intrinsic dynamics and is thought to be insensitive to low-amplitude external disturbances[1]. Moreover, oscillators are self-excited: their oscillations, once triggered by an initial disturbance, however small, would persist even if the disturbance is subsequently removed and there was no noise whatsoever in the system. What enables the oscillations to persist is a continuous supply of kinetic energy from the baseflow. The oscillations dominate the entire flow and are at a well-defined natural frequency – and may also contain harmonics, as Strykowski and Niccum (1991) and Davitian et al. (2010) have shown. Examples of oscillators include counterflowing mixing layers, low-density jets, swirling jets, crossflowing jets, buoyant jet diffusion flames, and wakes at Reynolds numbers above the onset of von Kármán vortex shedding.

1.2.3 Global instability

If a flow has a sufficient region of absolute instability that it acts as a hydrodynamic oscillator, it is referred to as a globally unstable flow. A globally unstable flow thus oscillates with high amplitude at a discrete natural frequency. The oscillations are spectrally discrete because all temporally growing wavepackets with non-zero group velocity must, by definition, move away from the impulsive source. When viewed in the laboratory frame, therefore, the flow and its natural frequency (also called the global frequency) are left to be determined by the most upstream region of absolute instability, termed the 'wavemaker' by Pier (2003). Details on how to predict the global frequency can be found in Appendix A.

In a combustion system, the sensitivity of a globally unstable injector flow to upstream perturbations depends on the position of the wavemaker. If the flow is absolutely unstable everywhere, the global mode has a high amplitude everywhere and is thus relatively insensitive to external forcing. If, however, the flow is convectively unstable over an appreciable region between the injector lip and the wavemaker, the external forcing can amplify within this region, overwhelm the absolute instability, and hence dictate the frequency of the global mode.

---

[1] This assumption was first proposed over twenty years ago by Huerre and Monkewitz (1990) and has since been cited throughout the literature, even though it has only ever been justified with phenomenological models, such as the forced Landau equation.

1.3 Globally unstable flows

Global instability can arise in a number of different shear flows. This section focuses on the three that are most relevant to this thesis: non-reacting wakes, non-reacting jets, and jet diffusion flames.

1.3.1 Non-reacting wakes

Wake flows have played a central role in efforts to understand how absolute instability relates to global instability. Perhaps nowhere is this better exemplified than in the seminal study conducted by Koch (1985). Using a linear analysis, he computed the spatiotemporal stability of the wake behind a bluff body. From the findings, he hypothesised that in the absence of pressure feedback[1], the periodic self-excited nature of vortex shedding is caused entirely by hydrodynamic resonance arising from a region of absolute instability in the near wake.

Independent support for Koch's hypothesis emerged soon after, in the form of experimental evidence. In wind tunnel tests, Strykowski (1986) and Provansal et al. (1987) studied the dynamics of vortex shedding behind a cylinder at low Reynolds numbers. The Reynolds number was defined as $Re_d \equiv U_\infty d/\nu$, where U_∞ is the freestream velocity, d is the cylinder diameter, and ν is the kinematic viscosity. By impulsively raising Re_d above a critical value, the researchers were able to monitor the temporal evolution of the wake: from exponential amplitude growth in the initial linear regime through to nonlinear saturation in the form of self-sustained global oscillations, commonly known as von Kármán vortex streets.

Illustrating the emergence of the global oscillations, figure 1.2 shows time traces of Re_d and of the local fluctuating velocity in the wake, both measured by Strykowski (1986) with hot-wire anemometry. Immediately after Re_d is raised above a critical value of 46, the flow oscillations start to grow exponentially in time and eventually saturate into a finite-amplitude limit cycle. According to Zebib (1987), such an abrupt change in the dynamical behaviour of the system, as a control parameter is varied, indicates a Hopf bifurcation to a global mode.

---

[1] This is also known as hydroacoustic resonance, which can arise from the edge-tone mechanism of Powell (1961) or the shear-layer tone mechanism of Hussain and Zaman (1978).

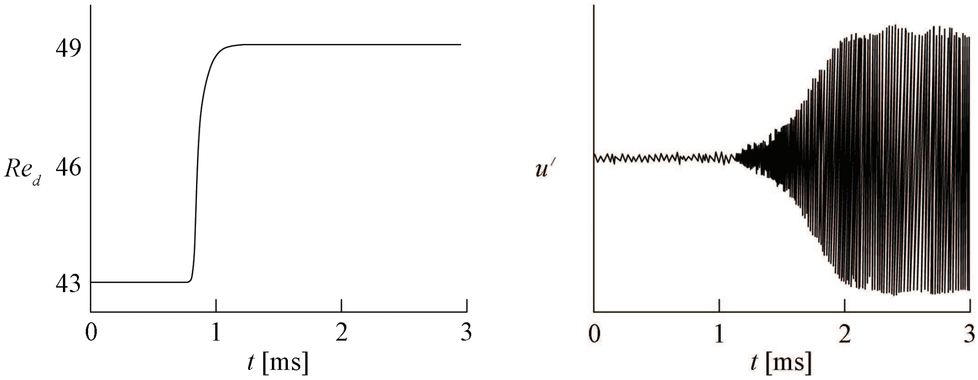

(a) (b)

Figure 1.2: Transition to global instability in a cylinder wake, triggered by a step increase in the Reynolds number above $Re_d = 46$. Originally published by Strykowski (1986), the plots show (a) the low-pass filtered Re_d and (b) the local fluctuating velocity in the wake.

To strengthen the causality between absolute and global instability, Chomaz et al. (1988) examined the evolution of a spatially developing flow[1] using a simplified Ginzburg–Landau model. In agreement with Zebib (1987), they found that hydrodynamic resonance can indeed occur via a Hopf bifurcation but only if the flow contains a sufficient region of absolute instability. After exploring the bifurcation in detail, the researchers proposed a sequence of transitions through which global instability can arise. That sequence involves the flow starting out as being stable, then becoming locally convectively unstable, then becoming locally absolutely unstable, then becoming linearly globally unstable, and finally reaching a nonlinear self-excited state or a limit cycle.

The link between absolute and global instability can be further strengthened by comparing spatiotemporal calculations to experimental data. Examining two-dimensional wakes at near-critical Reynolds numbers, Monkewitz (1988) found that although the transition from stability to convective instability occurs at just $Re_d \approx 5$, the first instance of absolute instability does not appear until $Re_d \approx 25$. Experiments by Williamson (1996) later showed that only above even higher values of the Reynolds number, $45 < Re_d < 47$, does vortex shedding arise. This

---

[1] This means that the flow is nonuniform in the streamwise direction.

sequence of wake transitions is consistent with the idea that for global instability to arise, a sufficient region of the flow must first become absolutely unstable.

The link between absolute and global instability becomes even more convincing when the effects of other parameters are considered. For an inviscid incompressible non-buoyant two-dimensional jet or wake bounded by two vortex sheets, Yu and Monkewitz (1990) solved the linear dispersion relations for both varicose and sinuous disturbances. Among the parameters considered were the density ratio, $s \equiv \rho_{in}/\rho_{out}$, and the shear ratio, $\Lambda \equiv (U_{in} - U_{out})/(U_{in} + U_{out})$, where the subscripts *in* and *out* denote the inner and outer fluid streams, respectively. To delineate the boundary between absolute and convective instability, the researchers presented their findings in s–Λ parameter space: figure 1.3.

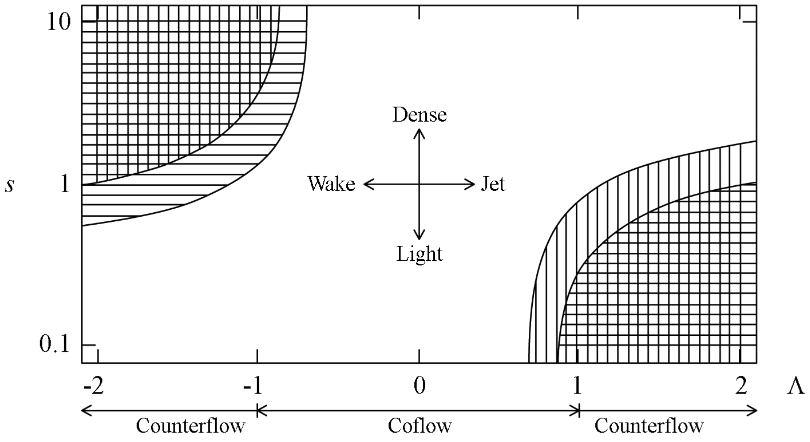

Figure 1.3: Regions of absolute instability as a function of density and shear for a two-dimensional inviscid shear flow, as calculated by Yu and Monkewitz (1990). The horizontal hatching denotes sinuous disturbances, and the vertical hatching denotes varicose disturbances.

There are three important features to note in figure 1.3. First, in both jets and wakes, counterflow ($|\Lambda| > 1$) promotes absolute instability, whereas coflow ($|\Lambda| < 1$) suppresses it. Physically this means that absolute instability is promoted if shear, the force driving the instability, dominates over advection, the force carrying the instability away. Second, in both jets and wakes, low density of the faster moving fluid, or high density of the slower moving fluid, also promotes absolute instability. This effect arises because the group velocity of the perturbations is weighted more heavily towards the velocity of the denser fluid. Third, in wakes the sinuous mode is always more unstable than the varicose mode, but in jets it is the other way round. All three of these features have been verified to various degrees by experiments.

Concerning the effect of shear, a common way to control Λ in wakes is to vary the velocity of the inner fluid. This can be done by changing the porosity of a bluff body exposed to a uniform freestream. Similar in concept to base bleed[1], this technique has been in use for over half a century to suppress unwanted von Kármán vortex shedding (Wood, 1964). A striking example can be seen in the smoke-visualisation photos taken by Inoue (1985). Shown in figure 1.4, they depict a freestream moving from left to right, at a Reynolds number of about 3000, past and around four flat plates, each with a different open area ratio, $\beta \equiv$ (open plate area)/(total plate area), a measure of the plate porosity. By qualitative inspection, the researcher found the existence of a critical value of β above which vortex shedding is suppressed. At low β (figures 1.4a and 1.4b), the outer flow is substantially faster than the inner flow, and hence the shear forces are large. This causes the wake to be absolutely unstable, with a global mode in the form of large-scale sinuous oscillations. Reducing the shear just slightly, however, by increasing β from 0.37 (figure 1.4b) to 0.39 (figure 1.4c), causes a noticeable dampening of the oscillation. Reducing the shear further, by increasing β to 0.55 (figure 1.4d), causes a complete suppression of the global mode. In its place emerges a far-wake instability consisting of small-scale vortices that roll up and grow downstream. This new instability, convective and no longer absolute, is driven by upstream disturbances and background turbulence rather than by hydrodynamic resonance[2]. Recent numerical simulations by Arcas and Redekopp (2004) have verified these findings, as well as addressing other areas of vortex control such as the effect of nonuniform momentum-flux distribution in the wake.

---

[1] Pioneered by Canadian engineer Gerald Bull, base bleed is a technique for extending the range of artillery. It involves releasing, on ignition, a small volume of gas, stored in a pressurised chamber at the back of a shell, into the low-pressure wake, thus reducing the pressure imbalance responsible for form drag. (Gerald Bull was murdered in mysterious circumstances in 1990.)

[2] In other words, if all noise sources were somehow removed, there would be nothing for the convective instability to amplify and the flow would thus be steady (but unstable).

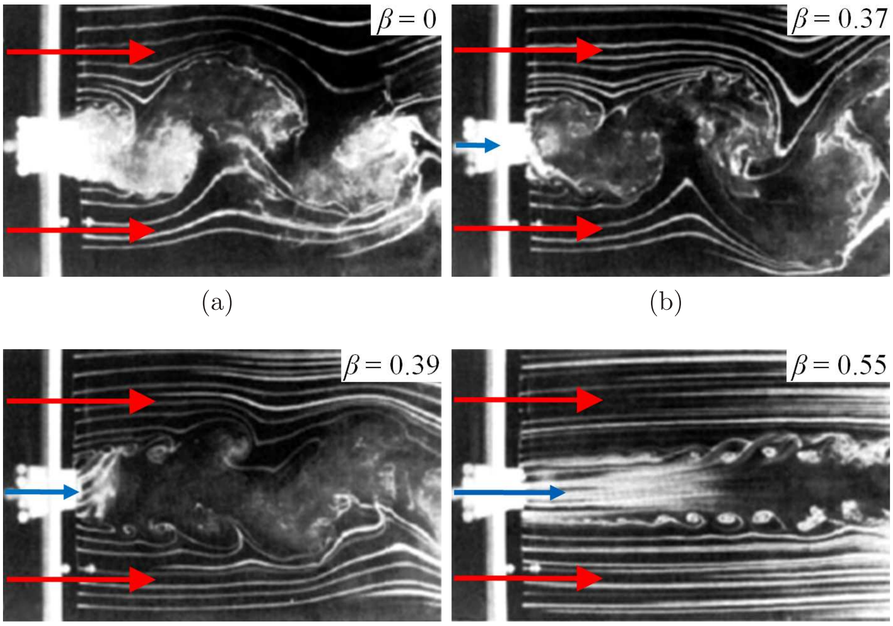

(a) (b)

(c) (d)

Figure 1.4: Suppression of von Kármán vortex shedding due to a reduction in shear, achieved by the use of porous flat plates with different open area ratios: (a) $\beta = 0$ or solid plate, (b) $\beta = 0.37$, (c) $\beta = 0.39$, and (d) $\beta = 0.55$. The freestream, made visible with smoke seeding, moves from left to right, as indicated by the red arrows. The flat plate is at the centre left, and the velocity through it is indicated by the blue arrows, whose length represents the velocity magnitude. All the images were taken by Inoue (1985).

As for the effect of density, figure 1.3 predicts that absolute instability – and thus global instability – can be suppressed if the wake is lighter than its surroundings. This effect has been observed in laboratory experiments (Berger and Schumm, 1988; Mori et al., 1986), numerical simulations (Hannemann and Oertel Jr, 1989), and theoretical analyses (Sevilla and Martínez-Bazán, 2006).

In the laboratory, the easiest way to produce a reduction in density, besides changing fluids, is to add heat. Because the viscosity of a real fluid depends on temperature, however, doing this raises the question of whether the suppression of global instability might be due to a modification (an increase if the fluid is a gas) of the viscous forces. To answer this, Yu and Monkewitz (1990) conducted a spatiotemporal analysis, specifying an ideal gas, a finite Reynolds number, a temperature profile similar to the velocity profile, and the use of Sutherland's relation to model the dependency of viscosity on temperature. On finding similar results with both constant and temperature-dependent viscosity fluids, they concluded that the suppression of absolute instability is caused primarily by density variations and the modification of inertial forces, rather than by viscosity variations. This conclusion has since paved the way for the popular practice of using heat addition to achieve low density in experiments on global instability.

1.3.2 Non-reacting jets

According to figure 1.3, jets discharging into a quiescent fluid can contain regions of absolute instability if s is sufficiently low. Using direct numerical simulation (DNS), Nichols et al. (2007) showed that this is because the KH instability, acting at the inflexion point in the radial profile of axial velocity (Rayleigh, 1879), becomes increasingly unstable as the density gradient steepens in the opposite direction to the velocity gradient. In particular, they found that the absolute growth rate ($\omega_{0,i}$) is proportional to the logarithm of an alignment integral:

$$\Sigma_{u\rho} = -\int_0^\infty \frac{\partial u}{\partial r}\frac{\partial \rho}{\partial r} r \mathrm{d}r, \tag{1.9}$$

where u is the streamwise velocity and r is the radial coordinate. Because ω appears in the exponent of (1.5), the initial growth rate is proportional to $\Sigma_{u\rho}$. If the velocity and density profiles align such that $\Sigma_{u\rho}$ becomes large enough to induce absolute instability ($\omega_{0,i} > 0$) over a significant length of the jet[1], global instability may develop, leading to self-sustained oscillations. The physical cause of instability is the destabilising action of baroclinicity[2] in the shear layers.

One of the most revealing studies on absolutely unstable jets was conducted over two decades ago by Monkewitz and Sohn (1988). Using a linear analysis, these researchers examined the instability characteristics of an axisymmet-

---

[1] The region of the jet that first becomes absolutely unstable is the potential core, because this is where the gradients of velocity and density are steepest.

[2] According to Green (1995), baroclinicity arises when the pressure and density gradients are not aligned – i.e. when isobars and isopycnals are not parallel. Its effect on the flow is a torque, proportional to $\nabla\rho \times \nabla p$, that can generate vorticity, even without the action of viscosity.

ric jet in response to a reduction in jet density. They used model profiles for the velocity and density, and assumed the fluid to be an inviscid ideal gas with a jet Reynolds number, $Re_j \equiv \rho_j U_j d_j / \mu_j = \infty$, where μ is the dynamic viscosity. They also neglected buoyancy, implying a jet Richardson number, $Ri_j \equiv g d_j (\rho_\infty - \rho_j)/\rho_j U_j^2 = 0$, with g denoting the gravitational acceleration. For a constant-density jet ($s = 1$), they did not find any velocity profile capable of supporting absolute instability. On reducing the jet density, however, they found the first instance of absolute instability[1] at $s = 0.72$. Its shape was varicose and its frequency, f, scaled with the Strouhal number[2] defined as $St_d \equiv f d_j / U_j$. The instability frequency thus scaled with the jet diameter, or the distance separating the shear layers, rather than with the momentum thickness. This suggests that the instability was caused by a resonant interaction between the shear layers (by a 'jet-column mode') rather than by actions of the individual shear layers (not by a 'shear-layer mode').

Inspired by the discovery of absolute instability in theoretical jets, experimentalists began searching for global instability in real jets. In the axisymmetric case, they include Sreenivasan et al. (1989), Monkewitz et al. (1990), Kyle and Sreenivasan (1993), Richards et al. (1996), Pasumarthi and Agrawal (2003), and Yildirim and Agrawal (2005). In the two-dimensional case, contributions have come from Yu and Monkewitz (1993), Raynal et al. (1996), and Yu et al. (2001). Their collective findings can be summarised as follows:

- Constant-density jets ($s = 1$), whether axisymmetric or two-dimensional but only when they are coflowing ($0 \leq \Lambda \leq 1$), are always globally stable[3]. This means that they are strongly receptive to external disturbances, acting as hydrodynamic amplifiers. Applying low-amplitude periodic forcing to the base of such jets, as Crow and Champagne (1971) have done, can cause a shortening of the potential core, a change in the spatial distribution of turbulence intensity, and an increase in the spread rate.

---

[1] This instability threshold was for a vorticity thickness equal to 8.7% of the jet diameter.

[2] Predicted values of the Strouhal number ranged between 0.25 and 0.50.

[3] A real flow that is 'globally stable' is sometimes referred to as 'convectively unstable' in order to emphasise that it behaves like a hydrodynamic amplifier. This does not imply that absolute instability is absent in the flow, but only that it does not exist over a region large enough to support a global mode.

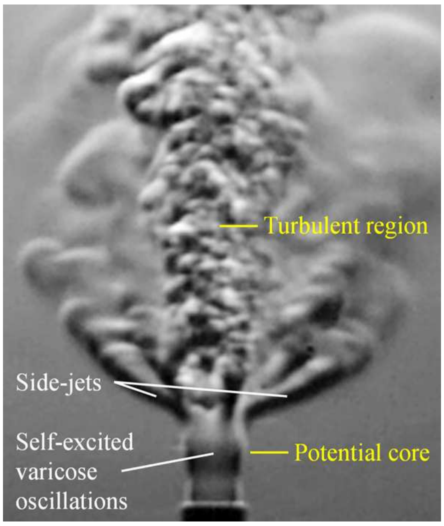

Figure 1.5: Schlieren image of a globally unstable low-density round jet. Self-excited varicose oscillations are visible around the potential core. Side-jets are visible in the near field, just downstream of the potential core but upstream of the fully-developed turbulent region. The jet fluid is helium and the ambient fluid is air. The jet conditions are: $d_j = 6$ mm, $s = 0.14$, $\Lambda = 1$, $Re_j = 1100$, and $Ri_j = 7.4 \times 10^{-4}$.

- Axisymmetric jets discharging into a quiescent fluid ($\Lambda = 1$) can become globally unstable if s is below a critical range of about 0.60–0.72, in agreement with the theoretical prediction by Monkewitz and Sohn (1988). The global instability manifests as self-excited oscillations of the varicose mode, also in agreement with theory. A globally unstable low-density round jet is shown in the schlieren image of figure 1.5.

- Two-dimensional jets discharging into a quiescent fluid ($\Lambda = 1$) can likewise become globally unstable if s is sufficiently low. But the critical range of s below which the transition occurs is both higher and wider than that for the axisymmetric case, with Raynal et al. (1996) having reported it at $s = 0.7$ and Yu and Monkewitz (1993) at $s = 0.9$. This range is nevertheless consistent with the predictions by Yu and Monkewitz (1990) and Monkewitz et al. (1993). Its greater scatter has been attributed by Raynal et al. (1996) to differences in the shapes of the velocity and density profiles – particularly the shear layer thickness.

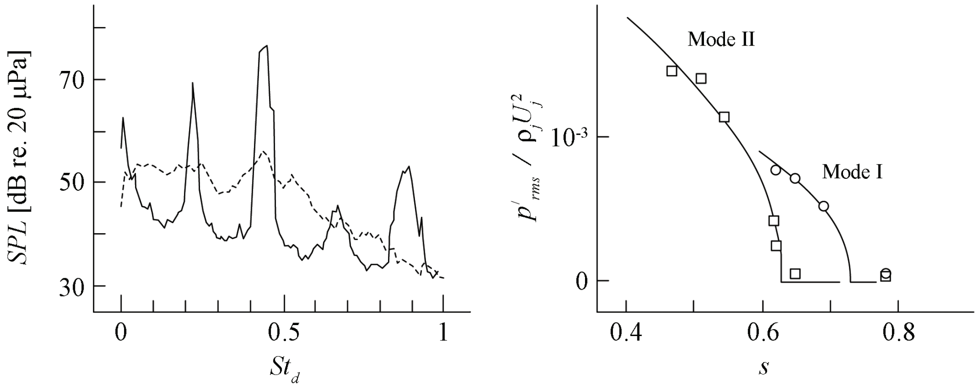

(a) (b)

Figure 1.6: Comparison between convectively and globally unstable round jets at $\Lambda = 1$, as published by Monkewitz et al. (1989). Subfigure (a) shows the near-field pressure spectra, with the convectively unstable jet ($s = 1$) indicated by the dashed line and the globally unstable jet ($s = 0.47$) indicated by the solid line. Subfigure (b) shows the amplitude of the near-field pressure fluctuations, normalised by the jet dynamic head, as a function of density for two distinct instability modes.

- Once triggered, a global mode causes the kinetic energy to concentrate at discrete frequencies, leading to sharp peaks in the measured spectra. In figure 1.6a, for example, which shows spectra of the sound pressure level (SPL) measured by Monkewitz et al. (1989), there are strong discrete peaks for the globally unstable jet, but only weak broadband peaks for the convectively unstable jet. In fact, the highest spectral peak for the globally unstable jet is nearly 30 dB higher than the background noise.

- The final saturated state of a globally unstable flow is a limit cycle, which is usually arrived at via a Hopf bifurcation, according to Huerre and Rossi (1998). A typical way to detect such an event is to plot the oscillation amplitude as a function of a control parameter. Known as a bifurcation diagram, the result resembles figure 1.6b, which, in this example, shows the root-mean-square (RMS) pressure fluctuation normalised by the jet dynamic head, $p'_{rms}/\rho_j U_j^2$, as a function of density, s. The bifurcation occurs at the value of s for which the oscillation amplitude begins to grow[1]. Once the bifurcation occurs, the oscillation amplitude increases in proportion to the square root of the deviation from the control parameter. This increase is accurately predicted by the Landau equation, as will be explained in §2.1.

- Compared to constant-density jets, low-density jets tend to spread more rapidly, often with spread rates[2] greater than unity. According to Sreenivasan et al. (1989), this is a near-field phenomenon, caused by an instability of the transition region and not by the dynamics of the far-field turbulent region. In axisymmetric jets, the spreading is asymmetric, involving intermittent ejections of fluid out of the jet column. These ejections, known as side-jets, are visible in the schlieren image of figure 1.5. Their physical cause is thought to be the Widnall instability acting in the primary vortex rings (Widnall et al., 1974). In two-dimensional jets, this instability is inactive owing to a lack of symmetry, and thus the side-jets are not observed.

- For detection of global instability, the jet shear layers must initially be laminar, which means that the Reynolds number must be kept low ($< 10^4$). Otherwise, Huerre and Monkewitz (1990) have shown that even a strongly globally unstable jet can revert back to behaving like a convectively unstable jet, for reasons that Meliga et al. (2008) later attributed to the stabilising effect of the Mach number. Another concern is mode competition. For a fixed injector geometry, increasing the Reynolds number causes a decrease in the shear layer thickness. Using spatiotemporal theory, Jendoubi and Strykowski (1994) showed that if the shear layer becomes sufficiently thin, other instability modes – such as the helical mode (azimuthal wavenumber $m = 1$) and the double-helical mode ($m = 2$) – can become absolutely unstable. The competition between these new modes and the existing varicose mode ($m = 0$) could disrupt the orderly roll-up process, leading to distortion in the spectral energy distribution, possibly via nonlinear mechanisms.

---

[1] For the Mode I instability of figure 1.6b, this occurs at $s \approx 0.72$. The coexistence of two (or more) global modes is typical not just of low-density jets but of most globally unstable flows, which is consistent with the analysis by Chomaz et al. (1988).

[2] This is defined as the ratio between the local half width (i.e. the radius where u is half its centreline value) and the streamwise distance at which that half width is measured.

1.3.3 Jet diffusion flames

In a reacting jet, the flame alters the hydrodynamic instability. Its heat release produces a peak in the radial profile of temperature, leading directly to a local reduction in density and indirectly, if the jet discharges upwards against gravity, to a modification of the velocity profile via the action of buoyancy. To explain how these changes affect the hydrodynamics, figure 1.7 shows an image taken by Roquemore et al. (2003) of a laminar methane jet diffusion flame surrounded by a small amount of annular air coflow. The image contains two separate signals: (i) elastic Mie scattering from TiO_2 particles[1], viewed perpendicular to a laser sheet passing through the jet centreline; and (ii) natural chemiluminescence from the flame, integrated over a line of sight. Figure 1.7a shows an overview of the entire flow field, while figure 1.7b shows a detailed view of the shear layers in the near field. Superimposed on figure 1.7b are the mean velocity and density profiles. The velocity profile was measured by Lingens et al. (1996a) using laser Doppler velocimetry (LDV). The density profile was derived by Lingens (1995) using data from a flamelet library, LDV measurements of the flame strain rate, and images of the hydroxyl radical – used as an indicator of the reaction-zone location – taken with planar laser-induced fluorescence.

In the near field (figure 1.7b), buoyancy causes the velocity profile to gain two additional inflexion points, labelled IP2 and IP3, on either side of the jet centreline (Durao and Whitelaw, 1974; Hegde et al., 1994; Lingens et al., 1996a) – bringing the total to three on either side[2]. Depending on the location of these inflexion points relative to the density profile, the flow can become more unstable or less unstable. This happens via the mechanism described in §1.3.2, whereby the KH instability becomes increasingly unstable as the density gradient steepens in the opposite direction to the velocity gradient. In buoyant jet diffusion flames, the inflexion point (IP3) in the shear layer just outside the flame surface (i.e. on the oxidiser side) has a steep gradient and coincides with a section of the density profile that also has a steep gradient but in the opposite direction. This inflexion point is therefore absolutely unstable and gives rise to a strong global mode in the

---

[1] Seeded in both the fuel jet and the coflow air is $TiCl_4$ vapor. As the fuel and air mix and combust, the $TiCl_4$ vapor reacts with H_2O to form micron-sized TiO_2 particles (and HCl).

[2] A non-reacting jet has just one inflexion point, labelled IP1, on either side of centreline.

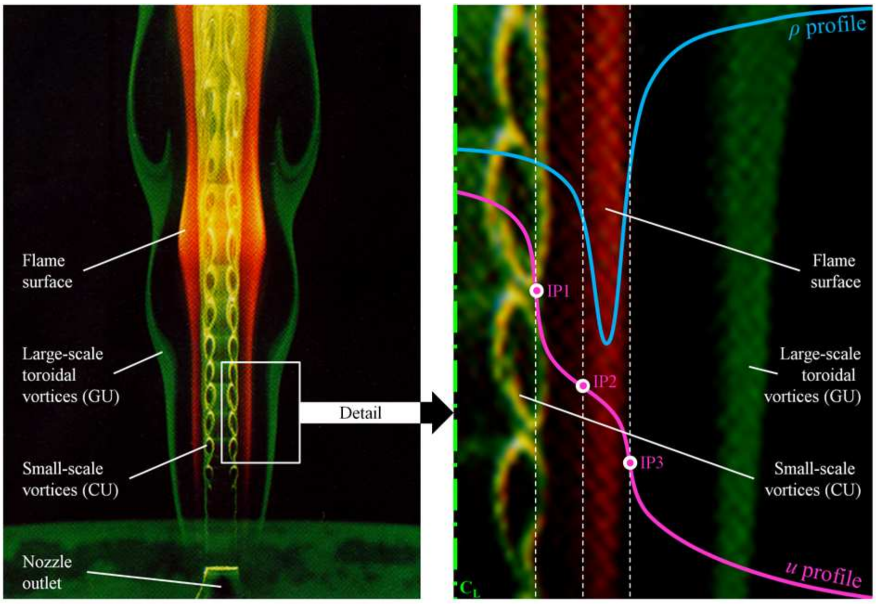

(a) (b)

Figure 1.7: Image of a laminar methane jet diffusion flame with a global mode in the form of large-scale toroidal vortices: (a) an overview of the entire flow field and (b) a detailed view of the shear layers in the near field, with the mean velocity and density profiles superimposed (see the text for a description). Originally published by Roquemore et al. (2003), the image contains two separate signals: Mie scattering from TiO_2 particles and natural chemiluminescence from the flame. The unburnt jet conditions are: $d_j = 10$ mm, $s = 0.55$, $\Lambda = 0.91$, $Re_j = 1867$, and $Ri_j = 8.4 \times 10^{-3}$. CU, convectively unstable; GU, globally unstable.

outer shear layer[1]. This global mode develops into large-scale toroidal vortices, rolling up periodically at low frequencies, typically on the order of 10–20 Hz. As these vortices grow downstream, they interact with the flame, stretching its surface, altering its local temperature, thickness and curvature, and even causing its extinction if the induced strain rates are sufficiently high[2] (Lewis et al., 1988). The result, according to Chen et al. (1989), is that the hydrodynamic global mode modulates the heat release in synchronisation.

---

[1] According to Maxworthy (1999), this is the same global mode that is responsible for the flickering of a candle flame.

[2] In terms of affecting combustion, the strain rate is perhaps the most influential, according to Lingens et al. (1996b). High strain rates can not only cause reductions in flame temperature and thickness (Katta and Roquemore, 1995), but can also affect the formation, oxidation, and spatial distribution of soot particles (Cuoci et al., 2009).

It has been known for some time that the flicker of a buoyant jet diffusion flame can be suppressed by adding two control cylinders[1] just downstream of the injector (Toong et al., 1965). Similarly, vortex shedding behind a cylinder can be suppressed by adding one control cylinder[2] just downstream (Strykowski, 1986; Strykowski and Sreenivasan, 1990). As noted in §1.3.1, vortex shedding behind a cylinder arises from a region of absolute instability in the near wake. What the control cylinder does, according to Strykowski and Sreenivasan (1990)[3], is diffuse the vorticity concentrated in the shear layers, thereby changing the wake from being absolutely unstable to convectively unstable. Recently, Giannetti and Luchini (2007) have suggested that the control cylinder works also by introducing force-momentum feedback. Regardless of the physical mechanisms involved, the fact that the same stabilising effect is observed in buoyant jet diffusion flames is strong evidence that they are also absolutely unstable at their base.

In buoyant jet diffusion flames, the inflexion point (IP3) that is responsible for absolute instability lies just outside the flame surface, where buoyancy causes the radial gradients of velocity and density to have opposite sign (Lingens et al., 1996a). Conversely, buoyancy causes the inner inflexion point (IP1) to become more stable – but not so stable that it prevents the inner shear layer from rolling up into small-scale convectively unstable vortices, clearly visible in figure 1.7. Consequently, unlike that of a non-reacting low-density jet (in which the inner inflexion point is absolutely unstable and controls the global mode), the global frequency of a buoyant jet diffusion flame is relatively insensitive to the velocity and diameter of the inner jet, as is well documented in the literature. Instead it is very sensitive to the factors affecting buoyancy, such as the gravitational acceleration and the adiabatic flame temperature (Lingens et al., 1996b). Ingenious experiments on aircraft and centrifuges have demonstrated this strong dependence on g and weak dependence on other factors (Durox et al., 1995, 1997; Sato et al., 2000).

---

[1] A control cylinder is simply a stationary cylinder placed in the flow. It does not have to move or vibrate to function. Usually its diameter is smaller than the characteristic lengthscale of the flow (e.g. smaller than the diameter of an injector or that of a main cylinder).

[2] Or one control plate, as in the experiments by Shao et al. (2007).

[3] Strykowski and Sreenivasan (1990) also suggested that the control cylinder diverts a small amount of fluid into the wake of the main cylinder, thus imparting a stabilising effect similar to that imparted by base bleed (page 19).

1.4 Nonlinear dynamics

The hydrodynamic stability theory discussed in §1.2.1 is based on linear analysis. Real hydrodynamic systems, however, are governed by nonlinear equations and can therefore exhibit much richer behaviour. There are in fact several different possibilities for the evolution of a nonlinear dynamical system, and those most often seen in self-excited flows are discussed in this section.

1.4.1 Unforced systems

In a linear stability analysis, the aim is to characterise the behaviour of infinitesimal perturbations around some base state. Usually that base state is a steady solution[1] of the governing equations, known as a 'fixed point'[2]. If all infinitesimal perturbations around this solution decay in time, it is called a 'stable fixed point'. If at least one infinitesimal perturbation grows in time, it is called an 'unstable fixed point'.

No natural system can grow indefinitely, however. If the fixed points are unstable, perturbations grow until they are no longer small. Nonlinear effects then take over and the system tends to another solution of the governing equations. In most cases, the system tends to a periodic solution, which maps onto itself every cycle. In some cases, it tends to a biperiodic solution, which maps onto itself every two cycles, or to a quasiperiodic solution. All periodic solutions[3] are limit cycles because they are the solutions to which the system tends as time approaches $\pm\infty$ ($+\infty$ for a stable limit cycle and $-\infty$ for an unstable limit cycle). In rare cases, the system even tends to a chaotic solution[4], which never maps onto itself. All of these solutions have been discussed before (e.g. by Strogatz, 1994) and have been seen in the celebrated Lorenz (1963) waterwheel as well as in a real thermoacoustic system (Kabiraj et al., 2011).

---

[1] Alternatively the base state can be a periodic solution, in which case the technique is called a Floquet stability analysis (Drazin and Reid, 2004).

[2] Also known as a 'point attractor' in phase space.

[3] In phase space, such solutions correspond to closed trajectories around 'periodic attractors'.

[4] A chaotic solution is aperiodic. In phase space, it sweeps out a non-repeating trajectory around one or more 'strange attractors'.

1.4.1.1 Simple oscillators

There are many toy models for oscillators. The simplest is a damped mass on a spring:

$$m\ddot{x} + b\dot{x} + kx = 0, \tag{1.10}$$

where m is the mass, x is its position, b is the damping coefficient, and k is now the spring constant (not the axial wavenumber). The overdot denotes differentiation with respect to time. The model of (1.10) has a single fixed point at $x = \dot{x} = 0$, whose stability is determined by the sign of b: it is stable for $b > 0$ (positive damping) and unstable for $b < 0$ (negative damping).

Without a periodic solution, however, the damped mass on a spring is not a suitable model for this thesis. Because this thesis concerns self-excited flows, it needs a model with self-excited solutions. One such model is the van der Pol (VDP) oscillator. Named after its Dutch discoverer, van der Pol (1926), the VDP oscillator was originally proposed as a model for electrical circuits (Cartwright, 1960). Over the years, though, it has been used throughout the biological and physical sciences to explain various nonlinear phenomena, such as the alternating hypomanic–depressive episodes in bipolar II disorder (Daugherty et al., 2009), vortex shedding behind a cylinder (Baek and Sung, 2000), and others[1]. Similarly, it will be used in §4.2.4 to explain experimental observations on two different self-excited flows: a low-density jet and a jet diffusion flame.

According to Fay (2009), the VDP oscillator has periodic solutions as well as a fixed point (at $x = \dot{x} = 0$). This means that, for certain model parameters, the oscillations can take on a stable limit cycle. The homogeneous equation describing those oscillations is:

$$\ddot{x} - \epsilon(1 - x^2)\dot{x} + \omega_n^2 x = 0, \tag{1.11}$$

where ω_n is the natural angular frequency and ϵ is a positive scalar parameter

---

[1] Other examples include the response of nerve membranes (Fitzhugh, 1961) and the interaction between two tectonic plates (Cartwright et al., 1999).

that controls the degree of self-excitation and nonlinear self-limitation. To see how this system reaches a limit cycle, consider the sign of $-\epsilon(1-x^2)$ as x oscillates. This quantity is like a damping coefficient, analogous to the constant b in (1.10). When $|x| < 1$, it is negative, causing self-excitation and therefore growth. When the system grows to $|x| > 1$, however, it becomes positive, causing self-limitation and therefore decay. The system thus alternates between positive and negative damping as x oscillates. Eventually the positive damping cancels out the negative damping over a cycle and the system settles into a limit cycle.

For small ϵ, the system has just a small degree of nonlinearity and its trajectory in phase plane is almost a perfect circle (with radius 2 and period 2π). This limit cycle is stable, attracting all other trajectories regardless of whether they originate inside or outside the circle[1]. For large ϵ, the system has more nonlinearity and its trajectory is no longer circular. Instead it exhibits 'relaxation oscillations', described by van der Pol (1926) as periodic oscillations that have a slow gradual buildup followed by a fast sudden discharge (or vice versa).

1.4.1.2 Hydrodynamic oscillators

In hydrodynamics, periodic solutions, or limit cycles, are known as nonlinear global modes. For some of these, such as the 'steep-fronted nonlinear global mode' and the 'elephant mode', Chomaz (2005) proposed that the global frequency is determined by the wavemaker – the most upstream region of absolute instability (page 15). In the self-excited flows of this thesis, the wavemaker is thought to have the same effect. In low-density jets, the wavemaker is at the exit plane of the nozzle (Lesshafft et al., 2006). In jet diffusion flames, it is at an unknown distance downstream (§1.3.3).

1.4.1.3 Thermoacoustic oscillators

For most thermoacoustic limit cycles, the energy input from combustion each cycle and the energy drain from damping each cycle tend to be just small fractions of the total acoustic energy already in the cycle[2] (Culick, 2006). One consequence

---

[1] In other words, the entire phase plane is a basin of attraction for this periodic attractor.

[2] According to Lieuwen and McManus (2002), to maintain a pressure amplitude of 1 psi requires the transfer, to the acoustic field, of less than 0.01% of the thermal energy released by

of this, alluded to in §1.1.1, is that there are two well-separated timescales: a fast timescale over which the system oscillates and a slow timescale over which its amplitude and phase vary. Another consequence is that the thermoacoustic oscillations have similar frequencies to the natural acoustic modes of the combustor. In other words, although there is always a frequency shift between the two due to heat release and damping, it is usually small relative to the oscillation frequency itself (Culick, 2006).

It follows that a thermoacoustic system should be decomposed into a set of coupled oscillators, based on the natural acoustic modes of the system. This approach was started by Crocco's group at Princeton in the 1960s and was continued by Culick's group at Caltech from then until the present day. A summary of that work can be found in the monograph by Culick (2006). The main analysis involves an expansion of the full governing equations in terms of two small parameters: the acoustic Mach number, M', which measures the magnitude of the velocity perturbations relative to the speed of sound, and the mean flow Mach number, $\overline{M}$, which measures by proxy the magnitude of the heat release.

Solving the full system of coupled oscillators is technically challenging[1]. Many of the qualitative features can be examined with a single oscillator instead, in this case that which represents the first fundamental acoustic mode of the chamber:

$$\ddot{x} + \omega^2 x = f(x, \dot{x}), \tag{1.12}$$

This was the approach taken by Culick (1971, 2006) to identify the features that thermoacoustic systems share with the toy models of §1.4.1.1. This type of equation can be analysed with a two-timing technique (chapter 7 of Strogatz, 1994) or a time-averaging technique (Culick, 1971).

The terms on the left hand side of (1.12) are linear and represent an oscillation at angular frequency ω. The ensemble term f represents heat release, damping, and other effects such as nonlinear acoustics[2]. The linear component of f that is

---

a typical combustion process.

[1] Recent developments in continuation analysis, nevertheless, make it possible, as Jahnke and Culick (1994) and Juniper (2011) have shown.

[2] Nonlinear acoustics acts as an extra source of damping in this model.

in phase with x causes a frequency shift between the thermoacoustic mode and the natural acoustic mode. The linear component of f that is in phase with $\dot{x}$ causes growth or decay of the oscillations, depending on its sign – just as it does for the damped-mass-on-a-spring example of (1.10). The nonlinear components of f, which include the heat release, damping and acoustics, determine the amplitude of the periodic solution. The relative influence of each of these nonlinear components depends on the exact system. Gas turbines, for example, have low acoustic Mach numbers and are most influenced by nonlinear heat release. Solid-fuelled rockets, by contrast, have high acoustic Mach numbers and are therefore also influenced by nonlinear acoustics.

The key point is that, to a first approximation, both hydrodynamic and thermoacoustic systems can be regarded as harmonic oscillators with small nonlinear terms.

1.4.2 Forced systems

Introducing external forcing to a self-excited oscillating system can induce a response that is more complicated than that which typically arises without forcing.

1.4.2.1 Simple oscillators

The simplest forced oscillator is a forced damped mass on a spring:

$$m\ddot{x} + b\dot{x} + kx = F, \tag{1.13}$$

where F is an external forcing function. This second-order ordinary differential equation can be solved with the Complementary Function and Particular Integral technique. The solution has a contribution at the (undamped) natural frequency, $\sqrt{k/m}$, which dies away if the system is damped ($b > 0$). If the forcing is harmonic, the solution has a contribution at the forcing frequency, which persists into the steady state.

As explained in §1.4.1.1, however, the damped mass on a spring is not a suitable model for this thesis. It does not have a periodic solution and so can not model a self-excited flow. Even when forced, it has only a stable or unstable fixed point at $x = \dot{x} = 0$. The steady state solution either ends up at the forcing frequency, if the transients are damped, or blows up to infinity, if the forcing is at the natural frequency and is sufficiently strong to negate the damping terms.

Instead the VDP oscillator will be used. The reasoning behind this choice was explained in §1.4.1.1. When unforced, the VDP oscillator has periodic solutions as well as a fixed point. When forced at frequencies around its natural frequency[1], it has quasiperiodic[2] solutions as well as lock-in[3] solutions (van der Pol and van der Mark, 1927). For certain forcing conditions, it even has chaotic solutions (Davis, 1962; Ott, 2002). Thus, with its rich dynamics, the VDP oscillator should be a suitable model with which to examine the effect of forcing on self-excited flows. The success of this will be discussed in §4.2.4.

1.4.2.2 Hydrodynamic oscillators

As noted in §1.3, there are three self-excited systems that are particularly relevant to this thesis: (i) vortex shedding in a cylinder wake, (ii) bulging of a low-density jet, and (iii) bulging of a jet diffusion flame. The effect of open-loop[4] sinusoidal forcing on the first two systems has been investigated before.

In wind tunnel tests, Provansal et al. (1987) examined the forced dynamics of vortex shedding in a cylinder wake at near-critical Reynolds numbers. Using

---

[1] This is done by adding a forcing function to the right hand side of (1.11).

[2] A quasiperiodic solution can be regarded as a combination of several periodic solutions, each with a different natural frequency. These natural frequencies, however, must be incommensurable, which means that they cannot be rational multiples of each other. In the Fourier transform of the system motion, quasiperiodicity manifests as a train of delta functions at integer combinations of the different natural frequencies (Nayfeh and Mook, 1995). The spectrum of a quasiperiodic solution is thus dominated by discrete tones, and can be readily distinguished from that of a chaotic solution, which is dominated by broadband tones.

[3] Known as 'entrainment' in the field of dynamical systems, lock-in is defined as being when the natural frequency of a self-excited oscillator shifts to the forcing frequency. It is accompanied by a suppression of spectral energy around the natural frequency. The spectrum of a locked-in solution is thus dominated by the forced mode – sometimes with weaker components at the harmonics and subharmonics – and shows no evidence of the natural mode. The term 'entrainment' will not be used in this thesis, however, because it could be confused with the entrainment of fluid mass. Instead the term 'lock-in' will be used.

[4] The term 'open-loop' implies that the properties of the forcing signal (i.e. its amplitude, frequency, phase, and duty cycle) do not depend on the state of the system being forced. This is in contrast to 'closed-loop' forcing, which involves feedback and active control.

a loudspeaker mounted in the upstream plenum, these researchers forced their wake at several amplitudes and frequencies. For certain forcing conditions, they found that the self-excited oscillations, at a natural frequency f_n, can lock into the applied forcing and take on its frequency, f_f. To show these forcing conditions, they plotted the critical forcing amplitude required for lock-in, A_{loc}, as a function of f_f. Referred to as a 'lock-in map', this is reproduced in figure 1.8. When f_f is close to f_n, only a low forcing amplitude is required for lock-in. When f_f is far from f_n, however, a high forcing amplitude is required for lock-in. The relationship between A_{loc} and $|f_f - f_n|$ is linear, giving rise to a distinctive $\vee$-shaped curve (which will be seen again in other self-excited systems). According to the researchers, this linear relationship is accurately predicted by a simplified Stuart–Landau model (Appendix B). Others who have observed similar lock-in behaviour include Koopmann (1967) and Stansby (1976). Unlike Provansal et al. (1987), though, these researchers used mechanical vibration, rather than acoustics, to force their cylinder wakes. Even so, their experimental data, compiled together by Blevins (2006) and plotted in figure 1.9, show similar increases in A_{loc} with increasing $|f_f - f_n|$.

Lock-in can also occur in self-excited jets. This was demonstrated, for example, by Sreenivasan et al. (1989) using open-loop forcing on a globally unstable low-density jet[1]. With a loudspeaker mounted upstream, these researchers forced their jet at several amplitudes but over only a narrow range of frequencies. Their lock-in map, verified by Hallberg and Strykowski (2008), is reproduced in figure 1.10 for comparison with figures 1.8 and 1.9. It shows that in order for the fundamental global mode – in the form of varicose oscillations and labelled '1/1 Lock-in' – to lock into the applied forcing, the forcing amplitude must be increased above a critical threshold, A_{loc}, which itself increases in proportion to $|f_f - f_n|$. The map shows also that lock-in can occur at subharmonics[2] of the fundamental global frequency. The result is a set of $\vee$-shaped curves, which bear a striking resemblance to the ones seen earlier for self-excited cylinder wakes.

---

[1] Mixtures of helium and air were used to create the light jet fluid.

[2] Subharmonic lock-in refers to the situation where a self-excited oscillator locks into some external forcing whose frequency is near a sub-rational multiple of the fundamental frequency of the natural mode. Besides occurring in low-density jets, subharmonic lock-in occurs in wakes behind a flat plate, as Fang and Chen (2000) have shown.

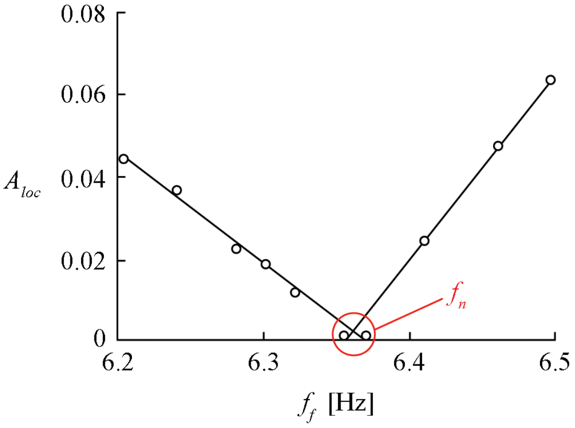

Figure 1.8: Lock-in map for a self-excited cylinder wake, as published by Provansal et al. (1987). The linear lock-in relationship is typical of most globally unstable flows. The abscissa intercept corresponds to the natural frequency of vortex shedding (the fluctuations in the natural frequency are due to thermal-induced fluctuations in the freestream velocity). The definition of A_{loc} is the upstream velocity fluctuation, due to forcing, at the onset of lock-in normalised by the natural velocity fluctuation in the wake.

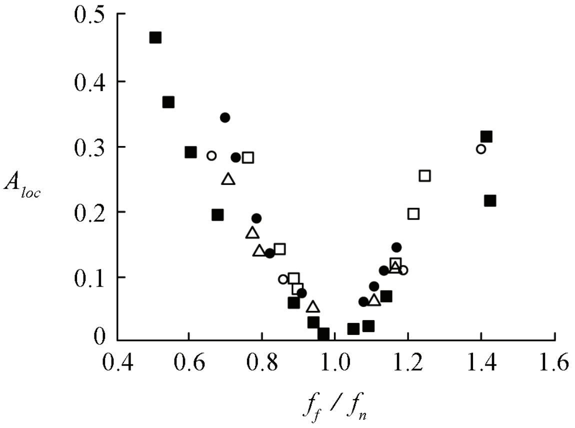

Figure 1.9: As for figure 1.8 but with data supplied by Koopmann (1967) and Stansby (1976). The forcing frequency is now normalised by the natural frequency of vortex shedding. The definition of A_{loc} is the cylinder vibration amplitude at the onset of lock-in normalised by the cylinder diameter. The different symbols represent data at different Reynolds numbers: $100 < Re_d < 9200$. Details can be found in the book by Blevins (2006).

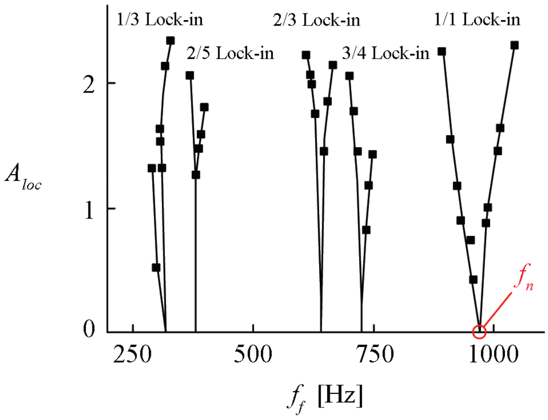

Figure 1.10: Lock-in map for a self-excited low-density jet, as published by Sreenivasan et al. (1989). The units of A_{loc} are arbitrary. The abscissa intercept of the '1/1 Lock-in' data points corresponds to the fundamental frequency of the global varicose oscillations. The other data points are included to show the possibility of subharmonic lock-in.

Another self-excited flow with similar lock-in behaviour is a crossflowing jet. According to the DNS of Bagheri et al. (2009), this system becomes globally unstable if the jet-to-crossflow velocity ratio falls below approximately 3. Recognising this, Davitian et al. (2010) applied open-loop acoustic forcing to a crossflowing jet under such conditions and compiled a map of the forcing amplitudes and frequencies at which lock-in occurred. Their lock-in map, reproduced in figure 1.11, shows the familiar $\vee$-shaped curve (thick solid line).

Lock-in is just one type of forced response, however. Some self-excited flows can exhibit quasiperiodicity as well. Quasiperiodicity tends to arise when f_f and f_n are close but incommensurable and when the forcing amplitude is insufficient to cause complete lock-in (i.e. when $A < A_{loc}$). For example, Sreenivasan et al. (1989), examining globally unstable low-density jets, mentioned that they saw this type of response, but they did not show the results. For another example, Davitian et al. (2010), examining globally unstable crossflowing jets, showed hot-wire spectra containing strong evidence of quasiperiodicity – a train of spectral peaks surrounding the forced and natural modes (see their figure 11c) – at forcing amplitudes just below A_{loc}, but they did not discuss that evidence in detail. For yet another example, Baek and Sung (2000), examining globally unstable

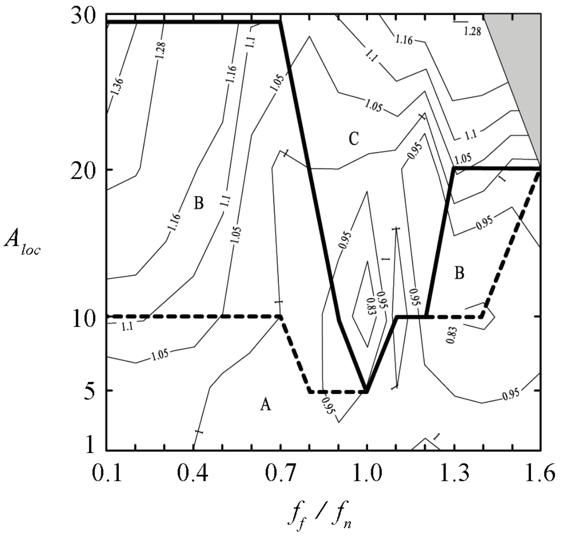

Figure 1.11: Lock-in map for a self-excited crossflowing jet, as published by Davitian et al. (2010). The jet-to-crossflow velocity ratio is 1.2. The thin lines represent contours of the ratio between u'_{rms} with and without forcing, measured by a hot-wire probe placed two jet diameters downstream. The definition of A_{loc} is the velocity fluctuation due to forcing at the nozzle outlet normalised by the mean jet velocity there (expressed as a percentage). The letters 'A', 'B', and 'C' denote the three types of spectral response observed. Lock-in is indicated by 'C' or the region above the thick solid line. Response types 'A' and 'B' are described in detail by Davitian et al. (2010).

cylinder wakes, discussed quasiperiodicity in the context of phase portraits and circle maps, but they did not do much more.

In this thesis, the universal lock-in behaviour found in various *non-reacting* self-excited flows – ranging from a cylinder wake to a low-density jet to a crossflowing jet – will be found in a *reacting* self-excited flow, a jet diffusion flame. The possibility of quasiperiodicity will also be explored, by measuring how the flame, as well as a low-density jet, responds to forcing when the forcing amplitude is just below the critical value required for lock-in.

1.4.2.3 Thermoacoustic oscillators

Only a handful of researchers have ever examined the forced response of a self-excited thermoacoustic system. Their findings show that low-amplitude forcing usually leads to a linear response[1] but that high-amplitude forcing can lead to a much richer nonlinear response.

Intrigued by the richness of nonlinearity, Lieuwen's group at Georgia Tech conducted a series of experiments on the interaction between forced modes and self-excited modes in a premixed swirl-stabilised flame[2] enclosed in a combustor (Bellows et al., 2005, 2006; Lieuwen and Neumeier, 2002). The forced modes were produced by loudspeakers mounted in an upstream plenum. The self-excited modes were produced by thermoacoustic resonance, not by hydrodynamic resonance. This means that without acoustic coupling (i.e. if the combustor were removed), the flame would not be self-excited and hence would not naturally oscillate. Of course it would still have some unsteadiness owing to the turbulent structures and convective instabilities in the underlying baseflow, but these would be relatively broadband and weaker than any self-excited resonant mode.

Forcing their flame and measuring the changes in dynamic pressure, Lieuwen's group observed two different types of response. In one type, lock-in cannot occur, even when $f_f \approx f_n$ and when the forcing amplitude is high. Instead the natural amplitude[3] always remains above the background noise level and the natural frequency merely shifts to a nearby non-harmonic value.

In the other type of response[4], lock-in can occur, albeit only when $f_f < f_n$. This behaviour is illustrated in figure 1.12: a lock-in map by Bellows et al. (2006) showing A_{loc} as a function of f_f. Again, as seen before in various self-excited hydrodynamic systems (§1.4.2.2), A_{loc} increases with $|f_f - f_n|$. The high degree of data scatter in this example, though, makes establishing a linear relationship difficult. The linear fit shown is from another article by Bellows et al. (2005) (but is based on the same experimental data) and can be regarded as the left half of a typical $\vee$-shaped lock-in curve. For every data point shown, the final state of lock-in is arrived at in the same way: as the forcing amplitude is increased (for

---

[1] A linear response implies that the forced modes do not interact with the self-excited modes. The response amplitude at the forcing frequency should therefore increase in proportion to the forcing amplitude. The response could take on various forms; for example, it could be the velocity fluctuation or the heat-release fluctuation, the latter only if the flow is reacting.

[2] The reactants were methane and air at room temperature and atmospheric pressure.

[3] Defined as the amplitude of the flame response at the natural self-excited frequency.

[4] This type of response occurs at the same equivalence ratio and flow rate as the first. The only difference is that f_n is slightly higher owing to a shorter combustor length.

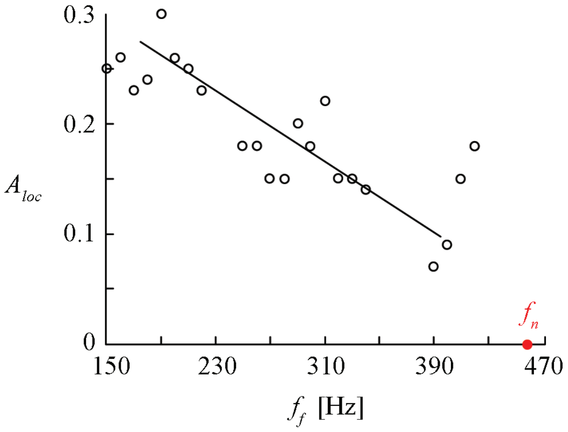

Figure 1.12: Lock-in map for a self-excited premixed flame, as published by Bellows et al. (2006). The self-excitation is due to thermoacoustic (not hydrodynamic) resonance arising from coupling with a combustor. The natural frequency of the combined flame–combustor system is $f_n = 461$ Hz, as indicated by the red circular marker. The definition of A_{loc} is the velocity fluctuation due to forcing at the burner outlet normalised by the mean flow velocity there.

$f_f < f_n$), the natural amplitude decreases monotonically until it settles onto the background noise level ($\approx 0.25\%$ of the mean chamber pressure). This decrease in the natural amplitude, the researchers found, is consistent with the prediction by a VDP-type model. That relationship was not explored in detail, however, leaving many open questions which will be addressed in this thesis (§1.5).

1.4.3 Coupled systems

As §1.4.2 has shown, most studies on forced systems – whether hydrodynamic or thermoacoustic – rely on the use of open-loop forcing. This type of forcing, however, is not an accurate representation of the forcing present in real systems, because it does not have any provisions for feedback. In a combustion system, for example, the frequency and amplitude of the thermoacoustic modes that force the flame depend on the heat release from the flame itself – in particular on how that heat release interacts with the natural acoustic modes of the chamber. A more realistic approach would be to consider the system as two coupled oscillators: one representing the flame and the other the chamber acoustics. Each oscillator would have its own natural frequency, and so would the coupled-oscillator system[1]. The stability of this coupled-oscillator system would then depend crucially on the way in which the individual oscillators force each other.

1.4.3.1 Simple oscillators

The governing equations for two coupled damped harmonic oscillators can be reduced to the standard form:

$$\ddot{x}_1 + b_1\dot{x}_1 + \omega_1^2 x_1 + C_{21}x_2 = 0, \tag{1.14}$$

$$\ddot{x}_2 + b_2\dot{x}_2 + \omega_2^2 x_2 + C_{12}x_1 = 0, \tag{1.15}$$

where the coupling function C_{21} is the effect of oscillator 2 on oscillator 1. If the two oscillators are assumed to lock into each other such that they share the same frequency and growth rate, then the governing equations can be further reduced to a quartic characteristic equation in the growth rate. The stability of the resultant system around the fixed point $\dot{x}_1 = x_1 = \dot{x}_2 = x_2 = 0$ is given by the Routh–Hurwitz criterion[2] (Hurwitz, 1964; Routh, 1877). It is obvious that the coupled system is unstable when either of the oscillators is individually unstable. It is less obvious that, for certain coupling functions, the coupled system can be unstable even when both oscillators are individually stable.

The technique above has been used by Awad and Culick (1986) and Yang and Culick (1990) to study pairs of coupled thermoacoustic modes. The output is a set of criteria for the coupling function that leads to different types of nonlinear instabilities. This is an area of promising research, for which the results in this thesis will be valuable.

---

[1] In reality, the natural frequency of the coupled-oscillator system (i.e. that of the thermoacoustics) is close to, but not necessarily equal to, one of the natural acoustic frequencies of the chamber. This is because, as noted in §1.4.1.3, the energy exchanged during a typical thermoacoustic limit cycle is only a small fraction of the total energy already in the cycle.

[2] This technique is commonly used to study coupled-mode flutter of aircraft wings, according to Blevins (2006).

1.4.3.2 Thermoacoustic oscillators

Most flame models assume that the heat-release fluctuations are functions of the velocity or pressure fluctuations within the combustor. Implicitly, these models assume that all flames are globally stable, that they all act as frequency-dependent amplifiers of external perturbations. What the models overlook is the fact that some flames may be globally unstable, that they can act as self-excited oscillators with their own intrinsic frequencies. If the oscillation frequency of a globally unstable flame is close to one of the acoustic frequencies of the chamber, lock-in would be expected, leading to high-amplitude pressure oscillations.

If, however, the oscillation frequency of the flame is far from the acoustic frequencies of the chamber, lock-in would not be expected. In such a situation, the thermoacoustic system would have two different frequencies: (i) one near the frequency of vortex shedding due to the hydrodynamic global mode, which scales with the Strouhal number, $St \equiv fd/U$, where d is the characteristic flame dimension[1]; and (ii) the other near the natural acoustic frequency of the chamber, which scales with the Helmholtz number, $He \equiv fL/c$, where L is the characteristic chamber dimension. Such coexistence of multiple modes has been observed by Chakravarthy (2010) in experiments on dump combustors[2]. It has also been investigated by Matveev and Culick (2003) using theory. These researchers wrote, however, that for their theory to be applied any further, the characteristics of unsteady flow and combustion must be determined more accurately. Of particular importance is the relationship between external forcing and heat release, and how it relates to the innate strength of a hydrodynamic global mode.

---

[1] Such as the injector diameter, bluff-body width, or height of a backward-facing step.

[2] It was demonstrated that even a simple variation of the Reynolds number can be a powerful diagnostic tool. If, in response, St remains constant (with He varying linearly), the instability can be regarded as hydrodynamic in origin. If, however, He remains constant (with St varying hyperbolically), the instability can be regarded as acoustic in origin.

1.5 Motivation and aim

If the fact that a flame is oscillating at one frequency means that its response near the natural acoustic frequencies of the chamber in which it sits is reduced, then the amplitude of the thermoacoustic oscillations may also be reduced. This would be very beneficial for industrial combustors. Before this hypothesis can be tested, however, it is necessary to test whether hydrodynamically self-excited flames are indeed insensitive to external forcing.

To that end, this thesis examines the response of jet diffusion flames to open-loop acoustic forcing (chapter 4). This type of flame is considered because[1] it has a hydrodynamic global mode whose innate strength can be adjusted – either by varying the coflow velocity or by making small changes to the fuel composition. Separately, a non-reacting low-density jet is examined in order to verify the experimental methodology (chapter 3). For both jets, the forcing is applied around the global frequency, at varying amplitudes, and the response examined over a range of frequencies (not just at the forcing frequency). In §4.2.4, this response will be compared to that of the VDP oscillator, which is a simple form (a single mode) of the oscillator used by Matveev and Culick (2003).

Both jets are expected to be broadly insensitive to forcing until the forcing amplitude is sufficient to cause lock-in. The response leading up to lock-in will be carefully examined because it will determine the extent to which the heat release can be decoupled from the incident pressure perturbations. Although Lieuwen's group has looked at a similar problem before (§1.4.2.3), their flames are fundamentally different. They did not have the ability to dial in the strength of the global mode, because it was intrinsically linked to the combustor acoustics. The flames examined in this thesis, by contrast, are self-excited by hydrodynamic resonance, and therefore have global modes whose strengths can be adjusted relatively easily. The aim is to answer the following questions:

- Are globally unstable flows actually insensitive to low-amplitude forcing at frequencies away from their natural frequencies?

---

[1] Another reason for considering jet diffusion flames is that their global frequencies are low enough (around 10–20 Hz) for simple diagnostics to be effective.

- How does the strength of a global mode affect the flow response at the forcing and natural frequencies?
- What happens to the flow response at frequencies away from the forcing and natural frequencies?
- Is there any difference between forcing above the natural frequency and forcing below it?
- Are the flows ever quasiperiodic? If so, under what conditions?
- How does the strength of a global mode affect the forcing amplitudes required for lock-in?
- Why do some flows lock into external forcing more readily than do others?
- What happens to the response amplitude as the forcing amplitude is increased through lock-in?
- Why is the lock-in curve always $\vee$ shaped?
- Can the flow response, including the phenomenon of lock-in, be predicted accurately by a forced VDP oscillator?

Chapter 2

Experimental methods

This chapter is divided into two parts. The first is an introduction to the techniques available for detecting and controlling global instability. The second is a discussion of the measurement diagnostics used in this thesis, including the technical details of two different injectors. The history and theory behind the diagnostics will not be discussed in detail, however, to avoid filling this chapter with information that can be easily found in reference texts.

2.1 Detecting global instability

The hydrodynamics community has been investigating self-excited flows for over three decades. In that time, their members have developed several proven techniques with which to detect global instability. According to Huerre and Monkewitz (1990), these can be divided into two categories: steady and transient.

In this thesis, only the steady category of experiments is used. A steady experiment involves examining the flow after it has bifurcated into a global mode and has settled into a limit cycle[1]. The focus is therefore on the final saturated state, rather than on the transient details of the bifurcation (which is the focus of the transient category of experiments). Often stability properties such as the global frequency and the saturation amplitude are measured for the periodic system, which may or may not be forced externally.

---

[1] The term 'steady' refers to the fact that the limit-cycle amplitude does not vary with time.

There are three ways to conduct a steady experiment, and this thesis makes use of all three. They are listed below in increasing order of the strength of the evidence that they provide for the existence of global instability:

- **Local spectral measurements.** Because global modes are self-sustained, they tend to oscillate at discrete natural frequencies. Their spectra are thus dominated by lines at the fundamental frequency of the oscillation. The signal being measured often does not oscillate exactly sinusoidally, so there may be additional peaks at integer multiples of the fundamental frequency, which represent harmonics. The spectra can be of any fluctuating quantity, such as the velocity, pressure, or temperature. In figure 1.6a, for instance, it was the sound pressure level.

- **Response to periodic forcing.** A more reliable way to detect global instability is to examine how the flow responds to periodic forcing applied at the frequency of a suspected global mode. If the flow is convectively unstable, acting as a hydrodynamic amplifier, the response amplitude should be proportional to the forcing amplitude – provided the latter is small enough to remain in the linear regime. If the flow is globally unstable, acting as a hydrodynamic oscillator, the response amplitude should be less sensitive to the same forcing. An example of this difference can be seen in figure 2.1a, which shows the response amplitude[1] of a counterflowing mixing layer as a function of the forcing amplitude. The forcing is sinusoidal and at the same frequency as the suspected global mode. The data shows that as the counterflow velocity (or the shear, Λ) is increased, the response amplitude becomes less sensitive to the applied forcing. This reduction in sensitivity indicates an emerging global mode. What also indicates a global mode is that when the flow is forced around its natural frequency and at sufficient amplitudes, it locks into the forcing frequency – in much the same way as self-excited nonlinear oscillators do.

- **Varying a control parameter.** Perhaps the most reliable way to detect global instability, short of performing a transient experiment, is to measure

---

[1] Here the response amplitude, measured with a hot wire, is defined as the local RMS velocity fluctuation normalised by twice the mean advective velocity of the two fluid streams.

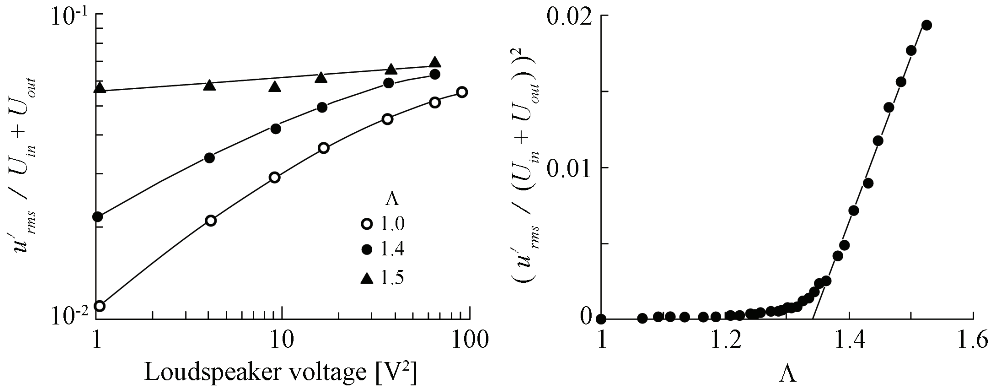

(a) Forced response (b) Bifurcation diagram

Figure 2.1: Oscillation amplitude of a counterflowing mixing layer as a function of (a) forcing amplitude and (b) shear ratio, both as published by Strykowski and Niccum (1991). In subfigure (a), the forcing, produced by a loudspeaker mounted $10d_j$ downstream, is at the same frequency as the suspected global mode. In subfigure (b), the oscillation amplitude – or more precisely, the saturation amplitude – is measured on the high-speed side of the mixing layer at $0.26d_j$ downstream. The data can be extrapolated back with a linear fit to the bifurcation point: $\Lambda_{bif} = 1.34$ where $(u'_{rms}/(U_{in} + U_{out}))^2 = 0$.

> the change in saturation amplitude due to a variation in some control parameter. The bifurcation occurs at the value of the control parameter for which the saturation amplitude begins to rise above the background noise. According to the Landau equation (Appendix B, last paragraph), for small deviations from the Hopf point and in the absence of forcing, the saturation amplitude should be proportional to the square root of the deviation from the control parameter. This dependence is illustrated in figure 1.6b for a low-density jet and in figure 2.1b for a counterflowing mixing layer.

Although transient experiments are not conducted for this thesis, they will be explained anyway for completeness. In a transient experiment, the flow behaviour is resolved in time as some control parameter is impulsively varied to induce a bifurcation. The global mode that emerges is thus monitored from its inception, through the initial exponential growth stage, to nonlinear saturation. The information gathered can be used not only as an indicator of global instability but also for comparison with theoretical predictions of the global frequency and the temporal growth rate. However, although transient experiments can provide information that is more conclusive than can steady experiments, they are far more difficult to perform. This is because the control parameter must be varied on a timescale that is at least one order of magnitude shorter than the period of the eventual global mode. In the laboratory, this difficulty often restricts the choice of the control parameter to the flow geometry[1], as the ability to make abrupt changes to the flow or fluid properties is impaired by inertial and diffusivity effects. Researchers who nevertheless have had success with transient experiments include Mathis et al. (1984), Strykowski (1986), and Provansal et al. (1987).

For both steady and transient experiments, the test facility must be designed and operated such that background noise is kept to a minimum. The key concern is that if external sources of flow excitation – such as acoustic cavity resonance and mechanical vibration – are not adequately attenuated, they can emulate the role of continuous forcing. If selectively amplified by the convectively unstable modes in a globally unstable flow, such forcing can disrupt or obscure the naturally occurring global mode. What is worse, if the flow is globally stable to start with, the continuously amplified forcing could mimic an otherwise absent global mode.

2.2 Controlling global instability

The strength of the global instability in any flow can be changed by changing the flow parameters. The most effective parameter depends on the flow. In the low-density jet (chapter 3), the jet velocity is used because the flow is momentum-dominated and inertia drives the global instability.

In the jet diffusion flame (chapter 4), however, the global instability is driven by buoyancy – specifically by a buoyancy-induced modification of the velocity profile that creates an absolutely unstable inflexion point just outside the flame surface (IP3 in figure 1.7). Consequently, two different methods are used to control the global instability[2]. In the first, coflow air is added around the flame base. This reduces the shear and advects perturbations downstream, both of which

---

[1] For example, Monkewitz et al. (1990) inserted a pin into their low-density jet to suppress the global mode, and then impulsively retracted the pin to enable the global mode to re-emerge.

[2] A third possible method is via the jet velocity, but this is similar to adding coflow (§4.1.2.2).

weaken the instability. In the second, the relative concentrations of the fuel (methane) and dilutant (nitrogen) are changed. Reducing the methane concentration, for example, increases the stoichiometric mixture fraction. This causes the flame to shift towards the jet centreline, closer to the shear layer. The resultant changes to the density and velocity profiles are such that the flame becomes less unstable, according to Füri et al. (2002).

It should be noted that changing the relative concentrations of the fuel and dilutant has three secondary effects: the density ratio of the unburnt mixture changes, the flame temperature changes, and the density profile changes because the thermal diffusivity of the reactants changes. Experimental measurements of the velocity and temperature profiles would be required to examine these effects in detail, but this is not required for this thesis. What is important for this thesis is that the global instability of the flame can be changed by changing the relative concentrations of methane and nitrogen, without changing the overall flow rate.

2.3 Injector A

The low-density jet is examined on Injector A, which was kindly lent by Daniel Durox from Laboratoire EM2C. Shown in figure 2.2, it is a bench-top burner with a single round outlet, $d_1 = 6$ mm in diameter. Upstream of the outlet is a contraction section, whose area ratio is 52. This creates a nearly top-hat velocity profile with thin boundary layers (§3.1.1), which is ideal for creating regions of absolute instability. Farther upstream, in the settling chamber, is a series of fine-mesh screens and honeycomb[1] used for flow conditioning. At the base of the injector, a loudspeaker[2] is installed for acoustic forcing of the flow. The loudspeaker is driven by an amplified[3] (monochromatic) sinusoidal voltage signal from a function generator[4]. The amplitude and frequency of the voltage signal are monitored with a data acquisition system (DAQ)[5] and a digital oscilloscope[6].

---

[1] Cell height of 31.75 mm, cell diameter of 3.175 mm.

[2] AuraSound® 20 W 8 Ω extended-range driver (model NS3-193-8A).

[3] Matrix Amplification® power amplifier, mono mode on one channel.

[4] Thurlby Thandar Instruments® TG120, precision uncertainty of ±5% FS.

[5] National Instruments® USB–6009, 14-bit, installed 100 Ω bias resistor for removal of electrical noise while allowing for some common-mode voltage rejection.

[6] Tektronix TDS220®.

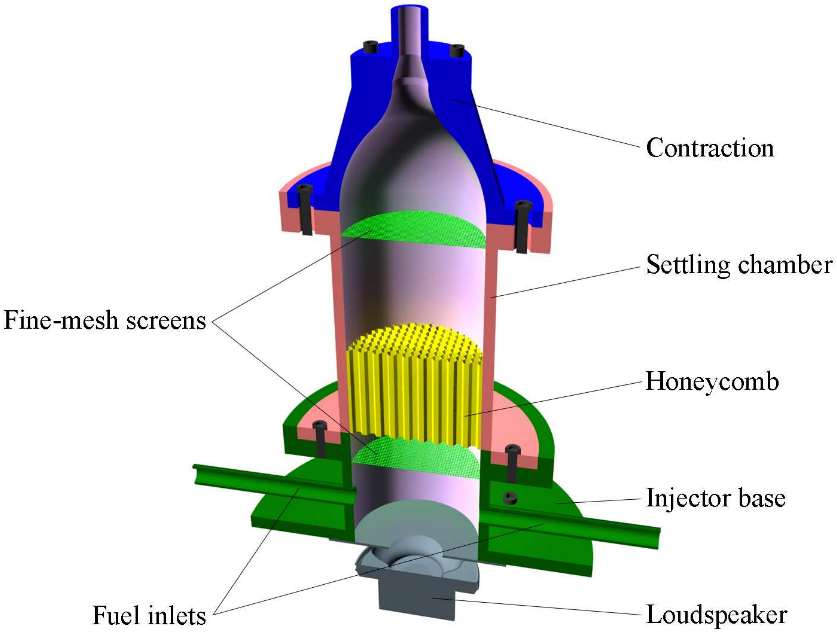

Figure 2.2: Rendering of Injector A.

2.4 Injector B

The jet diffusion flame is examined on Injector B, which was designed and built specifically for this thesis. Shown in figure 2.3, it resembles Injector A in that its (inner) outlet is round and has a diameter of $d_1 = 6$ mm. It likewise has a series of fine-mesh screens[1] and honeycomb[2] in its settling chamber for flow conditioning. It has the same model of loudspeaker installed at its base, for acoustic forcing of the flow. The loudspeaker is driven by an amplified[3] (monochromatic) sinusoidal voltage signal from a function generator[4]. The amplitude and frequency of the voltage signal are monitored with a DAQ[5] and a digital oscilloscope[6]. Figure 2.4 shows an electrical diagram of this setup, including connections for two-microphone measurements (§2.5.2) and for high-speed imaging (§2.5.3).

---

[1] Plain weave, mesh count of 20 per inch, wire diameter of 0.355 mm, open area of 51%.

[2] Cell height of 31.75 mm, cell diameter of 3.175 mm.

[3] Alesis® RA150 power amplifier, fanless, phono input.

[4] Thurlby Thandar Instruments® TG1000, precision uncertainty of ±3% FS.

[5] National Instruments® USB–6211, 16-bit, installed 100 Ω bias resistor for removal of electrical noise while allowing for some common-mode voltage rejection.

[6] Tektronix TDS220®.

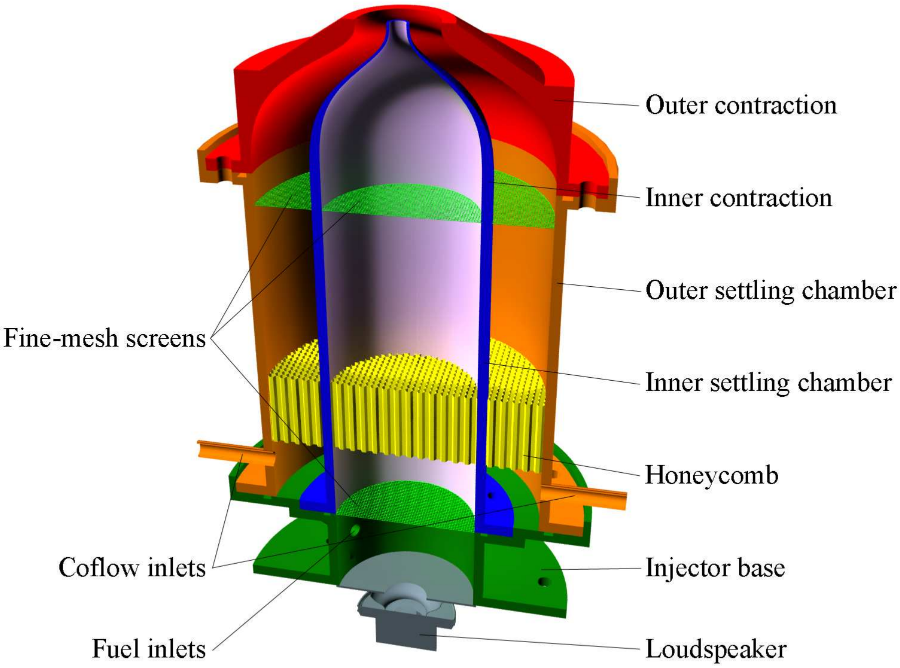

Figure 2.3: Rendering of Injector B.

Injector B differs from Injector A in that it has an outer contraction, with an outlet diameter of $d_2 = 30$ mm, through which coflow can be introduced (the coflow cannot be forced, however). Because the inner nozzle tapers to a knife edge at the exit plane, its wall thickness there is zero and the annular gap is 12 mm all around. The size of this gap is necessary to ensure that the flame anchors to the inner nozzle, rather than to the outer one[1]. The entire injector is machined from Type 308 stainless steel for added heat resistance. Appendix C contains technical drawings of each component.

In §4.1.1, it will be seen that the flow in Injector B is both flatter and quieter than that in Injector A. This is not surprising given that the design criteria included thin boundary layers and a low turbulence intensity. Both the inner and outer contractions of Injector B are designed on the basis of principles used in wind tunnel engineering (Mikhail, 1979; Morel, 1975), resulting in delicately smooth

---

[1] Experiments on a preliminary version of Injector B with a smaller outer contraction ($d_2 = 11$ mm) and hence a smaller annular gap (2.5 mm) show that the flame anchors only to the outer nozzle. This occurs because the fuel rapidly diffuses outwards from the inner jet and because the knife edge of the inner nozzle prevents the formation of recirculation zones.

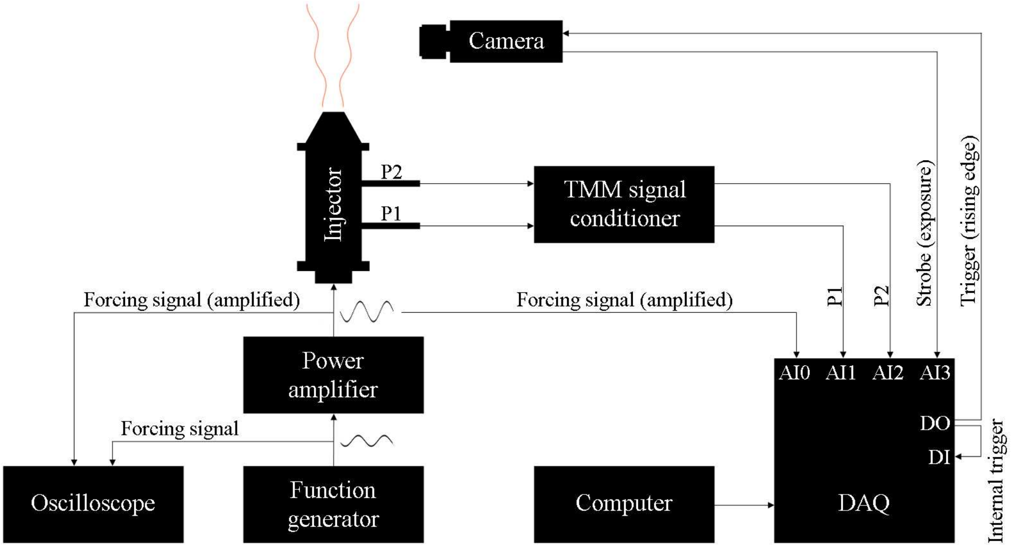

Figure 2.4: Electrical diagram for the combustion experiments with Injector B. Connections are also shown for two-microphone measurements (§2.5.2) and for high-speed imaging (§2.5.3). A timing diagram of the data acquisition process can be found in Appendix D. P1–2, pressure signals; AI0–3, analogue inputs; DI, digital input; DO, digital output.

contours[1] and a large area ratio[2]. The fine-mesh screens mounted upstream impose a small static pressure drop on the flow ($\Delta P \propto u^2$), dampening fluctuations in the streamwise velocity (Mehta, 1985). They also realign the incident flow in the local normal direction, dampening fluctuations in the cross-stream velocity. The Reynolds number of the screen wires is $\mathcal{O}(1)$, low enough to prevent vortex shedding. The honeycomb, meanwhile, functions as a flow straightener, removing the radial components of velocity associated with large-scale turbulent eddies (Mehta and Bradshaw, 1979).

---

[1] The shape of the inner contour is a high-order polynomial, whose first and second spatial derivatives are zero at the exit plane. The coefficients of this polynomial are optimised on simulations to prevent internal flow separation whilst maintaining thin boundary layers.

[2] The area ratio of the inner contraction is 100.

2.5 Measurement diagnostics

In this section, the measurement diagnostics used in this thesis are discussed. All experimental uncertainties are calculated with the Method of Partial Differentiation, the official standard of the American Society of Mechanical Engineers (Abernethy et al., 1985).

2.5.1 Hot-wire anemometry

Hot-wire anemometry (HWA) is a method for measuring the local instantaneous velocity in a homogeneous flow. Most commonly, it involves resistively heating a thin metallic wire, exposed to a flow, and measuring the voltage required to keep the wire at constant temperature, against the cooling effect of forced convection. The voltage measured thus is a proxy for the flow velocity at the wire – subject to limits at low velocities when natural convection dominates. The history and theory behind HWA have been written about by many researchers, Brunn (1995) being one of the most recent.

In this thesis, HWA is used to characterise the baseflows in both Injector A (§3.1.1) and Injector B (§4.1.1). It is also used to measure the natural and forced dynamics of the low-density jet (chapter 3) and to provide a calibration reference for the two-microphone method in the combustion experiments (chapter 4).

The equipment consists of a DANTEC® constant-temperature anemometer (MiniCTA) and a DANTEC® 55P16 single-normal probe operated at an overheat ratio of 1.8. The wire element of the probe, constructed of platinum-plated tungsten, is 5 μm in diameter and 1.25 mm in length. Its manufacturer-specified frequency response is 10 kHz, well above the expected flow frequencies. The probe is positioned using a three-axis linear traverse, with an uncertainty of ±0.1 mm in each axis. The voltage from the anemometer is digitised on a 16-bit DAQ[1] and saved for post-processing and analysis. A custom LabVIEW program is used to control all the data acquisition and storage routines.

In most of the experiments, the HWA voltage is sampled at a frequency of

---

[1] National Instruments® USB–6211.

16384 Hz for 16 seconds, resulting in 2^{18} data points[1]. This particular sampling frequency is chosen to satisfy – by more than a factor of ten – the Nyquist criterion, as the flow frequencies are expected to be $\mathcal{O}(10^3)$ Hz. A long sampling duration is used because the frequency resolution[2] of the power spectral density (PSD)[3] increases with the number of data points in the time series. The PSD is computed on MATLAB® using a built-in fast Fourier transform (FFT) algorithm: `pwelch`. Originally proposed by Welch (1967), `pwelch` has four main steps . First, in preparation for window-averaging, the time series is segmented into two halves of equal length, each with 50% overlap[4]. Second, each segment is windowed with a Hamming window in order to reduce spectral leakage[5]. Third, an FFT is applied to each windowed segment and the periodogram is computed. Fourth, the periodograms are averaged together, forming the final PSD.

---

[1] The only exception is for characterisation of the baseflow, when the sampling duration is extended to 32 seconds, or 2^{19} data points.

[2] In most cases, the frequency resolution is ±0.125 Hz, after window-averaging.

[3] The PSD is used to describe the statistics of stationary stochastic data (Bendat and Piersol, 1986). Formally known as the auto-spectral density, it is a convenient way of estimating the mean-square value of a time-domain signal in a given frequency band. By Parseval's theorem, which states that the integral of the square of a function is equal to the integral of the square of its Fourier transform, the total area under a PSD curve (in theory, over all frequencies) is equal to the square of the RMS of the time-domain signal. Because the PSD is a statistical estimate, a long time series, capturing many periods of the oscillating phenomenon, is required for statistically significant results. This, along with the improved frequency resolution, is why all the data in this thesis are recorded with sampling times that are as long as possible, subject to physical memory constraints. A final note is that although having more data points in the time series increases the frequency resolution of the PSD, the accuracy is not affected.

[4] The number of segments and the overlap percentage can be adjusted according to the desired accuracy and resolution. If n is the number of segments, the standard deviation of the PSD is reduced by a factor of $\sqrt{n}$. Such segmenting (and averaging later on), however, also reduces the length of each segment and therefore reduces the frequency resolution of the PSD. For example, if each of the n segments contains $2N$ data points, the PSD will have just $N + 1$ frequency bins, from DC to the Nyquist frequency (half the sampling frequency). Overlapping the n segments by 50% further reduces the variance of the PSD by a factor of about $9n/11$. There is not a full factor of n reduction because the overlapping segments are not statistically independent.

[5] Computing the FFT of a time series of length n is equivalent to the multiplication of an infinitely long input by a square window function of length n and of unity magnitude over n. Because a square window function has steep gradients at its ends, high-frequency components are created, which can contaminate the PSD by creating sidelobes around the main lobe, an effect known as spectral leakage. A typical way to reduce spectral leakage is to apply window functions that attenuate the time series at its ends. There are many suitable types of window function, their differences being mostly in the various measures used to describe the sharpness of peaks in the PSD (e.g. highest sidelobe level, sidelobe falloff rate, 3 dB bandwidth).

The application of thermal anemometry to inhomogeneous flows, such as a low-density helium jet (chapter 3), is a recognised challenge. This is because the HWA probe deduces the flow velocity from the convective heat transfer, which depends on both the flow velocity itself and the thermal diffusivity of the fluid. In view of this, many researchers have chosen not to use predetermined HWA calibrations, which are usually done in air, relying instead on the raw bridge voltages. This has worked surprisingly well, particularly for PSD estimates, as can be seen in the experiments by Sreenivasan et al. (1989), Kyle and Sreenivasan (1993), and Hallberg et al. (2007). In this thesis, the same simplification is used but only when the HWA probe is outside the potential regions of the flow.

That simplification, however, cannot be used for baseflow characterisation (§3.1.1 and §4.1.1). For this, an absolute HWA calibration is required. In this thesis, it is obtained with the procedure proposed by Johnson et al. (2005), the steps of which are detailed in the flowchart of figure 2.5. First, the velocity profile across a laminar air jet (diameter of 25.58 mm) is measured with a trial calibration based on the plug-flow approximation[1] and is integrated to get an estimate of the flow rate. This estimate is then compared to the reading from a precision mass flow controller[2]. If the difference is $> 1\%$, a plug-flow correction factor is iteratively applied to the trial calibration until convergence is achieved. This is repeated at several flow rates, for velocities up to 12 m s^{-1}, resulting in a set of correction factors for the final HWA calibration. Figure 2.6 shows a typical final HWA calibration, along with a polynomial fit.

2.5.2 Two-microphone method

When examining the forced response of a flow, it is helpful to know the amplitude and phase of the applied forcing. In this thesis, these quantities are measured with the two-microphone method (TMM). Originally proposed by Seybert and Ross (1977), the TMM involves the simultaneous measurement of the static pres-

---

[1] As the HWA probe approaches the nozzle walls (within 2–3 mm), the heat transfer from the wire increases as a result of thermal conduction, leading to the spurious reporting of higher velocities. In this thesis, this effect is corrected for with the method proposed by Lekakis (1996).

[2] Bronkhorst® EL-FLOW F-203AC-SAA-55-V, 536.5 LPM FS air at STP, precision uncertainty of ±0.6% FS including linearity.

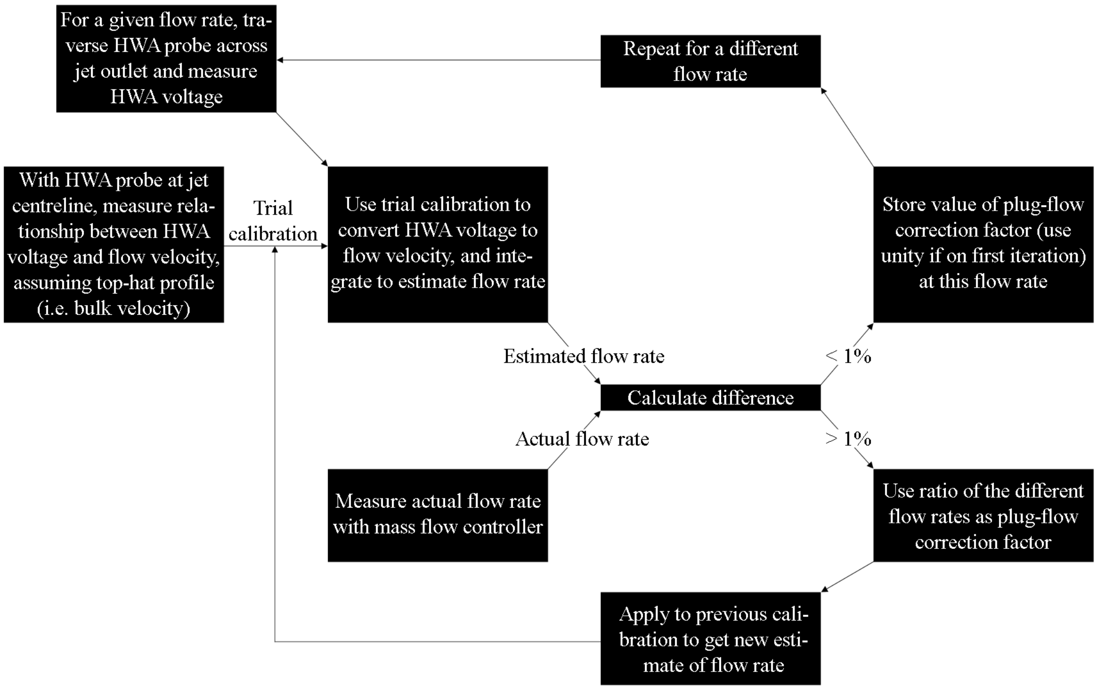

Figure 2.5: Flowchart of the HWA calibration procedure.

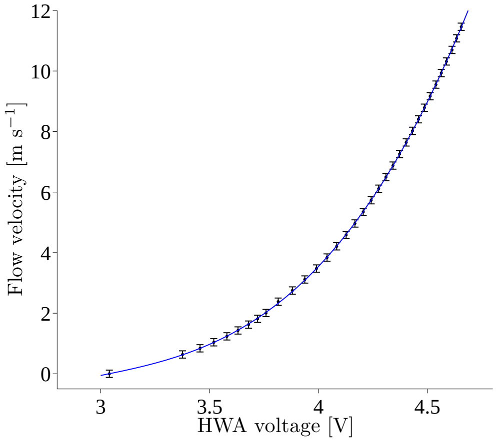

Figure 2.6: Typical final HWA calibration obtained via the procedure described in the text. The error bars for the flow velocity denote a precision uncertainty of ±0.12 m s^{-1}. The blue curve is a fifth-order polynomial fit; this particular regression model is chosen because it has the highest coefficient of determination.

sures at two different locations along a duct, $p(x_1)$ and $p(x_2)$ – or in the case of this thesis, along the inner settling chamber of Injector B (§2.4). From these, the acoustic modes of the system are decomposed into forward- and backward-propagating waves. This decomposition enables both the acoustic pressure, p', and the acoustic particle velocity, u', to be extrapolated anywhere along the duct, including at its ends, thus providing estimates of the forcing amplitude and phase.

The theory and error sources of the TMM have been discussed before in the literature (e.g. by Abom and Boden, 1988; Boden and Abom, 1986; Seybert and Soenarko, 1981), so for brevity only the basics are reviewed here. The theory considers a constant-area duct, forced periodically at one end but terminated at the other end by some unknown passive impedance. For small perturbations such that $p'/\overline{p} \ll 1$ and $\rho'/\overline{\rho} \ll 1$, the compressible continuity and Euler equations can be linearised to give the homogeneous acoustic equation for pressure:

$$\frac{\partial^2 p'}{\partial t^2} = \overline{c}^2 \nabla^2 p', \tag{2.1}$$

where the mean speed of sound, $\overline{c}$, is evaluated at mean values of $\overline{p}$ and $\overline{\rho}$. For a one-dimensional planar wave propagating in the x direction, (2.1) simplifies to:

$$\frac{\partial^2 p'}{\partial t^2} = \overline{c}^2 \frac{\partial^2 p'}{\partial x^2}. \tag{2.2}$$

Expressing the acoustic pressure field as a Fourier integral yields:

$$p'(x,t) = \int_{-\infty}^{\infty} \hat{p}'(x,f)\, e^{i2\pi f t}\, \mathrm{d}f, \tag{2.3}$$

where $\hat{p}'(x,f)$, with a hat, is the Fourier transform of $p'(x,t)$. Substitution of (2.3) into (2.2) gives:

$$\frac{\partial^2 \hat{p}'}{\partial x^2} + k^2 \hat{p}' = 0, \tag{2.4}$$

where the wavenumber $k \equiv 2\pi f/\overline{c}$. Solutions to (2.4) should account for contributions from both forward- and backward-propagating waves:

$$\hat{p'}_{+} = B_{+}e^{-ixk_{+}}, \tag{2.5}$$

$$\hat{p'}_{-} = B_{-}e^{ixk_{-}}, \tag{2.6}$$

where the subscripts $+$ and $-$ denote wave propagation in the forward and backward directions, respectively. The coefficients B_{+} and B_{-} are the amplitudes of those waves, and they depend on the oscillation frequency but not on the axial position because the system is assumed to be non-dispersive[1]. For a mean flow travelling in the $+x$ direction at Mach number, $M \equiv \overline{u}/\overline{c}$, the wavenumbers of the forward- and backward-propagating waves are:

$$k_{+} = \frac{2\pi f}{\overline{c}+\overline{u}} = \frac{k}{1+M}, \tag{2.7}$$

$$k_{-} = \frac{2\pi f}{\overline{c}-\overline{u}} = \frac{k}{1-M}. \tag{2.8}$$

The general solution of the acoustic pressure field thus becomes:

$$\hat{p}' = \hat{p}'_{+} + \hat{p}'_{-} = B_{+}e^{-ixk_{+}} + B_{-}e^{ixk_{-}}. \tag{2.9}$$

Evaluating (2.9) at two different locations, say x_1 and x_2, enables the coefficients B_{+} and B_{-} to be expressed as functions of the experimentally measured pressures, $\hat{p}'_1 \equiv \hat{p}'(x_1, f)$ and $\hat{p}'_2 \equiv \hat{p}'(x_2, f)$:

$$B_{+} = \frac{\hat{p}'_1 e^{ix_2k_{-}} - \hat{p}'_2 e^{ix_1k_{-}}}{e^{i(x_2k_{-}-x_1k_{+})} - e^{i(x_1k_{-}-x_2k_{+})}}, \tag{2.10}$$

$$B_{-} = \frac{\hat{p}'_2 e^{-ix_1k_{+}} - \hat{p}'_1 e^{-ix_2k_{+}}}{e^{i(x_2k_{-}-x_1k_{+})} - e^{i(x_1k_{-}-x_2k_{+})}}. \tag{2.11}$$

---

[1] This means that all frequency components travel at the same speed, with the phase velocity equal to the group velocity everywhere (i.e. the wave retains the same shape as it propagates).

If energy losses due to momentum and thermal diffusion are neglected, the acoustic particle velocity can be related to the acoustic pressure:

$$\hat{p}'_+ = \overline{\rho c}\hat{u}'_+, \tag{2.12}$$

$$\hat{p}'_- = -\overline{\rho c}\hat{u}'_-. \tag{2.13}$$

Thus, for a one-dimensional planar wave propagating without attenuation, the acoustic particle velocity at axial position x is:

$$\hat{u}' = \frac{B_+ e^{-ixk_+} - B_- e^{ixk_-}}{\overline{\rho c}}. \tag{2.14}$$

In this thesis, the above equations are programmed in MATLAB® and solved to give the amplitude and phase of the velocity perturbation at the outlet ($x = 0$) of Injector B. The complex modal inputs, $\hat{p}'_1$ and $\hat{p}'_2$, are measured with two identical pressure transducers[1]. Both are mounted flush with the chamber wall, separated by a distance of $(x_2 - x_1) = 60$ mm. The output voltage from each transducer is fed into a separate isolated channel of a purpose-built signal conditioner. With two operational amplifiers per channel, this device provides gains of up to 60 dB with negligible drift and low electrical noise. It also has a low-pass filter, whose cutoff frequency is approximately 7 kHz at -3 dB. This filter is used to attenuate what is thought to be high-frequency electromagnetic interference from the surrounding laboratories. The outputs from the signal conditioner are fed into a DAQ and digitised for post-processing.

Before the TMM system can be used for actual testing, however, its components must be individually calibrated. First, the signal conditioner is checked to

---

[1] Kulite Sensors® XCS-093-140MBARD, piezoresistive, 2.4 mm diameter, differential range of 14000 Pa FS, sensitivity of 4.29×10^{-3} mV/Pa, precision uncertainty of ±0.25% FS, bias uncertainty removed by referencing to the atmosphere.

ensure that both its gain and phase remain at their set values over the entire range of expected frequencies ($\leq$ 35 Hz for the flame experiments). The concern is that if there was a resonance in the electronics, it would be indistinguishable from hydrodynamic or acoustic resonances in the flow. The findings show that for frequencies up to 300 Hz, the gain is constant, at 60 dB, as is the phase, at 0° (Appendix E). These are the actual settings used in the experiments.

Next, the factory calibrations for the two pressure transducers are checked ex-situ in a custom loudspeaker enclosure. This involves temporarily mounting both transducers beside a reference microphone[1], which has been calibrated beforehand with a pistonphone[2]. All three devices are then subjected to identical sinusoidal forcing by a loudspeaker, and their outputs measured and compared. The amplitude response of both pressure transducers is checked thus and found to be within ±0.5% of their respective factory calibrations. This precision uncertainty is on the order of the aggregate uncertainty of the calibration system and hence the factory calibrations are retained. The bias uncertainty is removed by exposing the back of both transducer diaphragms to atmospheric pressure, via flexible tubes threaded through the outer settling chamber (Injector B). As for the phase response, the coherence between the two pressure transducers is found to be close to unity for frequencies up to 300 Hz, which is well above the frequencies expected in the experiments.

With the signal conditioner and both pressure transducers calibrated, the TMM system is calibrated as a whole and in-situ. This is done against HWA, with the probe positioned on the jet centreline ($r/d_1 = 0$) at the exit plane ($x/d_1 = 0$) of Injector B. The hot-wire element itself is oriented perpendicular to the flow, which is forced by a loudspeaker, as described in §2.4. The sinusoidal voltage into the loudspeaker is kept at a constant amplitude as its frequency is swept from 7 to 35 Hz, in 0.5 Hz increments. This frequency range is chosen because it covers the typical global frequencies of jet diffusion flames (around 10–20 Hz). The lower end of that range, 7 Hz, is limited by the inability of the loudspeaker to generate the desired forcing amplitudes without incurring

---

[1] Brüel & Kjaer Type 4134 condenser microphone, 12.7 mm diameter, coupler measurement, sensitivity of 12.5 mV/Pa, powered by a Brüel & Kjaer Type 2807 supply unit.

[2] Brüel & Kjaer Type 4228 pistonphone, cam-operated cavity, constant $SPL = 124 \pm 0.09$ dB re. 20 μPa, pure tone at 250±0.25 Hz.

excessive cone motion[1]. The calibration is performed at flow rates similar to those used in the actual experiments, with two different gases: (i) air and (ii) a mixture of air and helium (48% air–52% He, by volume) having the same density and speed of sound as methane. This non-reacting methane surrogate is used to ensure that the TMM measurements would be accurate regardless of the mixture composition. Methane itself is not used because it is flammable – a safety risk exacerbated by the need to deactivate the local extraction during testing owing to excessive noise. Before the TMM is calibrated with the methane surrogate, though, the HWA probe is re-calibrated for this gas using the procedure in §2.5.1.

In order to account for deviations from plug-flow behaviour, correction factors are applied to the raw TMM data. They are found by taking the ratio between TMM and HWA readings over a wide range of flow rates, mixture compositions, and forcing amplitudes and frequencies (f_f). The aggregate data are regressed against f_f using a high-order polynomial, resulting in a set of coefficients for the correction factor that can then be applied to all the TMM data. A typical comparison of the forcing amplitudes measured with TMM and HWA is shown in figure 2.7. The forcing amplitude is defined, at the injector plane, as the amplitude of the velocity perturbation at f_f normalised by the bulk jet velocity: $A \equiv |u'_{1,\,f_f}|/U_1$. The comparison shows that the corrected TMM can be used to accurately measure the imposed velocity perturbations. Although the comparison is for air, results for the methane surrogate are similar in that they show agreement between TMM and HWA. Figure 2.7 also represents the acoustic response of the system. The response is smooth, free of resonant peaks[2], which is not surprising given that the injector does not have a combustor attached to it. As f_f increases, A increases (nearly linearly) because the loudspeaker becomes more efficient as it is operated away from very low frequencies.

---

[1] Excessive cone motion can damage the suspension of a loudspeaker. Most loudspeakers are not designed to be operated at frequencies below the audible range in humans (20–20×10^3 Hz).

[2] Some degree of acoustic coupling with the upstream supply lines usually occurs. In this thesis, however, a flashback arrestor is installed immediately upstream of the injector inlets. This device increases the acoustic impedance of the supply lines and therefore reduces their tendency to support acoustic modes that can affect the downstream flow.

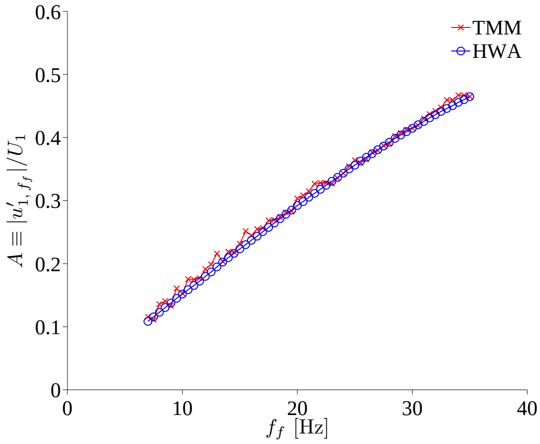

Figure 2.7: Typical comparison of the forcing amplitudes measured with TMM and HWA as a function of forcing frequency. The test fluid is air, the injector is Injector B, and the bulk velocity at the injector outlet is $U_1 = 3.0$ m s^{-1}. The peak-to-peak voltage into the loudspeaker is fixed at 400 mV$_{\mathrm{pp}}$.

2.5.3 Chemiluminescence

When examining the forced response of a flame, it is helpful to have an indicator of the heat release. For this thesis, that indicator is the natural flame chemiluminescence. Chemiluminescence is used because it is easy to measure, requiring no costly lasers or intensified cameras, and because it is well proven, having been used extensively in previous studies on flame dynamics (McManus et al., 1995). The history and theory behind it have been the subject of numerous texts (e.g. the book by Gaydon, 1974), so for brevity only the basics are reviewed here.

Chemiluminescence is the emission of photons from electronically excited radical species on their return to the ground state. In flames, the majority of such species are produced by chemical reactions at the flame front[1]. Consequently, the chemiluminescent intensity[2], which is directly related to the concentration of the excited species, depends on the rate at which those combustion reactions occur.

In hydrocarbon flames, the combustion reactions produce a variety of radical species, each of which emits photons of a specific wavelength[3]. Only some of them,

---

[1] Chemiluminescence is thus fundamentally different from fluorescence, in which the excited species are produced by the absorption of electromagnetic radiation, typically from a laser.

[2] This is defined as the number of photons emitted per unit area.

[3] The exact wavelength depends on the atomic structure of the excited species and on the

however, will emit with an intensity strong enough to be detectable above the background spectrum. In lean-premixed flames, the strongest chemiluminescence is from CH* (431 nm), OH* (309 nm), and CO_2* (broadband over 300–600 nm). In rich-premixed flames, there is also a contribution from C_2* (513 nm).

In premixed flames, chemiluminescence is regarded as a reliable indicator of the reaction-zone location and the heat-release rate (Hurle et al., 1968; Price et al., 1969). In fact, this assumption is often used in studies on flame dynamics (Cho et al., 1998; Langhorne, 1988), although it can fail in regions of high strain rate and high curvature, especially near the extinction limits (Najm et al., 1998).

In diffusion flames, such as those studied in this thesis, the chemiluminescent spectrum is qualitatively similar to that of rich-premixed flames. This does not, however, mean that the total radiative spectrum is similar, because diffusion flames tend to generate soot. The presence of soot can have several effects.

First, soot can positively bias a chemiluminescent measurement by emitting blackbody radiation. According to Solomon and Best (1991), the emitted spectrum is similar to that of a theoretical blackbody at the temperature of the soot, which means that it is continuous and retains the same overall shape (Planck's law)[1]. With the proper equipment, therefore, the effect of soot radiation can be corrected for relatively easily. The procedure, described by Hardalupas and Selbach (2002), involves measuring the chemiluminescent intensity at wavelengths around the target wavelength. If the correction is being made on a CH* measurement (431 nm), for example, the intensities at 420 nm and 440 nm are measured along with the target signal. By interpolating the intensities between 420 nm and 440 nm, it is possible to obtain an estimate of the contribution from soot radiation at 431 nm. This can then be subtracted from the total intensity measured at 431 nm, leaving just the intensity from chemically produced CH*.

Second, soot can affect both the spatial and temporal accuracies of image-based measurements. Concerning the spatial accuracy, soot can be transported to regions where there is no flame, thus biasing the reaction-zone location. To reduce this bias, it is important that the Stokes number of the soot particles is

---

quantum transition that it undergoes.

[1] Wien's displacement law, though, states that as the temperature increases, the spectral peak weakens and shifts to shorter wavelengths.

small, so that they can accurately track the carrier flow. A first-order calculation of the Stokes number, based on a soot diameter of 1 micron and a hydrodynamic timescale equal to the period of a typical global mode in a jet diffusion flame, gives values of $\mathcal{O}(10^{-4})$, which is indeed small.

Concerning the temporal accuracy, if a flame oscillates very rapidly, the timescale involved in the nucleation and growth of soot particles – plus the timescale involved in their subsequent heating and blackbody emission – could be larger than the timescale of the heat release. In this scenario, there would be a time delay between the emission of blackbody radiation from the soot and the emission of chemiluminescence from the flame. To reduce this delay, it is important that the flame oscillates very slowly (i.e. with a large oscillation timescale), which is fortuitously what jet diffusion flames tend to do naturally. Moreover, once an excited radical species is (chemically) produced, unless collisional quenching causes de-excitation first, light is usually emitted within the order of a microsecond (Garland and Crosley, 1988). This timescale is significantly shorter than the advection, diffusion, and instability timescales of the flame. For this thesis, therefore, chemiluminescence should serve as an accurate indicator of the location and frequency of the heat release, even though its intensity does not accurately represent the intensity of the heat release itself.

In the experiments, a high-speed camera (Phantom$^{\text{TM}}$ V4.2 CMOS) is used to record the flame chemiluminescence as a time series of line-of-sight images[1]. It is fitted with ultra-violent optics (Nikkor 105 mm f/4.5) but without spectral filters. The measured spectrum is thus broadband, with limits determined by the spectral characteristics of the camera–lens system. Line-specific imaging is not used for two reasons. First, the chemiluminescence from diffusion flames is contaminated with soot radiation, which, as discussed above, is broadband and affects a range of wavelengths. Second, to satisfy the Nyquist criterion requires the use of high frame rates and short exposure times. Without an image intensifier, however, capturing a sufficient signal-to-noise ratio (SNR) becomes difficult, so the broadband spectrum is measured in order to maximise the signal strength.

---

[1] Phase-averaging, whereby images are binned according to their phase in the oscillation cycle, is not used because the flows studied here tend to oscillate at multiple frequencies. There is therefore no dominant frequency to which the camera can be synched.

Table 2.1: Camera settings for the chemiluminescence videos.

Frame rate	180 frames s^{-1} (fixed)
Exposure time	40–5200 μs (variable*)
Image depth	8 bits (monochrome)
Resolution	256 (w) × 512 (h) pixels
Image scale	0.3435 mm pixel^{-1}
Field of view	Frame height $= (29.3)d_1$
Video length	5429 frames
Post-trigger	5429 frames
Auto-exposure	Off

$\star$ For each flame, the exposure time is adjusted such that the near field of the flow, where toroidal vortices begin to roll up, is not saturated.

The camera settings used to record the chemiluminescence videos are listed in table 2.1. For analysis of the flame dynamics, the intensity in each frame of each video is summed across every pixel column[1], generating a time series (five pixel rows in height) at each axial station: $I\,(x/d_1)$. This procedure is illustrated in figure 2.8. From the time series, two quantities are computed for further analysis. The first is the PSD, a measure of the spectral distribution of energy in $I\,(x/d_1)$. It is computed similarly to the HWA spectra, as described in §2.5.1 (page 54).

The second quantity is the reconstructed phase space. The phase space of a dynamical system contains all the independent state variables necessary to describe the system in full at any given time[2]. In this phase space, every possible state of the system is represented by a discrete point. As the system evolves in time, the active points trace out a 'phase trajectory'. Analysing the topology of this phase trajectory provides valuable information about the dynamics of the

---

[1] The intensity is not summed over the entire frame because doing so would conceal small-scale structures (i.e. those smaller than the field of view), leading to a bias towards large-scale structures. Photomultipliers that image an entire flame often suffer from such biasing, although few researchers recognise it. Nevertheless, this is not a major concern in thermoacoustics because most industrial flames are acoustically compact. To the acoustic field, the flame appears as a point heat source, so imaging it in its entirety (even though it may not be oscillating as a whole, everywhere in phase) is still a representative way to measure its response.

[2] Given knowledge of these state variables, therefore, one could in theory evolve the system forward in time to predict its state at some later time (Kabiraj et al., 2011).

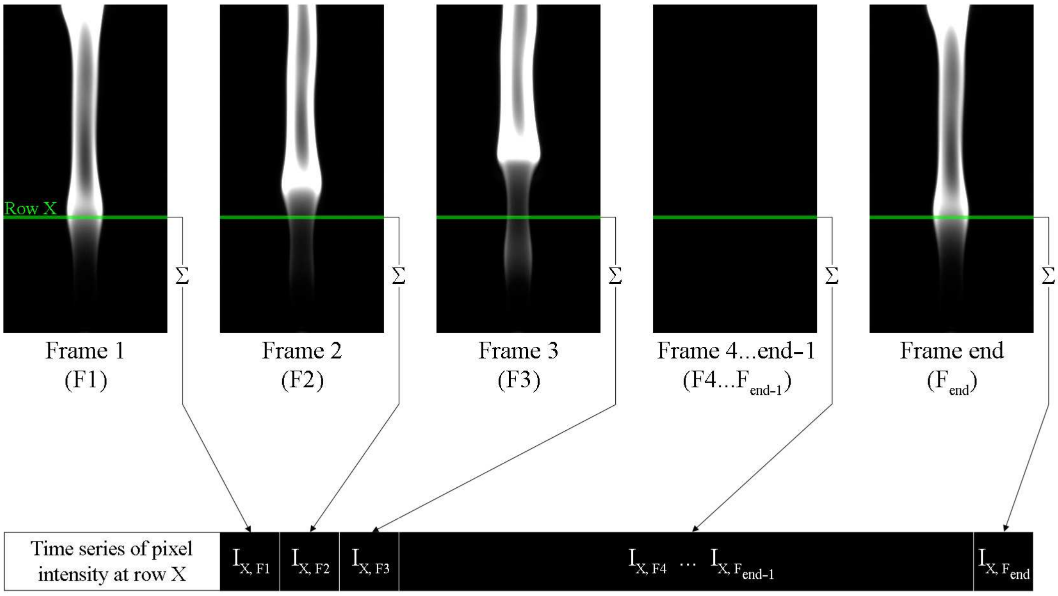

Figure 2.8: Visual representation of the image-processing procedure applied to the chemiluminescence videos.

underlying system[1]. If the system is periodic, the phase trajectory follows a closed orbit around a periodic attractor. If the system is quasiperiodic, it follows the surface of a torus. If the system is chaotic, it follows a non-repeating orbit around one or more strange attractors (fractal objects with self-similarity).

In a real-world system, the number of independent state variables (i.e. the dimension of the phase space) is not known a priori. It must therefore be estimated, and one way of doing this is with the state-space vector:

$$[\ I(t),\ I'(t),\ \ldots,\ I^{N-1}(t)\ ], \tag{2.15}$$

where N is the number of degrees of freedom (DOFs) in the system. For example, a two-DOF system, such as a swinging pendulum, has the state-space vector

---

[1] A natural question to ask is: why should we even bother with the phase space? The answer, Lieuwen (2002) suggests, is that it can be a very useful tool for identifying patterns and similarities in the system dynamics, because it uses data from many oscillation cycles – not just a few. This is its key advantage over analyses done in the time domain.

$[\Theta,\ \Theta']$, with Θ being the angular position of the pendulum. In practice, however, this method of representing the system involves numerical differentiation of experimental data, a process that is very sensitive to measurement noise.

To sidestep this problem, this thesis will use the method of time-delay embedding. Based on the embedding theorem of Ruelle and Takens (1971), it involves unfolding the geometric structure of the multivariate phase space into a m-dimensional system of time-delayed vectors[1] created from experimental data:

$$[\ I(t),\ I(t+\tau),\ I(t+2\tau),\ \ldots,\ I(t+(m-1)\tau)\ ], \tag{2.16}$$

where m is the embedding dimension – i.e. the dimension of the reconstructed phase space. The minimum value of m needed to fully capture the physical properties of an attractor depends on the number of DOFs in the underlying system. The time delay τ must be carefully chosen: if it is too small, the vector elements will be strongly correlated and statistical independence will be lost; if it is too large, numerical inaccuracies and noise will dominate, making the correlation between different time-delayed elements random. In this thesis, the optimal time delay is found by computing the first zero-crossing of the autocorrelation function, as recommended by Abarbanel (1996). Other available methods can be found in the books by Henry et al. (2000) and by Kantz and Schreiber (2003).

The reconstructed phase space is never identical to the original phase space, although, as Trauth (2010) has pointed out, its topological features are preserved – provided that m is at least one larger than the correlation dimension[2]. Several methods are available for visualising the reconstructed phase space, with two standing out in particular: the phase portrait and the Poincaré map. The phase portrait is a three-dimensional plot of the system motion (e.g. the pixel intensity) against that same motion shifted by τ, and by 2τ. The Poincaré map[3] is a

---

[1] These are sometimes called the reconstructed phase-space vectors.

[2] The correlation dimension is a measure of the number of DOFs in a dynamical system. It is an objective parameter that is useful for classifying the structure of attractors. Its value is one for a periodic limit cycle, two for a quasiperiodic oscillation with two independent modes, fractional for a chaotic motion, and infinite for purely random noise. The correlation dimension is usually estimated with the algorithm of Grassberger and Procaccia (1983); examples in combustion research include the papers by Gotoda and Ueda (2002) and Lieuwen (2002).

[3] The Poincaré map can be classified as being either a one-sided map or a two-sided map,

two-dimensional plot comprising data points from the geometric intersection of the trajectories in the phase portrait and an arbitrary plane – aptly named the Poincaré plane. Thus, whereas the phase portrait tracks the system as it evolves in time, the Poincaré map provides snapshots at discrete time intervals. Each class of nonlinear response, ranging from a limit cycle to a quasiperiodic oscillation to a chaotic motion, has its own distinctive features in the Poincaré map, and these will be discussed further in chapters 3 and 4.

2.5.4 Schlieren

Another type of flow visualisation that is used is schlieren. Invented by German physicist August Toepler in 1864, this technique works by intercepting light rays according to their degree of refraction (Weinberg, 1963). In the procedure, a collimated beam of light is projected through a target flow and focused onto a knife edge. Any spatial variations in refractive index in the flow, caused for example by spatial variations in density, would cause the light to be refracted either towards or away from the knife edge. The light that passes is recorded, creating a final image whose spatial illuminance variation is, to a first approximation, proportional[1] to the component of the density gradient that is perpendicular to the knife edge.

In this thesis, schlieren is applied to both the low-density jet and the jet diffusion flame. The setup, shown in figure 2.9, consists of two parabolic concave mirrors (both 152.4 mm in diameter and 1219 mm in focal length) aligned in a Z-type Herschelian configuration. A high-intensity light-emitting diode (white, phosphor-coated, 5 cd), mounted behind a pinhole aperture (1 mm in diameter), is used as an extended light source. A household razor blade, mounted on a linear translation stage, is used as a knife edge. The orientation of the knife edge can be varied to resolve either streamwise or cross-stream gradients of density. The same high-speed camera that is used for chemiluminescence is also used for schlieren. For most tests, the camera is fitted with a Nikkor 135 mm f/2.8 lens. The camera

---

depending on whether its data points represent motion of the phase trajectories in one direction or two. In this thesis, only two-sided maps will be shown.

[1] Linearity is valid only if the optical receiver is itself linear with respect to illuminance. Two examples for which this is not the case are the human eye and photographic film. Both of these respond logarithmically to incident illuminance, so for them to produce a linear response would require the use of a knife edge with an exponential contour.

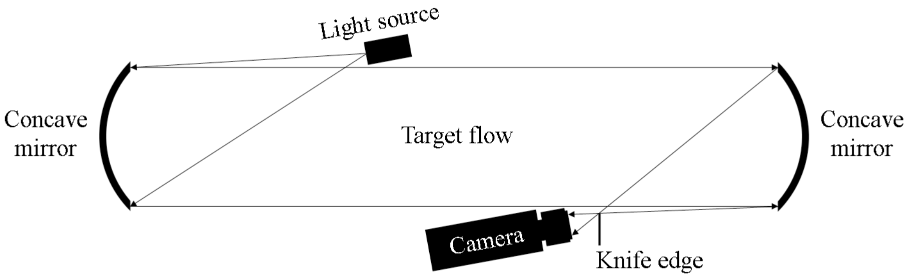

Figure 2.9: Schematic of the Z-type schlieren setup.

settings (i.e. pixel resolution, frame rate, and exposure time) are optimised to satisfy the Nyquist criterion – usually exceeding it by more than a factor of ten. The knife-edge cutoff is optimised for maximum contrast sensitivity without exceeding the dynamic range of the image sensor. The details of this optimisation procedure can be found in §3.2.1 of the book by Settles (2001).

2.5.5 Flow supply and metering

The flow rate of the various gases is measured with glass rotameters[1]. The flow temperature is measured at the injector outlet with a Type-K thermocouple[2]. For the prevention of flow pulsations, which could excite undesired instabilities, all the fuel and dilution gases – including air – are supplied from compressed cylinders, rather than from a centralised compressor or a shared manifold. Two-stage gas regulators are used to ensure a steady upstream supply pressure. Particulate filters are installed on the gas lines to prevent debris from entering the experiment and damaging the HWA probes. Most of the experiments are conducted at times of low vehicular traffic and low ambient noise, in order to reduce the influence of external disturbances. All the experiments are conducted at an ambient temperature of 293±2 K and at atmospheric pressure.

---

[1] Precision uncertainty of ±3%, bias uncertainty removed by calibrating against a mass flow controller: Bronkhorst® EL-FLOW F-203AC-SAA-55-V, 536.5 LPM FS air at STP, precision uncertainty of ±0.6% FS including linearity.

[2] Precision uncertainty of ±1 K.

Chapter 3

Low-density jets

In this chapter, the global instability of a non-reacting low-density jet is examined experimentally. First the jet is examined without forcing, in order to study its natural self-excited dynamics. Then it is examined with forcing applied around its natural frequency, in order to study how its natural dynamics at one frequency is affected by external forcing at other frequencies. As well as linking to previous studies in the literature, this provides a reference case for the combustion experiments in chapter 4.

According to the linear stability analysis by Monkewitz and Sohn (1986, 1988), a round inviscid unconfined jet begins to develop regions of local absolute instability when its density ratio falls below approximately[1] 0.7. The jet examined in this chapter is of helium gas, which, in air, has a density ratio of 0.14, well below the inviscid threshold for instability. The jet is examined on Injector A, with sinusoidal forcing applied by a loudspeaker mounted in the upstream settling chamber (§2.3).

---

[1] The exact threshold depends mildly on the shape of the velocity profile but is always around 0.7. Monkewitz and Sohn (1988), for instance, found that for a Mach number of zero and for a vorticity thickness equal to 8.7% of the jet diameter, the critical density ratio is 0.72.

3.1 Unforced

3.1.1 Baseflow characterisation

Before the jet dynamics is studied, the velocity profile at the outlet of Injector A is measured with HWA (§2.5.1). This is done by traversing a single-normal probe across the outlet, as close as possible to the exit plane ($x/d_1 \approx 0$). This is repeated in multiple azimuthal planes in order to test for flow symmetry. For brevity, however, only data from one representative plane are shown.

In these measurements, air is used as the jet fluid in order to conserve helium[1]. This is acceptable because the velocity profile depends primarily on the Reynolds number and the injector geometry, such as the contraction ratio and the surface roughness. It does not depend on the other transport properties of the fluid, such as the Prandtl and Schmidt numbers, which differ between air and helium.

Figure 3.1a shows radial profiles of the time-averaged streamwise velocity, normalised by the maximum across each profile, for a range of Reynolds numbers: $710 \leq Re_1 \leq 3530$. Figure 3.1b shows radial profiles of the turbulence intensity[2] for the same Reynolds numbers. This particular range of Re_1 is chosen because the jet bifurcates into a global mode within it, as will be discussed in §3.1.2.

For all values of Re_1, the velocity and the turbulence intensity are uniform over the central part of the flow and are symmetric about the jet centreline. As expected, the velocity approaches zero at the walls ($r/d_1 = \pm 0.5$) and the turbulence intensity peaks in the boundary layers. Away from the boundary layers, the turbulence intensity varies between 0.25 and 0.37%, depending on Re_1. This flat velocity profile with low turbulence intensity is ideal for creating well-characterised regions of absolute instability.

As Re_1 increases, the boundary layer thickness and the turbulence intensity both decrease. In other words, the flat part of the velocity profile extends to a

---

[1] Since the start of this thesis, the price of helium has more than doubled. This is partly due to growing demand, especially from the semiconductor industry and the medical imaging field. But it is also due to declining supplies, with 80% of global reserves existing in the American Southwest, as a component of natural gas (helium is extracted by fractional distillation). Many researchers have argued that the time of Peak Helium may have already passed.

[2] The turbulence intensity is defined as the RMS velocity fluctuation normalised by the time-averaged velocity: $u'_{rms}/\overline{u}$.

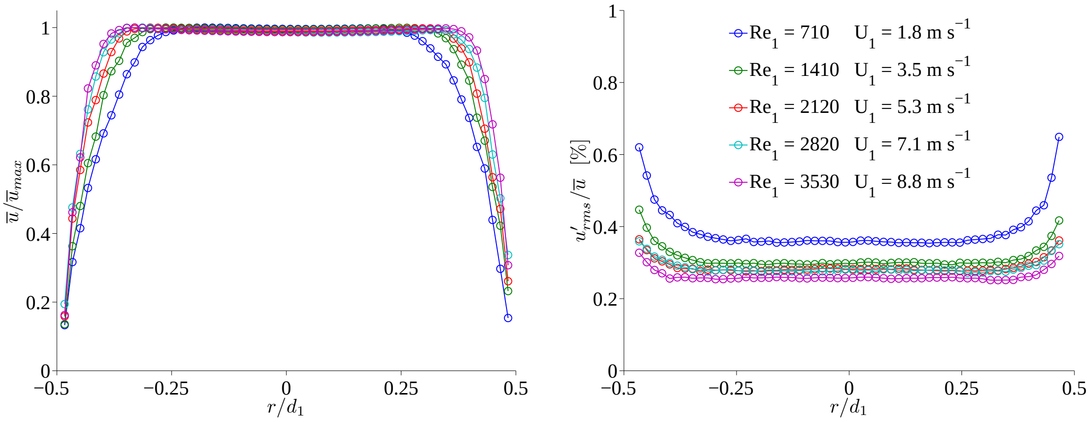

(a) Normalised time-averaged velocity

(b) Turbulence intensity

Figure 3.1: (a) Normalised time-averaged velocity and (b) turbulence intensity at the outlet of Injector A. They are plotted as a function of radial position for five Reynolds numbers: $710 \leq Re_1 \leq 3530$.

greater radius and has proportionately less turbulent fluctuation.

One of the key parameters determining the stability of a flow is the shear layer thickness. At the injector outlet, where the axial velocity in the surrounding air is zero, this is equal to the boundary layer thickness. The boundary layer thickness can be measured with two quantities: the displacement thickness, δ^*, and the momentum thickness, θ. In the experiments, both are found by fitting high-order polynomials to the velocity profiles shown in figure 3.1a and then integrating. Figure 3.2a shows δ^* and θ as a function of Re_1. As Re_1 increases, both δ^* and θ decrease, which is consistent with the earlier observation that the velocity profile becomes more uniform with increasing Re_1.

The ratio between δ^* and θ quantifies the shape of the boundary layer. Plotted in figure 3.2b, it varies by less than ±3% of its mean across the entire range of Re_1. This shows that, although the thickness of the boundary layer changes as Re_1 changes, its shape does not. This invariance is important because, as Kyle and Sreenivasan (1993) have noted, it implies that the velocity profile can be characterised by just one parameter: the transverse curvature, d_1/θ. According to Hallberg and Strykowski (2006), this is one of the most influential parameters controlling global instability; it is plotted in figure 3.3 as a function of $\sqrt{Re_1}$.

The trend is linear (blue line), indicating that the boundary layer is laminar. The transverse curvature will be useful for understanding the results that follow.

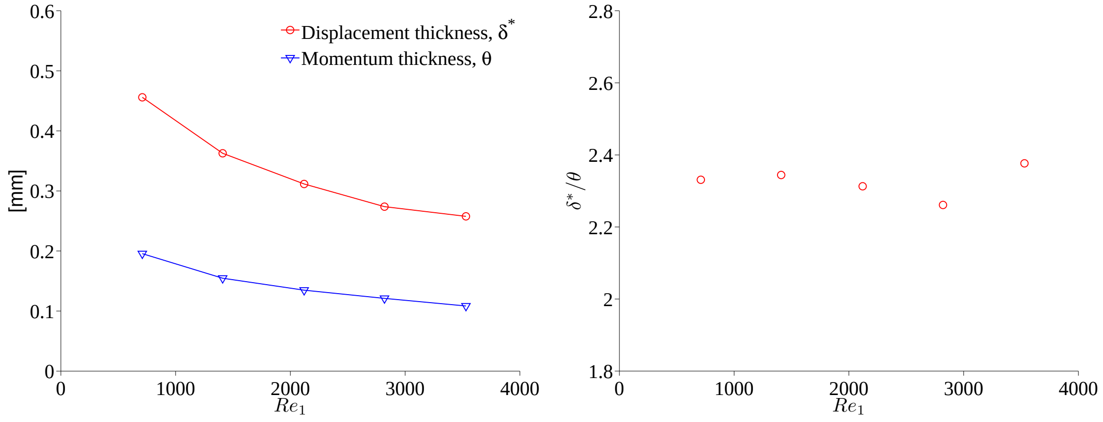

(a) δ^* and θ

(b) δ^*/θ

Figure 3.2: (a) Displacement thickness, δ^*, and momentum thickness, θ, and (b) their ratio at the outlet of Injector A. They are plotted as a function of the same Reynolds numbers as in figure 3.1.

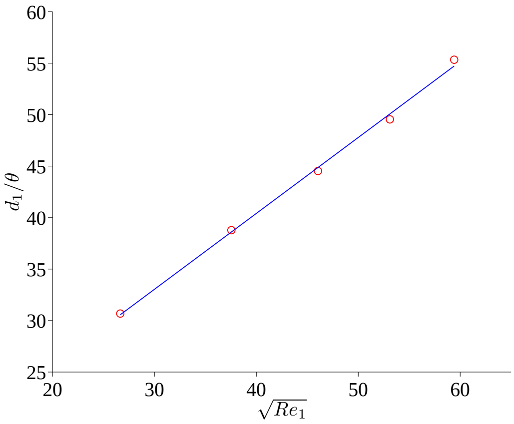

Figure 3.3: Transverse curvature, d_1/θ, at the outlet of Injector A. It is plotted as a function of the square root of the Reynolds numbers shown in figures 3.1 and 3.2. The blue line is a linear fit.

3.1.2 Global bifurcation

In figure 3.4, the PSD of the local streamwise velocity in the low-density jet is shown for eleven Reynolds numbers: $480 \leq Re_1 \leq 1900$. For comparison, the PSD of the same quantity but in a constant-density air jet is also shown (bottom in red). These measurements are made with a HWA probe positioned on the jet centreline, $1.5d_1$ downstream of the injector outlet. This particular axial station is chosen because it is where the amplitude of the eventual global mode is at a maximum. Fortuitously, it is also within the potential core, so the HWA calibration for helium can be validly used.

The PSD from the constant-density jet contains broadband noise, with a slight increase around 250 Hz but no clear peak. This is consistent with the fact that this jet has no pocket of absolute instability and is therefore not globally unstable. It is instructive to compare this to the behaviour of the low-density jet.

At $Re_1 = 480$, the low-density jet behaves like the constant-density jet: there is a slight increase in the PSD around a few hundred Hertz but no clear peak. This is because the low-density jet is not globally unstable at this Reynolds number, because the inertia of small perturbations is not sufficient to overcome the stabilising action of viscosity. The behaviour at $Re_1 = 630$ is marginal but, at $Re_1 \geq 710$, a clear peak emerges in the PSD, together with harmonics. This occurs because the jet has become globally unstable, behaving as an oscillator with a well-defined natural frequency rather than just as an amplifier. This is the classical global mode behaviour that was expected. The shape of the global mode is varicose, as can be seen from the schlieren image in figure 1.5. The frequency of the global mode is around 500 Hz at $Re_1 = 710$ and increases as Re_1 increases, for reasons that will be explained in §3.1.3.

The emergence of the global mode can be identified more clearly in a bifurcation diagram: figure 3.5a shows the square of the RMS velocity fluctuation normalised by the time-averaged velocity, $(u'_{rms}/\overline{u})^2$, as a function of the Reynolds number. At low Reynolds numbers ($480 \leq Re_1 \leq 630$), the jet is globally stable and its response is negligible. As the Reynolds number increases ($710 \leq Re_1 \leq 1900$), however, the jet becomes self-excited and its response increases. Close to the bifurcation point ($630 \leq Re_1 \leq 710$), the response seems to

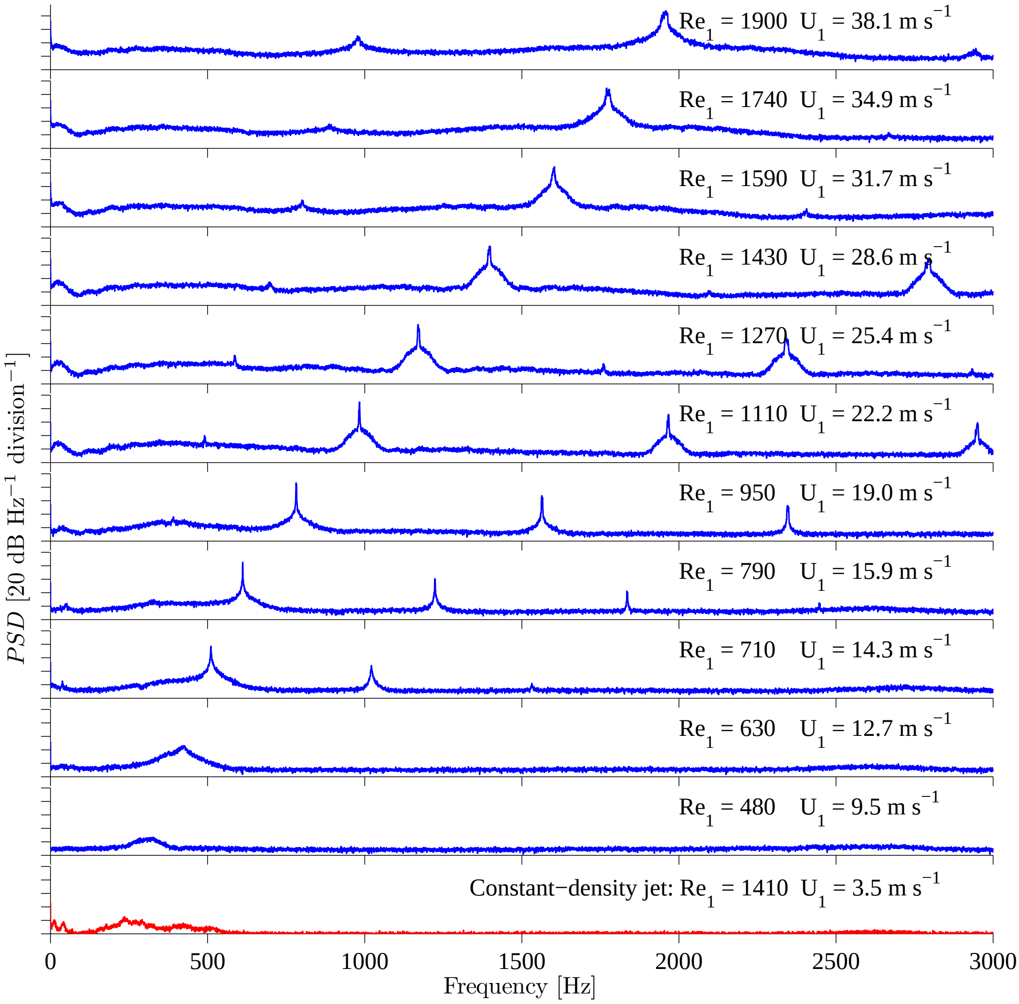

Figure 3.4: PSD of the local streamwise velocity in the low-density jet for eleven Reynolds numbers, $480 \leq Re_1 \leq 1900$, and in a constant-density jet at $Re_1 = 1410$. The velocity is measured with a HWA probe positioned on the jet centreline, $1.5d_1$ downstream of the injector outlet.

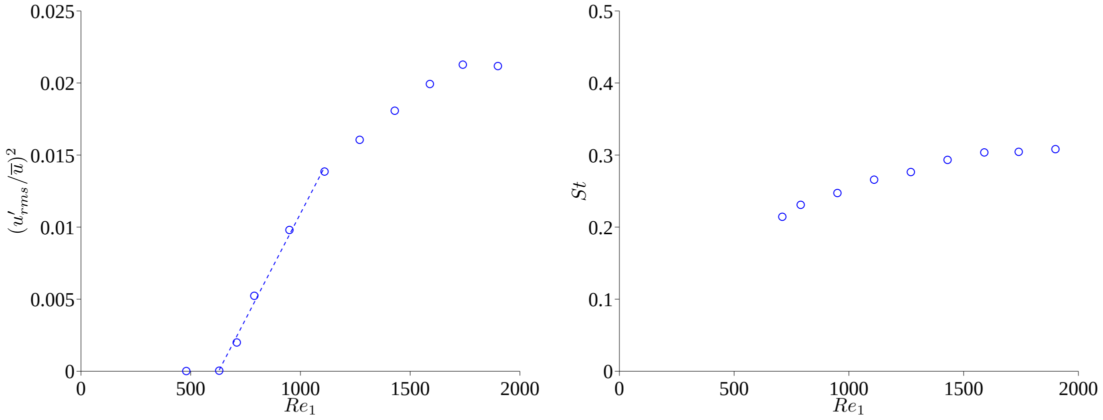

(a) Bifurcation diagram

(b) Strouhal number

Figure 3.5: Subfigure (a) shows the square of the RMS velocity fluctuation normalised by the time-averaged velocity, $(u'_{rms}/\overline{u})^2$, as a function of the Reynolds number. The linear increase near $630 \leq Re_1 \leq 710$ indicates a Hopf bifurcation to a global mode. Subfigure (b) shows the Strouhal number of that global mode as a function of the Reynolds number.

increase linearly with Re_1. This is the classical behaviour around a Hopf bifurcation, which can be modelled with a Landau equation containing just first- and third-order terms (Appendix B). Away from the bifurcation point, the increase is less than linear, as fifth- and higher-order terms become influential.

3.1.3 Global frequency

Because the global mode is caused by an inertial instability, its frequency should scale with an inertial timescale. One such timescale is d_1/U_1, which is the time that a fluid element takes to travel a distance of d_1 under its own inertia. Here the jet diameter is used because the global mode is thought to be caused by a jet-column instability (rather than by a shear-layer instability) whose characteristic lengthscale is the distance between diametrically opposed shear layers. If this timescale is used to non-dimensionalise the global frequency, the following form of the Strouhal number results: $St \equiv fd_1/U_1$. Figure 3.5b shows St as a function of Re_1. Despite Re_1 varying by a factor of three, St remains within a relatively narrow range, between 0.21 and 0.31.

3.2 Forced

The low-density jet is forced around its natural frequency, in order to study how its natural dynamics at one frequency is affected by external forcing at other frequencies. The jet response is measured with both a HWA probe and a pressure transducer, although only the HWA measurements will be shown because they are less influenced by external noise. As in §3.1.2 and §3.1.3, the HWA probe is positioned on the jet centreline, $1.5d_1$ downstream of the injector outlet.

For these forcing experiments, the jet Reynolds number is fixed at $Re_1 = 1100$. This particular value is chosen because it is sufficiently far from the supercritical Hopf bifurcation – which occurs between $Re_1 = 630$ and 710 – that the instantaneous Re_1 remains large enough to induce global instability even when the jet is forced very strongly. At this Re_1, the frequency of the natural global mode is $f_n = 983$ Hz, corresponding to a Strouhal number of 0.27. This is the axisymmetric Mode II instability discussed by Monkewitz et al. (1990).

The jet is forced at 13 different frequencies around its natural frequency, ranging from 823 Hz ($f_f/f_n = 0.84$) to 1143 Hz ($f_f/f_n = 1.16$). At each f_f, the forcing amplitude, A, defined as the peak-to-peak voltage into the loudspeaker, is incrementally increased until lock-in is achieved. There is, however, one value of f_f, 823 Hz, for which lock-in cannot be achieved, even with the use of high A. This value of f_f is far from f_n, so this result is not surprising.

3.2.1 Response before lock-in

With f_f (1023 Hz) slightly above f_n, figure 3.6a shows time traces of the local streamwise velocity for nine forcing amplitudes: $200 \leq A \leq 900$ mV$_{\mathrm{pp}}$. For comparison, a time trace of the same quantity but without forcing is also shown (bottom). The corresponding PSD curves are shown in figure 3.6b.

When unforced, the jet has a global mode at a discrete natural frequency, represented in the PSD by a sharp peak at $f_n = 983$ Hz. There are similar, but weaker, peaks at the harmonics. The presence of harmonics indicates that the natural varicose oscillation of the jet is not perfectly sinusoidal. In particular, the peak at the first subharmonic, $f_n/2 = 491.5$ Hz, suggests a period-doubling

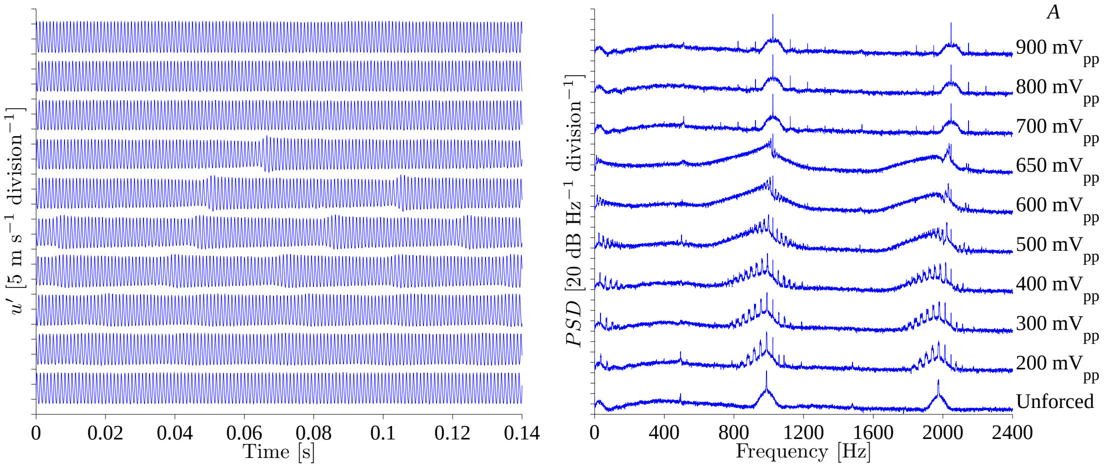

(a) Time trace (b) *PSD*

Figure 3.6: (a) Time trace and (b) *PSD* of the local streamwise velocity in the low-density jet forced at a frequency, $f_f = 1023$ Hz, slightly above the natural frequency, $f_n = 983$ Hz: $f_f/f_n = 1.04$. Data are shown for nine forcing amplitudes, $200 \leq A \leq 900$ mV$_{\text{pp}}$, and for the unforced case. The onset of lock-in occurs at $A_{loc} = 700$ mV$_{\text{pp}}$. The arbitrary reference for the dB scale in the *PSD* varies from curve to curve.

motion, commonly associated with vortex pairing.

When forced at low amplitudes ($200 \leq A \leq 400$ mV$_{\text{pp}}$), the jet responds at f_f as well as f_n. Around these two frequencies, there are multiple spectral peaks. Known as sidebands, they are caused by nonlinear interactions between the natural mode and the forcing. Their presence suggests that the jet is quasiperiodic (page 34), behaving like a typical forced oscillator before lock-in[1].

Additional spectral peaks arise at low frequencies, $f < 100$ Hz. Among these, the highest corresponds to the beat frequency: $|f_f - f_n|$. In the time traces (figure 3.6a), this beating phenomenon can be seen as low-frequency (long-wavelength) modulations of the signal amplitude.

The spectral peaks around f_n and f_f, as well as those at low f due to beating, can be explained by wavenumber-triad interactions. According to Pope (2000) (§6.4, eqn 6.146), if the Navier–Stokes equations are written in Fourier space, the

---

[1] In dynamical systems, quasiperiodicity tends to arise when a self-excited oscillator is driven at a low amplitude and at a frequency that is not a rational multiple of the natural frequency.

nonlinear convection term gives rise to a convolution sum. Each Fourier mode, say of wavenumber k_1, is forced by combinations of two other Fourier modes, k_2 and k_3, such that $k_1 = k_2 + k_3$. Two high-wavenumber (short-wavelength) modes, for example $k_2 = \pm\ 19$ and $k_3 = \pm\ 20$, can thus force a low-wavenumber (long-wavelength) mode, here $k_1 = \pm\ 1$. This low-wavenumber mode would resemble the beating mode observed above. Similarly, mode $k_1 = \pm\ 1$ could interact with the two modes forcing it, $k_2 = \pm\ 19$ and $k_3 = \pm\ 20$, generating multiple spectral peaks around them. These would resemble the sidebands observed above. Moreover, even the natural harmonics seen in the unforced jet can be explained by such interactions: the self-interaction of wavenumber k with itself causes the forcing of wavenumber $2k$.

As A increases from 400 to 650 $\mathrm{mV_{pp}}$, f_n shifts towards f_f, which remains fixed. This decrease in $|f_f - f_n|$ leads to an identical decrease in the dominant beat frequency. Meanwhile, the spectral peaks around f_n and f_f become closer and their envelope widens. By $A = 650\ \mathrm{mV_{pp}}$, they are almost imperceptible, their envelope showing a subtle bias towards frequencies below f_n, as indicated by the more marked tail.

Once A reaches a critical value of 700 $\mathrm{mV_{pp}}$, the natural mode locks into the forcing: the PSD becomes dominated by f_f and its harmonics (i.e. $2f_f$, $3f_f$,...), with no sign of the original natural mode. The PSD of the locked-in jet looks similar to that of the unforced jet, except that the dominant frequency is f_f.

The above features are seen not only when $f_f > f_n$ but also when $f_f < f_n$. Figure 3.7 shows time traces and PSD curves for $f_f = 943$ Hz, with the natural global mode at $f_n = 983$ Hz as before. The response leading up to lock-in is the same regardless of whether f_f is above or below f_n. In fact, even the subtle bias in the PSD envelope seen before lock-in is present, although with $f_f < f_n$ the tail of that envelope is now more marked on the high-frequency side of f_n.

The jet dynamics can be understood more easily by inspecting phase portraits and Poincaré maps. A phase portrait is a three-dimensional plot of the system motion (here u) against that same motion shifted by a time delay, and by two time delays[1]. A two-dimensional slice through that set of phase trajectories gives the

---

[1] As noted in chapter 2, the optimal time delay is found by computing the first zero-crossing of the autocorrelation function, as recommended by Abarbanel (1996).

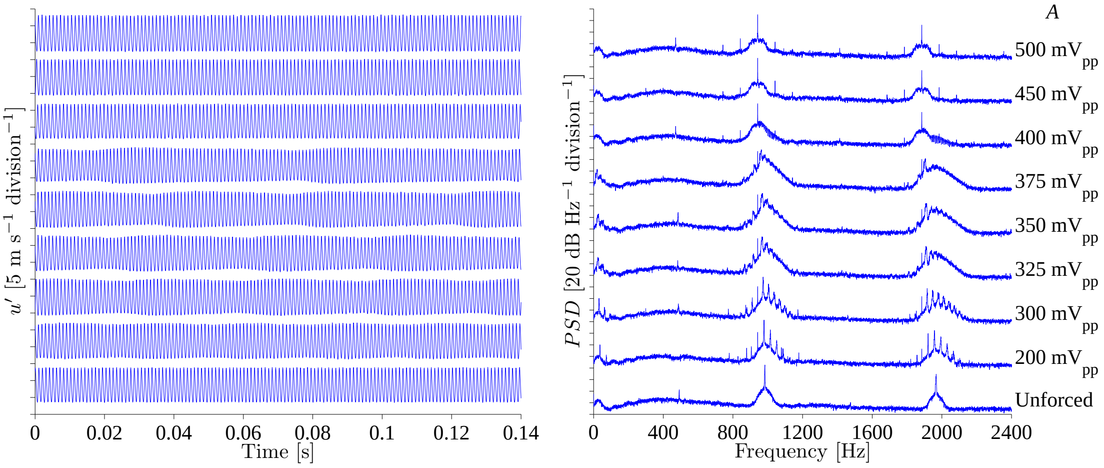

(a) Time trace (b) PSD

Figure 3.7: (a) Time trace and (b) PSD of the local streamwise velocity in the low-density jet forced at a frequency, $f_f = 943$ Hz, slightly below the natural frequency, $f_n = 983$ Hz: $f_f/f_n = 0.96$. Data are shown for eight forcing amplitudes, $200 \leq A \leq 500$ mV$_{\mathrm{pp}}$, and for the unforced case. The onset of lock-in occurs at $A_{loc} = 400$ mV$_{\mathrm{pp}}$. The arbitrary reference for the dB scale in the PSD varies from curve to curve.

Poincaré map. The phase portraits and Poincaré maps for the forcing conditions of figure 3.6 are shown in figure 3.8.

For the unforced jet (figure 3.8a), the phase trajectory is closed, indicating that the jet oscillates periodically at a limit cycle (of f_n). A cross-section of this trajectory contains data points scattered around two blobs. If the system were free of noise, the trajectory would be perfectly closed and the Poincaré map would show two discrete points.

As A increases, the phase trajectory follows the surface of a torus. In the Poincaré map, this is seen as two rings. The appearance of a torus-like surface is characteristic of quasiperiodicity. For weak forcing ($200 \leq A \leq 650$ mV$_{\mathrm{pp}}$), the rings grow as A increases. For strong forcing ($700 \leq A \leq 900$ mV$_{\mathrm{pp}}$), they close again to another limit cycle, this time at f_f. The final limit cycle resembles the one for the unforced jet, but has slightly less scatter because the flow is now forced by an external signal.

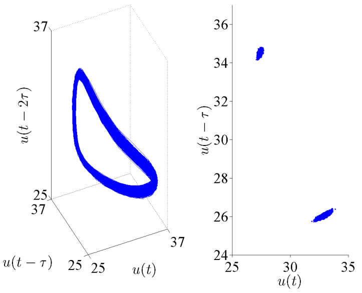

(a) $A = 0$ mV$_{\text{pp}}$

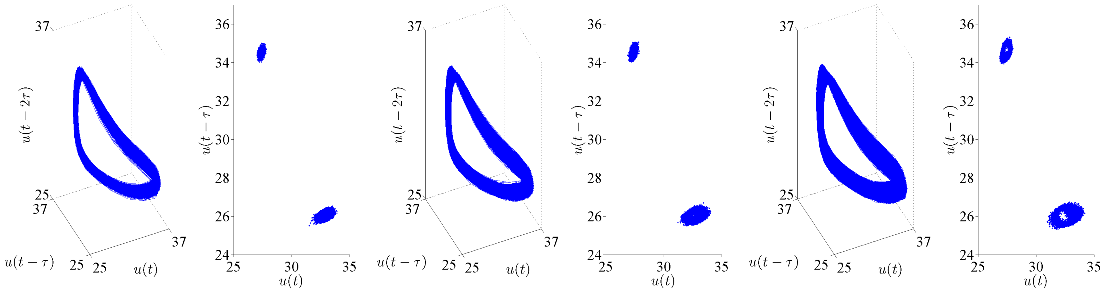

(b) $A = 200$ mV$_{\text{pp}}$ (c) $A = 300$ mV$_{\text{pp}}$ (d) $A = 400$ mV$_{\text{pp}}$

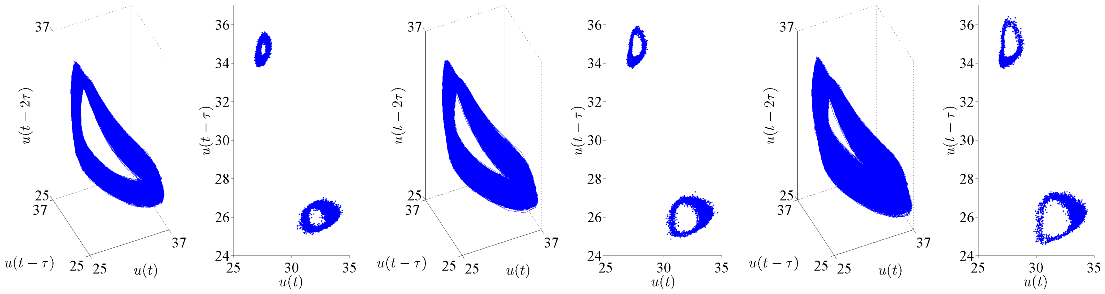

(e) $A = 500$ mV$_{\text{pp}}$ (f) $A = 600$ mV$_{\text{pp}}$ (g) $A = 650$ mV$_{\text{pp}}$

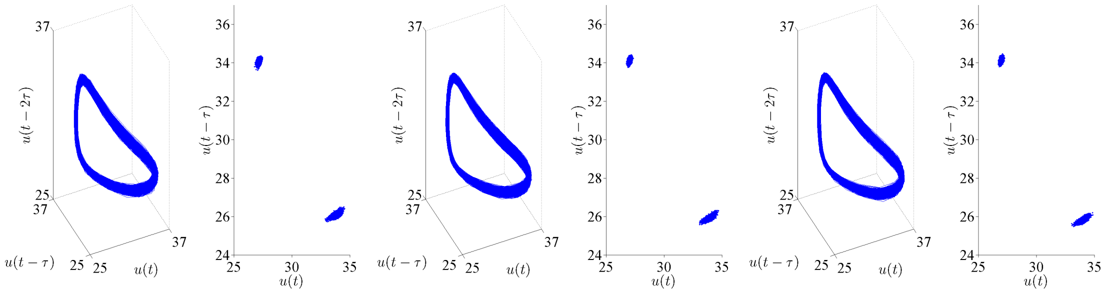

(h) $A = 700$ mV$_{\text{pp}}$ (i) $A = 800$ mV$_{\text{pp}}$ (j) $A = 900$ mV$_{\text{pp}}$

Figure 3.8: Phase portraits (left) and Poincaré maps (right) for the low-density jet forced at the conditions of figure 3.6. Each subfigure is for a different forcing amplitude: $A =$ (a) 0, (b) 200, (c) 300, (d) 400, (e) 500, (f) 600, (g) 650, (h) 700, (i) 800, and (j) 900 mV$_{\text{pp}}$.

3.2.2 Response at lock-in

The jet dynamics at lock-in can be examined via the relationship between the minimum forcing amplitude required for lock-in, A_{loc}, and the normalised forcing frequency, f_f/f_n. This is shown in figure 3.9 (circular markers) to form a lock-in map. The diagonal lines through the data around $f_f/f_n = 1$ are linear fits. The data at $f_f/f_n < 1$ are regressed separately from the data at $f_f/f_n > 1$.

Also shown on the figure are contours of the jet response, defined as the ratio of the RMS velocity fluctuation with forcing to the same quantity without forcing: $u'_{rms,\,for}/u'_{rms,\,unf}$. Globally unstable flows, such as this low-density jet, oscillate at discrete frequencies even when unforced, so normalising the response by that of the unforced jet provides a useful baseline.

When f_f is near f_n, A_{loc} is low; otherwise it is high. Around $f_f/f_n = 1$, A_{loc} increases in proportion to $|f_f - f_n|$, indicating a Hopf bifurcation to a global mode. This linear relationship gives rise to a $\vee$-shaped lock-in curve, similar to the ones seen in other self-excited flows (§1.4.2).

As A increases for $f_f > f_n$ or $< f_n$, the jet response first decreases below unity, reaches a minimum near the onset of lock-in (circular markers), and then increases back towards unity. As A increases for $f_f = f_n$, however, the jet response simply increases above unity without ever falling below it. The former finding shows that the jet oscillations at lock-in are weaker than those of the unforced jet. This suggests that, for thermoacoustic systems, lock-in may not be as detrimental as it is thought to be.

Finally, the $\vee$-shaped lock-in curve is asymmetric: A_{loc} is lower for $f_f < f_n$ than for $f_f > f_n$. In these experiments, A is assumed to be directly proportional to the acoustic power from the loudspeaker, as is common in the literature (Kyle and Sreenivasan, 1993; Sreenivasan et al., 1989). It is better, though, to have direct measurements of A, such as the acoustic pressure or velocity, because these would eliminate the unknown relationship between the loudspeaker voltage and flow fluctuations. For this reason, the two-microphone method will be used in the combustion experiments (chapter 4) in order to express the forcing in terms of the velocity perturbation at the injector outlet.

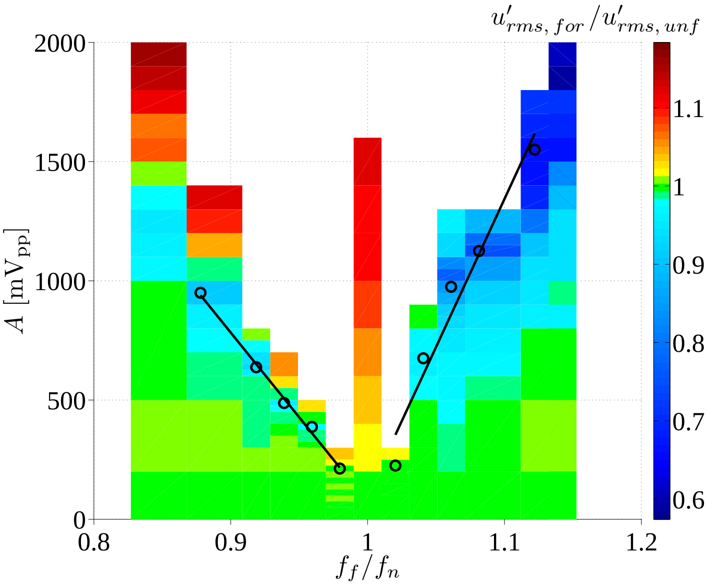

Figure 3.9: Lock-in map for the low-density jet, shown on contours of the normalised response (defined in the text). The critical forcing amplitude required for lock-in, A_{loc}, is indicated by the circular markers. On the colorscale, a jet response of unity is in green, with values above unity in warmer (red/yellow) hues and values below unity in cooler (blue/cyan) hues.

Chapter 4

Jet diffusion flames

In this chapter, the global instability of a range of jet diffusion flames is examined experimentally. First the flames are examined without forcing, in order to study their natural self-excited dynamics. Then they are examined with forcing applied around their natural frequencies, in order to study how their natural dynamics at one frequency are affected by external forcing at other frequencies.

The experiments are performed on Injector B (§2.4), with flames created from mixtures of methane and nitrogen. The flames are forced sinusoidally by a loudspeaker mounted upstream, and their responses measured with a high-speed camera via broadband chemiluminescence (§2.5.3).

4.1 Unforced

4.1.1 Baseflow characterisation

Before the flame dynamics is studied, the velocity profile at the outlet of Injector B is measured with HWA (§2.5.1). Air is used as the test fluid, as in the measurements on Injector A (§3.1.1).

Figures 4.1–4.3 are analogous to figures 3.1–3.3 but are for Injector B rather than for Injector A. Figure 4.1a shows radial profiles of the time-averaged streamwise velocity, normalised by the maximum across each profile, for a range of Reynolds numbers: $470 \leq Re_1 \leq 3290$. Figure 4.1b shows radial profiles of the

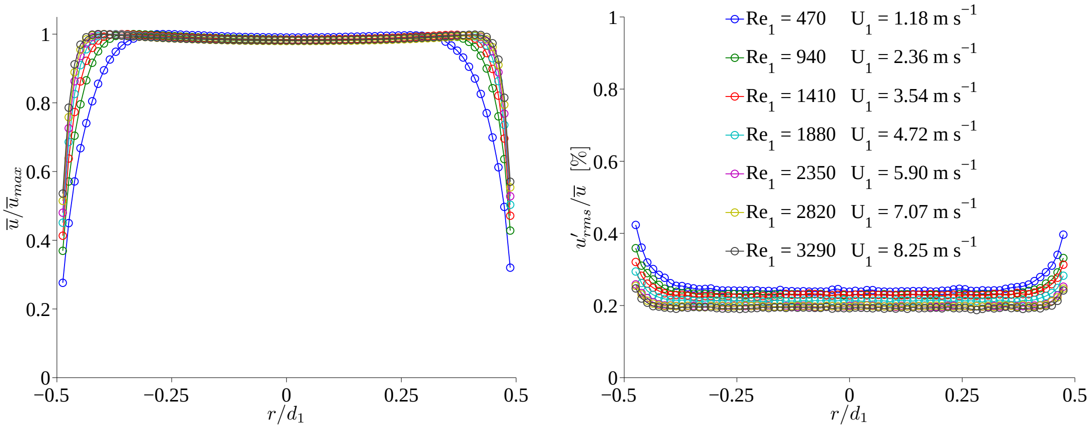

(a) Normalised time-averaged velocity (b) Turbulence intensity

Figure 4.1: (a) Normalised time-averaged velocity and (b) turbulence intensity at the outlet of Injector B. They are plotted as a function of radial position for seven Reynolds numbers: $470 \leq Re_1 \leq 3290$.

turbulence intensity[1] for the same Reynolds numbers. Figure 4.2 shows δ^* and θ, as well as their ratio, while figure 4.3 shows the transverse curvature, all as a function of the Reynolds number.

These figures show that the baseflow characteristics of Injector B are similar to those of Injector A. In both injectors, the velocity and the turbulence intensity are uniform over the central part of the flow and are symmetric about the jet centreline. The velocity approaches zero at the walls ($r/d_1 = \pm 0.5$) and the turbulence intensity peaks in the boundary layers. As Re_1 increases, the boundary layer thickness and the turbulence intensity both decrease. In other words, the flat part of the velocity profile extends to a greater radius and has proportionately less turbulent fluctuation.

There are, nevertheless, two notable differences. First, the turbulence intensity in Injector B is lower than that in Injector A. This is seen across the entire outlet, from the jet centreline to the boundary layers. In the central part of the flow, for example, the turbulence intensity in Injector B varies between 0.20 and 0.25% over $470 \leq Re_1 \leq 3290$ (figure 4.1b), whereas that in Injector A varies between 0.25 and 0.37% over a similar range of Re_1 (figure 3.1b). As for the

---

[1] As in chapter 3, the turbulence intensity is defined as the RMS velocity fluctuation normalised by the time-averaged velocity: $u'_{rms}/\overline{u}$.

second difference, the boundary layers in Injector B are thinner than those in Injector A – for any given value of Re_1. This can be seen in the lower values of δ^* and θ (figure 4.2a compared to figure 3.2a), as well as in the higher values of the transverse curvature (figure 4.3 compared to figure 3.3).

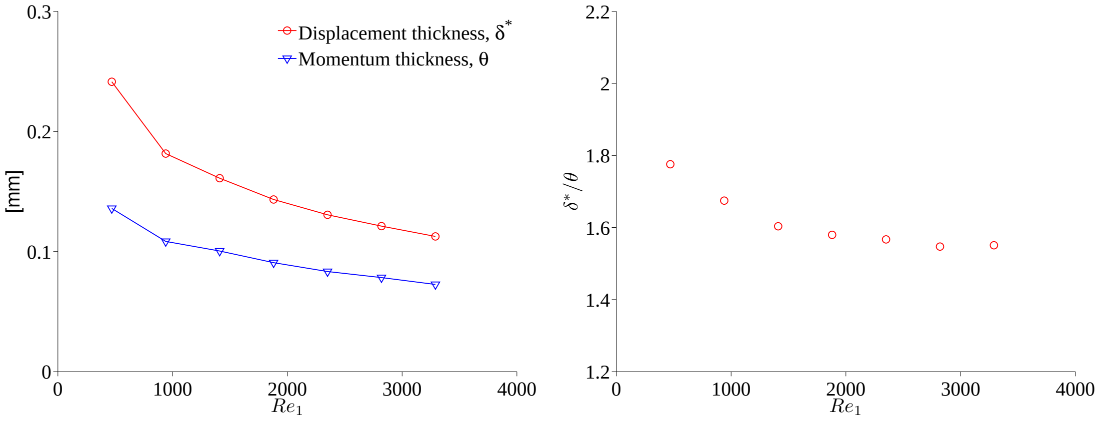

(a) δ^* and θ (b) δ^*/θ

Figure 4.2: (a) Displacement thickness, δ^*, and momentum thickness, θ, and (b) their ratio at the outlet of Injector B. They are plotted as a function of the same Reynolds numbers as in figure 4.1.

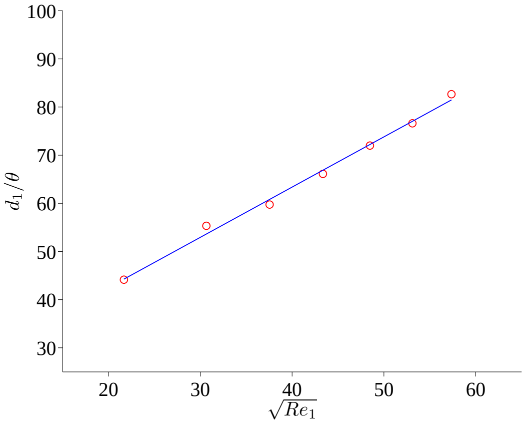

Figure 4.3: Transverse curvature, d_1/θ, at the outlet of Injector B. It is plotted as a function of the square root of the Reynolds numbers shown in figures 4.1 and 4.2. The blue line is a linear fit.

4.1.2 Global bifurcation

As noted in §2.2, the strength of the global instability in a jet diffusion flame can be changed by changing the flow parameters. Three of these are examined below: the mixture composition, the jet velocity, and the coflow velocity.

4.1.2.1 Mixture composition

The natural flame oscillation is measured as the volumetric concentration of methane, [CH_4], is varied between 36.7 and 100% (N_2 makes up the balance)[1]. For each flame, the total flow rate of the reactants is fixed at 5×10^{-5} m^3 s^{-1}, for a jet velocity of $U_1 = 1.77$ m s^{-1}. The oscillation amplitude is plotted in figure 4.4a as a function of [CH_4] and x/d_1. It is defined as the square of the local RMS intensity fluctuation normalised by the local time-averaged intensity: $(I'_{rms}/\overline{I})^2$.

At low methane concentrations ($36.7 \leq [CH_4] \leq 40\%$), the oscillation amplitude is low everywhere except near $x/d_1 \approx 18$ where it increases slightly, peaking around 0.35. Although the flame is globally stable throughout, it is convectively unstable in the upstream region. Small perturbations at the injector amplify in this region but remain undetectable until their amplitudes are sufficient to cause the flame to oscillate. An inspection of the high-speed videos shows that the flame begins to oscillate at $x/d_1 \approx 18$, a location that coincides with the measured increase in the oscillation amplitude.

Once $[CH_4] > 40\%$, the flame bifurcates into a global mode. This can be seen in the bifurcation diagram[2] of figure 4.4b, which shows the oscillation amplitude as a function of [CH_4] at four axial stations, all upstream of the location of peak amplitude. The global bifurcation causes an abrupt increase in the oscillation amplitude. Near the bifurcation point, the increase in the square of the intensity fluctuation is linear, indicating a Hopf bifurcation to a global mode. The exact value of the bifurcation point depends on the downstream distance: the base of the global mode moves upstream as [CH_4] increases. This spatial dependence has been reported before in counterflowing jets, by Strykowski and Niccum (1991), and in crossflowing jets, by Davitian et al. (2010). Beyond the bifurcation point,

---

[1] For $[CH_4] < 36.7\%$, the flame blows off and cannot be studied.

[2] The data in this figure are taken from horizontal slices through figure 4.4a.

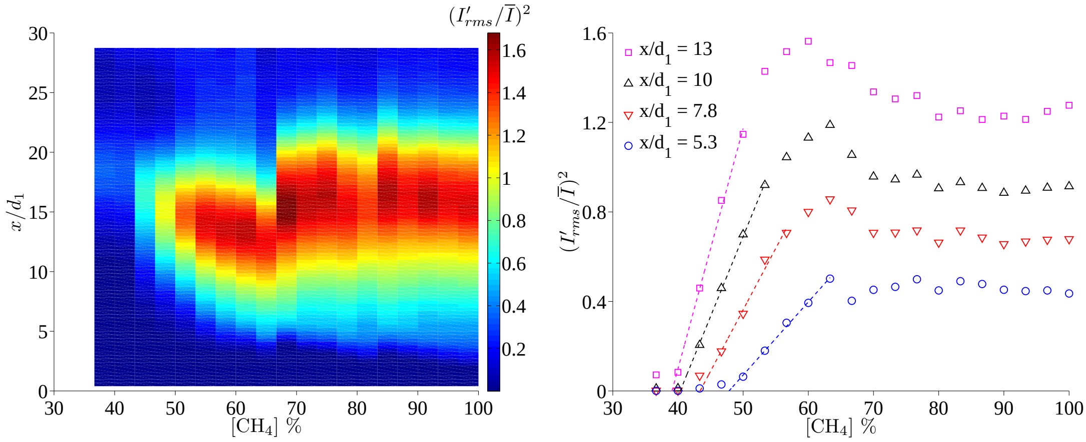

(a) Oscillation amplitude (b) Bifurcation diagram

Figure 4.4: Oscillation amplitude of CH$_4$–N$_2$ jet diffusion flames as a function of (a) methane concentration and axial distance, and (b) methane concentration at four axial stations. The oscillation amplitude is defined as the square of the local RMS intensity fluctuation normalised by the local time-averaged intensity: $(I'_{rms}/\overline{I})^2$. In subfigure (b), the dashed lines are linear fits to the data after the global bifurcation.

the oscillation amplitude continues to grow. Once [CH$_4$] > 63.3%, however, it remains roughly constant, all the way to [CH$_4$] = 100%, indicating that the saturated amplitude of the global mode has reached a maximum.

Further on the spatial dependence of the global mode, figure 4.4a shows that as [CH$_4$] increases above 40%, the location of peak amplitude shifts upstream. This happens until [CH$_4$] = 63.3%, after which it shifts to $x/d_1 \approx 16$ and stays there for higher [CH$_4$]. This curious behaviour is not investigated further.

4.1.2.2 Other control parameters

Changing the mixture composition is not the only way to control the global instability in a jet diffusion flame. It can also be done by changing the jet velocity or by adding coflow. Both of these methods have been tried in this thesis, but for brevity only an overview of the results is given.

For the globally unstable flames ($43.3 \leq$ [CH$_4$] $\leq 100\%$), increasing the jet velocity causes the oscillation amplitude to decrease and its peak to shift downstream. Above a critical jet velocity, the global mode becomes suppressed, resulting in a globally stable flame[1]. This critical jet velocity is highest for the most unstable flame ($[CH_4] = 100\%$) but decreases as the flame becomes less unstable (i.e. as $[CH_4]$ decreases). For the globally stable flames ($36.7 \leq [CH_4] \leq 40\%$), a similar decrease in the oscillation amplitude occurs with increasing jet velocity.

The decrease in the oscillation amplitude is caused by the increase in the group velocity of perturbations that arises from an increase in the jet velocity. In effect, the speed at which the kinetic energy of perturbations is advected downstream increases, making the flow less absolutely unstable, or even convectively unstable, thereby making the flow less globally unstable. This stabilising effect of the jet velocity is not, however, observed in all globally unstable flows. In the low-density jet (chapter 3), for example, increasing the jet velocity causes the oscillation amplitude to increase. To explain this behaviour, it is necessary to consider the physical mechanisms behind the global instability. In the low-density jet, the global instability arises from shear, and this increases with the jet velocity[2]. In the jet diffusion flame, the global instability arises from buoyancy[3] and is advected away by the jet velocity. The jet velocity therefore drives the instability in the low-density jet but damps it in the jet diffusion flame, which is why its increase leads to different effects on the two flows.

The effect of coflow air around the flame base has also been examined. The findings show that increasing the coflow velocity has a similar effect to increasing the jet velocity: the oscillation amplitude decreases and its peak shifts downstream. The physical cause is also similar: increasing the coflow velocity increases the group velocity of perturbations, increasing the mean advection. Compared to the jet velocity, the coflow velocity may even be more effective at sweeping away the instability, because the group velocity is weighted more heavily towards the velocity of the denser fluid. In buoyant jet diffusion flames, the denser fluid around the inflexion point (IP3 in figure 1.7) causing global instability is the ambient fluid, which is replaced by the coflow fluid when coflow is used.

---

[1] This suppression of global instability is seen throughout the entire flame, and is not just an artefact of the instability shifting outside the field of view.

[2] Advection also increases with the jet velocity but not enough to carry away the instability.

[3] Specifically from a buoyancy-induced modification of the velocity profile that creates an absolutely unstable inflexion point just outside the flame surface (IP3 in figure 1.7).

In this thesis, the coflow velocities used ($0 \leq U_2/U_1 \leq 0.14$) are not sufficient to fully damp the global mode but are sufficient to reduce its oscillation amplitude. For the globally stable flames ($36.7 \leq [CH_4] \leq 40\%$), introducing even a small amount of coflow ($U_2/U_1 \approx 0.01$) causes the flame to lift off from the injector lip[1]. Because this thesis does not concern lifted flames, however, these conditions are not investigated further.

In some experiments, hydrogen is used as the fuel. Compared to methane, hydrogen has a lower density, a lower stoichiometric mixture fraction, and a higher flame temperature. These features help make a hydrogen flame more globally unstable than an equivalent methane flame, though this is not the only reason it is used. Research by Juniper et al. (2009) has shown that a hydrogen flame can be made globally stable in similar ways as a methane flame can be: for example, by diluting the fuel with nitrogen or helium. The use of hydrogen, in place of methane, therefore enables a wider range of self-excited dynamics to be studied.

In this thesis, experiments with hydrogen are limited to just a few exploratory tests, for two main reasons. The first is related to safety. Among flammable gases, hydrogen is particularly dangerous owing to its wide explosion limits and low ignition energy. This danger is exacerbated by the measurement procedure, which requires that the local extraction be deactivated during data acquisition in order to prevent exhaust updrafts from disturbing the sensitive flame oscillations.

The second reason for not using hydrogen more extensively is related to optical diagnostics. The chemiluminescent emission from a hydrogen flame is weak, resulting in a low SNR in the high-speed videos. This problem is exacerbated partly because an image intensifier is not available and partly by the need to use short exposure times for resolving the dominant flame frequencies. Consequently, methane is preferred over hydrogen because its chemiluminescent emission is stronger and can be imaged more reliably with the available equipment.

In the limited tests involving hydrogen, only schlieren imaging is used. Schlieren works well for this because hydrogen has a low density and thus produces high density gradients when combusting in atmospheric air.

---

[1] The flame can be 'stabilised' with its base perfectly steady up to $5d_1$ above the injector lip. This stability is a testament to the symmetry and quietness of the baseflow in Injector B.

4.2 Forced

The flames are forced around their natural frequencies, in order to study how their natural dynamics at one frequency are affected by external forcing at other frequencies. In total, six different flames are studied (table 4.1): five globally unstable and one marginally globally stable. For each flame, the total flow rate of the reactants is fixed at 5×10^{-5} m^3 s^{-1}, for a jet velocity of $U_1 = 1.77$ m s^{-1}.

The globally unstable flames (Flames 1–5) all have similar natural frequencies: $12.5 \leq f_n \leq 14.7$ Hz. The marginally globally stable flame (Flame 6) has two natural frequencies, 14.8 and 16.1 Hz, when unforced. These, however, are replaced by a lightly damped global mode, at $f_n = 14.3$ Hz, whenever forcing is applied – however low its amplitude and even if its frequency is far from f_n.

All six flames are forced sinusoidally by a loudspeaker mounted upstream (§2.4), over a range of frequencies ($7 \leq f_f \leq 35$ Hz)[1] around the natural global frequency. This f_f range is wide, covering f_n and its second harmonic, $2f_n$. It also covers the high-frequency side of the first subharmonic, $f_n/2$. The low-frequency side is not covered because the loudspeaker cannot produce sufficient forcing amplitudes without damaging its suspension. Moreover, as f_f decreases, the waveform of the sinusoidal forcing signal becomes increasingly distorted, leading to undesired harmonics in the measured spectra.

The forcing amplitude, A, is measured with the two-microphone method (§2.5.2). It is defined, at the injector plane, as the amplitude of the velocity perturbation at f_f normalised by the bulk jet velocity: $A \equiv |u'_{1,f_f}|/U_1$. At each f_f, A is incrementally increased to 0.90, even though lock-in often occurs earlier[2]. Lock-in is defined as being when f_n locks into f_f, leaving no sign of the natural global mode in the PSD. This is a qualitative change, meaning that the onset of lock-in can be identified simply by inspecting the PSD.

The flame response is measured with the high-speed imaging setup described in §2.5.3. As mentioned in that section, the intensity in each frame of each video is summed across every pixel column, generating a time series – five pixel rows

---

[1] The f_f increment is 1 Hz, except if f_n is more than 0.25 Hz from an integer frequency value, in which case an additional setting, at the 0.5 Hz increment, is used.

[2] The A increment is usually 0.20 but is reduced to 0.050 around lock-in and to 0.025 if lock-in occurs at $A < 0.10$.

Table 4.1: Flow conditions of the six flames under investigation. The properties listed are at a temperature of 293 K and a pressure of 101.3 kPa. GU, globally unstable; MGS, marginally globally stable; U_2/U_1, coflow-to-jet velocity ratio; f_n, natural global frequency; s, cold density ratio; Z_{st}, stoichiometric mixture fraction; T_{ad}, adiabatic flame temperature; Re_1, cold jet Reynolds number.

Flame		$[CH_4]\%$	$[N_2]\%$	U_2/U_1	f_n [Hz]	s	Z_{st}	T_{ad} [K]	$Re_1^\star$
1	GU	100	0	0	12.5	0.554	0.055	2330	647
2		100	0	0.083	13.9	0.554	0.055	2330	647
3		80	20	0	13.0	0.637	0.077	2290	488
4		60	40	0	13.3	0.719	0.112	2230	496
5		60	40	0.083	14.7	0.719	0.112	2230	496
6	MGS	40	60	0	$14.3^{\star\star}$	0.802	0.175	2120	543

$\star$ The mixture viscosities used in calculating Re_1 are approximated by the method of Wilke (1950), with data for the pure components provided by Poling et al. (2001).

$\star\star$ This is the frequency of the marginal global mode, which is detectable only with forcing. Without forcing, Flame 6 exhibits two weak modes at 14.8 and 16.1 Hz.

in height – at each axial station, $I\,(x/d_1)$ (see figure 2.8 for details). In most of this chapter, however, only one axial station is considered: $x/d_1 = 10$. This station is chosen for three reasons: (i) it is just far enough downstream that the chemiluminescent emission leads to a reliable SNR without saturation; (ii) it is sufficiently far downstream that the global mode (if one exists) has time to grow and interact with the forcing; but (iii) it is not so far downstream that it coincides with the location of vortex roll-up, where the strain rates can be high enough to cause local flame extinction[1], especially if high forcing amplitudes are used. The other axial stations will be considered later, when the flame response is examined via the flame describing function (§4.2.3).

---

[1] Lingens et al. (1996b) showed that in jet diffusion flames, the axial velocity gradient caused by the natural roll-up of toroidal structures can reach up to 360 s^{-1}, which is near the critical strain rates for extinction (350–410 s^{-1}, for methane) reported by Tsuji and Yamaoka (1971) and Dixon-Lewis et al. (1985).

4.2.1 Response before lock-in

The flame response before lock-in is examined because it will determine how decoupled the heat release can be from the applied perturbations. A globally unstable flame is considered first, followed by a marginally globally stable flame.

4.2.1.1 Globally unstable flame

Flame 5 is used as a representative flame because it exhibits most clearly the dynamics common to all five globally unstable flames. As an added benefit, its oscillations are particularly clean and axisymmetric – probably because the coflow stream shields the sensitive buoyant plume from external disturbances such as indoor drafts and ambient noise – which should help in the search for spectral features and trends.

4.2.1.1.1 Forcing near the fundamental: f_n

With f_f (16 Hz) slightly above f_n, figure 4.5a shows time traces of the intensity from Flame 5 forced at five amplitudes: $0.025 \leq A \leq 0.30$. For comparison, a time trace of the same signal from the same flame but without forcing is also shown (bottom). The corresponding PSD curves are shown in figure 4.5b.

The response of this flame is qualitatively similar to that of the low-density jet from chapter 3. When unforced, the flame has a global mode at a discrete natural frequency, represented in the PSD by a sharp peak at $f_n = 14.7$ Hz. There are similar, but weaker, peaks at the harmonics. The presence of harmonics indicates that the natural varicose oscillation of the flame is not perfectly sinusoidal.

When forced at a low amplitude ($A = 0.025$), the flame responds at f_f as well as f_n. Around these two frequencies, there are multiple spectral peaks. Known as sidebands, they are caused by nonlinear interactions between the natural mode and the forcing (as explained on page 79). Their presence suggests that the flame is quasiperiodic, behaving like a typical forced oscillator before lock-in[1].

Additional spectral peaks arise at low frequencies, $f < 3$ Hz. Among these, the highest corresponds to the beat frequency: $|f_f - f_n|$. In the time traces (figure

---

[1] In dynamical systems, quasiperiodicity tends to arise when a self-excited oscillator is driven at a low amplitude and at a frequency that is not a rational multiple of the natural frequency.

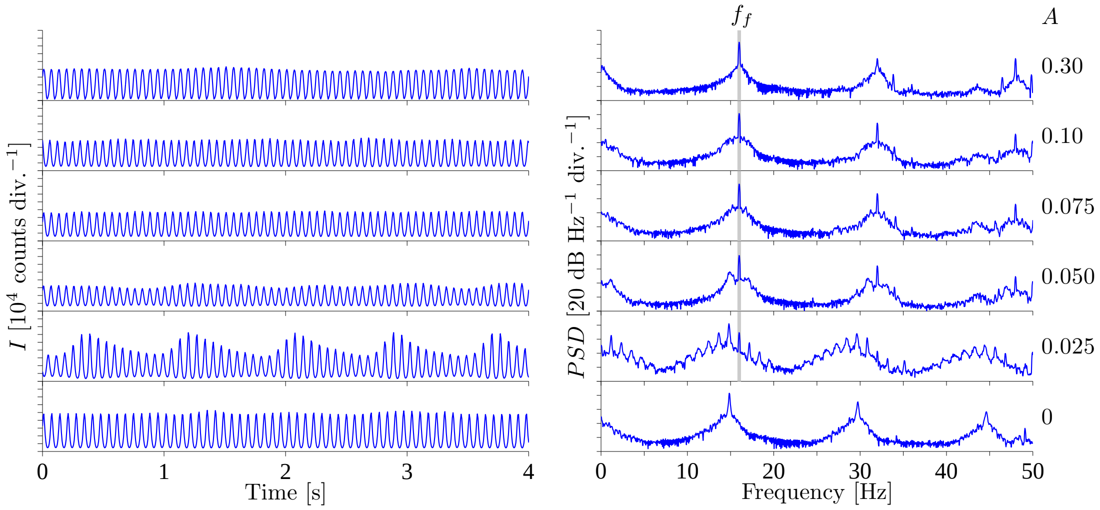

(a) Time trace (b) PSD

Figure 4.5: (a) Time trace and (b) PSD of the intensity from Flame 5 forced at a frequency, $f_f = 16$ Hz, slightly above the natural frequency, $f_n = 14.7$ Hz: $f_f/f_n = 1.09$. Data are shown for five forcing amplitudes, $0.025 \leq A \leq 0.30$, and for the unforced case, all at $x/d_1 = 10$. The onset of lock-in occurs at $A_{loc} = 0.075$.

4.5a), this beating phenomenon can be seen as low-frequency (long-wavelength) modulations of the signal amplitude.

As A increases from 0.025 to 0.050, f_n shifts towards f_f, which remains fixed. This decrease in $|f_f - f_n|$ leads to an identical decrease in the dominant beat frequency. Meanwhile, the spectral peaks around f_n and f_f become closer and their envelope widens. By $A = 0.050$, they are almost imperceptible, although a subtle bias can be seen for $f < f_n$, as indicated by the more marked tail on that side of the spectral envelope.

Once A reaches a critical value of 0.075, the natural mode locks into the forcing: the PSD becomes dominated by f_f and its harmonics (i.e. $2f_f$, $3f_f$,...), with no sign of the original natural mode. The PSD of the locked-in flame looks similar to that of the unforced flame, except that the dominant frequency is f_f.

The above features are seen not only when $f_f > f_n$ but also when $f_f < f_n$. Figure 4.6 is analogous to figure 4.5 but for $f_f = 14$ Hz or $f_f/f_n = 0.95$. A comparison of these two cases reveals both similarities and differences between forcing above and below the natural frequency. The similarities are mostly in the

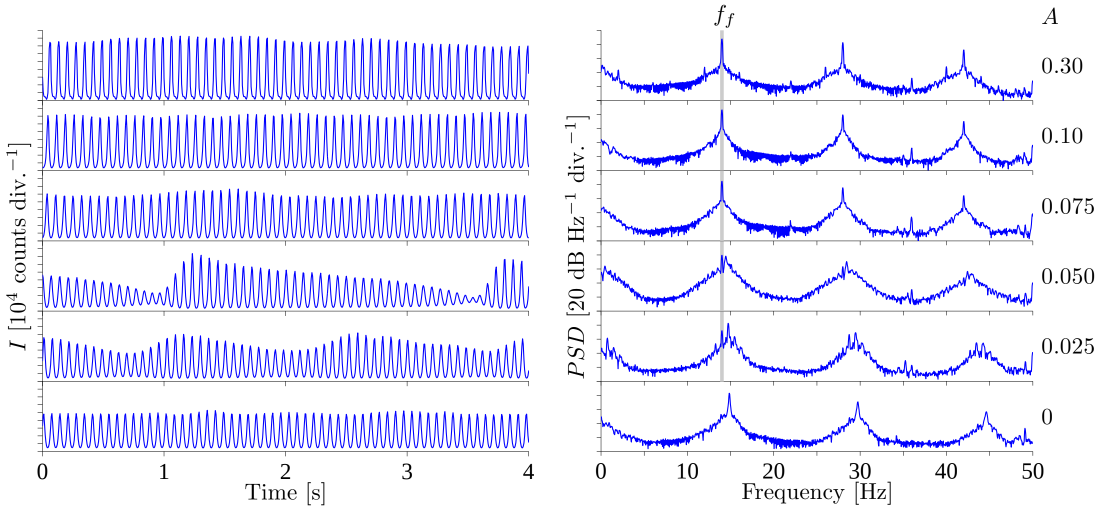

(a) Time trace

(b) *PSD*

Figure 4.6: (a) Time trace and (b) *PSD* of the intensity from Flame 5 forced at a frequency, $f_f = 14$ Hz, slightly below the natural frequency, $f_n = 14.7$ Hz: $f_f/f_n = 0.95$. Data are shown for five forcing amplitudes, $0.025 \leq A \leq 0.30$, and for the unforced case, all at $x/d_1 = 10$. The onset of lock-in occurs at $A_{loc} = 0.075$.

shape of the *PSD*: almost all of the features seen for $f_f > f_n$ (figure 4.5b) are seen for $f_f < f_n$ (figure 4.6b). In fact, even the subtle bias in the *PSD* envelope seen before lock-in is present, although with $f_f < f_n$ the tail of that envelope is now more marked on the high-frequency side of f_n.

As for the differences, the main one is in the amplitude of the flame oscillations, particularly around lock-in. When forced to lock into a frequency $< f_n$ (figure 4.6), the flame oscillates with an amplitude that is higher than the unforced amplitude. When forced to lock into a frequency $> f_n$ (figure 4.5), however, the flame oscillates with an amplitude that is lower than the unforced amplitude. This difference appears even before the flame fully locks in ($A = 0.025$–0.050 in both cases) and remains after it does, despite the fact that further increases in A cause the oscillation amplitude to increase for either $f_f < f_n$ or $> f_n$. This amplitude dependence on f_f is also detectable in the magnitude of the *PSD* peaks (figures 4.5b and 4.6b) and will be examined more carefully in §4.2.2.

Sample images of Flame 5 oscillating through one complete cycle are shown in figure 4.7 for both $f_f < f_n$ ($f_f/f_n = 0.95$) and $f_f > f_n$ ($f_f/f_n = 1.09$), as well as for the unforced case. For the unforced case (figure 4.7e), the roll-up of toroidal vortices due to the natural (hydrodynamic) global mode causes the flame intensity to vary axisymmetrically with high temporal repeatability. The flame intensity is strongest just downstream of the passing vortex core, but is weakest just upstream of it, suggesting that the variations in heat release are caused by variations in flame stretch. According to Lingens et al. (1996b) and Katta and Roquemore (1995), the heat release from a laminar diffusion flame is a strong function of the strain rate at the fuel–oxidiser layer. High strain rates, as induced by the passage of a vortex, can lead to decreases in the flame temperature and the reaction-zone thickness, thus leading to decreases in the local heat release.

As A increases for $f_f < f_n$ (figure 4.7c), the flame surface becomes more convoluted, exhibiting seemingly larger curvatures. This is probably due to nonlinear interactions between the vortical waves from the applied forcing and the vortical waves from the natural mode. At lock-in (figure 4.7a), the flame oscillations are particularly strong. This is probably because the toroidal vortices, which no longer roll up naturally but are driven by the forcing, are now of sufficient size and strength that they are able to readily penetrate to the reaction zone and readily affect its curvature and thickness.

As A increases for $f_f > f_n$ (figure 4.7d), the flame initially remains similar to the unforced flame. At lock-in (figure 4.7b), however, the flame oscillations are markedly weaker, with no noticeable roll-up of coherent structures. These observations concur with the data presented earlier (figures 4.5 and 4.6).

To complement figure 4.7, figure 4.8 shows axial distributions of the PSD from Flame 5 for the same forcing conditions. The primary purpose of this figure is to show that all of the spectral features noted earlier at $x/d_1 = 10$ can be extended throughout the flame body. The secondary purpose is to show generally how the PSD varies in space. Close upstream, the PSD is weak because the chemiluminescent intensity – and hence the SNR – is low. With downstream development, however, it increases across the entire measured bandwidth, saturating at $x/d_1 \approx 10$ or around where most of the data in this chapter is examined. This is also the location where, just before lock-in (figure 4.8d), the spectral peaks around f_f and f_n have the widest envelope. Finally, once A_{loc} is reached (figures 4.8a and 4.8b), lock-in occurs simultaneously everywhere in the flame.

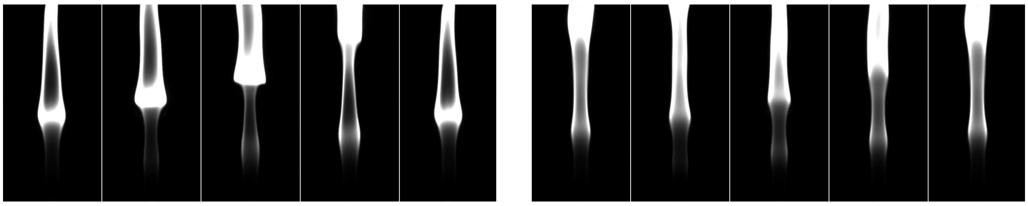

(a) $f_f = 14$ Hz, $A = 0.075$ (Locked-in) (b) $f_f = 16$ Hz, $A = 0.075$ (Locked-in)

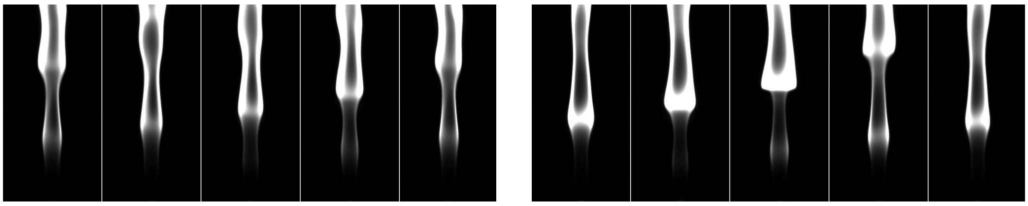

(c) $f_f = 14$ Hz, $A = 0.025$ (Not locked-in) (d) $f_f = 16$ Hz, $A = 0.025$ (Not locked-in)

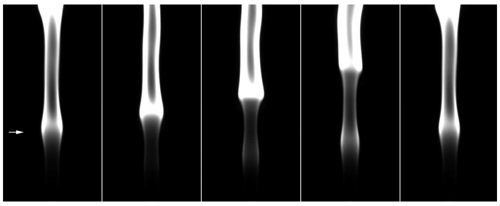

(e) Unforced

Figure 4.7: Image sequence of Flame 5 oscillating through one complete cycle. The forcing conditions range from (e) unforced, to weakly forced without lock-in (c) below and (d) above f_n, to strongly forced with lock-in (a) below and (b) above f_n. For the cases with lock-in (a, b), the images are separated in time by a quarter period of the forcing. For the cases without lock-in (c, d, e), the images are separated in time by a quarter period of the natural mode ($f_n = 14.7$ Hz). The sequences run from left to right, and the white arrow in subfigure (e) indicates the axial station at which the data are examined ($x/d_1 = 10$). The field of view extends downstream to $x/d_1 = 29$.

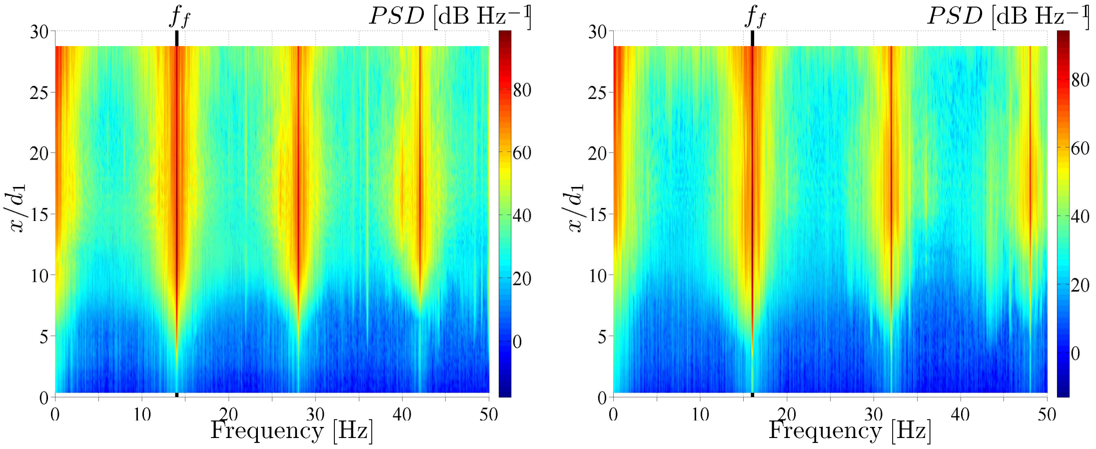

(a) $f_f = 14$ Hz, $A = 0.075$ (Locked-in)

(b) $f_f = 16$ Hz, $A = 0.075$ (Locked-in)

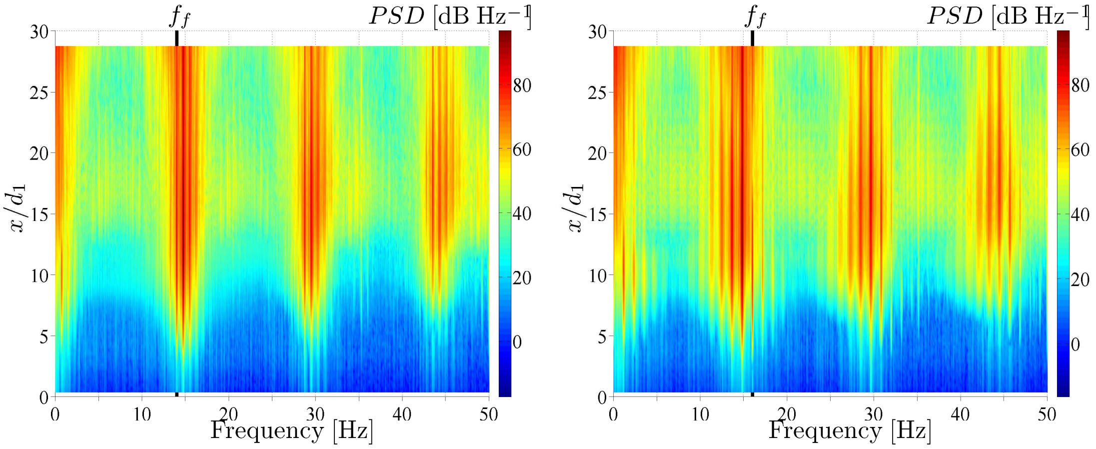

(c) $f_f = 14$ Hz, $A = 0.025$ (Not locked-in)

(d) $f_f = 16$ Hz, $A = 0.025$ (Not locked-in)

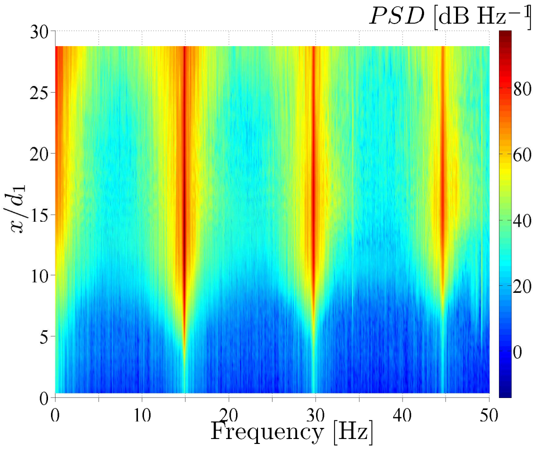

(e) Unforced

Figure 4.8: PSD of the intensity from Flame 5 as a function of downstream distance, x/d_1. The forcing conditions are the same as those in figure 4.7.

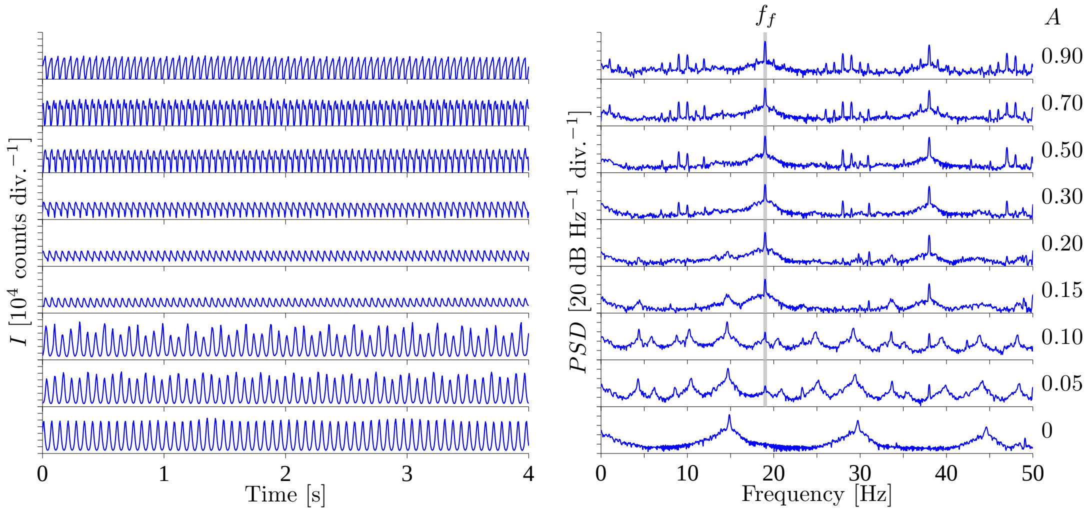

(a) Time trace (b) PSD

Figure 4.9: (a) Time trace and (b) PSD of the intensity from Flame 5 forced at a frequency, $f_f = 19$ Hz, well above the natural frequency, $f_n = 14.7$ Hz: $f_f/f_n = 1.29$. Data are shown for eight forcing amplitudes, $0.05 \leq A \leq 0.90$, and for the unforced case, all at $x/d_1 = 10$. The onset of lock-in occurs at $A_{loc} = 0.20$.

The flame responds to forcing not just when f_f and f_n are close together but also when they are far apart. Figure 4.9 is analogous to figures 4.5 and 4.6 but for $f_f = 19$ Hz or $f_f/f_n = 1.29$. It shows that when f_f is far from f_n, lock-in still occurs, though it does not involve f_n shifting to f_f progressively. Instead it occurs abruptly once A reaches a critical value: $A_{loc} = 0.20$. Before lock-in ($A = 0.05$–0.10), there is beating between f_n and f_f, as indicated by the low-frequency peak in the PSD at around 4.3 Hz. The amplitude of this peak is higher than the amplitude of the f_f peak. On approach to lock-in ($A = 0.15$–0.20), the amplitude of the natural mode at f_n falls to the background noise level. After lock-in ($A = 0.30$–0.90), further increases in A give rise to identical sets of spectral peaks between DC and f_f as well as between the harmonics of f_f.

The flame dynamics can be understood more easily by inspecting phase portraits and Poincaré maps. A phase portrait is a three-dimensional plot of the system motion (here I) against that same motion shifted by a time delay, and by two time delays[1]. A two-dimensional slice through that set of phase trajectories

---

[1] As noted in chapter 2, the optimal time delay is found by computing the first zero-crossing

gives the Poincaré map. The phase portraits and Poincaré maps for Flame 5 forced at 16 Hz (the forcing conditions of figure 4.5) are shown in figure 4.10.

For the unforced flame (figure 4.10a), the phase trajectory is closed, indicating that the flame oscillates periodically at a limit cycle (of f_n). A cross-section of this trajectory contains data points scattered around two blobs. If the system were free of noise, the trajectory would be perfectly closed and the Poincaré map would show two discrete points.

The blobs are elongated for this flame but are circular for the low-density jet from chapter 3. The cause of this is not known but may be related to asymmetries in the flame intensity signal. A comparison of figures 4.5a and 3.6a shows that the amplitude modulation in the flame signal occurs mostly at the top of the waveform (at high intensity values), whereas the amplitude modulation in the jet signal occurs at both the top and bottom. In other words, the amplitude modulation in the flame signal is not symmetric about the mean: the troughs remain relatively steady while the crests move up and down significantly. This behaviour may explain why the Poincaré maps for the flame show trajectories with lots of movement along one axis but not much movement along the other axis. As for why the troughs of the flame signal remain steady, several explanations are plausible. Local extinction is one, although inadequate camera sensitivity could also produce a similar effect.

As A increases, the phase trajectory follows the surface of a torus. In the Poincaré map (figure 4.10b), this is seen as two rings. The appearance of a torus-like surface is characteristic of quasiperiodicity. For weak forcing ($A = 0.025$–0.050), the rings grow as A increases. For strong forcing ($A = 0.075$–0.30), they close again to another limit cycle, this time at f_f. The final limit cycle resembles the one for the unforced flame, but has slightly less scatter because the flow is now forced by an external signal.

For completeness, the phase portraits and Poincaré maps for Flame 5 forced at 14 Hz are shown in Appendix F. They are qualitatively similar to those for $f_f = 16$ Hz and therefore need not be discussed again.

---

of the autocorrelation function, as recommended by Abarbanel (1996).

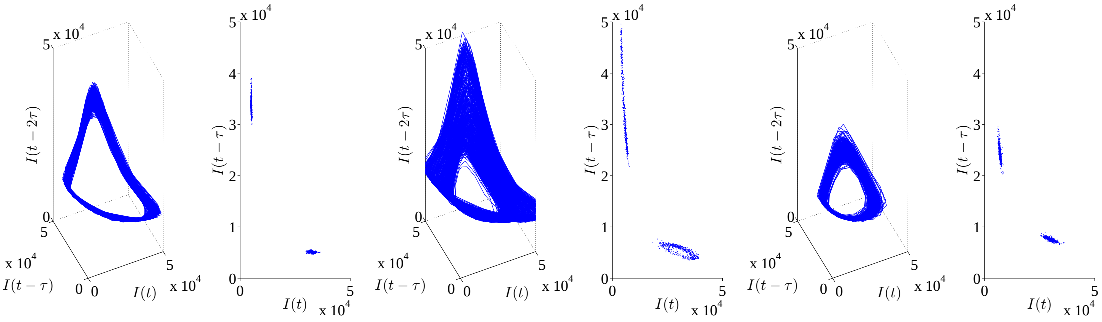

(a) $A = 0$ (b) $A = 0.025$ (c) $A = 0.050$

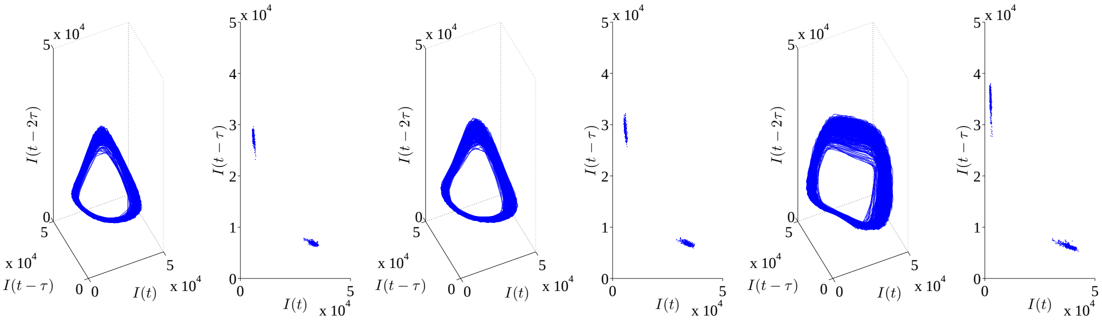

(d) $A = 0.075$ (e) $A = 0.10$ (f) $A = 0.30$

Figure 4.10: Phase portraits (left) and Poincaré maps (right) for Flame 5 forced at 16 Hz ($f_f/f_n = 1.09$) with five amplitudes, plus the unforced case.

4.2.1.1.2 Forcing near the first subharmonic: $f_n/2$

Lock-in can also be achieved by forcing the flame near the first subharmonic of its natural fundamental frequency. With f_f (8 Hz) slightly above $f_n/2$ (7.35 Hz), figure 4.11a shows time traces of the flame intensity for seven forcing amplitudes: $0.10 \leq A \leq 0.70$. For comparison, a time trace of the same signal from the same flame but without forcing is also shown (bottom). The PSD curves for these signals are shown in figure 4.11b, and their phase portraits and Poincaré maps are shown in figure 4.12.

When unforced, the flame oscillates periodically at a limit cycle ($f_n = 14.7$ Hz) with substantial energy in the harmonics, as expected. When forced at a low amplitude ($A = 0.10$), it responds at both f_f and f_n, also as expected. There is again beating between f_n and f_f, giving rise to a spectral peak at $f_n - f_f = 14.7 - 8 = 6.7$ Hz, on the low-frequency side of f_f. Further interactions occur between this primary beat frequency and f_f itself, giving rise to another spectral peak, this time at $f_f - (f_n - f_f) = 8 - (14.7 - 8) = 1.3$ Hz. The nonlinear interactions between the natural, forcing, and beat frequencies become stronger as A increases. The result is that just before lock-in ($A = 0.30$), a train of spectral peaks develops in the PSD (figure 4.11b) and a torus-like structure develops in the phase portrait and Poincaré map (figure 4.12c). Taken together, these features indicate that the flame oscillates quasiperiodically before lock-in, with the forcing and the natural mode competing nearly equally for control of the oscillations.

Once A reaches a critical value of 0.35, subharmonic lock-in occurs. The time traces, nevertheless, show that the waveform of the flame intensity signal is far from sinusoidal: it contains secondary crests halfway between primary crests. The primary crests, at a frequency of 8 Hz, are caused by the flame locking into the forcing. The secondary crests, at the same frequency but shifted in phase by π, team up with the primary crests to create a strong spectral peak at the second harmonic of the forcing signal, $2f_f$. The phase portrait at lock-in (figure 4.12d) shows a trajectory that goes through two loops before overlapping onto itself. Compared to a single-loop trajectory, this twin-loop trajectory takes twice as long to complete a limit cycle, which is why it is often referred to as a 'period-2 oscillation'. A telltale sign of a period-2 oscillation is the appearance

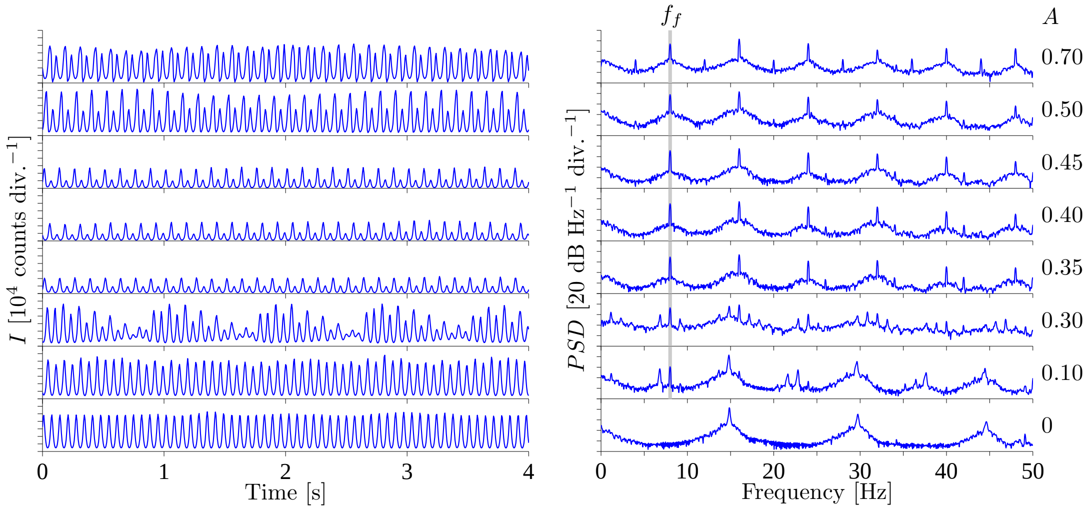

(a) Time trace (b) PSD

Figure 4.11: (a) Time trace and (b) PSD of the intensity from Flame 5 forced at a frequency, $f_f = 8$ Hz, slightly above the first subharmonic, $f_n/2 = 7.35$ Hz: $f_f/(f_n/2) = 1.09$. Data are shown for seven forcing amplitudes, $0.10 \leq A \leq 0.70$, and for the unforced case, all at $x/d_1 = 10$. The onset of lock-in occurs at $A_{loc} = 0.35$.

of four discrete points in the Poincaré map. Figure 4.12d does indeed show four discrete blobs, and these remain relatively intact as A increases. The time traces, meanwhile, show that the oscillation amplitude of the (subharmonic) locked-in flame is much lower than that of the unforced flame. A similar reduction in the oscillation amplitude was seen earlier for f_f slightly above f_n (figure 4.5a), so seeing it here for f_f slightly above $f_n/2$ is not entirely surprising. Still, this behaviour will be examined more carefully in §4.2.2.

At higher forcing amplitudes ($A = 0.50$–0.70), there is a spectral peak at the first subharmonic of the forcing frequency: $f_f/2 = 4$ Hz (figure 4.11b). Its presence suggests that the flame is undergoing a period-doubling motion, commonly associated with vortex pairing.

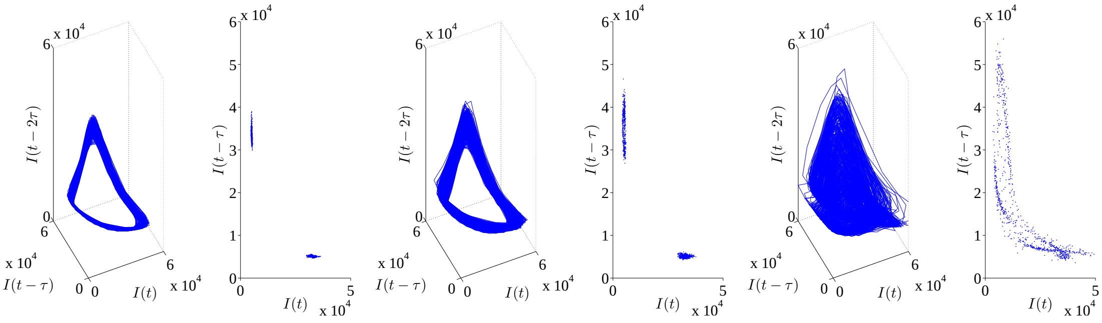

(a) $A = 0$ (b) $A = 0.10$ (c) $A = 0.30$

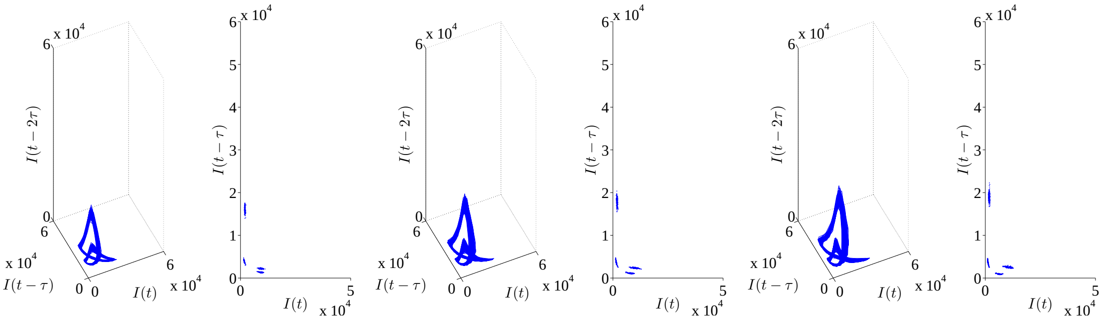

(d) $A = 0.35$ (e) $A = 0.40$ (f) $A = 0.45$

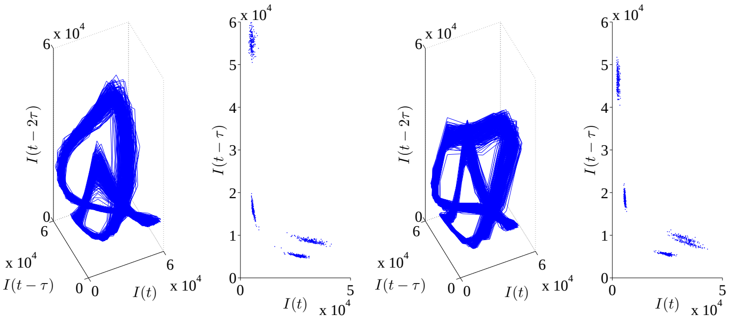

(g) $A = 0.50$ (h) $A = 0.70$

Figure 4.12: Phase portraits (left) and Poincaré maps (right) for Flame 5 forced at 8 Hz ($f_f/(f_n/2) = 1.09$) with seven amplitudes, plus the unforced case.

4.2.1.1.3 Forcing near the second harmonic: $2f_n$

The flame dynamics become more complex when the forcing is applied near the second harmonic of the natural fundamental frequency. With f_f (29 Hz) slightly below $2f_n$ (29.4 Hz), figure 4.13 shows time traces and PSD curves of the flame intensity for five forcing amplitudes ($0.10 \leq A \leq 0.90$) and for the unforced case. The phase portraits and Poincaré maps are shown in figure 4.14.

When unforced, the flame oscillates periodically at a limit cycle ($f_n = 14.7$ Hz) with substantial energy in the harmonics, as expected. When forced at a low amplitude ($A = 0.10$), it responds with typical nonlinear interactions between f_f and f_n, including some between $f_f/2$ and f_n. According to the phase portrait (figure 4.14b), the flame could be quasiperiodic, although the noisiness of the data makes it difficult to be certain.

When forced at moderate amplitudes ($A = 0.30$–0.50), the flame appears to oscillate predominately at f_f, according to the PSD. This would normally be sufficient to classify it as being locked-in. The time traces and the phase portraits (figures 4.14c and 4.14d), however, suggest that the dynamics are much richer than that. The time traces show a complex modulation of the signal amplitude, with sharp gradients and no clear dominance of a sinusoid at f_f. The phase portraits show an apparent period-2 oscillation, although both the path of the trajectories and the randomness of their Poincaré sections suggest that the flame may be approaching a chaotic state. Consequently, the flame is not considered to be locked-in at these forcing conditions.

When forced at high amplitudes ($A = 0.70$–0.90), the flame exhibits a fundamental change in its response, but is still not considered to be locked-in. Its PSD contains significantly more broadband noise, with spectral peaks appearing – almost randomly – across the measured bandwidth, although the component at f_f still dominates. Curiously, the first subharmonic of f_f becomes damped, its spectral energy spreading to two new modes straddling $f_f/2$. The phase portraits (figures 4.14e and 4.14f) continue to show behaviour suggestive of chaos, with random trajectories that never overlap onto themselves. The time trace at $A = 0.90$ shows a marked reduction in amplitude, perhaps due to local flame extinction arising from interruptions to the fuel flow.

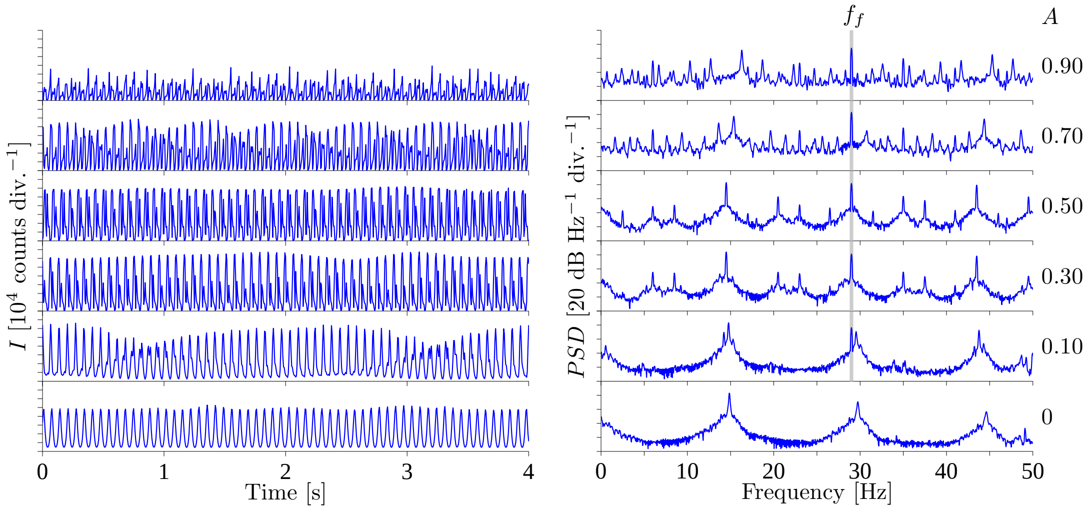

(a) Time trace (b) PSD

Figure 4.13: (a) Time trace and (b) PSD of the intensity from Flame 5 forced at a frequency, $f_f = 29$ Hz, slightly below the second harmonic, $2f_n = 29.4$ Hz: $f_f/2f_n = 0.99$. Data are shown for five forcing amplitudes, $0.10 \leq A \leq 0.90$, and for the unforced case, all at $x/d_1 = 10$.

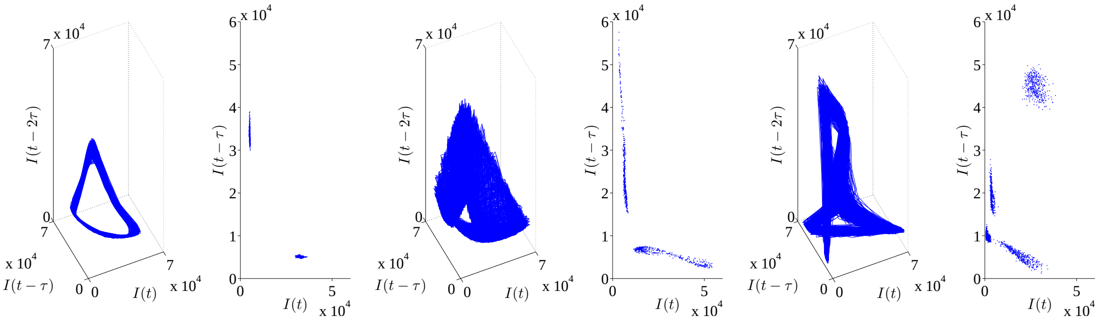

(a) $A = 0$ (b) $A = 0.10$ (c) $A = 0.30$

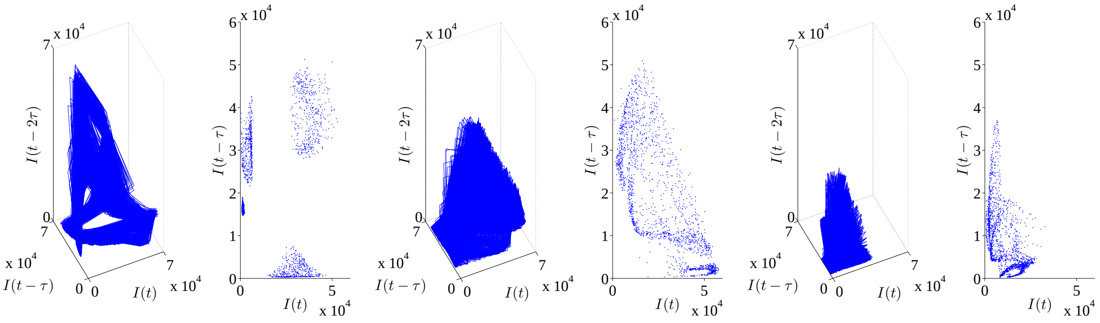

(d) $A = 0.50$ (e) $A = 0.70$ (f) $A = 0.90$

Figure 4.14: Phase portraits (left) and Poincaré maps (right) for Flame 5 forced at 29 Hz ($f_f/2f_n = 0.99$) with five amplitudes, plus the unforced case.

4.2.1.1.4 Consolidated PSD

The flame response at other forcing frequencies can be examined in the consolidated PSD: a contour plot of the PSD with the response frequency on the horizontal axis and f_f on the vertical axis. Figure 4.15 shows this for Flame 5 forced at four amplitudes: $A = 0.10$, 0.30, 0.50, and 0.70. On each subfigure, there are three black lines running diagonally from the bottom left to the top right. These are used as guidelines to show the response at f_f and at its harmonics ($2f_f$ and $3f_f$). There are similar (red) guidelines for f_n and its harmonics ($2f_n$ and $3f_n$), as well as (blue and green) ones[1] for interactions between f_f and the harmonics of f_n.

Several features are common to all the consolidated PSD plots. The natural mode is indicated by a contiguous stripe that runs vertically at f_n through all values of f_f except those to which the flame is locked-in. Its second ($2f_n$) and third ($3f_n$) harmonics are similarly indicated. At lock-in[2], the forcing dominates and the response therefore consists of a stripe along the diagonal $f = f_f$. The f_f band in which lock-in occurs expands vertically as A increases (figure 4.15a→4.15d), a feature that will be examined more carefully in §4.2.2.

Away from lock-in, nonlinear interactions occur between the natural mode and the forcing, giving rise to spectral peaks at low f as well as around f_f and f_n – especially if the two are close. Similar interactions occur between f_f and the harmonics of f_n, but not between f_n and the harmonics of f_f. The result is that between the vertical stripes marking f_n and its harmonics, there are spectral peaks set in a distinctive diamond pattern. The diamond pattern is most visible at low values of A because that is when the natural and forced modes interact most equally, limiting the locked-in regions to a narrow band of frequencies around f_n.

For completeness, plots of the consolidated PSD for the other globally unstable flames (Flames 1–4, table 4.1) are shown in Appendix H.

---

[1] These are shown only on subfigure 4.15a in order to minimise clutter.

[2] The ability of a self-excited flame to lock into external forcing has also been observed in a real thermoacoustic system, the Cambridge Intermediate Pressure Combustion Facility. Appendix G shows, by courtesy of Dr. David Dennis, two examples of the consolidated PSD (dynamic pressure) from the combustor, in which a liquid-fuelled spray flame is forced acoustically by a siren. As in figure 4.15, lock-in can be detected as an interruption of the response around the natural frequency (the break in the vertical cyan stripe).

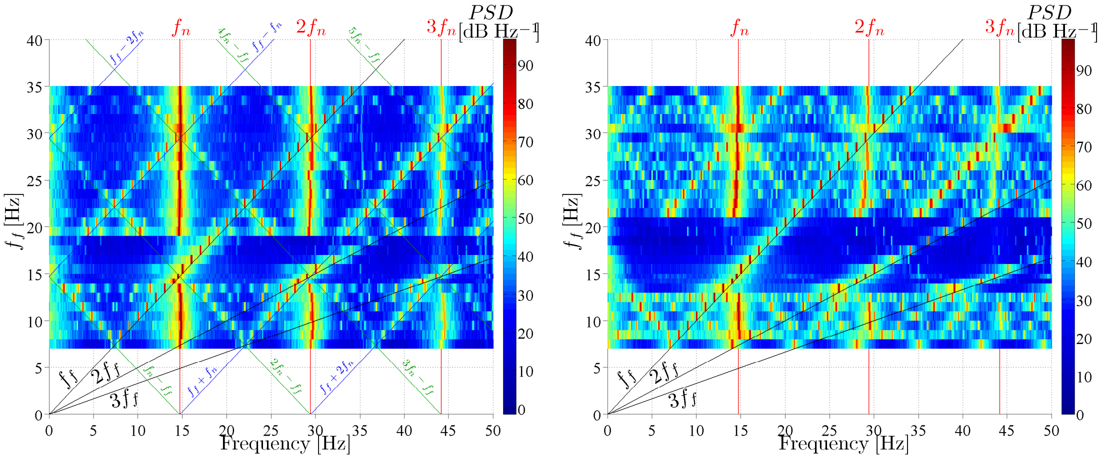

(a) $A = 0.10$ (b) $A = 0.30$

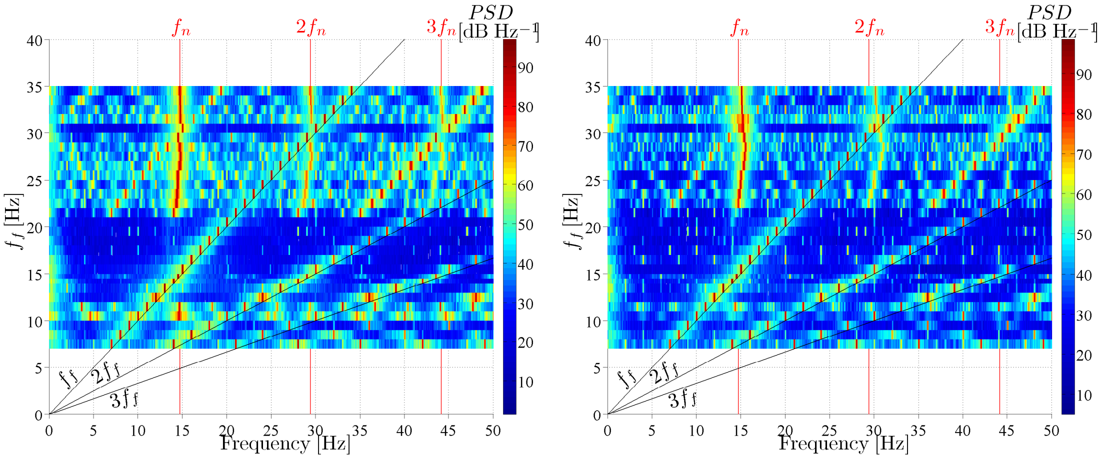

(c) $A = 0.50$ (d) $A = 0.70$

Figure 4.15: Consolidated PSD for Flame 5 forced at four amplitudes: A = (a) 0.10, (b) 0.30, (c) 0.50, and (d) 0.70. The spectra are of the chemiluminescence at $x/d_1 = 10$.

4.2.1.2 Marginally globally stable flame

A marginally globally stable flame (Flame 6) is examined for comparison with the globally unstable flame (Flame 5) of the previous section.

4.2.1.2.1 Forcing near the fundamental: f_n

Following the outline of §4.2.1.1.1, this section begins with a case in which f_f (16 Hz) is slightly above f_n: $f_f/f_n = 1.12$. Figure 4.16a shows time traces[1] of the intensity from Flame 6 forced at seven amplitudes: $0.05 \leq A \leq 0.50$. For comparison, a time trace of the same signal from the same flame but without forcing is also shown (bottom). The PSD curves are shown in figure 4.16b, and the phase portraits and Poincaré maps are shown in figure 4.17.

When unforced, Flame 6 is virtually steady, oscillating with an amplitude just 1.9% of that with which Flame 5 oscillates. It is not perfectly steady because the baseflow is convectively unstable near the injector, where small perturbations amplify, causing measurable perturbations downstream. The PSD contains two broad peaks, at 14.8 and 16.1 Hz, and weak harmonics.

These two broad peaks are replaced by one sharp peak, at $f_n = 14.3$ Hz, whenever forcing is applied – however low its amplitude and even if its frequency is far from f_n (not shown). According to the high-speed videos, this new natural frequency corresponds to the typical global mode in a jet diffusion flame, which develops as axisymmetric toroidal vortices (§1.3.3). Based on this evidence, it is speculated that the forcing activates an underlying global mode in Flame 6, one that should behave similarly to the natural global mode in Flame 5.

Such behaviour is not uncommon in hydrodynamics. According to Ho and Huerre (1984), Flame 6 typifies a lightly damped global mode, oscillating only in the presence of continuous external forcing. A canonical example is the 'preferred mode' in a constant-density jet[2], which, when forced, responds like a damped

---

[1] The divisions on the ordinate axis for Flame 6 are a factor of 10 smaller than those for Flame 5: 10^3 versus 10^4 counts division^{-1}. This difference arises because Flame 6 oscillates with a much lower amplitude than does Flame 5.

[2] Sometimes called the 'jet-column mode', this instability arises from the spatial amplification of background noise, due to interactions between the diametrically opposed shear layers at the potential core. It is not to be confused with the 'shear-layer mode', which oscillates at a higher frequency and arises from the most amplified wave of the initial shear layer.

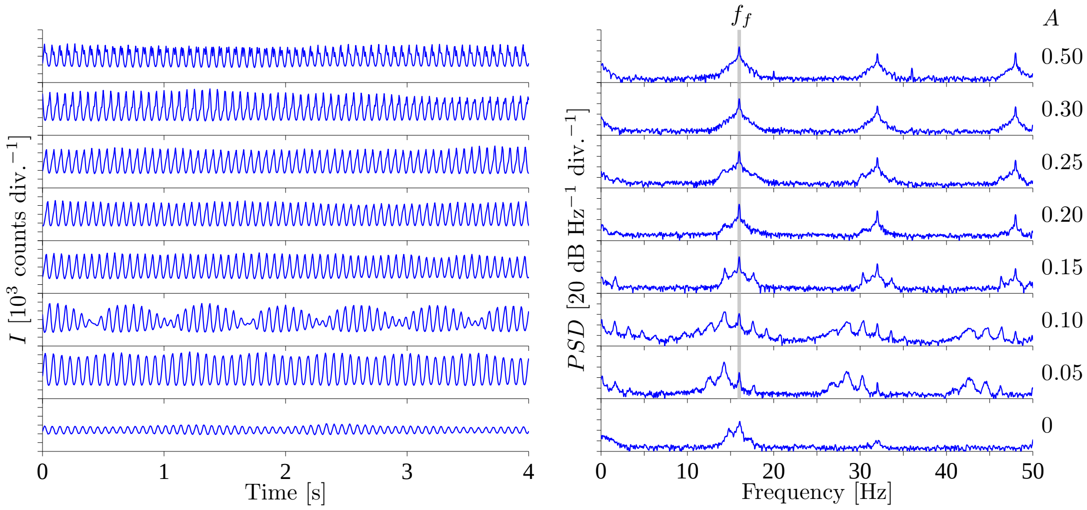

(a) Time trace (b) PSD

Figure 4.16: (a) Time trace and (b) PSD of the intensity from Flame 6 forced at a frequency, $f_f = 16$ Hz, slightly above the natural frequency, $f_n = 14.3$ Hz: $f_f/f_n = 1.12$. Data are shown for seven forcing amplitudes, $0.05 \leq A \leq 0.50$, and for the unforced case, all at $x/d_1 = 10$. The onset of lock-in occurs at $A_{loc} = 0.20$.

linear oscillator near resonance. The gain of this mode, Crow and Champagne (1971) have shown, is broadly receptive to forcing, peaking for $St \equiv fd/U \approx 0.3$, where f is the passage frequency of the vortical structures at the end of the potential core. Thus, although Flame 6 is what Huerre and Monkewitz (1990) would call 'marginally globally stable', it is in fact globally unstable for this thesis, because the focus is on the *forced* response. The study of a globally stable flame with a strongly damped global mode is left for future work.

Once the marginal global mode in Flame 6 is activated by forcing, it responds just like a natural global mode does. In particular, all of the spectral features seen in Flame 5 (§4.2.1.1.1) are also seen in Flame 6. They include (i) nonlinear interactions between the natural, forcing, and beat frequencies, which all coexist; (ii) a bias in the PSD towards frequencies on the side of f_n opposite to f_f; (iii) quasiperiodicity before lock-in (figure 4.17c); and (iv) the ability of the flame to lock into the forcing above some critical value of A. These features have been discussed before (§4.2.1.1.1) and need not be discussed again.

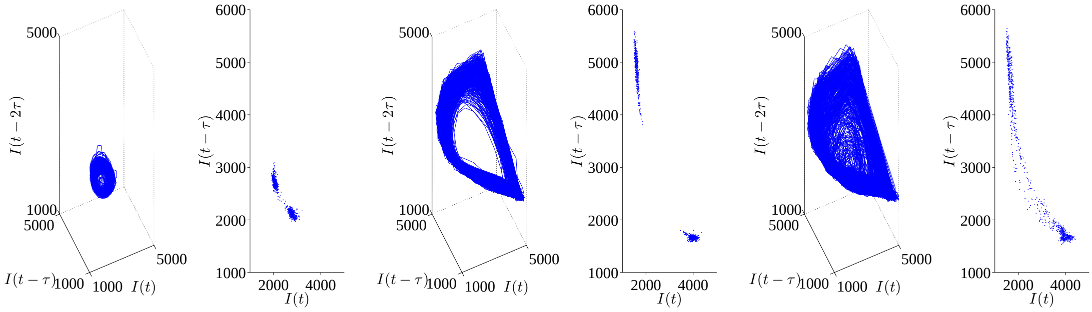

(a) $A = 0$ (b) $A = 0.05$ (c) $A = 0.10$

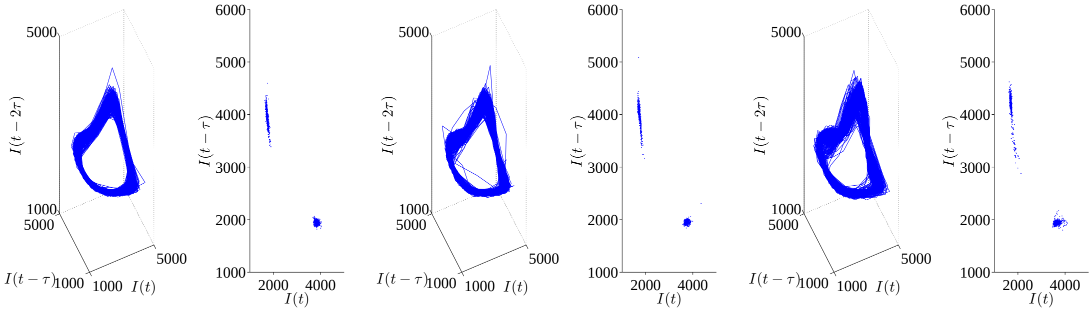

(d) $A = 0.15$ (e) $A = 0.20$ (f) $A = 0.25$

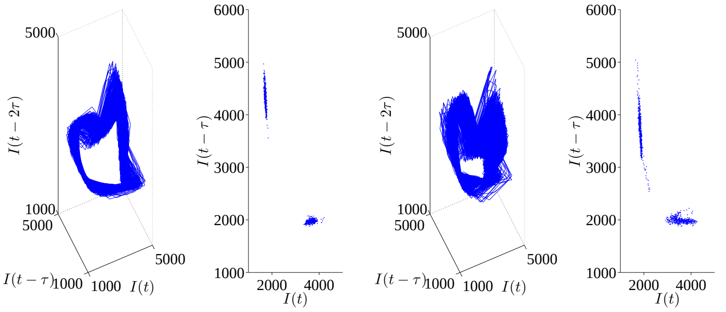

(g) $A = 0.30$ (h) $A = 0.50$

Figure 4.17: Phase portraits (left) and Poincaré maps (right) for Flame 6 forced at 16 Hz ($f_f/f_n = 1.12$) with seven amplitudes, plus the unforced case.

As is the case for Flame 5, the above features are seen not only when $f_f > f_n$ but also when $f_f < f_n$. Figure 4.18 is analogous to figure 4.16 but for $f_f = 13$ Hz or $f_f/f_n = 0.91$. A comparison of these two figures reveals the same similarities and differences noted earlier (§4.2.1.1.1, page 94) between forcing above and below the natural frequency. The reader is referred to that discussion for a reminder of the details. For completeness, the phase portraits and Poincaré maps for Flame 6 forced at 13 Hz are shown in Appendix I.

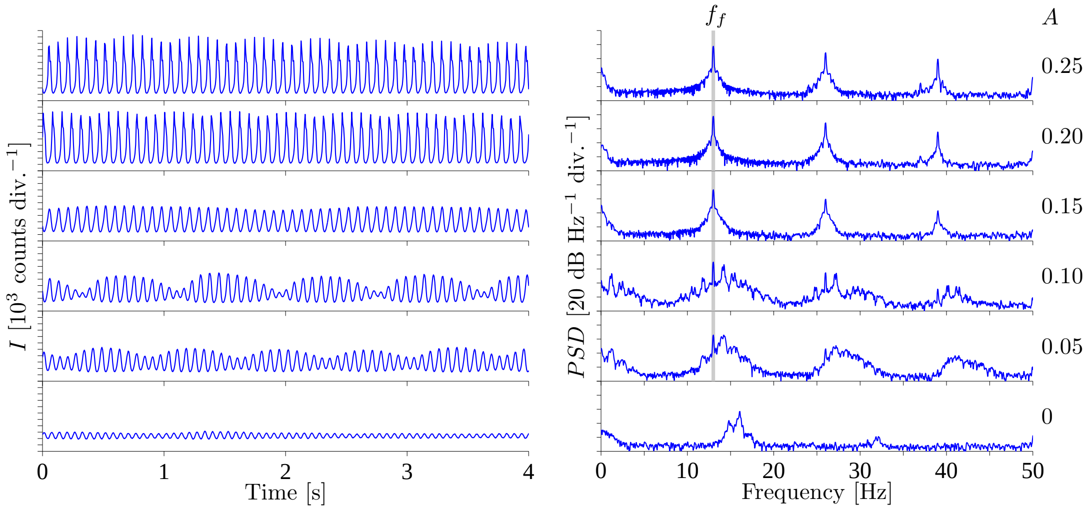

(a) Time trace

(b) PSD

Figure 4.18: (a) Time trace and (b) PSD of the intensity from Flame 6 forced at a frequency, $f_f = 13$ Hz, slightly below the natural frequency, $f_n = 14.3$ Hz: $f_f/f_n = 0.91$. Data are shown for five forcing amplitudes, $0.05 \leq A \leq 0.25$, and for the unforced case, all at $x/d_1 = 10$. The onset of lock-in occurs at $A_{loc} = 0.15$.

4.2.1.2.2 Forcing near the first subharmonic: $f_n/2$

The similarities in response between Flame 6 and Flame 5 arise also when the forcing is applied near the first subharmonic of the natural fundamental frequency. With f_f (8 Hz) slightly above $f_n/2$ (7.15 Hz), figure 4.19a shows time traces of the intensity from Flame 6 forced at seven amplitudes: $0.10 \leq A \leq 0.70$. For comparison, a time trace of the same signal from the same flame but without forcing is also shown (bottom). The PSD curves are shown in figure 4.19b, and the phase portraits and Poincaré maps are shown in figure 4.20.

The main observation is that once its global mode is activated by forcing, however weak and whatever the value of f_f, Flame 6 responds similarly to Flame 5 – even though the global mode in the latter flame develops naturally. The discussion for this section is therefore similar to that for §4.2.1.1.2.

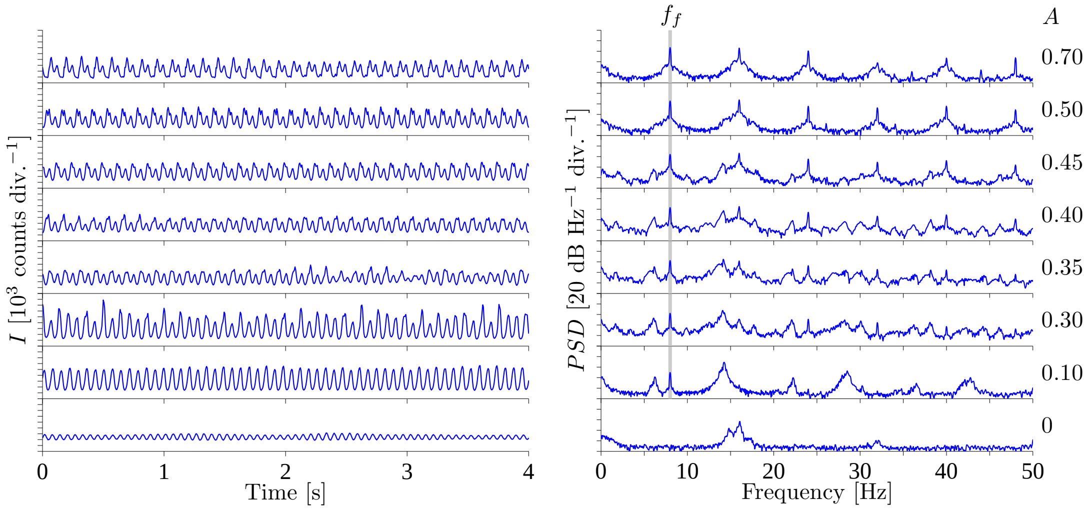

(a) Time trace

(b) PSD

Figure 4.19: (a) Time trace and (b) PSD of the intensity from Flame 6 forced at a frequency, $f_f = 8$ Hz, slightly above the first subharmonic, $f_n/2 = 7.15$ Hz: $f_f/(f_n/2) = 1.12$. Data are shown for seven forcing amplitudes, $0.10 \leq A \leq 0.70$, and for the unforced case, all at $x/d_1 = 10$. The onset of lock-in occurs at $A_{loc} = 0.50$.

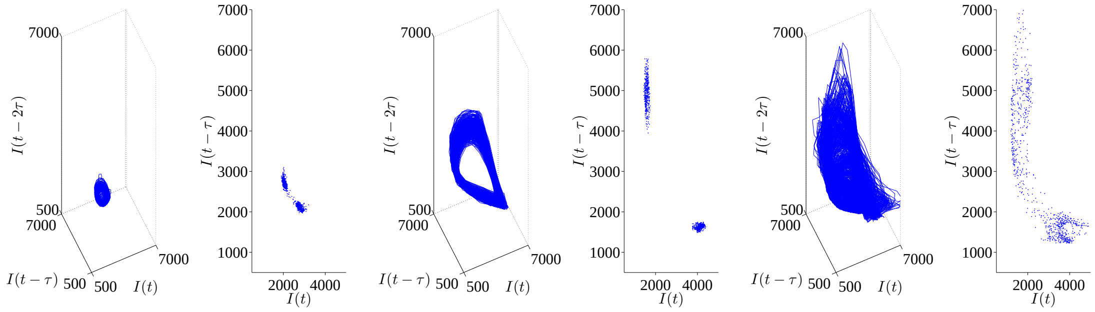

(a) $A = 0$ (b) $A = 0.10$ (c) $A = 0.30$

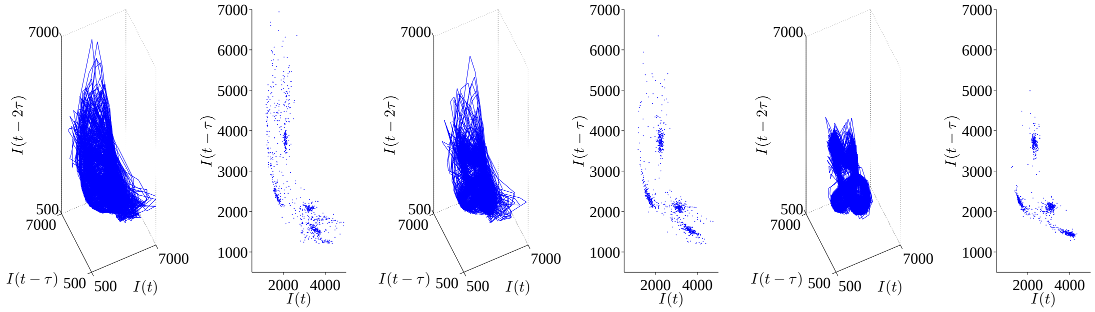

(d) $A = 0.35$ (e) $A = 0.40$ (f) $A = 0.45$

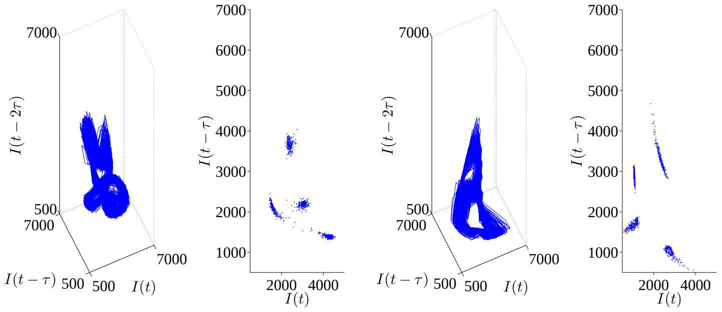

(g) $A = 0.50$ (h) $A = 0.70$

Figure 4.20: Phase portraits (left) and Poincaré maps (right) for Flame 6 forced at 8 Hz ($f_f/(f_n/2) = 1.12$) with seven amplitudes, plus the unforced case.

4.2.1.2.3 Forcing near the second harmonic: $2f_n$

The similarities in response between Flame 6 and Flame 5 extend to the case in which the forcing is applied near the second harmonic of the natural fundamental frequency. With f_f (28 Hz) slightly below $2f_n$ (28.6 Hz), figure 4.21a shows time traces of the intensity from Flame 6 forced at four amplitudes: $0.10 \leq A \leq 0.70$. For comparison, a time trace of the same signal from the same flame but without forcing is also shown (bottom). The *PSD* curves are shown in figure 4.21b, and the phase portraits and Poincaré maps are shown in figure 4.22.

As with forcing near the fundamental (§4.2.1.2.1) and forcing near the first subharmonic (§4.2.1.2.2), forcing near the second harmonic produces a response that is similar to that which is produced by the naturally globally unstable flame (Flame 5). The discussion for this section is therefore similar to that for §4.2.1.1.3.

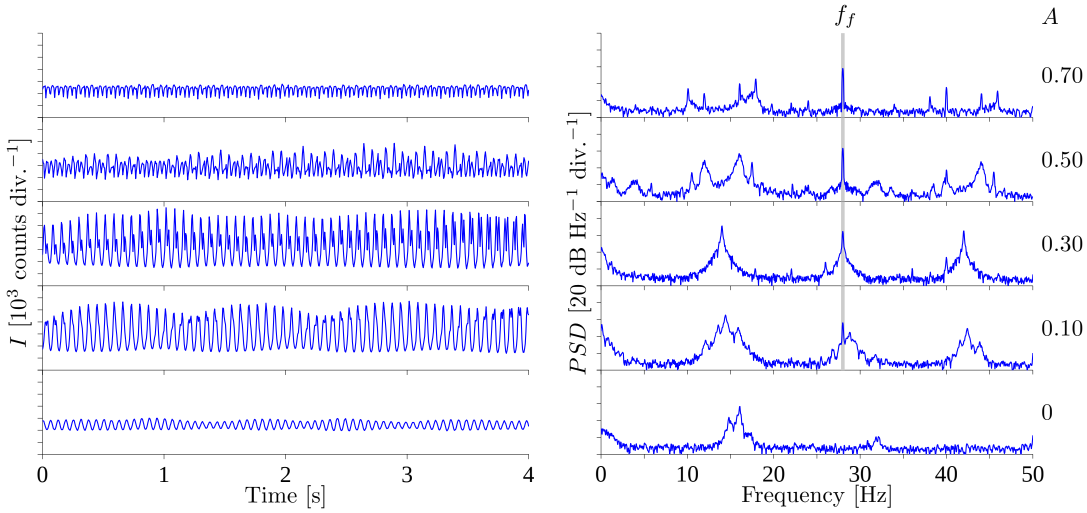

(a) Time trace (b) *PSD*

Figure 4.21: (a) Time trace and (b) *PSD* of the intensity from Flame 6 forced at a frequency, $f_f = 28$ Hz, slightly below the second harmonic, $2f_n = 28.6$ Hz: $f_f/2f_n = 0.98$. Data are shown for four forcing amplitudes, $0.10 \leq A \leq 0.70$, and for the unforced case, all at $x/d_1 = 10$.

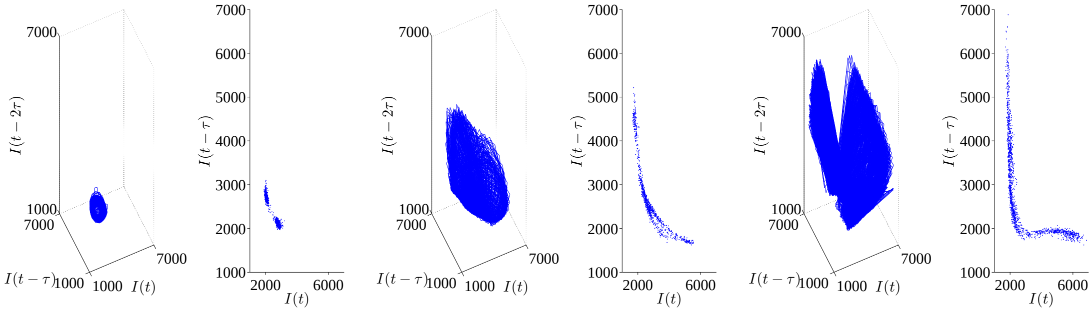

(a) $A = 0$

(b) $A = 0.10$

(c) $A = 0.30$

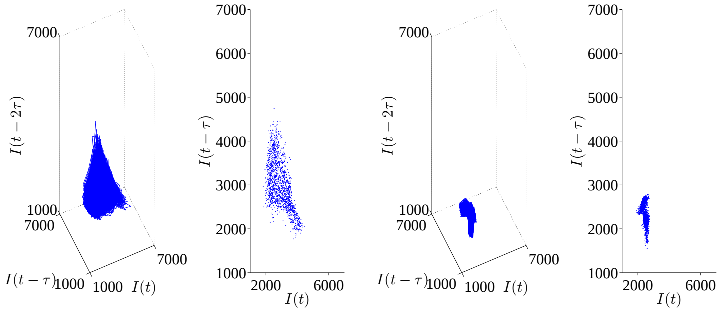

(d) $A = 0.50$

(e) $A = 0.70$

Figure 4.22: Phase portraits (left) and Poincaré maps (right) for Flame 6 forced at 28 Hz ($f_f/2f_n = 0.98$) with four amplitudes, plus the unforced case.

4.2.1.2.4 Consolidated PSD

Plots of the consolidated PSD for Flame 6 are presented in figure 4.23. Not surprisingly, they show the same qualitative features found in the analogous plots for Flame 5 (figure 4.15). At lock-in, the response is dominated by the forcing, represented by a stripe along the diagonal $f = f_f$, with no sign of the natural global mode. Away from lock-in, the nonlinear interactions between the natural, forcing, and beat frequencies give rise to a distinctive diamond pattern.

There is, however, one feature that seems to be unique to Flame 6. For $A \geq 0.30$ (figures 4.23b–4.23d), but only in the band $f_n < f_f < 2f_n$ and only away from lock-in, the natural mode does not oscillate at a single frequency (originally $f_n = 14.3$ Hz). Instead it oscillates at two different frequencies: a strong component at 15.9–16.1 Hz and a weaker, more sporadic one at 14.8 Hz. These two natural frequencies are not new: they are the frequencies at which this marginally globally stable flame oscillates when it is unforced (§4.2.1.2.1). Although intriguing, this frequency-shifting behaviour will not be examined further in this thesis.

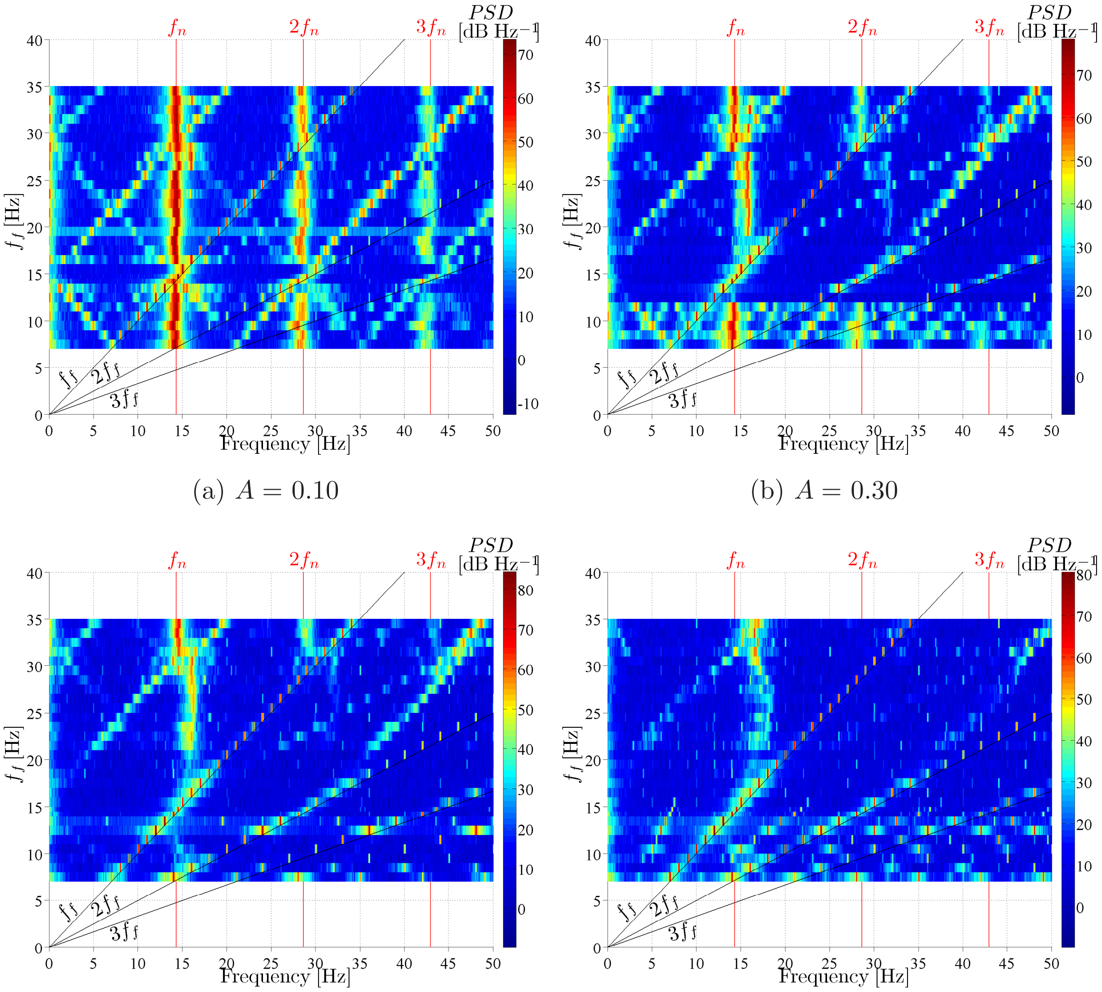

(a) $A = 0.10$

(b) $A = 0.30$

(c) $A = 0.50$

(d) $A = 0.70$

Figure 4.23: Consolidated PSD for Flame 6 forced at four amplitudes: A = (a) 0.10, (b) 0.30, (c) 0.50, and (d) 0.70. The spectra are of the chemiluminescence at $x/d_1 = 10$.

4.2.2 Response at lock-in

The flame response at lock-in is examined because it will determine just how detrimental lock-in actually is for thermoacoustic systems. The first relationship to be considered is that between the minimum forcing amplitude required for lock-in, A_{loc}, and the normalised forcing frequency, f_f/f_n. This is shown in figure 4.24a for all six flames. The data are representative of every axial station ($0 \leq x/d_1 \leq 29$) because, once A_{loc} is reached, lock-in occurs simultaneously everywhere in the flame. The diagonal lines through the data around $f_f/f_n = 1$ are linear fits. For lock-in around the fundamental, the data at $f_f/f_n < 1$ are regressed separately from the data at $f_f/f_n > 1$. For lock-in around the subharmonic, the data are not regressed at all because the trends do not fit a linear model.

Several features are shared by all six flames. When f_f is near f_n or $f_n/2$, A_{loc} is low; otherwise it is high. Around the fundamental, A_{loc} increases in proportion to $|f_f - f_n|$, indicating a Hopf bifurcation to a global mode (Appendix B). This linear relationship gives rise to $\vee$-shaped curves, similar to those seen for other self-excited flows: low-density jets (figures 1.10 and 3.9), crossflowing jets (figure 1.11), cylinder wakes (figures 1.8 and 1.9), and premixed flames (figure 1.12). For each flame, despite the use of strong forcing, there is a limit to how far f_f can deviate from f_n before lock-in is not possible: $f_f/f_n \approx 1.2$–1.4. Around the subharmonic, the relationship between A_{loc} and $|f_f - f_n|$ is not as linear as that around the fundamental, although the overall trends are similar.

Several differences exist between the six flames. As noted in §2.2 and §4.1.2.2, adding coflow weakens their global instability, which should make them more receptive to forcing, enabling lock-in to occur at lower A. Such behaviour is indeed observed when Flame 1 is compared to Flame 2, and when Flame 4 is compared to Flame 5. The flames with coflow (Flames 2 and 5) lock in more readily than do their counterparts without coflow (Flames 1 and 4). This is seen not only for f_f around f_n but also for f_f on the high-frequency side of $f_n/2$.

Another way to weaken global instability is to reduce the fuel concentration. According to figure 4.24a, reducing [CH_4] from 100% (Flame 1) to 80% (Flame 3) to 60% (Flame 4) has only a small effect on A_{loc}. Although the curves seem to shift downwards, the change is so small that it is within the experimental uncertainty.

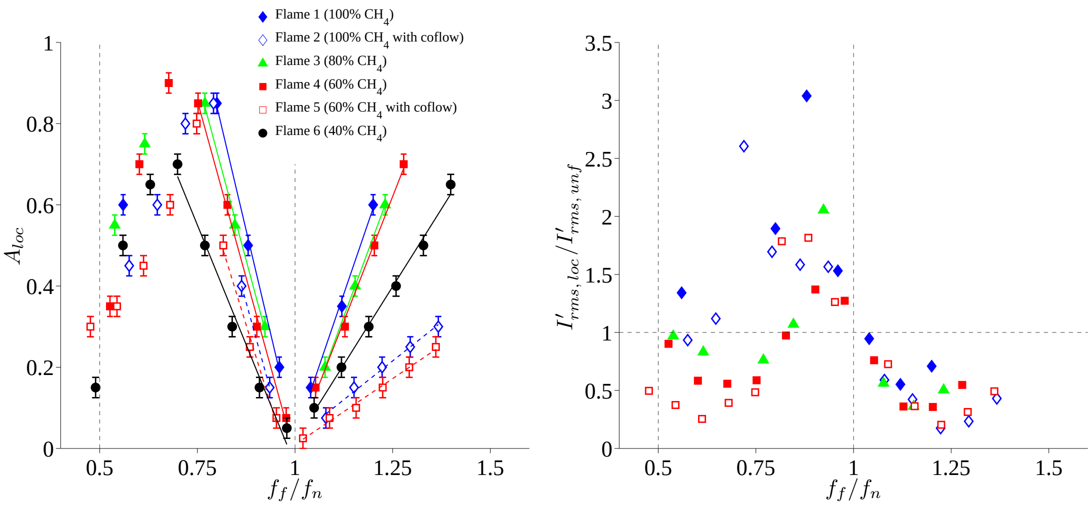

(a) Lock-in map (b) Response at A_{loc}

Figure 4.24: Lock-in for the six CH_4–N_2 jet diffusion flames: (a) map of the lock-in boundaries and (b) normalised RMS response at $x/d_1 = 10$ at the onset of lock-in. Flames 1–5 are naturally globally unstable, while Flame 6 is globally unstable only when forced. On subfigure (a), the error bars denote the increment by which A is varied, and the diagonal lines through the data around $f_f/f_n = 1$ are linear fits. On subfigure (b), the horizontal line denotes a response of unity.

Reducing $[CH_4]$ further to 40% (Flame 6), however, causes a marked decrease in the slopes of the $\vee$-shape. This suggests that the flame with a weak global mode (Flame 6) locks in more readily than do the flames with strong global modes (Flames 1, 3, and 4).

A final observation concerns the asymmetry of the lock-in curves about f_n: lock-in occurs more readily for $f_f/f_n > 1$ than it does for $f_f/f_n < 1$. This asymmetry is more pronounced for the flames with coflow (Flames 2 and 5) than for those without coflow (Flames 1, 3, 4, and 6). As §4.2.4 will show, simple model equations, such as the van der Pol oscillator, have symmetric lock-in curves, which means that the asymmetry is a feature of the flow, and not a feature of lock-in. Previous work has shown that when there is competition between two modes at different frequencies, one will take over and saturate nonlinearly before the other (Pier, 2003). A possible explanation of asymmetric lock-in is that forcing applied at higher frequencies induces higher peak accelerations at the flame base[1]. In isothermal jets, higher peak accelerations have been found to promote vortex-ring formation (Külsheimer and Büchner, 2002). Forcing at higher frequencies could therefore cause toroidal vortices to roll up earlier, perhaps closer to the injector. If the vortices caused by the forcing roll up before the vortices caused by the natural global mode, they will dominate, increasing the tendency of the flame to lock in. A detailed analysis of the downstream development of the forced and natural modes is left for future work[2].

The fact that lock-in occurs asymmetrically suggests that there may be other asymmetries between forcing above and below f_n. To investigate this, figure 4.24b shows the flame response at the onset of lock-in as a function of f_f/f_n. Here the flame response is defined as the RMS intensity fluctuation at $A = A_{loc}$ normalised by the same quantity but without forcing: $I'_{rms,\,loc}/I'_{rms,\,unf}$. As before, a representative axial station ($x/d_1 = 10$) is considered, although the findings are applicable to most of the flame body (Appendix J). In the definition of the flame response, the RMS is used because it is independent of frequency, providing a weighted average of the signal energy over time[3]. Data are shown for the globally unstable flames (Flames 1–5) but not for the marginally globally stable flame (Flame 6). That is because this latter flame is virtually steady when unforced, meaning that it has a fundamentally different normalisation. The response of this flame will be considered separately, in figure 4.25.

Figure 4.24b shows that there are several features common to all the globally unstable flames. When lock-in occurs for f_f/f_n slightly above 0.5 or 1, the flame response is always below unity[4] – reaching a minimum of 0.17–0.55 at $1.12 <$

---

[1] For sinusoidal forcing, the peak acceleration is proportional to frequency.

[2] The lock-in curve for the low-density jet from chapter 3 is also asymmetric, but in the opposite direction. As figure 3.9 shows, A_{loc} is lower on the low-frequency side of f_n than it is on the high-frequency side. This must be interpreted with caution, however, because A in those experiments is assumed to be proportional to the loudspeaker voltage (measurements of the velocity perturbation were not available). Nevertheless, if valid, the fact that the asymmetry is in the opposite direction implies that it is caused by the exact mechanism through which the forcing influences the flow development, and is not a general feature of all jets.

[3] By Parseval's theorem, the RMS of a time-domain signal is equal to the square root of the total area under the PSD. Typically it is used as a universal measure of the power contained in the fluctuations of the signal when no single frequency is of particular interest. Later in §4.2.3, the response at just f_f will be examined via the flame describing function.

[4] The only exception is around the subharmonic of Flame 1.

$f_f/f_n < 1.22$, depending on the particular flame. A response that is below unity implies that the flame oscillates with an amplitude lower than that with which it oscillates when unforced[1]. When lock-in occurs for f_f/f_n slightly below 1, however, the flame response is always above unity – reaching a maximum of 1.37–3.04, again depending on the particular flame.

In order to examine this asymmetry more closely, figure 4.25 shows contours of the flame response as a function of A and f_f/f_n – and therefore not just at the onset of lock-in. As before, two representative flames are considered: one globally unstable (Flame 5, §4.2.1.1) and one marginally globally stable (Flame 6, §4.2.1.2). Measured at $x/d_1 = 10$, the flame response is defined as the ratio of the RMS intensity fluctuation with forcing to the same quantity without forcing: $I'_{rms,\,for}/I'_{rms,\,unf}$. Also shown on the figure are selected data from figure 4.24a indicating the onset of lock-in.

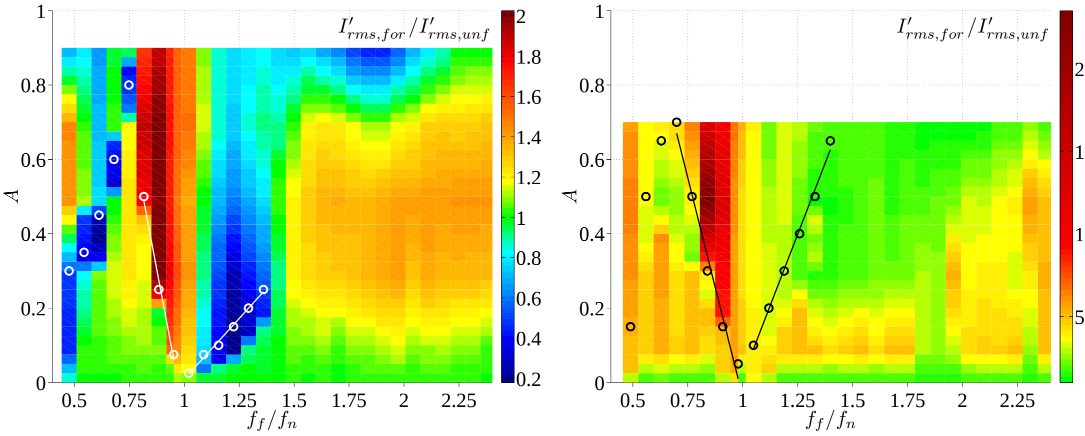

(a) GU: Flame 5

(b) MGS: Flame 6

Figure 4.25: Flame response at $x/d_1 = 10$ as a function of forcing amplitude and frequency: (a) globally unstable and (b) marginally globally stable. The critical forcing amplitude required for lock-in, A_{loc}, is indicated by the circular markers. On the colorscale, a flame response of unity is in green, with values above unity in warmer (red/yellow) hues and values below unity in cooler (blue/cyan) hues. In subfigure (b), the highest value of A is only 0.70 (not the usual 0.90) because Flame 6 blows off at $A > 0.70$.

---

[1] This implication is valid only if all frequency components are considered, because here the response is defined by the RMS and not at any particular frequency.

For the globally unstable flame (figure 4.25a), as A increases for f_f/f_n slightly above 0.5 or 1, the response first decreases below unity, reaches a minimum near the onset of lock-in (circular markers), and then increases back towards unity. For f_f/f_n slightly below 1, however, the response increases above unity and then saturates. Forcing very close to the fundamental causes a response that is between these two extremes. For $f_f/f_n > 1.36$, lock-in is not possible even with the use of high A. Instead, over a wide band of forcing frequencies ($1.36 < f_f/f_n < 2.38$), increasing A causes a gradual rise in the response above unity, which peaks at $A \approx 0.30 - 0.50$ before decreasing for higher A.

For the marginally globally stable flame (figure 4.25b), introducing even a little forcing causes a response greater than unity, regardless of f_f. This occurs because the response is normalised with respect to the unforced response, which is exceptionally low for this quasisteady flame. The response amplitudes are therefore an order of magnitude higher than those of the globally unstable flame (figure 4.25a). For most combinations of A and f_f, the response is relatively constant but high, indicating that the flame is broadly receptive to forcing. There is a band of frequencies immediately below the natural frequency ($0.84 < f_f/f_n < 0.98$) in which the flame is particularly receptive to forcing. In this band, the response increases abruptly at the onset of lock-in and then keeps increasing until $A \approx 0.50$ before decreasing for higher A.

In summary, lock-in occurs most readily for flames with weak global instability and for f_f near f_n, as expected. What was not expected, though, was that the lock-in behaviour would depend on whether f_f is above or below f_n. When forced below f_n, the flame is more resistant to lock-in, and its oscillations at lock-in are stronger than those of the unforced flame. When forced above f_n, the flame is less resistant to lock-in, and its oscillations at lock-in are weaker than those of the unforced flame. This last finding suggests that, for thermoacoustic systems, lock-in may not be as detrimental as it is thought to be.

4.2.3 Flame describing function

In the analysis of thermoacoustic systems, the flame response is usually characterised by the flame describing function (FDF). The flame is considered to act as a filter that transforms an input signal to an output signal: i.e. velocity fluctuation due to forcing → flame intensity fluctuation. The FDF is thus similar to the transfer function, which measures how sensitive a flame is to a disturbance of a given f_f. Unlike the transfer function, however, the FDF depends on A as well as f_f, and hence can be defined for systems that are nonlinear. This is a useful feature because in real systems it is almost always the nonlinear combustion dynamics that controls the saturation of thermoacoustic oscillations. Nonlinearity also plays a central role in triggering, and is the process by which energy at one frequency can excite other frequencies. According to Durox et al. (2008), inserting the FDF into the dispersion relations can yield limit-cycle amplitudes, frequency shifts during transient growth, mode switching, and even hysteresis.

The FDF is calculated by taking the ratio of the relative heat-release fluctuation to the relative velocity (or pressure) fluctuation, both at the same frequency: f_f. The focus is on this frequency because, when integrated over many cycles, the contribution to acoustic energy gain from every other frequency sums to zero[1]. Focusing on f_f alone, however, overlooks the fact that the forcing can affect the heat release at other frequencies, and that these components can affect the transient behaviour of the system. When applied to self-excited flames, the FDF has another limitation: the nonlinear interactions between f_f and f_n, as well as those involving their harmonics, are not captured[2]. These drawbacks aside, though, the FDF is presented below in order to permit comparison with other studies.

The global FDF is considered first:

$$FDF_g \equiv \frac{\sum_{i=1}^{N} (I'_{f_f}/\overline{I})_{x/d_1=i}}{A}, \tag{4.1}$$

---

[1] This is true only if the pressure signal is sinusoidal; otherwise, the higher-order harmonics also contribute and should be considered.

[2] On the consolidated PSD, the FDF is equivalent to inspecting the response along the diagonal $f = f_f$. Thus, although defined for nonlinear systems, the FDF is in fact a quasilinear indicator because it cannot capture the response at $f \neq f_f$.

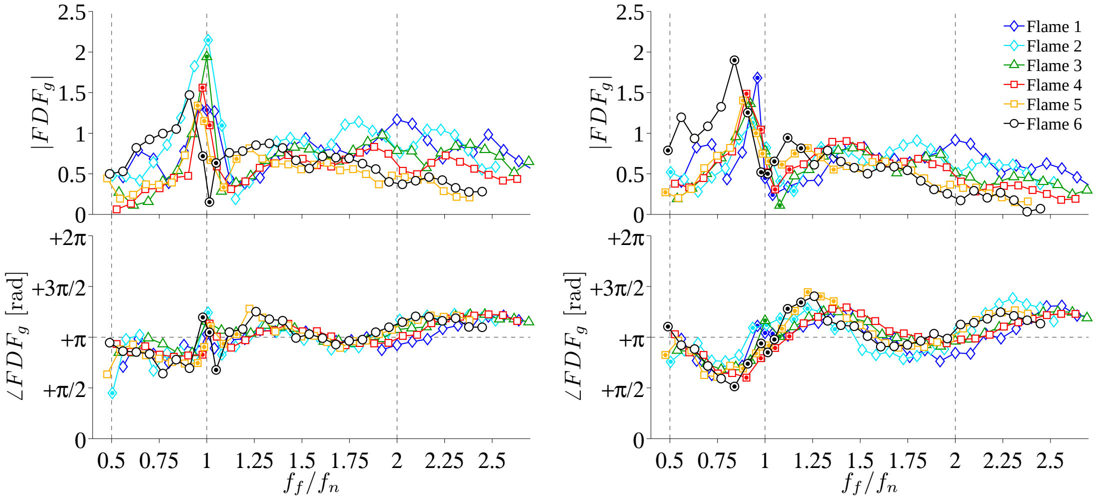

(a) $A = 0.10$

(b) $A = 0.30$

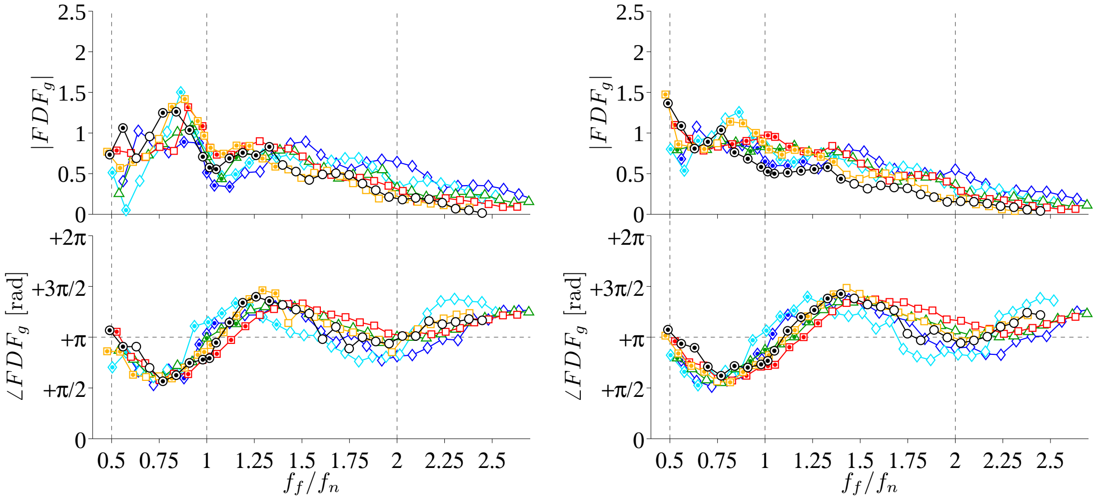

(c) $A = 0.50$

(d) $A = 0.70$

Figure 4.26: Gain and phase of the global FDF for Flames 1–6 forced at four amplitudes: $A =$ (a) 0.10, (b) 0.30, (c) 0.50, and (d) 0.70. The filled markers denote locked-in conditions.

where N is the image height. The numerator, $I'_{f_f}/\overline{I}$, is the complex amplitude of the FFT (not the PSD) of the local intensity fluctuation at f_f normalised by the local time-averaged intensity. The denominator is the forcing amplitude: $A \equiv |u'_{1,\,f_f}|/U_1$. The gain is simply the absolute value, and the phase is the angle by which the flame signal leads the forcing signal[1].

Figure 4.26 shows the gain and phase of FDF_g for all six flames. At every value of A, $|FDF_g|$ peaks just below $f_f/f_n = 1$. Above $f_f/f_n = 1$, it dips but then rises as f_f/f_n increases. Although a quantitative comparison between the flames is made difficult by the scatter, all the gains seem to saturate to around the same values as A increases. Likewise, $\angle FDF_g$ does not vary markedly either: it shifts between $\pm\pi$ around $f_f/f_n = 1$, indicating that the flame leads the forcing when $f_f/f_n < 1$ but that the forcing leads the flame when $f_f/f_n > 1$.

All the flames are long relative to the wavelength of their global modes: the average flame length[2] is measured to be ≈ 0.32 m and the instability wavelength can be approximated as $U_1/2f_n \simeq 0.065$ m, for a ratio of nearly 5:1. Consequently, the flames do not oscillate as a whole, everywhere in phase. This can be seen in figure 4.27, which shows the spatiotemporal evolution of the intensity from Flame 5 (unforced). As noted earlier, the variations in intensity are caused by the roll-up and passage of toroidal structures. Before one structure advects out of the flame, another forms at the base. This suggests that both the gain and phase of the FDF should depend on x/d_1 as well.

The FDF is redefined locally in order to examine how the response varies along the flame length. This is done by using the local pixel intensity (without the summation) in the definition: $FDF_l \equiv (I'_{f_f}/\overline{I})_{x/d_1}/A$. Figure 4.28 shows the gain and phase for Flame 5, while figure 4.29 shows the same for Flame 6 (for Flames 1–4, see Appendix K). The data are plotted against downstream distance[3], $0 \leq x/d_1 \leq 29$, for four forcing amplitudes. The black horizontal bars at the top and bottom of each plot indicate lock-in. The colorscale for gain varies from plot

---

[1] The phase is computed with cross-correlation, as per Balasubramanian and Sujith (2008). Note that leading by more than π is equivalent to lagging by less than π.

[2] The flame length is determined by inspecting a series of randomly sampled wide-angle photographs of the flame intensity, and is defined as the axial station where the most downstream, but contiguous, piece of flame is visible.

[3] The data near the injector, $x/d_1 \leq 5.3$, are unreliable owing to a low SNR.

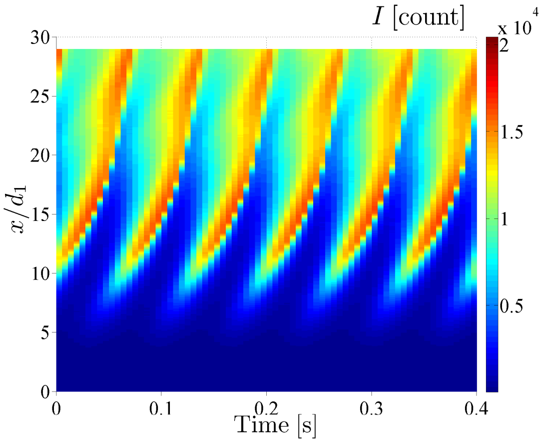

Figure 4.27: Spatiotemporal evolution of the intensity from Flame 5 (unforced).

to plot, but that for phase does not: blue hues show that the flame leads the forcing and red hues show that the forcing leads the flame.

The local gain depends on both frequency and space. As f_f decreases below f_n, the spatial distribution of $|FDF_l|$ shifts downstream and spreads axially. Its maximum occurs at the lowest frequency for which lock-in is possible, which is consistent with the behaviour of the global gain (figure 4.26) and the local normalised RMS response (figure 4.25). As A increases, $|FDF_l|$ saturates to similar values in all the flames and new regions of high gain appear far downstream.

The local phase also depends on both frequency and space. The axial distance between the peaks of $\angle FDF_l$ is a measure of the wavelength of the instability, which propagates as a vortical wave at the speed of advection[1]. This separation distance decreases as f_f increases because the wavelength shortens with frequency. At lock-in (black horizontal bars), the spatial distribution of $\angle FDF_l$ is particularly defined because the dispersion between vortical waves of different frequencies is reduced. In some cases (figures 4.28a and 4.29a–4.29d), there is a new phase peak, which may be related to the emergence of a higher-order harmonic.

Finally, perhaps the most important observation is that the spectral-spatial distribution of FDF_l differs between Flame 5 and Flame 6 (and indeed between all the flames): different flames release heat in different places depending on the

---

[1] If the disturbance propagated as an acoustic wave at the speed of sound, the phase would not vary much with downstream distance (Birbaud et al., 2007).

particular combination of f_f and A. This means that two local FDFs from two different flames cannot be compared to each other even if they are measured at the same axial station. The global FDFs shown in figure 4.26 are the cumulative result of such gain and phase variations along the flame length.

In summary, the global FDFs of all the flames are similar to each other: the maximum gain occurs just below f_n, there is a small reduction in gain just above f_n, and the phase increases as f_f increases through f_n and through $2f_n$. Stability analyses based on the FDF are valid only in the long-time limit and would therefore predict similar behaviour from all the flames. This, however, does not account for the response at $f \neq f_f$, which would affect the transient behaviour. The implication of this for a thermoacoustic system in which the flame and acoustics are coupled is left for future work.

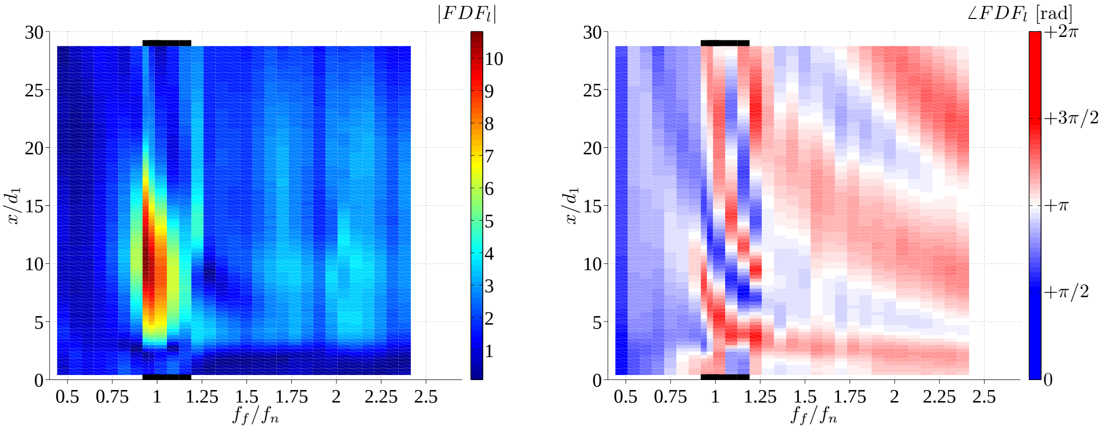

(a) $A = 0.10$

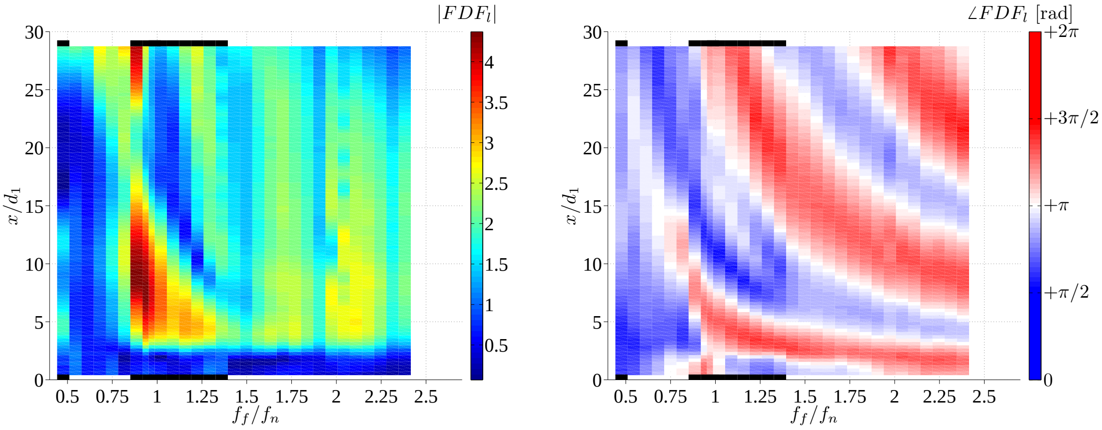

(b) $A = 0.30$

Figure 4.28: Gain and phase of the local FDF for Flame 5 forced at four amplitudes: $A =$ (a) 0.10, (b) 0.30, (c) 0.50, and (d) 0.70. The data are shown as a function of downstream distance: $0 \leq x/d_1 \leq 29$. The frequencies at which there is lock-in are indicated by the black horizontal bars at the top and bottom of the plots. (Continued on next page)

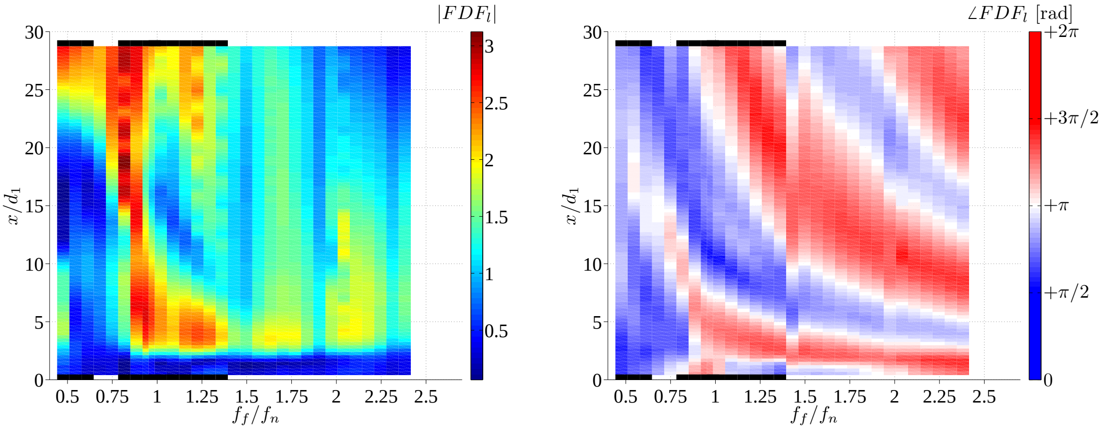

(c) $A = 0.50$

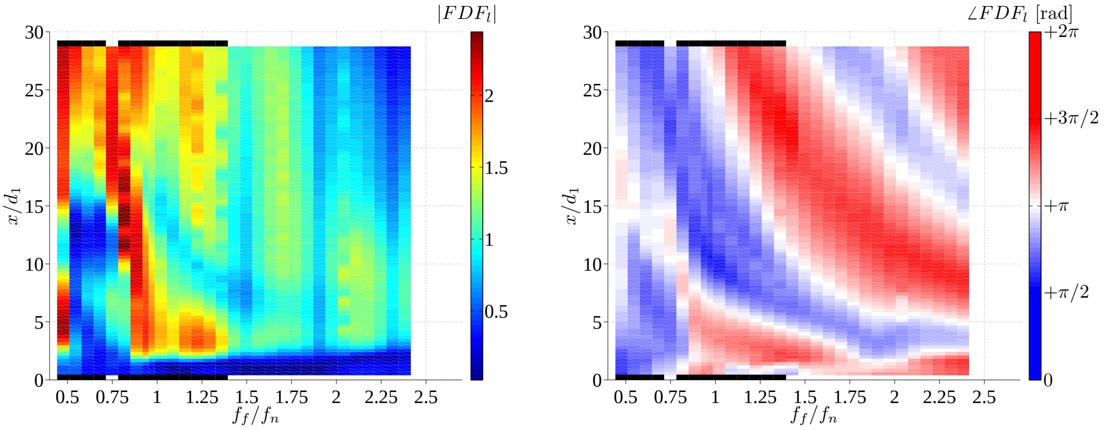

(d) $A = 0.70$

Figure 4.28: Continued from previous page.

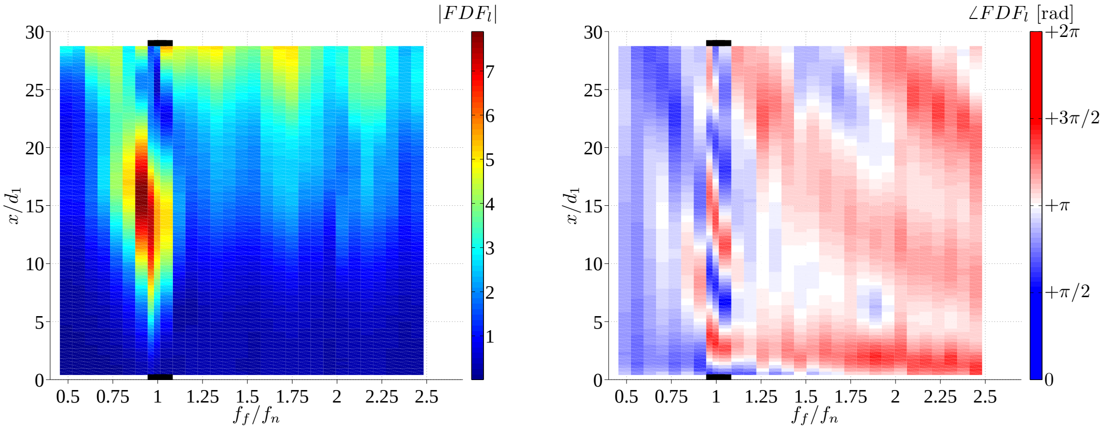

(a) $A = 0.10$

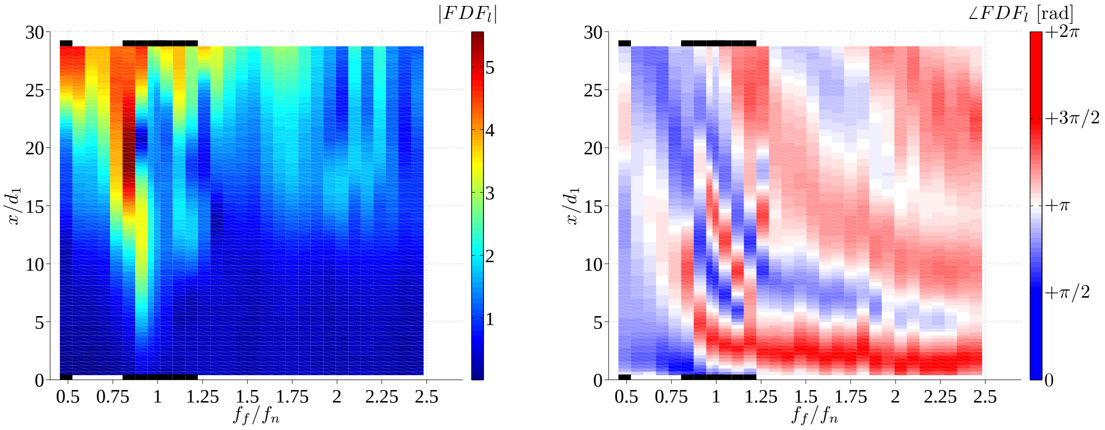

(b) $A = 0.30$

Figure 4.29: Gain and phase of the local FDF for Flame 6 forced at four amplitudes: $A =$ (a) 0.10, (b) 0.30, (c) 0.50, and (d) 0.70. The data are shown as a function of downstream distance: $0 \leq x/d_1 \leq 29$. The frequencies at which there is lock-in are indicated by the black horizontal bars at the top and bottom of the plots. (Continued on next page)

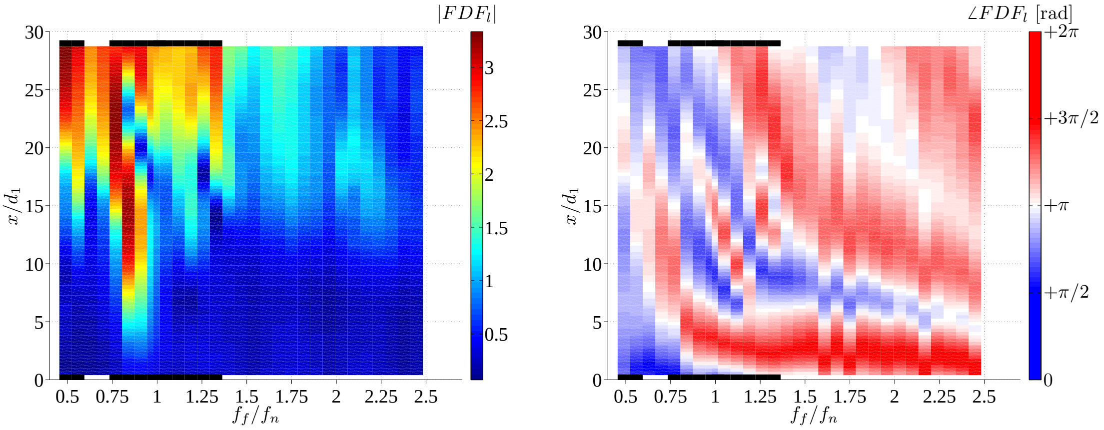

(c) $A = 0.50$

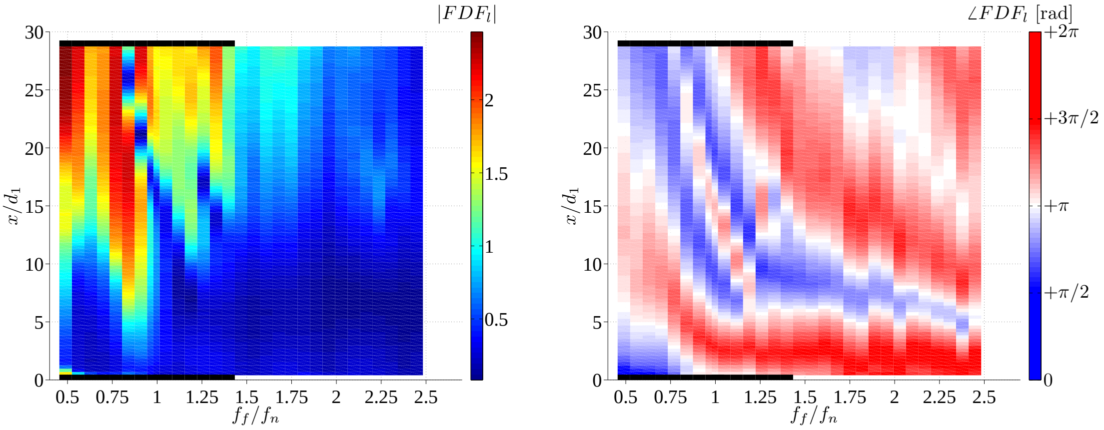

(d) $A = 0.70$

Figure 4.29: Continued from previous page.

4.2.4 Van der Pol oscillator

The forced flame system is modelled with the forced van der Pol (VDP) oscillator. This particular model is used because, as explained in §1.4.1.1, it is one of the simplest models with self-excited solutions, an essential feature for modelling self-excited flows. As in the experiments, the forcing is sinusoidal (right hand term):

$$\ddot{x} - \epsilon(1 - x^2)\dot{x} + \omega_n^2 x = A_{vdp}\,\sin(\omega_f\, t), \tag{4.2}$$

where A_{vdp} is the forcing amplitude and ω_f is its angular frequency. The parameter ϵ, which controls the degree of self-excitation and nonlinear self-limitation, is fixed at an arbitrarily small value of 0.1. The natural angular frequency, ω_n, is 1. Equation (4.2) is solved numerically using a fourth-order Runge–Kutta method. This is done for a range of forcing frequencies ($0.3 \leq \omega_f \leq 2.5$) and amplitudes ($0 \leq A_{vdp} \leq 0.4$) in order to replicate the experimental conditions.

With ω_f (1.03) slightly above ω_n, figure 4.30a shows time traces of the steady-state solution for five forcing amplitudes: $0.05 \leq A_{vdp} \leq 0.13$. For comparison, a time trace of the same signal from the same oscillator but without forcing is also shown (bottom). The corresponding PSD curves are shown in figure 4.30b. These figures are analogous to those for the self-excited Flame 5 (figure 4.5).

The forced response of the VDP oscillator is qualitatively similar to that of the flame. When unforced, the VDP oscillator has a dominant natural frequency, represented in the PSD by a sharp peak at $\omega_n = 1$. There are, however, no harmonics because the solution is perfectly sinusoidal.

When forced at a low amplitude ($A_{vdp} = 0.05$), the VDP oscillator responds at ω_f as well as ω_n, with multiple spectral peaks arising between these two frequencies. Thus, like the flame, the VDP oscillator is quasiperiodic before lock-in.

As A_{vdp} increases from 0.05 to 0.10, ω_n shifts towards ω_f, which remains fixed. The spectral peaks around ω_n and ω_f become closer and their envelope widens. By $A_{vdp} = 0.112$, that envelope develops a subtle bias for $\omega < \omega_n$, as indicated by the more marked tail. Once A_{vdp} reaches a critical value of 0.115, the VDP oscillator locks into the forcing. This occurs because the stable equilibrium points of the VDP oscillator change as the amplitude of the forcing term changes (see §7.5 of the book by Jordan and Smith, 2007).

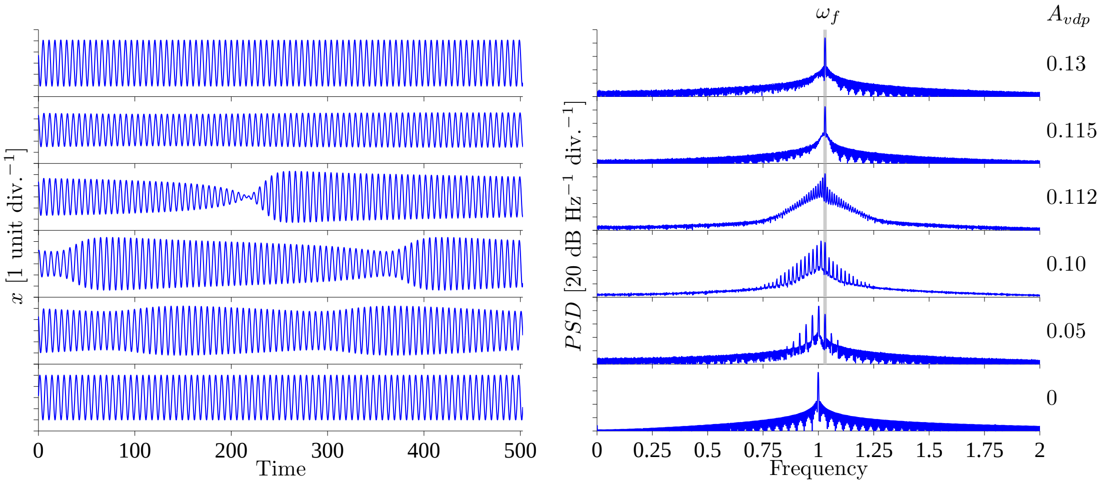

(a) Time trace

(b) PSD

Figure 4.30: (a) Time trace and (b) PSD of the motion of the VDP oscillator forced at a frequency, $\omega_f = 1.03$, slightly above the natural frequency, $\omega_n = 1$. Solutions are shown for five forcing amplitudes, $0.05 \leq A_{vdp} \leq 0.13$, and for the unforced case, all with $\epsilon = 0.1$. The onset of lock-in occurs at $A_{loc} = 0.115$.

The similarities between the VDP oscillator and the flame are also apparent in the phase portraits and Poincaré maps: figure 4.31. When unforced, the solution starts off as a limit cycle, but becomes quasiperiodic as A_{vdp} increases towards lock-in. After lock-in, it converges to a new limit cycle and the phase trajectory converges to a new orbit.

The consolidated PSD (figure 4.32) resembles the analogous plot for the flame (figure 4.15). The vertical stripe is the response of the natural mode. When forced around ω_n, however, this response locks into the forcing, represented by the diagonal stripe at $\omega = \omega_f$. There is no diamond pattern because the VDP oscillator is sinusoidal.

The lock-in map is shown in figure 4.33, with A_{loc} indicated by circular markers. The colorscale is the VDP response, defined as the RMS of the forced solution normalised by that of the unforced solution: $x'_{rms,\,for}/x'_{rms,\,unf}$. This response decreases below unity as A_{vdp} increases towards lock-in, regardless of whether ω_f is above or below ω_n. At lock-in, it reaches a minimum, and its value decreases as ω_f deviates from ω_n. The lock-in curve is $\vee$ shaped and symmetric about ω_n.

Although most of these features are observed in the flame, two are not: (i) the flame response at lock-in is above (not below) unity when $f_f < f_n$; and (ii) the flame's lock-in curve is not symmetric about f_n.

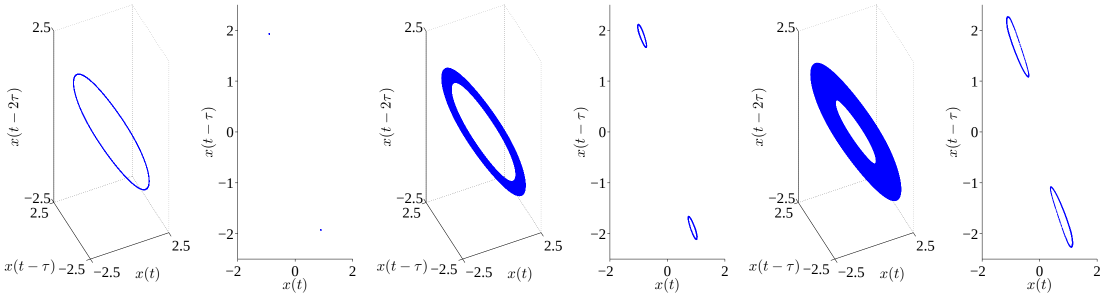

(a) $A_{vdp} = 0$ (b) $A_{vdp} = 0.05$ (c) $A_{vdp} = 0.10$

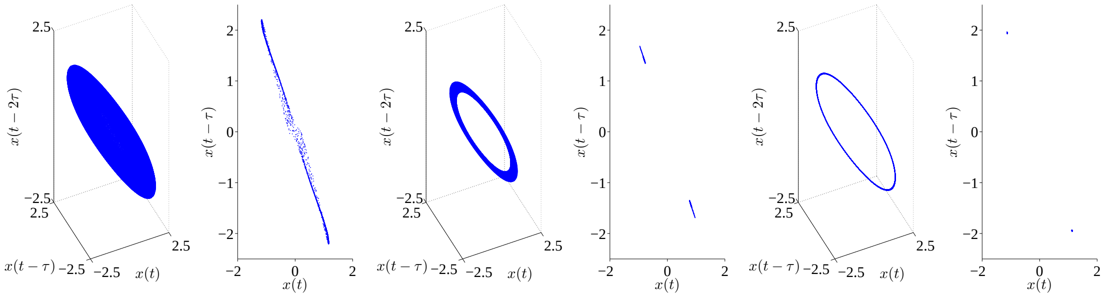

(d) $A_{vdp} = 0.112$ (e) $A_{vdp} = 0.115$ (f) $A_{vdp} = 0.13$

Figure 4.31: Phase portraits (left) and Poincaré maps (right) for the VDP oscillator forced at $\omega_f = 1.03$ with five amplitudes, plus the unforced case.

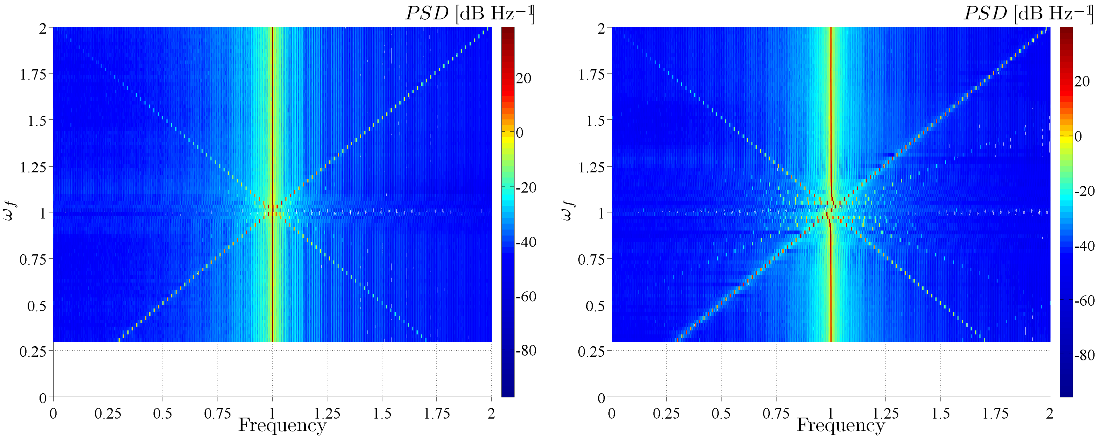

(a) $A_{vdp} = 0.03$

(b) $A_{vdp} = 0.12$

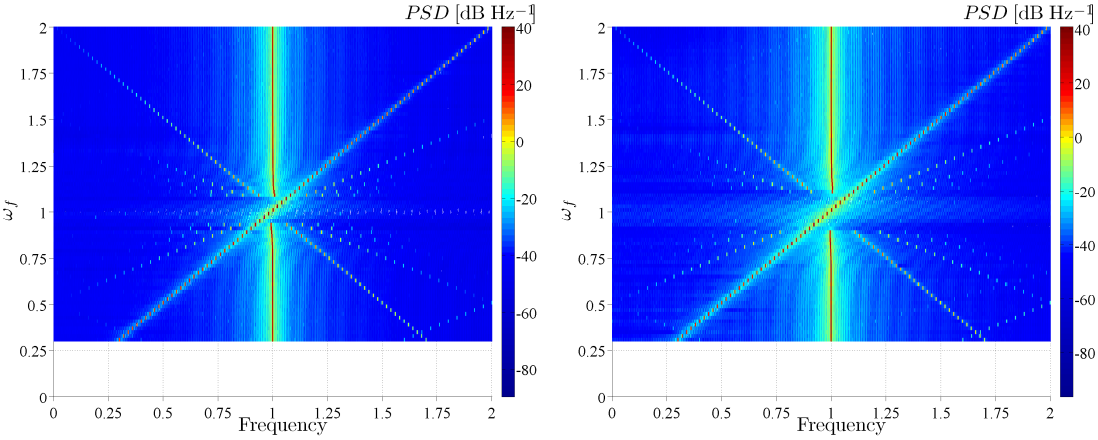

(c) $A_{vdp} = 0.21$

(d) $A_{vdp} = 0.30$

Figure 4.32: Consolidated PSD for the VDP oscillator forced at four amplitudes: A_{vdp} = (a) 0.03, (b) 0.12, (c) 0.21, and (d) 0.30. This figure can be compared to figure 4.15, which is for a self-excited flame (Flame 5).

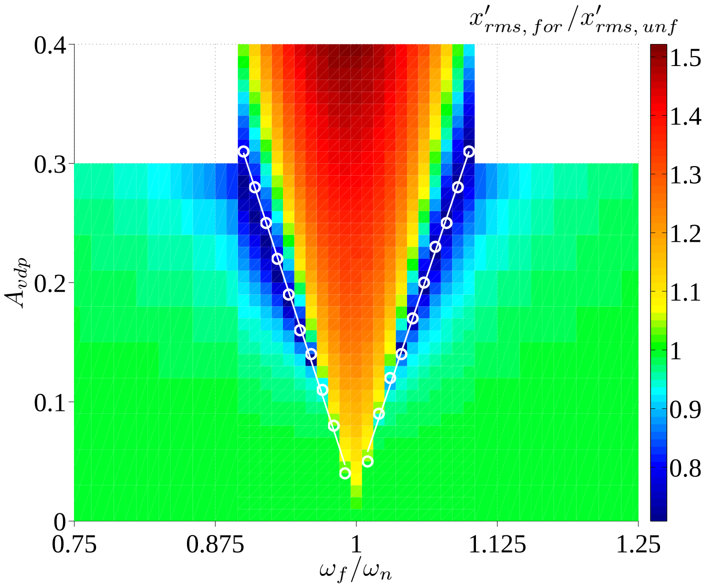

Figure 4.33: Response of the VDP oscillator as a function of ω_f and A_{vdp}. The critical forcing amplitude required for lock-in, A_{loc}, is indicated by the circular markers. On the colorscale, a response of unity is in green, with values above unity in warmer (red/yellow) hues and values below unity in cooler (blue/cyan) hues. This figure can be compared to figure 4.25a, which is for a self-excited flame (Flame 5).

Chapter 5

Conclusions

This final chapter is divided into two parts: the first is a summary of the results from chapters 3 and 4, and the second is a list of suggestions for future work.

5.1 Summary

In this thesis, the assumption that hydrodynamically self-excited flows are insensitive to forcing was tested experimentally. This was done by acoustically forcing two different self-excited flows: a non-reacting jet and a reacting jet. Both jets have regions of absolute instability at their base and this causes them to exhibit varicose oscillations at discrete natural frequencies. The forcing was applied around these frequencies, at varying amplitudes, and the response examined over a range of frequencies (not just at the forcing frequency). The overall system was then modelled as a forced van der Pol oscillator.

The results show that, contrary to some expectations, a hydrodynamically self-excited jet oscillating at one frequency is sensitive to forcing at other frequencies. When forced at low amplitudes, the jet responds at both frequencies as well as at several nearby frequencies, and there is beating, indicating quasiperiodicity. When forced at high amplitudes, however, it locks into the forcing. The critical forcing amplitude required for lock-in increases with the deviation of the forcing frequency from the natural frequency. This increase is linear, indicating a Hopf bifurcation to a global mode.

The lock-in curve has a characteristic $\vee$ shape, but with two subtle asymmetries about the natural frequency. The first asymmetry concerns the forcing amplitude required for lock-in. In the non-reacting jet, higher amplitudes are required when the forcing frequency is above the natural frequency. In the reacting jet, lower amplitudes are required when the forcing frequency is above the natural frequency. The second asymmetry concerns the broadband response at lock-in. In the non-reacting jet, this response is always weaker than the unforced response, regardless of whether the forcing frequency is above or below the natural frequency. In the reacting jet, that response is weaker than the unforced response when the forcing frequency is above the natural frequency, but is stronger than it when the forcing frequency is below the natural frequency.

In the reacting jet, weakening the global instability – by adding coflow or by diluting the fuel mixture – causes the flame to lock in at lower forcing amplitudes. This finding, however, cannot be detected in the flame describing function. That is because the flame describing function captures the response at only the forcing frequency and ignores all other frequencies, most notably those arising from the natural mode and from its interactions with the forcing. Nevertheless, the flame describing function does show a rise in gain below the natural frequency and a drop above it, consistent with the broadband response.

Many of these features can be predicted by the forced van der Pol oscillator. They include (i) the coexistence of the natural and forcing frequencies before lock-in; (ii) the presence of multiple spectral peaks around these competing frequencies, indicating quasiperiodicity; (iii) the occurrence of lock-in above a critical forcing amplitude; (iv) the ∨-shaped lock-in curve; and (v) the reduced broadband response at lock-in. There are, however, some features that cannot be predicted. They include (i) the asymmetry of the forcing amplitude required for lock-in, found in both jets; (ii) the asymmetry of the response at lock-in, found in the reacting jet; and (iii) the interactions between the fundamental and harmonics of both the natural and forcing frequencies, found in both jets.

Taken together, these results have conflicting implications for thermoacoustics. On one hand, they show that a flame's response at the forcing frequency cannot be eliminated simply by ensuring that it has a hydrodynamically self-excited mode at another frequency. In fact, the flame responds at several discrete frequencies, potentially exciting other acoustic modes in the combustor. On the other hand, the results also show that when lock-in occurs with the forcing frequency above the natural frequency, the flame oscillations are suppressed relative to the unforced case. This suggests that lock-in may not be as detrimental as it is thought to be.

5.2 Future work

Although this thesis has uncovered several features of forced self-excited jets that have not been seen before, two particular areas could benefit from further work. The first concerns the fact that the global FDFs were similar for all six flames (§4.2.3), despite the varying strengths of global instability. The most plausible explanation for this anomaly is that because the field of view of the chemiluminescence videos did not cover the entire flame, the data did not represent the entire heat release. This meant that if some flames released more heat downstream (i.e. out of the field of view) than did others, the global FDF would not be able to account for it. The experiments should therefore be repeated with a wide-angle lens[1]. Alternatively, shorter flames, such as premixed flames, could be studied. Like the diffusion flames studied here, some premixed flames – when stabilised behind a bluff body – contain sufficient regions of absolute instability that they are globally unstable (Anderson et al., 1996). As an added benefit, such premixed flames also contain less soot, although an image intensifier would be needed to measure the heat-release oscillations accurately if line-specific chemiluminescence (e.g. CH* or OH*) were to be used.

The second area concerns the type of forcing used to perturb the flame. In this thesis, it was open loop: the forcing signal was fixed, independent of the response of the system being forced. In real combustors, however, the frequency and amplitude of the thermoacoustic modes that force the flame depend on the heat release from the flame itself – in particular on how that heat release interacts with the natural acoustic modes of the chamber. A more realistic approach would be to consider the system as two coupled oscillators: one representing the flame and the other the chamber acoustics. Each oscillator would have its own natural frequency, and so would the coupled-oscillator system. In the laboratory, this

---

[1] The room in which the experiments were performed was too small to enable the entire flame to be imaged.

could be achieved by adding feedback between the flame system and the forcing system. For example, a photodiode could be set up to measure the oscillation amplitude of the flame intensity at some axial station. Its output would be used as input to an electronic oscillator[1], which would drive a loudspeaker that acts on the flame. Alternatively, if the preference is for premixed flames – which tend to have a higher natural frequency and hence a shorter, more manageable acoustic wavelength – an acoustic cavity could be installed around the flame in order to provide real thermoacoustic feedback.

Other areas in which there is scope for further work include:

- *Improving the VDP oscillator:* Although the VDP oscillator can predict most of the jet features, it fails to predict (i) the asymmetry of the forcing amplitude required for lock-in, found in both jets; and (ii) the asymmetry of the response at lock-in, found in the reacting jet. One of the next logical steps is to modify the original VDP oscillator so that it can predict both of these asymmetries. The VDP oscillator could also be modified so that its lock-in boundaries can be quantitatively related to those of actual flows. This would involve changing the magnitude of the limit-cycle amplitude term (whose value is unity in this thesis), which can be inferred from the amplitude of the natural flow oscillation.

- *Measuring the alignment between the velocity and density profiles:* An instructive exercise would be to examine how this alignment affects the inception and development of global instability, particularly the susceptibility of a flame to lock into external forcing. Given uninterrupted access to a laboratory, this could be done relatively easily using proven experimental techniques, such as particle image velocimetry, for the velocity profile, and Rayleigh scattering, for the density profile.

---

[1] Such as a resistor-inductor-capacitor circuit or an operational-amplifier circuit, whose natural frequency can be tuned around that of the flame.

Appendix A

Predicting the global frequency

Even before Chomaz et al. (1988) established a definitive link between local absolute instability and global instability, several researchers had already proposed criteria by which to predict the global frequency. The majority of such criteria were derived from local stability arguments, and three of the most widely used are listed in table A.1.

To test these criteria, Monkewitz and Nguyen (1987) compared the predicted global frequencies to experimental data from real globally unstable flows. Guided by the findings, these researchers suggested that the criterion of Pierrehumbert (1984) is best suited for flows that are unbounded. They also suggested that the criterion of Koch (1985) is most applicable to flows with small (but positive) absolute growth rates and with solid boundaries for efficient wave reflection. As for their own proposed criterion, they thought that it should perform best for flows with solid boundaries and large regions of absolute instability.

Although capable of predicting the global frequency, the three criteria performed poorly when applied to the (initial) temporal growth rate. In numerical simulations of wake flows, for example, Hannemann and Oertel Jr (1989) found reasonable agreement in the global frequency: 2.5% error with the criterion of Pierrehumbert (1984), 1.06% error with that of Koch (1985), and 14% error with that of Monkewitz and Nguyen (1987). However, they also found that the corresponding growth rates were more than double those reported by their simulations. This discrepancy is not entirely unexpected, though, as all three criteria are based on linear stability and should therefore be valid only at the onset of instability, not at the nonlinear saturated state for which the simulations were done.

Table A.1: Criteria for predicting the global frequency.

Source	Proposed criterion
Pierrehumbert (1984)	The global frequency is dominated by the *most unstable mode* within the absolutely unstable region. It is, in other words, dominated by the stationary mode with the highest temporal growth rate. The frequency of this mode is the real part of the branch point value where the imaginary part of the branch point frequency is at a maximum.
Koch (1985)	The global frequency is dominated by the local resonance acting at the *most downstream location* of absolute instability. It is, in other words, dominated by the local absolute frequency at the streamwise location where the flow first transitions from being absolutely unstable to convectively unstable. The resonance is due to coalescence between upstream-travelling and downstream-travelling waves.
Monkewitz and Nguyen (1987)	The global frequency is dominated by the local resonance acting at the *most upstream location* of absolute instability. It is, in other words, dominated by the local absolute frequency at the streamwise location where the flow first transitions from being convectively unstable to absolutely unstable.

In summary, criteria based on local stability can be used to predict the global frequency fairly accurately. Using the same criteria to predict the corresponding growth rate, however, can lead to large errors.

Appendix B

Forced Stuart–Landau model

The linear dependence of the critical forcing amplitude required for lock-in, A_{loc}, on the difference between the forcing and natural frequencies, $|f_f - f_n|$, can be predicted by the forced Stuart–Landau model (Landau and Lifshitz, 1959)[1]. In hydrodynamics, the Stuart–Landau model is used to describe the temporal evolution of flow oscillations. It involves expanding, as a sum, a non-stationary perturbation to a steady solution of the Navier–Stokes equations, followed by a truncation of all high-order nonlinear terms except for one. According to Provansal et al. (1987), if the imaginary part of this remaining (third-order) nonlinear term is also neglected, what remains can be expressed as:

$$\frac{\mathrm{d}u}{\mathrm{d}t} = (\sigma_r + i\sigma_i)u - \frac{1}{2}(l_r)|u|^2 u + Ae^{i\omega_f t}, \tag{1}$$

where u is the velocity fluctuation, σ is the coefficient of the linear term (σ_i being the natural angular frequency), l_r is the real part of the nonlinear term, A is the forcing amplitude, and ω_f is the forcing angular frequency. If a solution to (1) has the general form $|u|e^{i\phi}$, where ϕ is the phase of u, then it must satisfy the following differential equations:

$$\frac{\mathrm{d}|u|}{\mathrm{d}t} = \sigma_r|u| - \frac{1}{2}(l_r)|u|^3 + A\cos(\omega_f t - \phi), \tag{2}$$

---

[1] This model was proposed by Landau in the 1940s to describe the macroscopic features of superconductors, specifically second-order phase transitions. It is a phenomenological model in that it describes the observable features of phenomena without explaining the underlying microscopic mechanisms. About a decade after its proposal, the model was extended by Stuart (1958, 1960) to the stability of plane parallel flows.

$$\frac{|u|\,\mathrm{d}\phi}{\mathrm{d}t} = \sigma_i|u| + A\sin(\omega_f t - \phi). \tag{3}$$

For lock-in to occur, the solution must satisfy two further conditions: (i) the oscillation amplitude must not vary with time, meaning $\frac{\mathrm{d}|u|}{\mathrm{d}t} = 0$, and (ii) the oscillation must be at the same frequency as the forcing, which restricts the phase to be $\phi = \omega_f t + \psi$, where ψ is a constant phase shift. Using these two conditions to solve (2) and (3) gives the following at the limit of lock-in:

$$\frac{A_{loc}}{|u|} = |\omega_f - \sigma_i|, \tag{4}$$

or in non-angular-frequency form:

$$\frac{A_{loc}}{|u|} = 2\pi|f_f - f_n|. \tag{5}$$

This confirms the linear dependence of A_{loc} on $|f_f - f_n|$. The expected value of the slope, 2π, cannot be checked in this thesis, however, because the forcing amplitude, A, and the response amplitude, $|u|$, are measured as different physical quantities. The forcing amplitude is measured as the velocity perturbation at the injector outlet. The response amplitude is measured either as the velocity somewhere downstream (low-density jet, chapter 3) or as the chemiluminescent intensity (jet diffusion flame, chapter 4).

As noted by Monkewitz et al. (1990), the Stuart–Landau model also predicts that for small deviations from the bifurcation point ($R - R_{bif} \approx 0$, where R_{bif} is the value of the control parameter at the onset of bifurcation) and in the absence of forcing ($A = 0$), the temporal growth rate, σ_r in (2), is to a first approximation proportional to $(R - R_{bif})$. Consequently, with cubic damping ($l_r > 0$), the saturation amplitude is:

$$|u|_{sat} \propto (R - R_{bif})^{1/2} \;\; \text{for } A = 0,\;\; R \geq R_{bif},\;\; R - R_{bif} \approx 0. \tag{6}$$

Appendix C

Technical drawings of Injector B

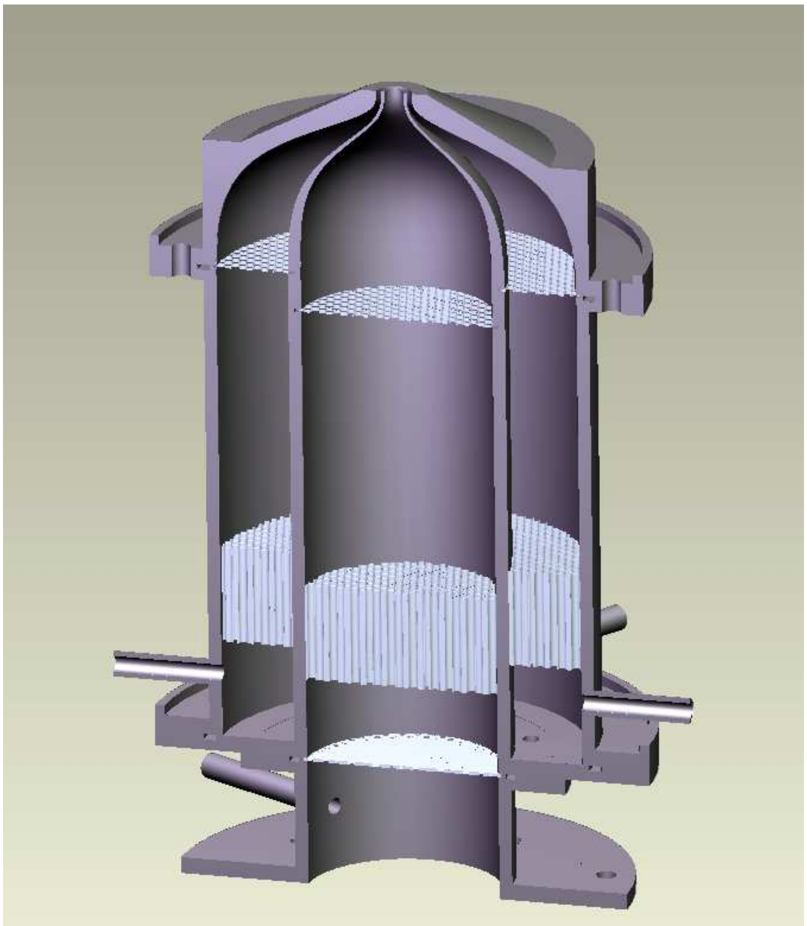

Figure C.1: General rendering (Injector B).

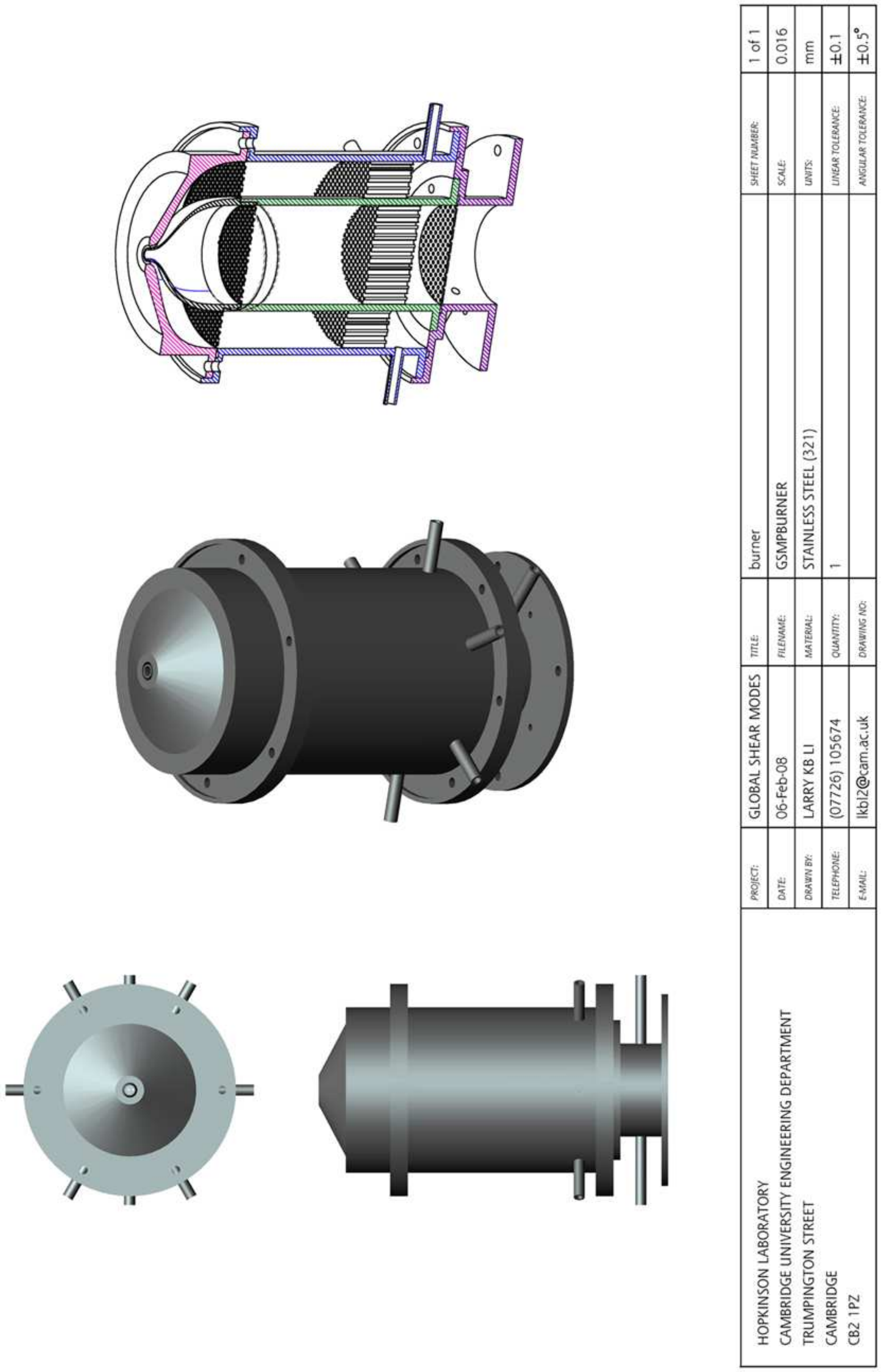

Figure C.2: Assembly drawing (Injector B).

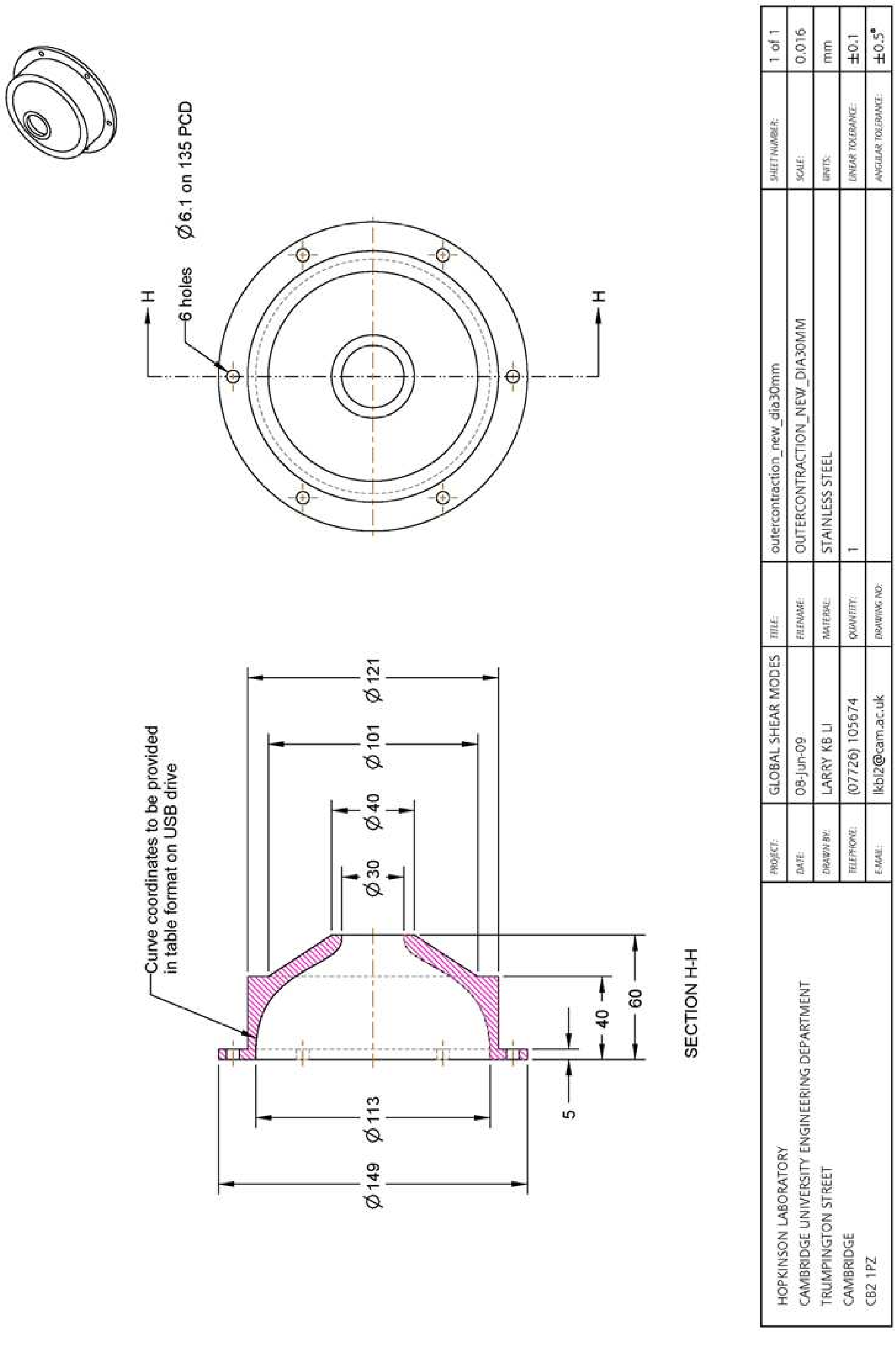

HOPKINSON LABORATORY CAMBRIDGE UNIVERSITY ENGINEERING DEPARTMENT TRUMPINGTON STREET CAMBRIDGE CB2 1PZ					
PROJECT:	GLOBAL SHEAR MODES	TITLE:	outercontraction_new_dia30mm	SHEET NUMBER:	1 of 1
DATE:	08-Jun-09	FILENAME:	OUTERCONTRACTION_NEW_DIA30MM	SCALE:	0.016
DRAWN BY:	LARRY KB LI	MATERIAL:	STAINLESS STEEL	UNITS:	mm
TELEPHONE:	(07726) 105674	QUANTITY:	1	LINEAR TOLERANCE:	±0.1
E-MAIL:	lkbl2@cam.ac.uk	DRAWING NO:		ANGULAR TOLERANCE:	±0.5°

Figure C.3: Outer contraction (Injector B).

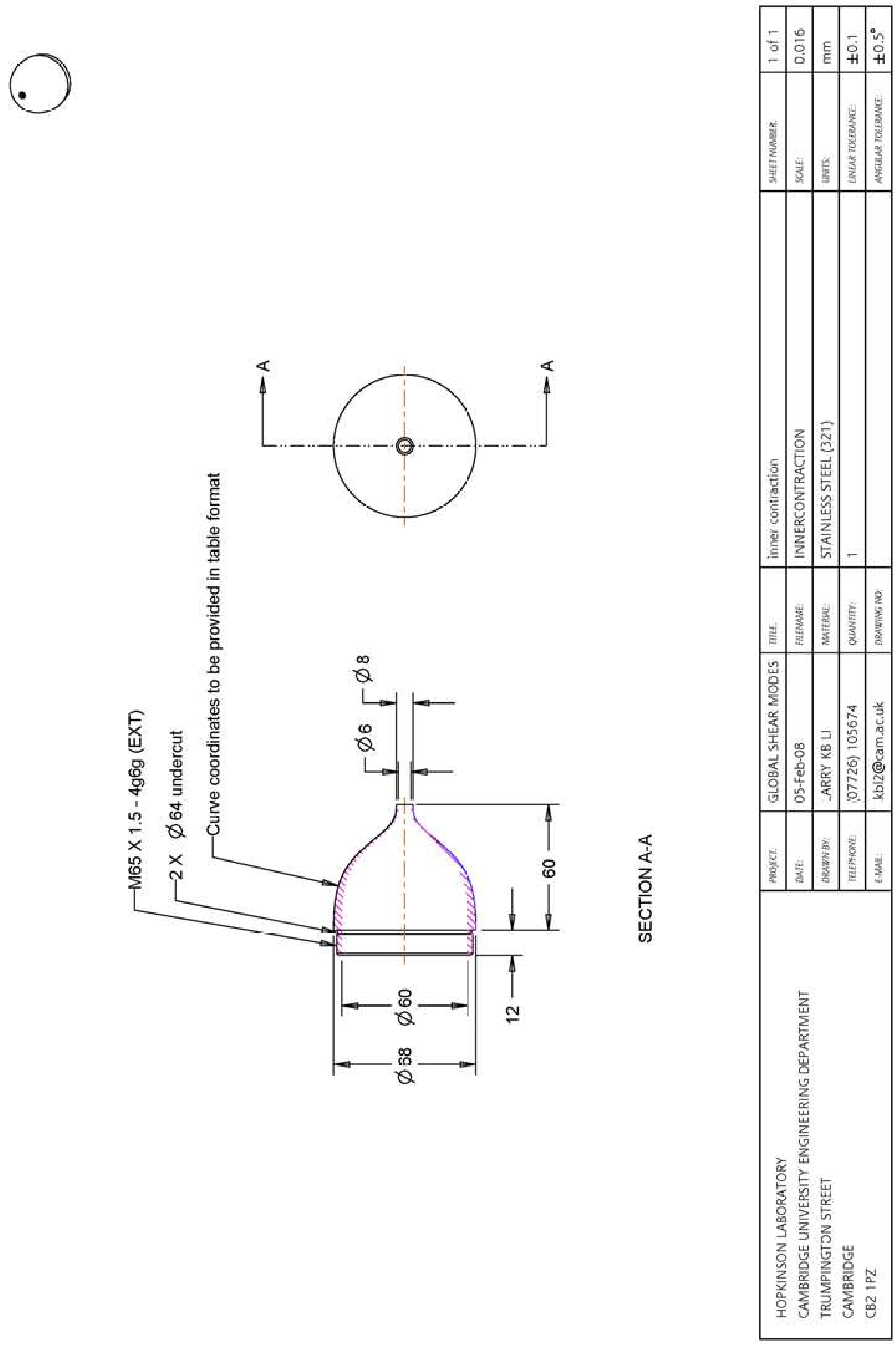

Figure C.4: Inner contraction (Injector B).

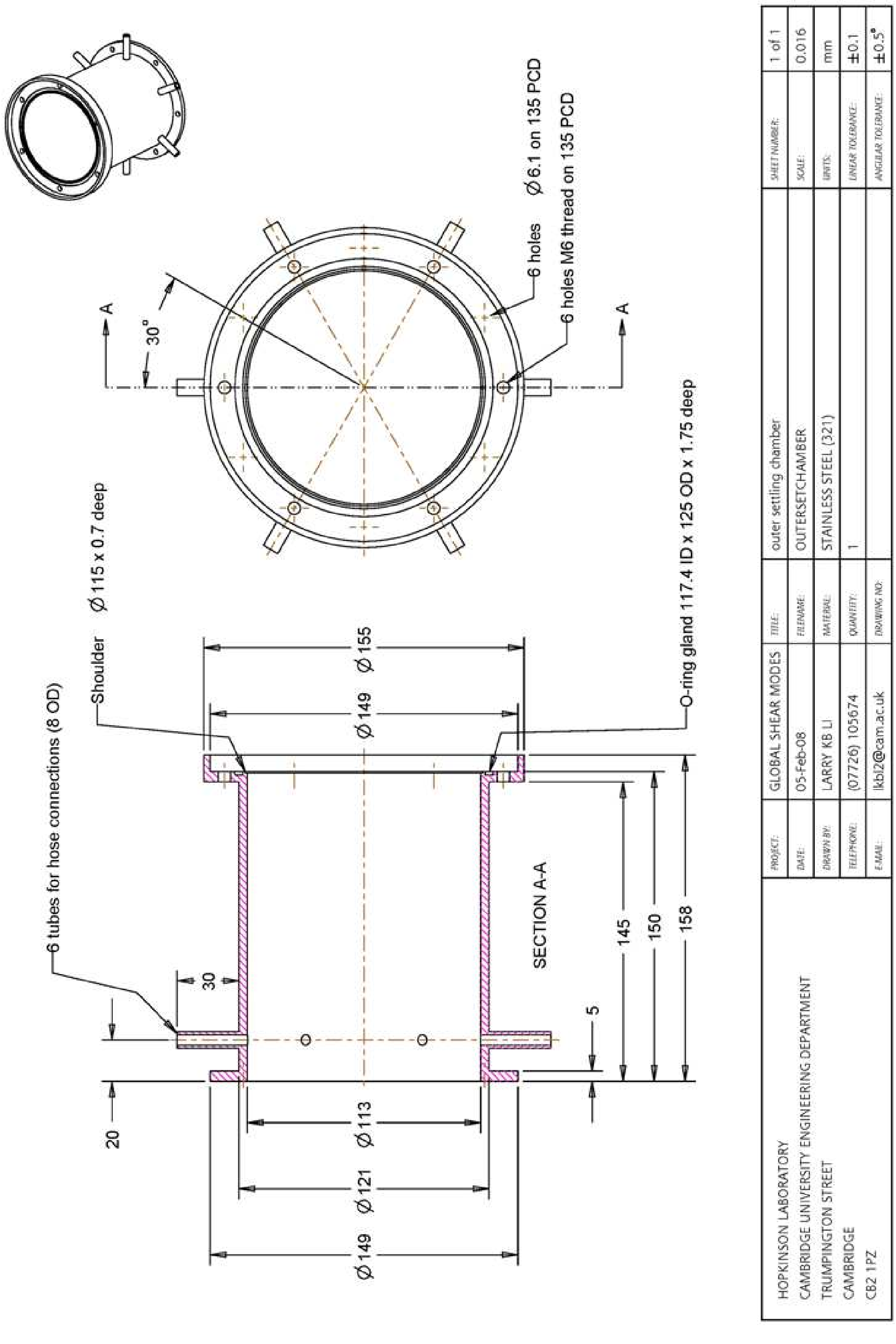

Figure C.5: Outer settling chamber (Injector B).

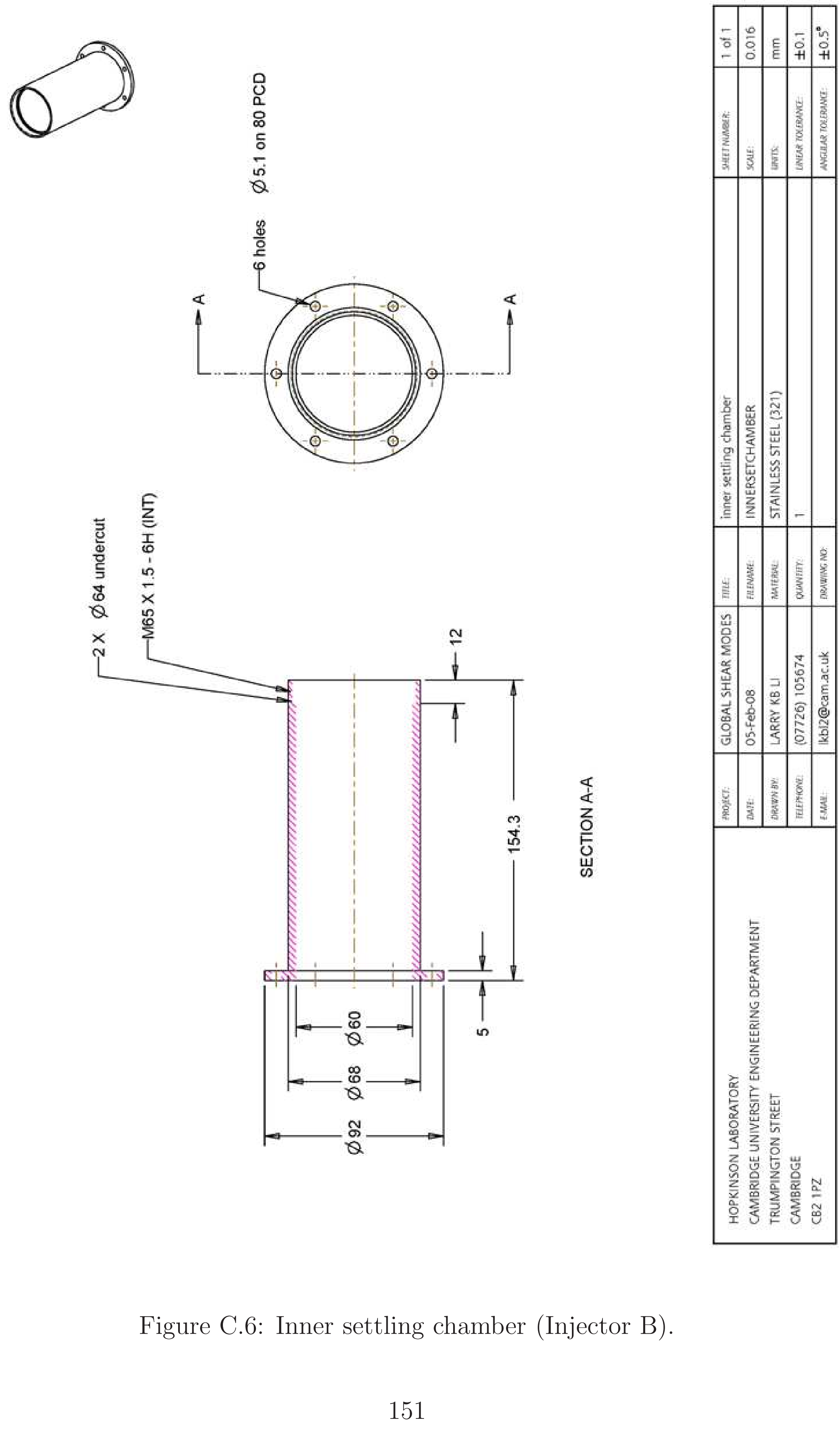

Figure C.6: Inner settling chamber (Injector B).

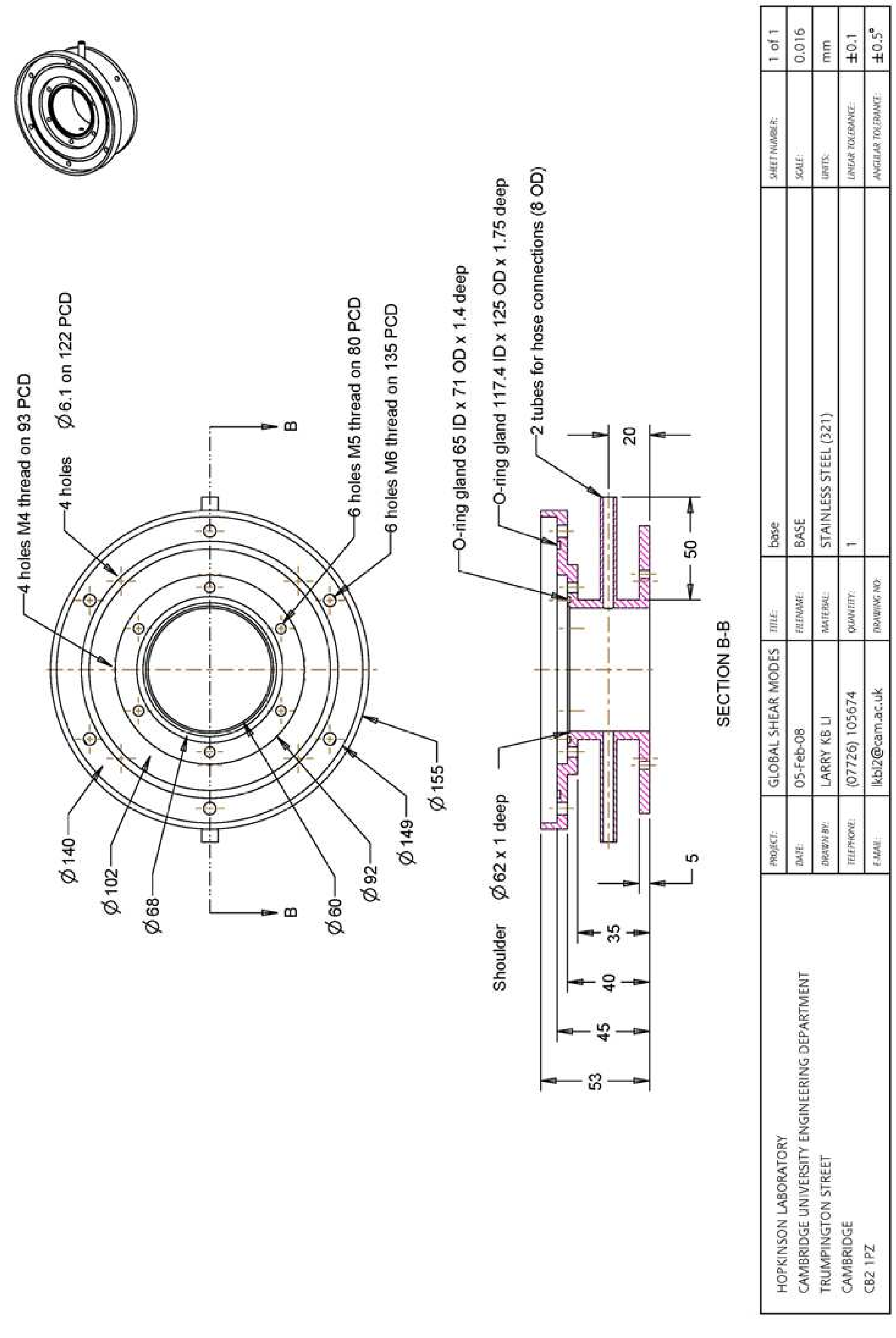

HOPKINSON LABORATORY
CAMBRIDGE UNIVERSITY ENGINEERING DEPARTMENT
TRUMPINGTON STREET
CAMBRIDGE
CB2 1PZ

PROJECT: GLOBAL SHEAR MODES
DATE: 05-Feb-08
DRAWN BY: LARRY KB LI
TELEPHONE: (07726) 105674
E-MAIL: lkbl2@cam.ac.uk
TITLE: base
FILENAME: BASE
MATERIAL: STAINLESS STEEL (321)
QUANTITY: 1
DRAWING NO:
SHEET NUMBER: 1 of 1
SCALE: 0.016
UNITS: mm
LINEAR TOLERANCE: ±0.1
ANGULAR TOLERANCE: ±0.5°

Figure C.7: Base (Injector B).

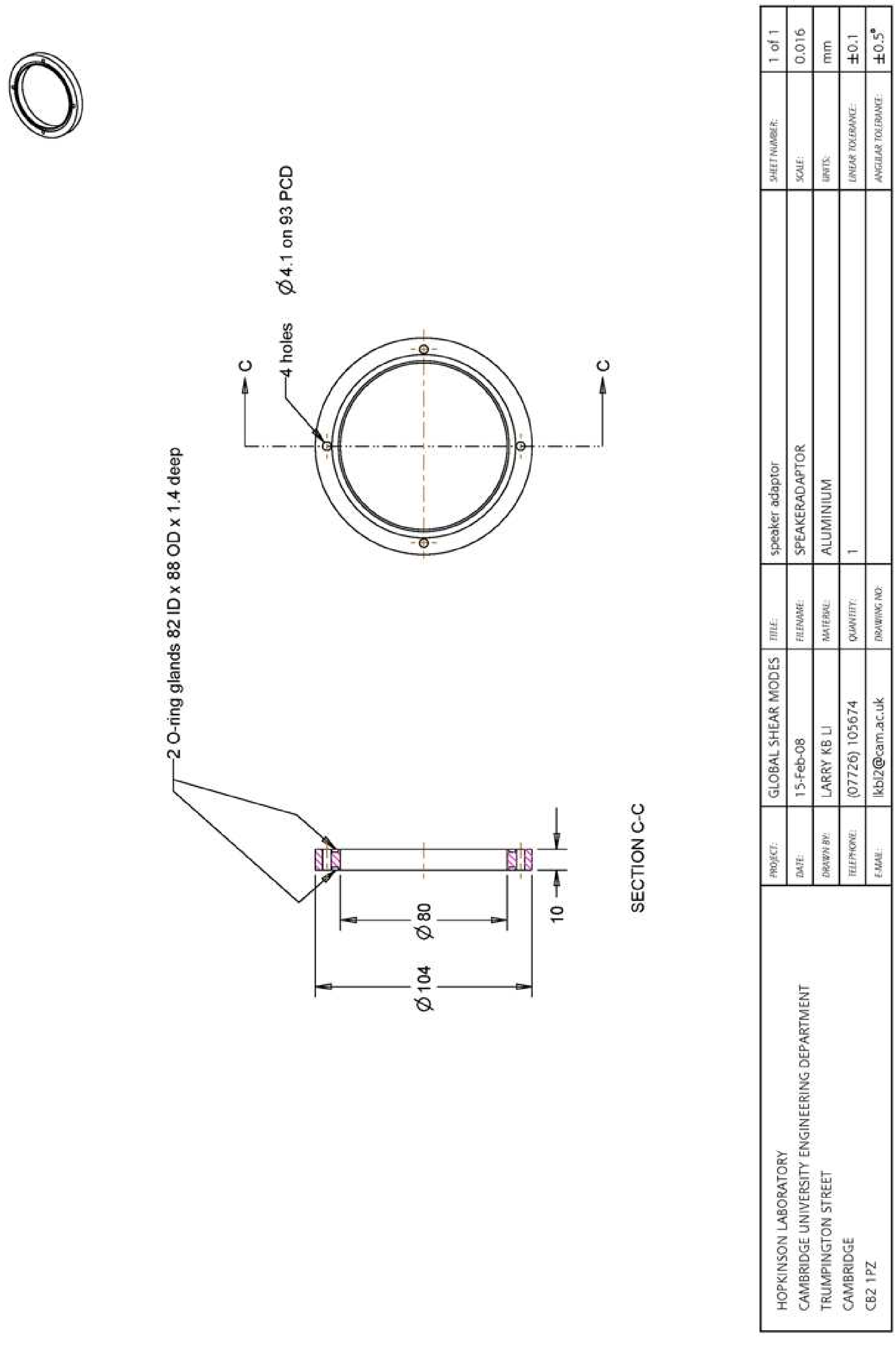

Figure C.8: Loudspeaker adaptor (Injector B).

Appendix D

Timing diagram for data acquisition

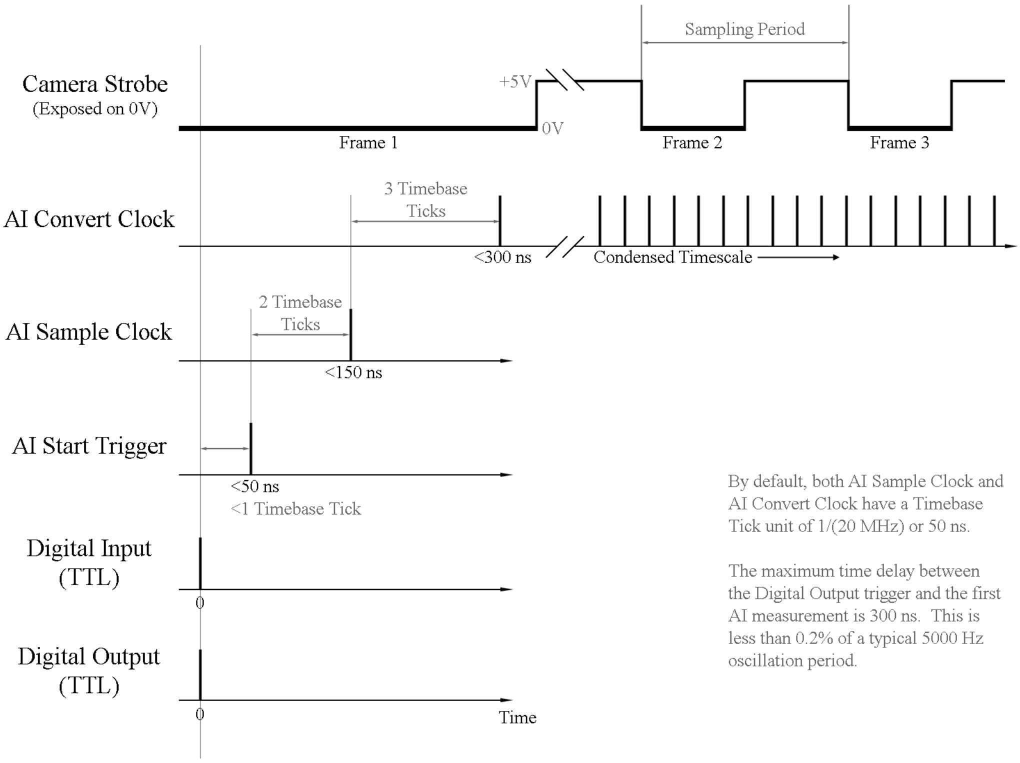

By default, both AI Sample Clock and AI Convert Clock have a Timebase Tick unit of 1/(20 MHz) or 50 ns.

The maximum time delay between the Digital Output trigger and the first AI measurement is 300 ns. This is less than 0.2% of a typical 5000 Hz oscillation period.

Figure D.1: Timing diagram of the data acquisition process used in the experiments. AI, analogue input; TTL, transistor–transistor logic.

Appendix E

Signal conditioner for TMM measurements

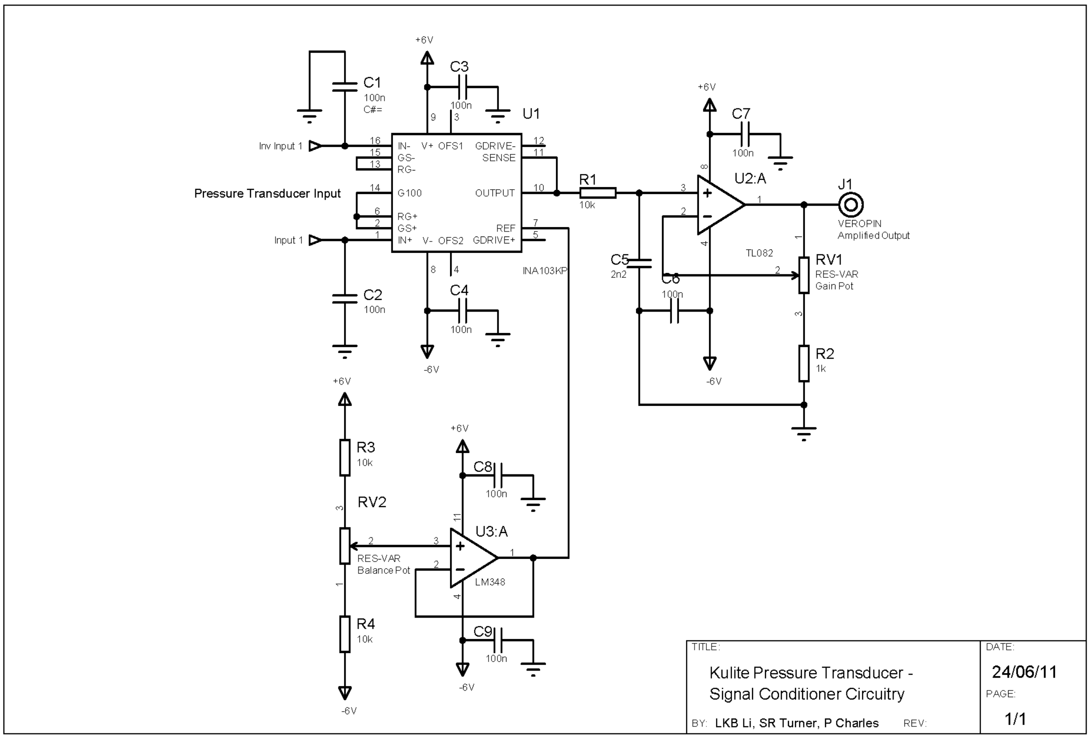

Figure E.1: Circuit diagram for the TMM signal conditioner. The circuitry shown is for one of two identical channels. Each channel has an adjustable gain (fixed at 60 dB for this thesis), a low-pass filter (the spectral response is shown in figure E.2), and a power source for transducer excitation.

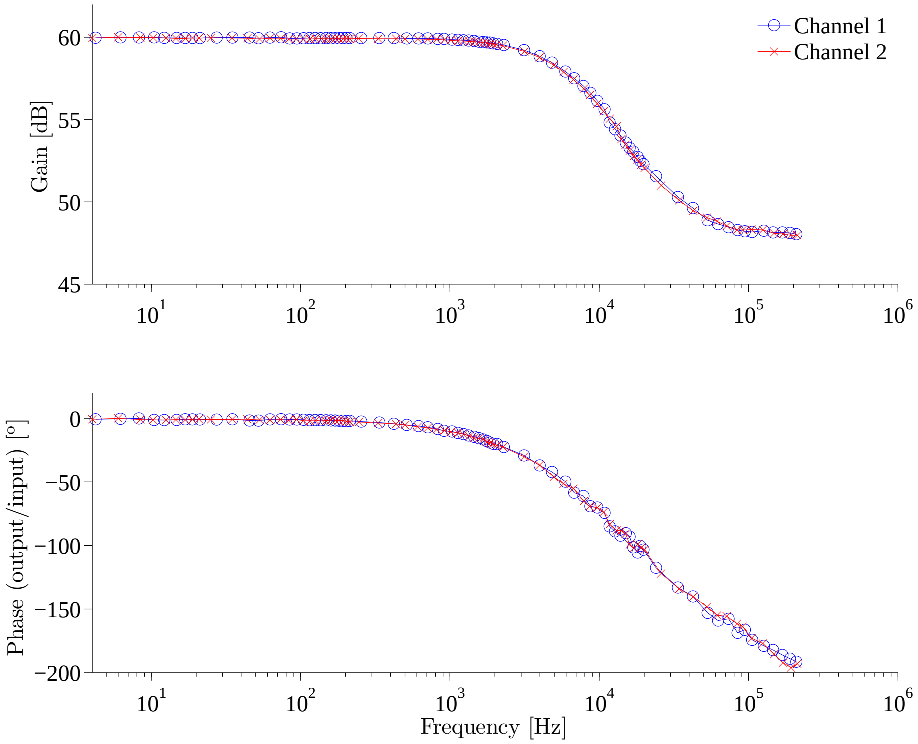

Figure E.2: Spectral response of the TMM signal conditioner. Each channel is tested independently, with the pressure transducer disconnected. The input voltage, sinusoidal and floating, is provided by a function generator (Thurlby Thandar Instruments® TG120). The output voltage, also sinusoidal but grounded, is measured with a digital oscilloscope (Tektronix® DPO3014).

Appendix F

Phase portraits for Flame 5 forced at 14 Hz: $f_f/f_n = 0.95$

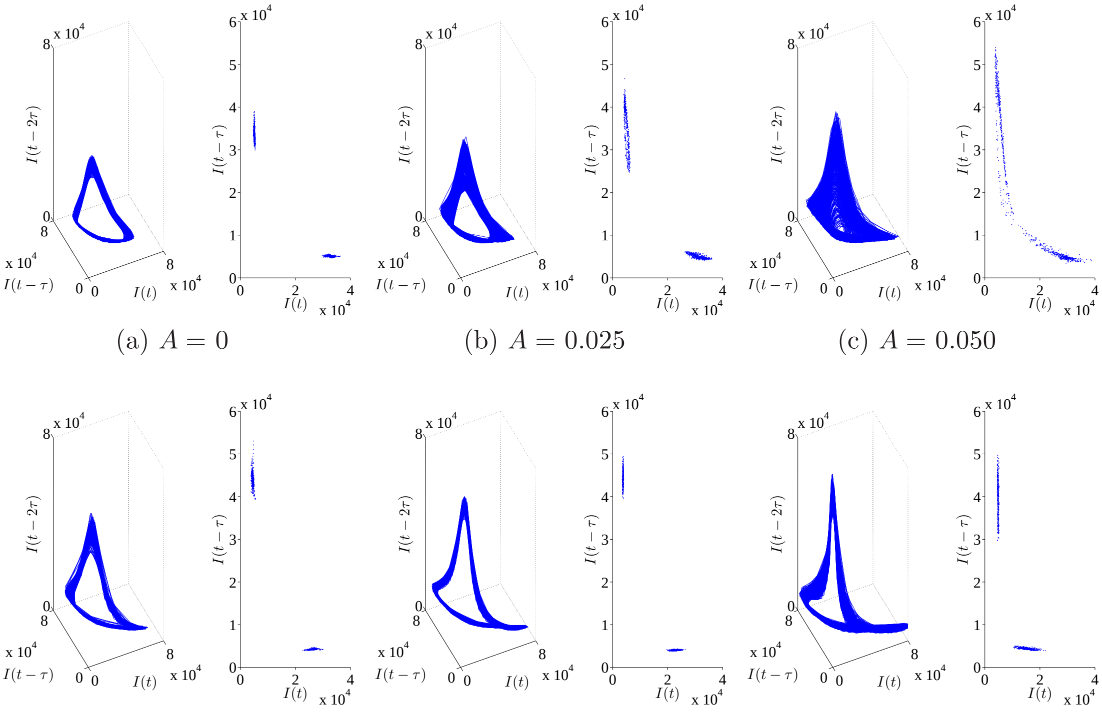

(a) $A = 0$

(b) $A = 0.025$

(c) $A = 0.050$

(d) $A = 0.075$

(e) $A = 0.10$

(f) $A = 0.30$

Figure F.1: Phase portraits (left) and Poincaré maps (right) for Flame 5 forced at 14 Hz ($f_f/f_n = 0.95$) with five amplitudes, plus the unforced case, all at $x/d_1 = 10$.

Appendix G

Pressure spectra in a real thermoacoustic system

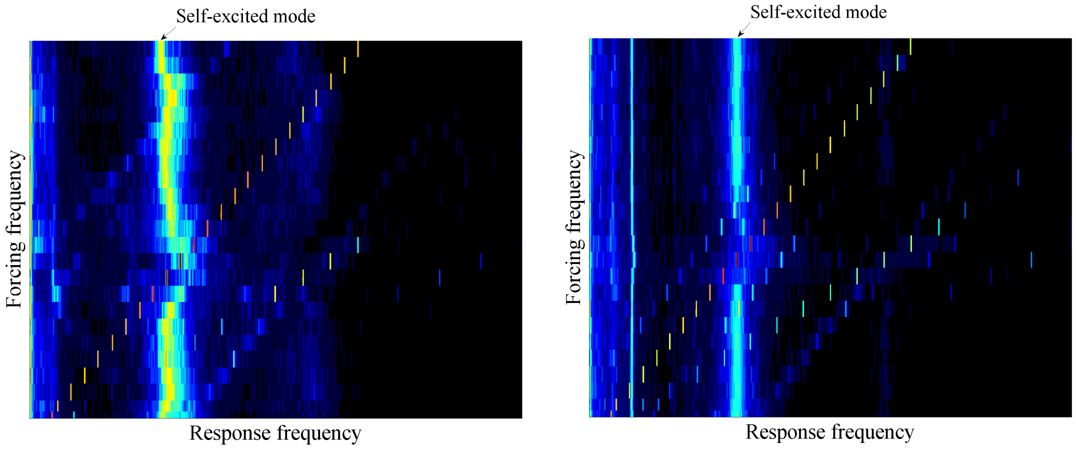

(a) Some injector (b) Another injector

Figure G.1: Consolidated PSD of the dynamic pressure in a combustor containing a liquid-fuelled spray flame forced by a siren. Provided by Dr. David Dennis, the data shown are for two different injectors, both installed in the Cambridge Intermediate Pressure Combustion Facility. Supporting the findings of this thesis, the plots show that lock-in can occur in a real thermoacoustic system and that, away from lock-in, there are rich interactions between the forcing and the self-excited mode. For intellectual property reasons, numerical values on the axes have been deliberately withheld.

Appendix H

Consolidated PSD for Flames 1–4

This appendix starts on the next page.

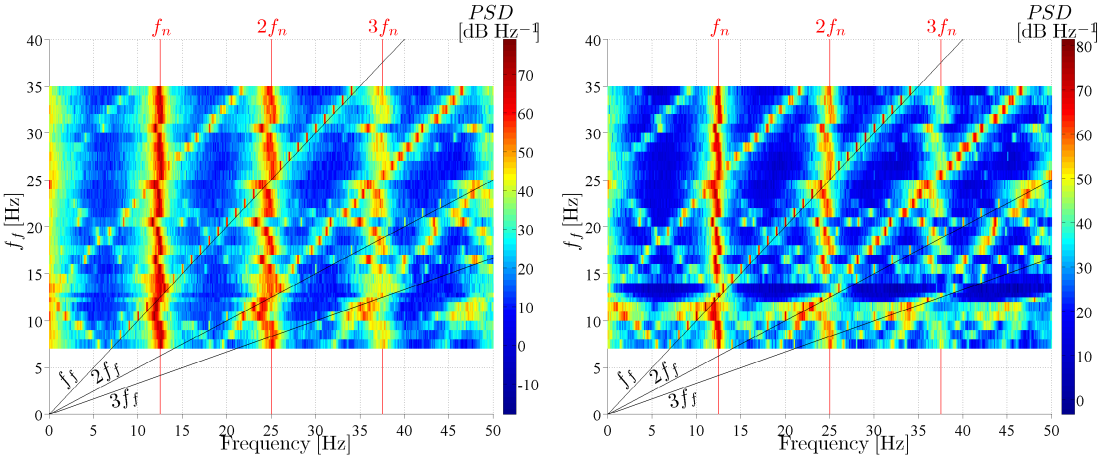

(a) $A = 0.10$

(b) $A = 0.30$

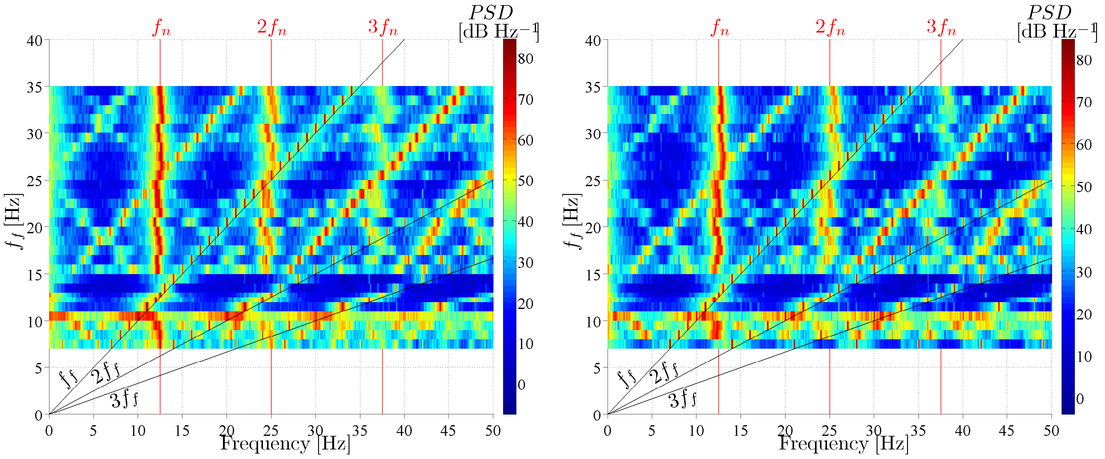

(c) $A = 0.50$

(d) $A = 0.70$

Figure H.1: Consolidated PSD for Flame 1 forced at four amplitudes: A = (a) 0.10, (b) 0.30, (c) 0.50, and (d) 0.70. The spectra are of the chemiluminescence at $x/d_1 = 10$.

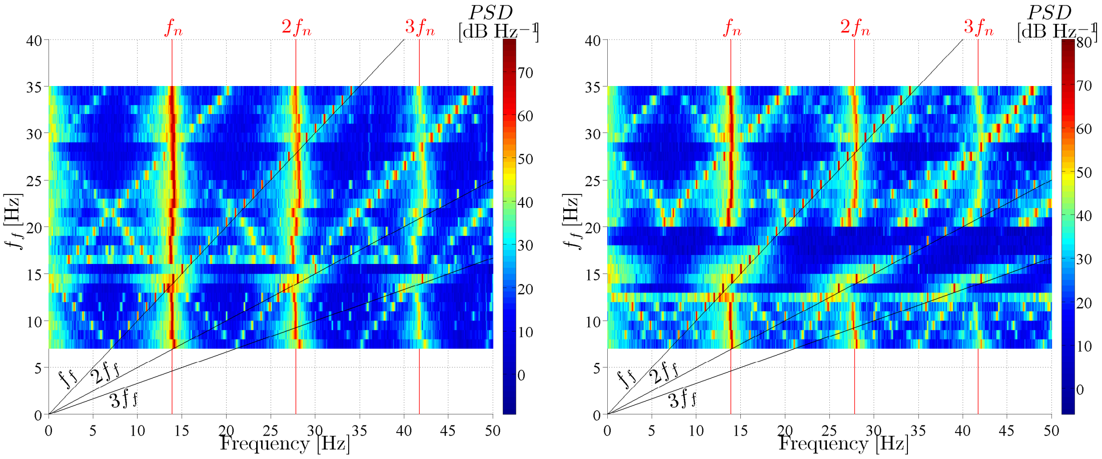

(a) $A = 0.10$ (b) $A = 0.30$

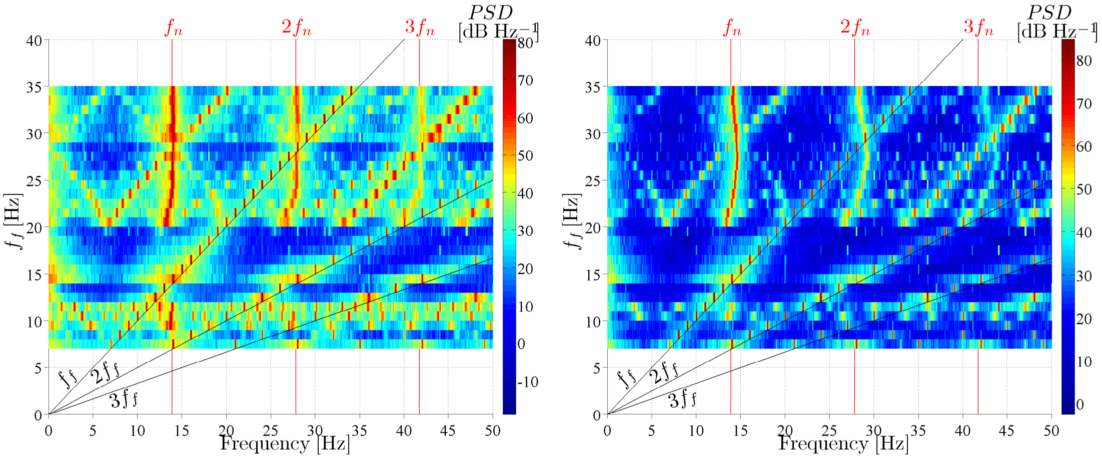

(c) $A = 0.50$ (d) $A = 0.70$

Figure H.2: Consolidated PSD for Flame 2 forced at four amplitudes: A = (a) 0.10, (b) 0.30, (c) 0.50, and (d) 0.70. The spectra are of the chemiluminescence at $x/d_1 = 10$.

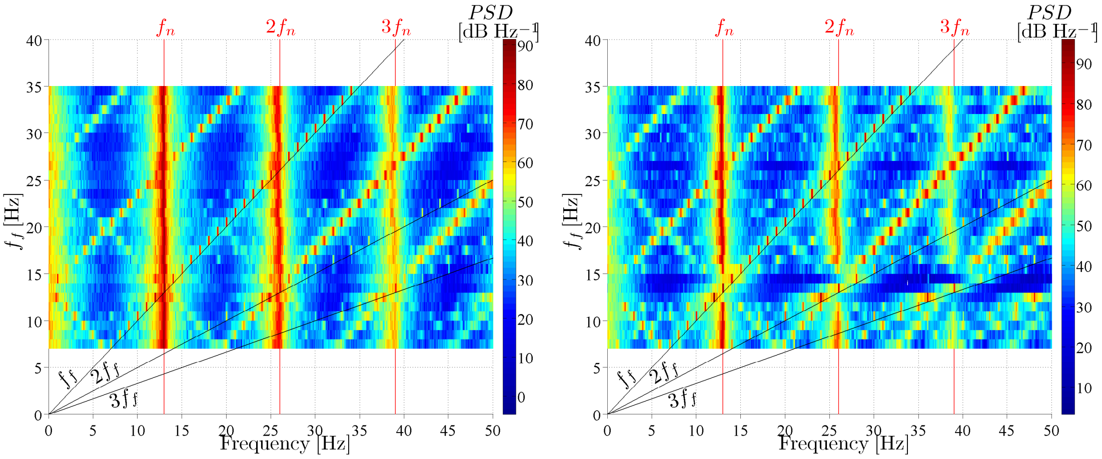

(a) $A = 0.10$ (b) $A = 0.30$

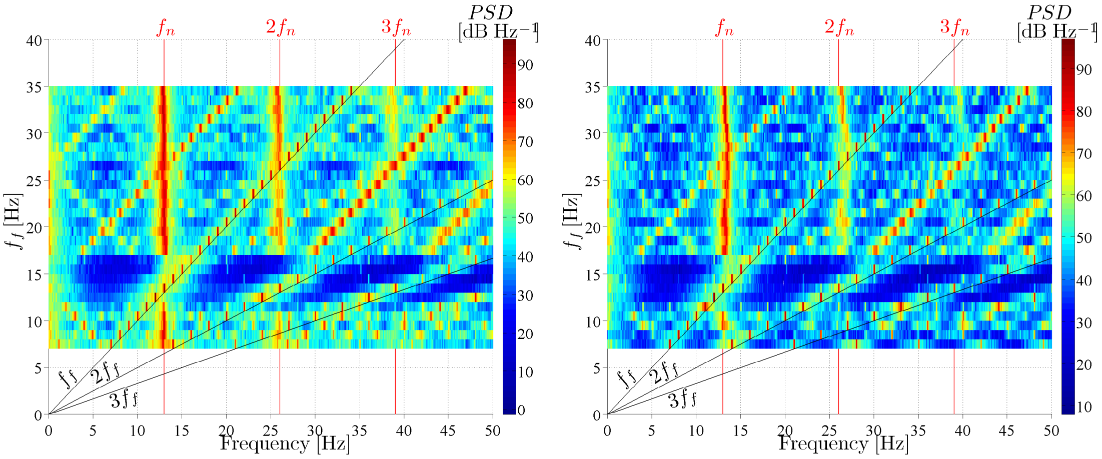

(c) $A = 0.50$ (d) $A = 0.70$

Figure H.3: Consolidated PSD for Flame 3 forced at four amplitudes: A = (a) 0.10, (b) 0.30, (c) 0.50, and (d) 0.70. The spectra are of the chemiluminescence at $x/d_1 = 10$.

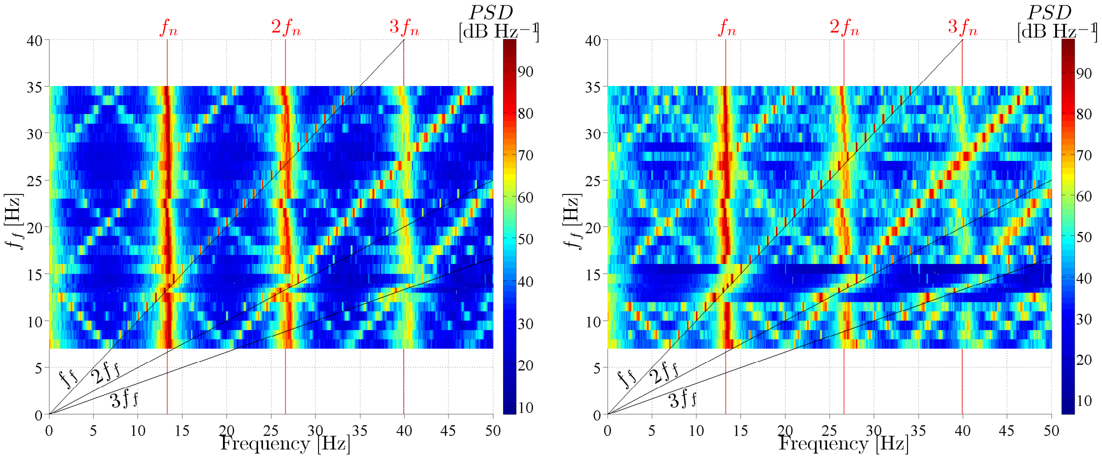

(a) $A = 0.10$ (b) $A = 0.30$

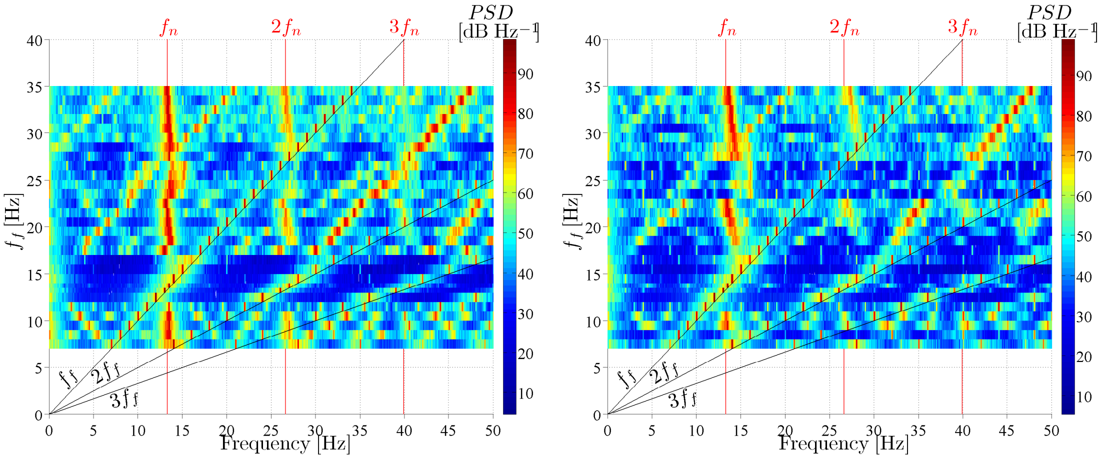

(c) $A = 0.50$ (d) $A = 0.70$

Figure H.4: Consolidated PSD for Flame 4 forced at four amplitudes: A = (a) 0.10, (b) 0.30, (c) 0.50, and (d) 0.70. The spectra are of the chemiluminescence at $x/d_1 = 10$.

Appendix I

Phase portraits for Flame 6 forced at 13 Hz: $f_f/f_n = 0.91$

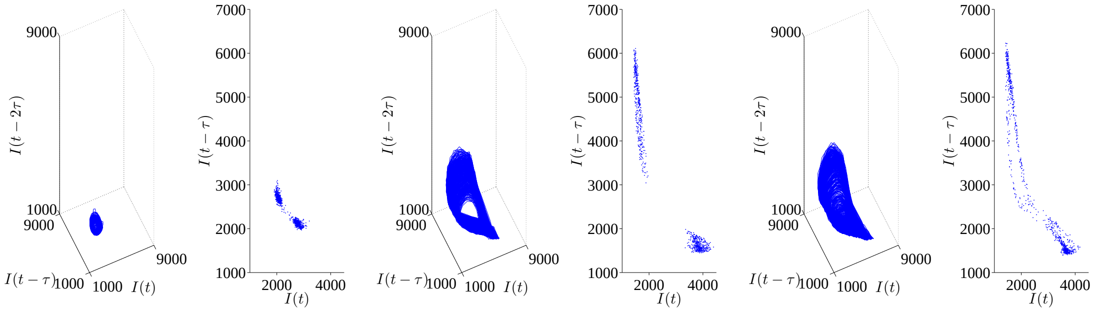

(a) $A = 0$ (b) $A = 0.05$ (c) $A = 0.10$

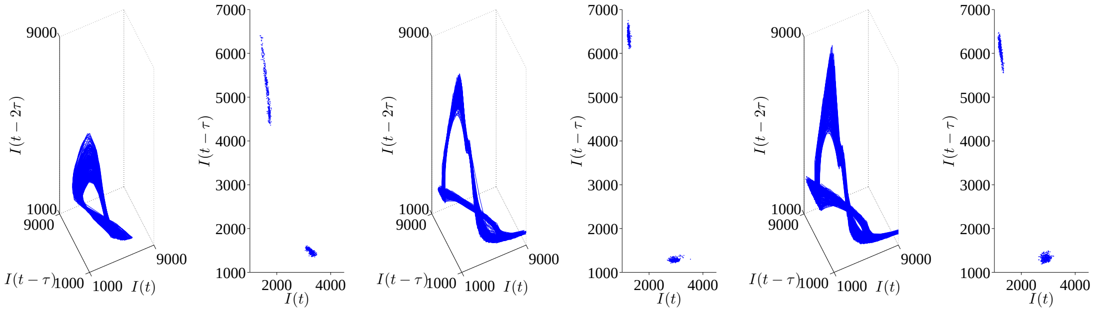

(d) $A = 0.15$ (e) $A = 0.20$ (f) $A = 0.25$

Figure I.1: Phase portraits (left) and Poincaré maps (right) for Flame 6 forced at 13 Hz ($f_f/f_n = 0.91$) with five amplitudes, plus the unforced case, all at $x/d_1 = 10$.

Appendix J

Applicability of local data to the flame body

Although the data shown in figure 4.24b are from just one axial station ($x/d_1 = 10$), their major features are seen throughout the flame body. For example, figure J.1 shows the local response of Flame 5 at $A = A_{loc}$ as a function of x/d_1 for three values of f_f: one slightly above the first subharmonic, $f_f = 8$ Hz or $f_f/(f_n/2) = 1.09$; one slightly above the fundamental, $f_f = 16$ Hz or $f_f/f_n = 1.09$; and one slightly below the fundamental, $f_f = 14$ Hz or $f_f/f_n = 0.95$. The absolute response $I'_{rms,\,loc}$ is shown in subfigure (a), the normalised response[1] $I'_{rms,\,loc}/I'_{rms,\,unf}$ is shown in subfigure (b), and the mean response $\overline{I}$ is shown in subfigure (c).

All three responses vary along the flame length for each individual f_f, but the relative trends between them do not. For lock-in around the fundamental ($f_f = 14$ and 16 Hz), the absolute response has an axial profile resembling that of the unforced response: it starts off weak but increases to a peak at $x/d_1 \approx 14.5$ before decreasing and then increasing again, albeit less steeply at the end. An inspection of the high-speed videos shows that the location of that peak corresponds to the roll-up of toroidal vortices. These coherent structures, Lingens et al. (1996b) have shown, periodically distort the flame, causing a weak response (thin reaction zone) in regions of high stretch and a strong response (thick reaction zone) in regions of low stretch. For lock-in around the subharmonic ($f_f = 8$ Hz), the absolute response starts off weaker than that for the other values of f_f, peaking farther downstream and with a lower amplitude, before levelling off. Eventually, though, it rises again, over $23 \leq x/d_1 \leq 29$, this time to a much higher value.

The normalised responses arising from the above behaviour are consistent

---

[1] This is normalised with respect to the unforced response at the same x/d_1.

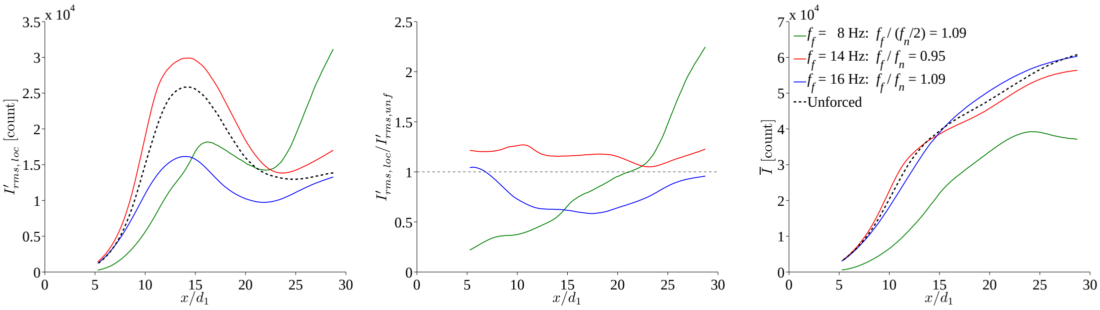

(a) Absolute response (b) Normalised response (c) Mean response

Figure J.1: Axial variation of the oscillation amplitude of Flame 5 at the onset of lock-in for three values of f_f: (a) absolute response, (b) normalised response, and (c) mean response. Data at $x/d_1 < 5.3$ are not shown because the SNR there is inadequate.

with the major features of the local data at $x/d_1 = 10$ (figure 4.24b). There are, nevertheless, notable exceptions at either ends of the image limits. Far upstream ($5 \leq x/d_1 \leq 7$), the normalised response for $f_f/f_n = 1.09$ is not yet below unity. This upstream region is where the chemiluminescent intensity is weakest and the SNR only marginal, making the data here the least reliable. Far downstream ($23 \leq x/d_1 \leq 29$), the normalised response for $f_f/(f_n/2) = 1.09$ is much greater than unity. This downstream region is where saturation of the image sensor is most severe – evidence of which can be detected in the mean response – which introduces an unknown bias to the data. These exceptions aside, however, the major features of the local data at $x/d_1 = 10$ (figure 4.24b) are seen throughout the flame body: $7 \leq x/d_1 \leq 23$.

Appendix K

Local FDF for Flames 1–4

This appendix starts on the next page.

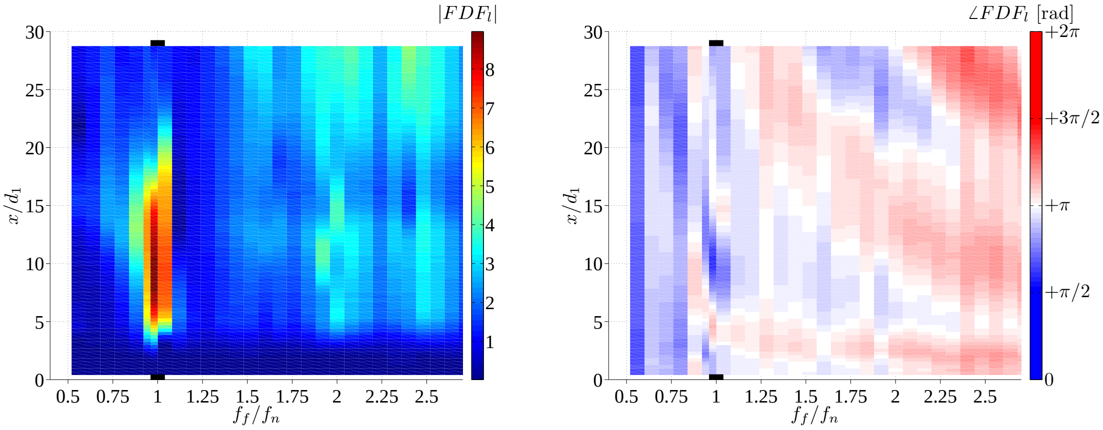

(a) $A = 0.10$

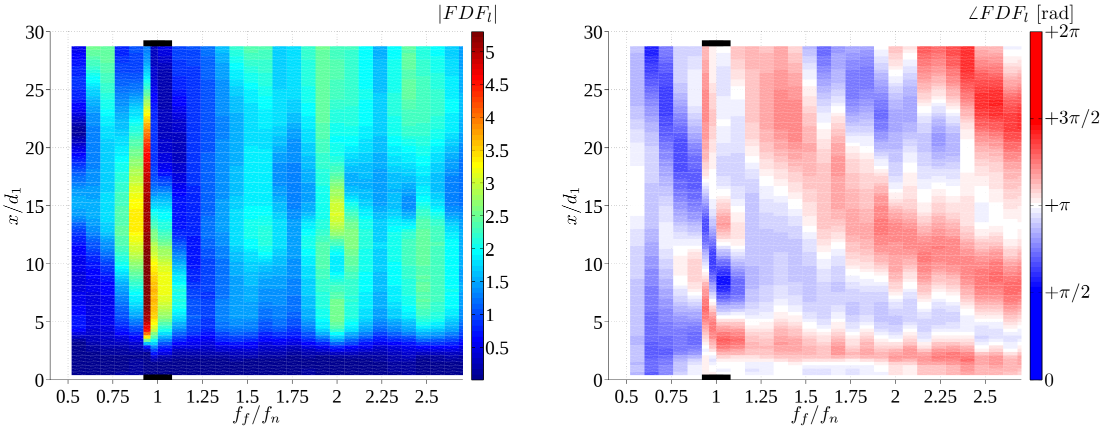

(b) $A = 0.30$

Figure K.1: Gain and phase of the local FDF for Flame 1 forced at four amplitudes: $A =$ (a) 0.10, (b) 0.30, (c) 0.50, and (d) 0.70. The data are shown as a function of downstream distance: $0 \leq x/d_1 \leq 29$. The frequencies at which there is lock-in are indicated by the black horizontal bars at the top and bottom of the plots. (Continued on next page)

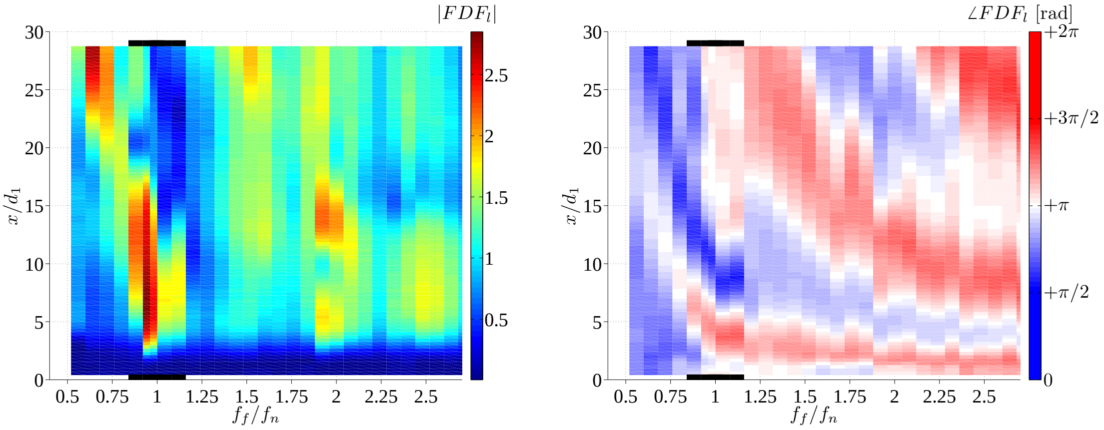

(c) $A = 0.50$

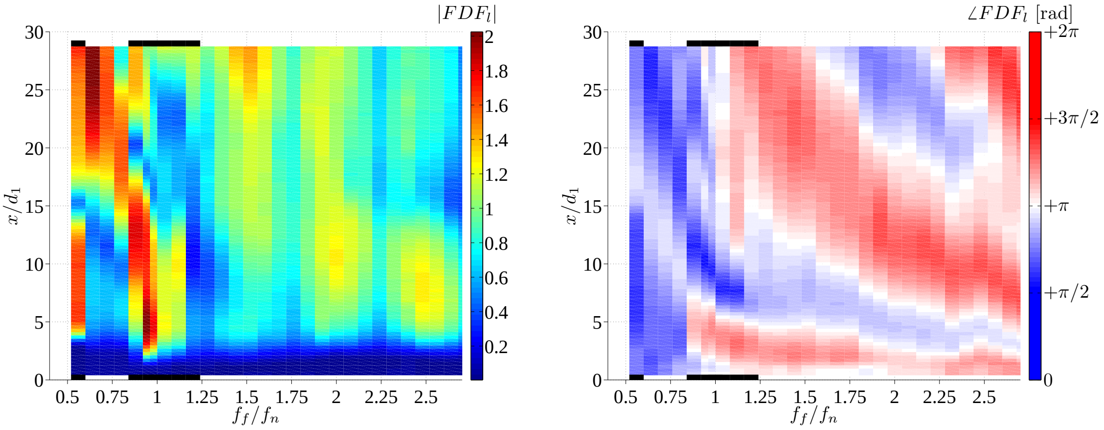

(d) $A = 0.70$

Figure K.1: Continued from previous page.

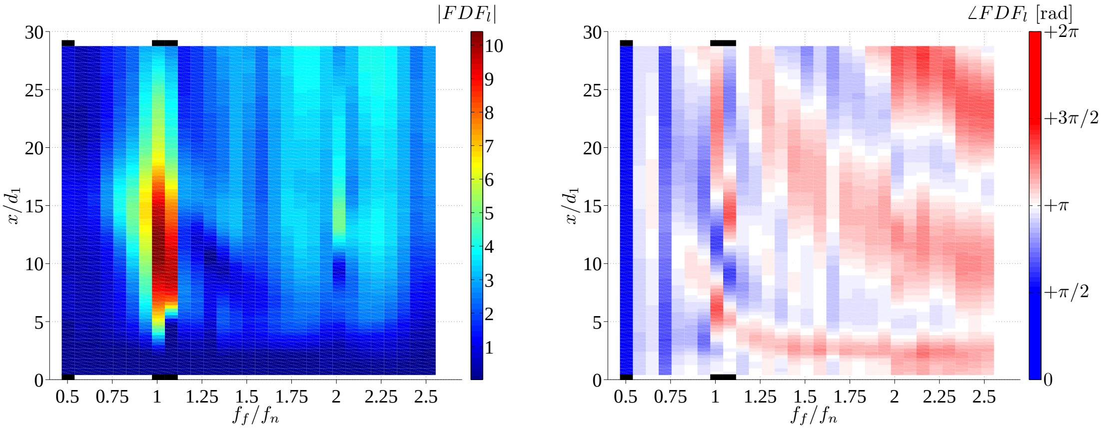

(a) $A = 0.10$

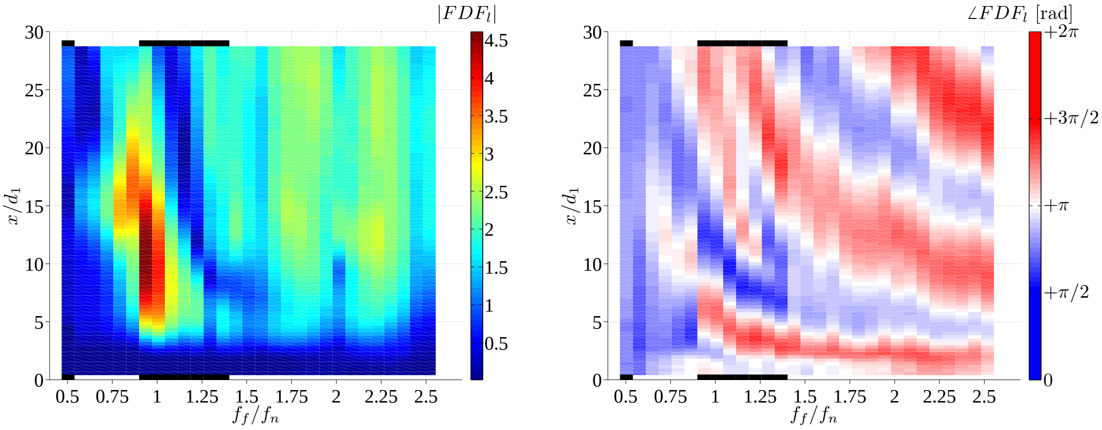

(b) $A = 0.30$

Figure K.2: Gain and phase of the local FDF for Flame 2 forced at four amplitudes: $A =$ (a) 0.10, (b) 0.30, (c) 0.50, and (d) 0.70. The data are shown as a function of downstream distance: $0 \leq x/d_1 \leq 29$. The frequencies at which there is lock-in are indicated by the black horizontal bars at the top and bottom of the plots. (Continued on next page)

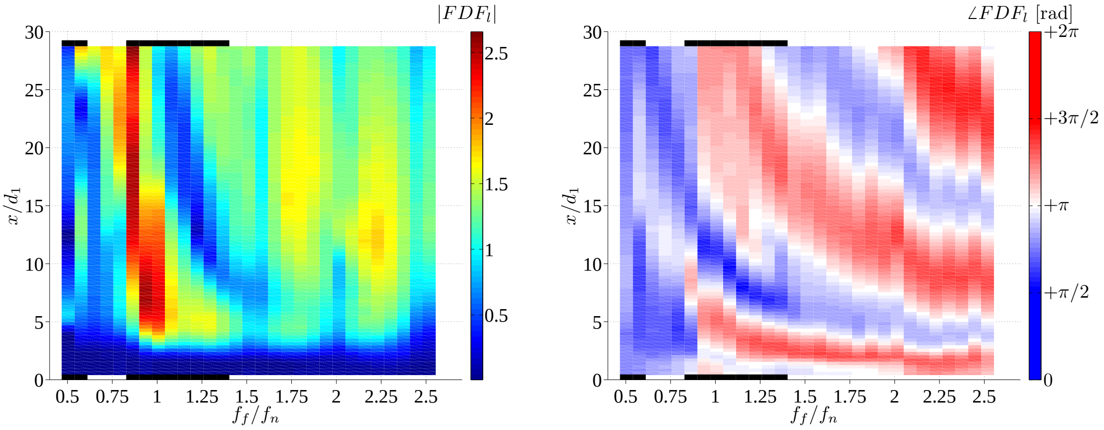

(c) $A = 0.50$

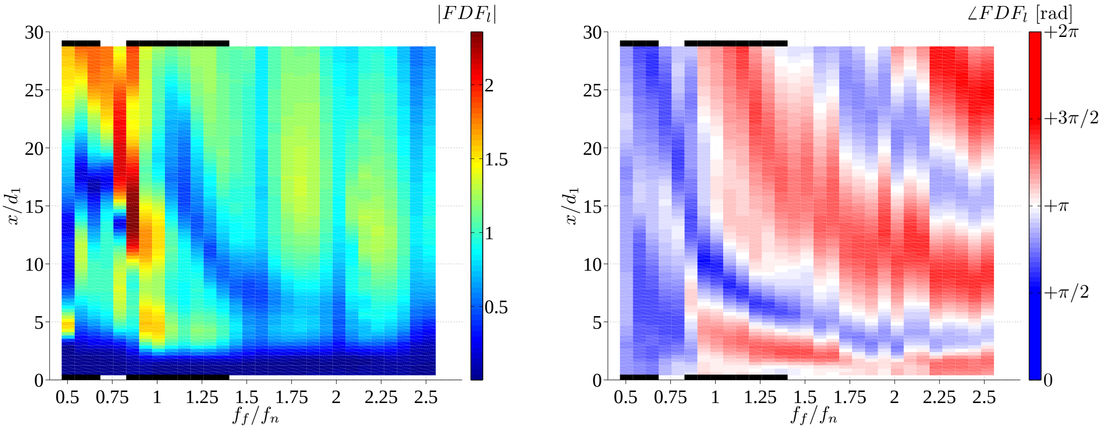

(d) $A = 0.70$

Figure K.2: Continued from previous page.

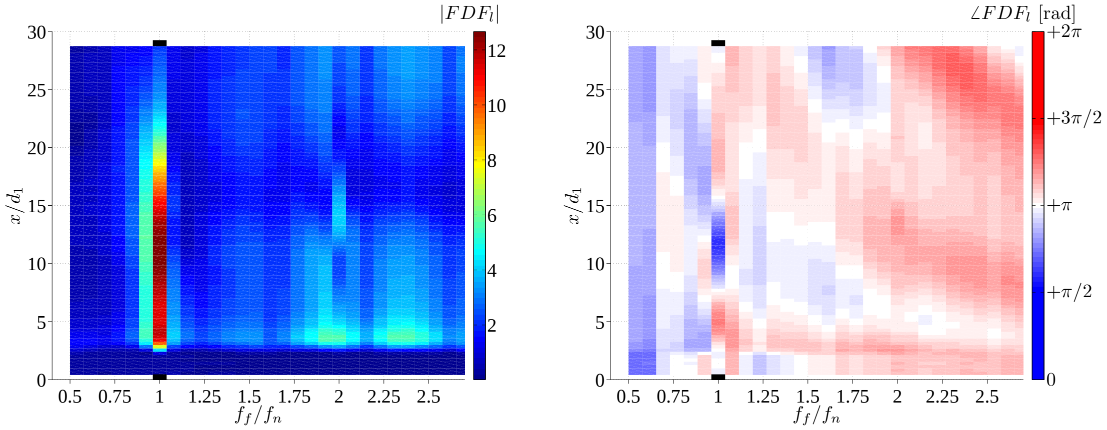

(a) $A = 0.10$

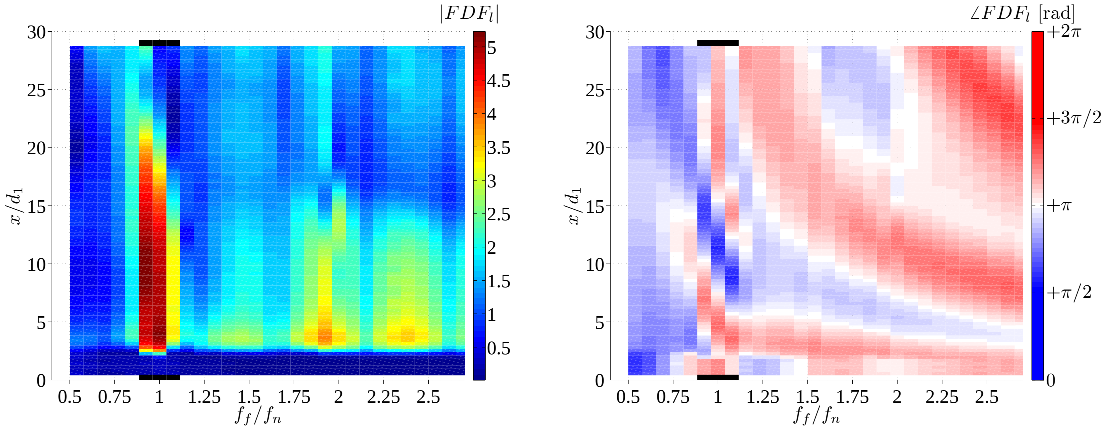

(b) $A = 0.30$

Figure K.3: Gain and phase of the local FDF for Flame 3 forced at four amplitudes: $A =$ (a) 0.10, (b) 0.30, (c) 0.50, and (d) 0.70. The data are shown as a function of downstream distance: $0 \leq x/d_1 \leq 29$. The frequencies at which there is lock-in are indicated by the black horizontal bars at the top and bottom of the plots. (Continued on next page)

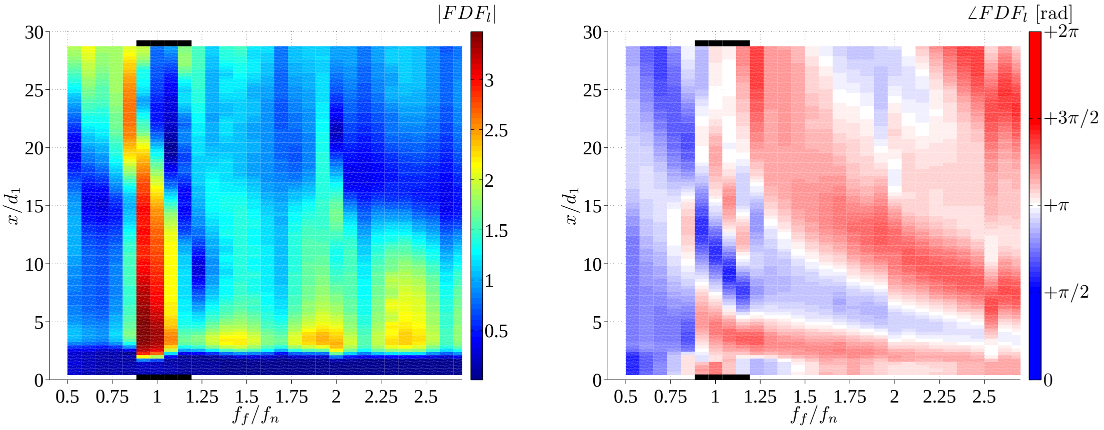

(c) $A = 0.50$

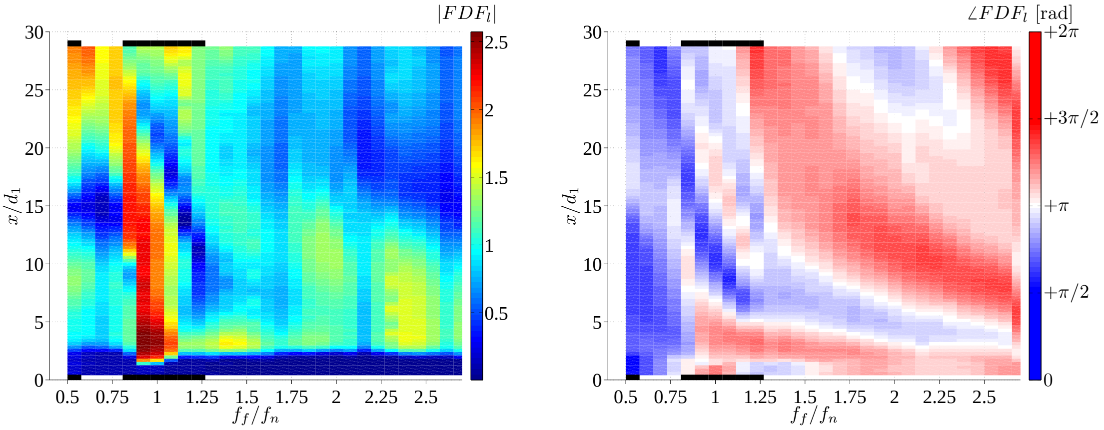

(d) $A = 0.70$

Figure K.3: Continued from previous page.

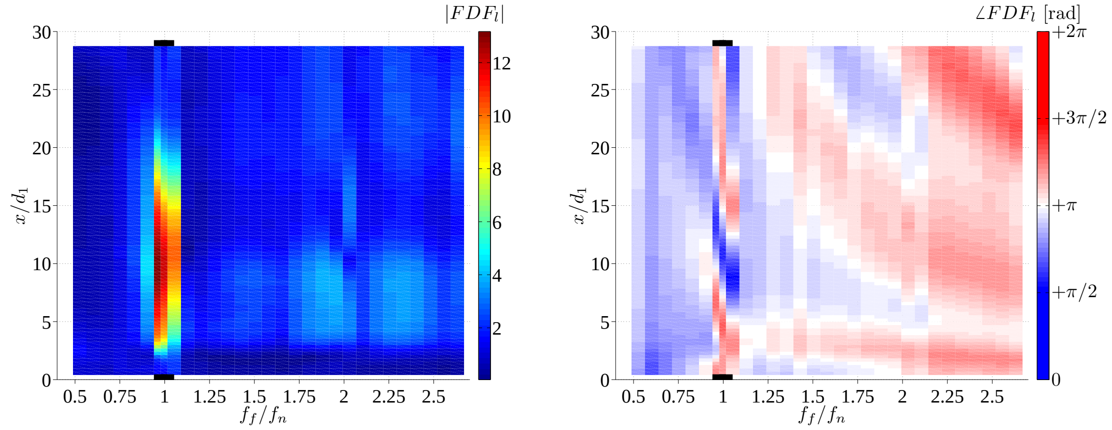

(a) $A = 0.10$

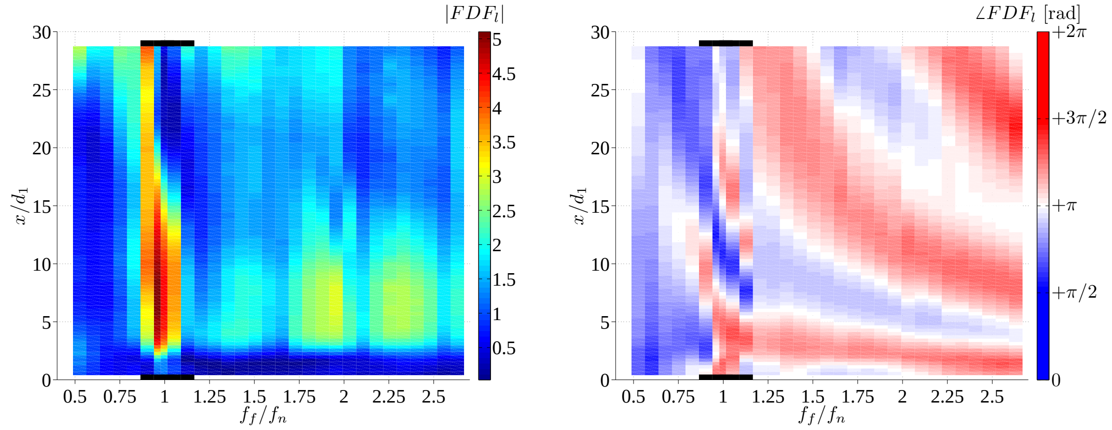

(b) $A = 0.30$

Figure K.4: Gain and phase of the local FDF for Flame 4 forced at four amplitudes: $A =$ (a) 0.10, (b) 0.30, (c) 0.50, and (d) 0.70. The data are shown as a function of downstream distance: $0 \leq x/d_1 \leq 29$. The frequencies at which there is lock-in are indicated by the black horizontal bars at the top and bottom of the plots. (Continued on next page)

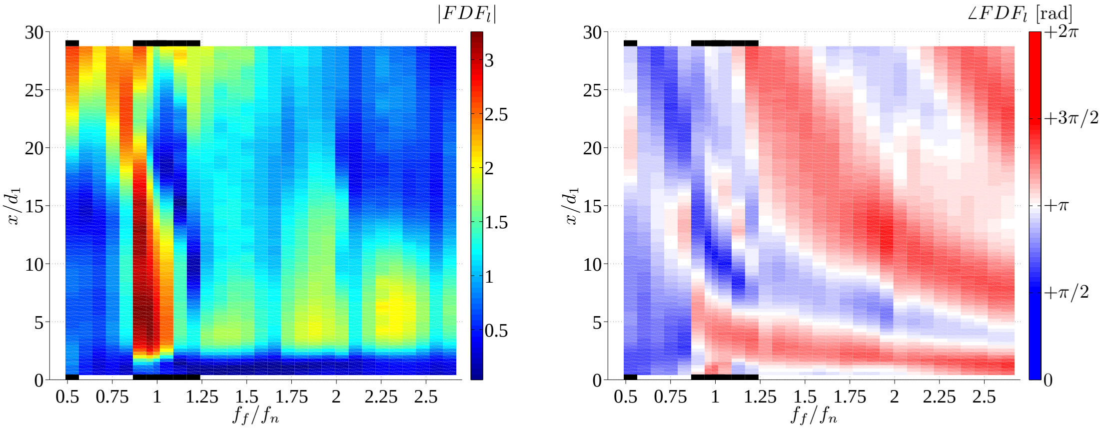

(c) $A = 0.50$

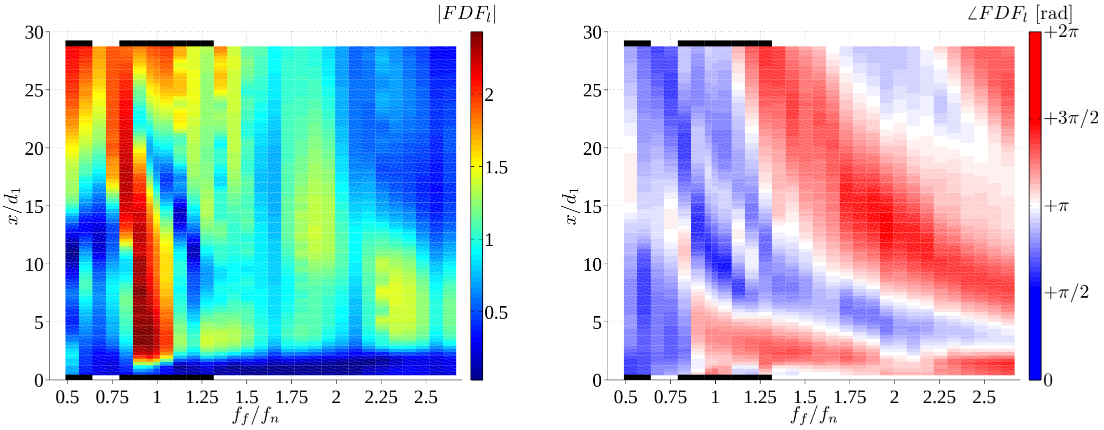

(d) $A = 0.70$

Figure K.4: Continued from previous page.

References

H.D.I Abarbanel. *Analysis of Observed Chaotic Data*. Springer–Verlag, New York, NY, USA, 1996. 67, 79, 100

R.B. Abernethy, R.P. Benedict, and R.B. Dowdell. Asme measurement uncertainty. *J. Fluid Eng. – T. ASME*, 107(2):161–164, 1985. 53

M. Abom and H. Boden. Error analysis of two-microphone measurements in ducts with flow. *J. Acoust. Soc. Am.*, 83(6):2429–2438, 1988. 57

K.R. Anderson, J. Hertzberg, and S. Mahalingam. Classification of absolute and convective instabilities in premixed bluff body stabilized flames. *Combust. Sci. Technol.*, 112(1):257–269, 1996. 140

A.M. Annaswamy, M. Fleifil, J.W. Rumsey, R. Prasmanth, J.P. Hathout, and A.F. Ghoniem. Thermoacoustic instability: model-based optimal control designs and experimental validation. *IEEE T. Contr. Syst. T.*, 8(6):905–918, 2000. 10

D.R. Arcas and L.G. Redekopp. Aspects of wake vortex control through base blowing/suction. *Phys. Fluids*, 16(2):452–456, 2004. 19

E. Awad and F.E.C. Culick. On the existence and stability of limit cycles for longitudinal acoustic modes in a combustion chamber. *Combust. Sci. Technol.*, 46(3–6):195–222, 1986. 41

S.J. Baek and H.J. Sung. Quasi-periodicity in the wake of a rotationally oscillating cylinder. *J. Fluid Mech.*, 408:275–300, 2000. 30, 37

S. Bagheri, P. Schlatter, P.J. Schmid, and D.S. Henningson. Global stability of a jet in crossflow. *J. Fluid Mech.*, 624:33–44, 2009. 37

R. Balachandran, B.O. Ayoola, C.F. Kaminski, A.P. Dowling, and E. Mastorakos. Experimental investigation of the nonlinear response of turbulent premixed flames to imposed inlet velocity oscillations. *Combust. Flame*, 143(1–2):37–55, 2005. 8

K. Balasubramanian and R.I. Sujith. Non-normality and nonlinearity in combustionacoustic interaction in diffusion flames. *J. Fluid Mech.*, 594:29–57, 2008. 6, 7, 126

F.Z. Batarseh, M. Gnir, I.V. Roisman, and C. Tropea. Fluctuations of a spray generated by an airblast atomizer. *Exp. Fluids*, 46(6):1081–1091, 2009. 9

B.J. Bayly, S.A. Orszag, and T. Herbert. Instability mechanisms in shear-flow transition. *Annu. Rev. Fluid Mech.*, 20:359–391, 1988. 9

B.D. Bellows, A. Hreiz, and T. Lieuwen. Nonlinear dynamics of an unstable swirl combustor: frequency locking and open loop control. In *Proceedings of the International Colloquium on the Dynamics of Explosions and Reactive Systems*, Montreal, Canada, 2005. 39

B.D. Bellows, A. Hreiz, and T. Lieuwen. Nonlinear interactions between driven and self-excited acoustic oscillations in a premixed combustor. In *44th AIAA Aerospace Sciences Meeting*. American Institute of Aeronautics and Astronautics, 2006. GT2006-0755. 39, 40

V. Bellucci, P. Flohr, C.O. Paschereit, and F. Magni. On the use of Helmholtz resonators for damping acoustic pulsations in industrial gas turbines. *J. Eng. Gas Turb. Power*, 126(2):271–275, 2004. 10

J.S. Bendat and A.G. Piersol. *Random Data: Analysis and Measurement Procedures*. Wiley-Interscience, New York, NY, USA, 2nd edition, 1986. 54

E. Berger and M. Schumm. Untersuchungen der instabilitaetsmechanismen im nachlauf von zylindern. Technical Report No. Be 343/18-1, Tech. University, Berlin, Germany, 1988. 20

A.L. Birbaud, D. Durox, S. Ducruix, and S. Candel. Dynamics of free jets submitted to upstream acoustic modulations. *Phys. Fluids*, 19(1):013602–19, 2007. 127

R.D. Blevins. *Flow-Induced Vibration.* Krieger Publishing Company, Malabar, FL, USA, 2nd edition, 2006. 35, 36, 41

F.S. Blomshield. Historical perspective of combustion instability in motors: case studies. *AIAA J.*, 2001. Paper No. 2001-3875. 3

R. Blonbou, A. Laverdant, S. Zaleski, and P. Kuentzmann. Active control of combustion instabilities in a Rijke tube using neural networks. *P. Combust. Inst.*, 28(1):747–755, 2000. 10

H. Boden and M. Abom. Influence of errors on the two-microphone method for measuring acoustic properties in ducts. *J. Acoust. Soc. Am.*, 79(2):541–549, 1986. 57

L. Boyer and J. Quinard. On the dynamics of anchored flames. *Combust. Flame*, 82(1):51–65, 1990. 8

R.J. Briggs. *Electron-Stream Interaction with Plasmas.* M.I.T. Press, Cambridge, MA, USA, 1964. 11

G.L. Brown and A. Roshko. On density effects and large structure in turbulent mixing layers. *J. Fluid Mech.*, 64(4):775–816, 1974. 8

H.H. Brunn. *Hot-Wire Anemometry: Principles and Signal Analysis.* Oxford University Press, Oxford, England, 1995. 53

S.M. Candel. Combustion instabilities coupled by pressure waves and their active control. *P. Combust. Inst.*, 24(1):1277–1296, 1992. 8

S.M. Candel. Combustion dynamics and control: progress and challenges. *P. Combust. Inst.*, 29(1):1–28, 2002. 8

J.H.E. Cartwright, V.M. Eguíluz, E. Hernández-García, and O. Piro. Dynamics of elastic excitable media. *Int. J. Bifurcat. Chaos*, 9(11):2197–2202, 1999. 30

M.L. Cartwright. Balthazar van der Pol. *J. London Math. Soc.*, 35(3):367–376, 1960. 30

S.R. Chakravarthy. Flow-acoustic-combustion lock-on in turbulent combustors. In *Indo-UK Advanced Instability Methods Workshop at IIT Madras*, Chennai, India, January 2010. 42

L.D. Chen, J.P. Seaba, W.M. Roquemore, and L.P. Goss. Buoyant diffusion flames. *P. Combust. Inst.*, 22(1):677–684, 1989. 27

N.A. Chigier. The atomization and burning of liquid fuel sprays. *Prog. Energ. Combust.*, 2(2):97–114, 1976. 9

S. Cho, J. Kim, and S. Lee. Characteristics of thermoacoustic oscillation in a ducted flame burner. In *36th AIAA Aerospace Sciences Meeting*. American Institute of Aeronautics and Astronautics, 1998. GT1998-0473. 63

J.M. Chomaz. Global instabilities in spatially developing flows: non-normality and nonlinearity. *Annu. Rev. Fluid Mech.*, 37:357–392, 2005. 31

J.M. Chomaz, P. Huerre, and L.G. Redekopp. Bifurcations to local and global modes in spatially developing flows. *Phys. Rev. Lett.*, 60(1):25–28, 1988. 17, 25, 142

B.T. Chu. On the energy transfer to small disturbances in fluid flow (Part I). *Acta. Mech.*, 1(3):215–234, 1964. 6

S.M. Correa. Power generation and aero-propulsion gas turbines: from combustion science to combustion technology. *P. Combust. Inst.*, 27(2):1793–1807, 1998. 3

L. Crocco and S.I. Cheng. Theory of combustion instability in liquid propellant rocket motors. Technical Report No. 0429886, Princeton University, 1956. 3

S.C. Crow and F.H. Champagne. Orderly structure in jet turbulence. *J. Fluid Mech.*, 48(3):547–591, 1971. 22, 110

J.E. Crump, K.C. Schadow, V. Yang, and F.E.C. Culick. Longitudinal combustion instabilities in ramjet engines: identification of acoustic modes. *J. Propul. Power*, 2(2):105–109, 1986. 3

F.E.C. Culick. Non-linear growth and limiting amplitude of acoustic oscillations in combustion chambers. *Combust. Sci. Technol.*, 3(1):1–16, 1971. 32

F.E.C. Culick. Nonlinear behavior of acoustic waves in combustion chambers: Ii. *Acta Astronaut.*, 3(9–10):735–757, 1976. 6

F.E.C. Culick. A note on Rayleigh's criterion. *Combust. Sci. Technol.*, 56(4–6): 159–166, 1987. 7

F.E.C. Culick. Unsteady Motions in Combustion Chambers for Propulsion Systems. North Atlantic Treaty Organisation, 2006. AGARDograph AG-AVT-039. 4, 31, 32

A. Cuoci, A. Frassoldati, T. Faravelli, and E. Ranzi. Soot formation in unsteady counterflow diffusion flames. *P. Combust. Inst.*, 32(1):1335–1342, 2009. 27

D. Daugherty, T. Roque-Urrea, J. Urrea-Roque, J. Troyer, S. Wirkus, and M.A. Porter. Mathematical models of bipolar disorder. *Commun. Nonlinear Sci.*, 14 (7):2897–2908, 2009. 30

H.T. Davis. *Nonlinear Differential and Integral Equations.* Dover Publications, Mineola, NY, USA, 2nd edition, 1962. 34

J. Davitian, D. Getsinger, C. Hendrickson, and A.R. Karagozian. Transition to global instability in transverse-jet shear layers. *J. Fluid Mech.*, 661:294–315, 2010. 15, 37, 38, 87

P.J. Dines. *Active Control of Flame Noise.* PhD thesis, University of Cambridge, Department of Engineering, 1983. 10

G. Dixon-Lewis, T. David, G.H. Gaskell, S. Fukutani, H. Jinno, J.A. Miller, R.J. Kee, M.D. Smooke, N. Peters, E. Effelsberg, J. Warnatz, and F. Behrendt.

Calculation of the structure and extinction limit of a methane–air counterflow diffusion flame in the forward stagnation region of a porous cylinder. *P. Combust. Inst.*, 20(1):1893–1904, 1985. 92

A.P. Dowling. Nonlinear self-excited oscillations of a ducted flame. *J. Fluid Mech.*, 346:271–290, 1997. 7

A.P. Dowling and J.E. Ffowcs-Williams. *Sound and Sources of Sound*. John Wiley & Sons, New York, NY, USA, 1983. 4

A.P. Dowling and A.S. Morgans. Feedback control of combustion oscillations. *Annu. Rev. Fluid Mech.*, 37:151–182, 2005. 10

P.G. Drazin and W.H. Reid. *Hydrodynamic Stability*. Cambridge Mathematical Library. Cambridge University Press, Cambridge, England, 2nd edition, 2004. 29

D.F.G. Durao and J.H. Whitelaw. Instantaneous velocity and temperature measurements in oscillating diffusion flames. *Proc. R. Soc. Lond. A*, 338:479–501, 1974. 26

D. Durox, T. Yuan, F. Baillot, and J.M. Most. Premixed and diffusion flames in a centrifuge. *Combust. Flame*, 102:501–511, 1995. 28

D. Durox, T. Yuan, and E. Villermaux. The effect of buoyancy on flickering in diffusion flames. *Combust. Sci. Technol.*, 124:277–294, 1997. 28

D. Durox, T. Schuller, N. Noiray, and S. Candel. Experimental analysis of nonlinear flame transfer functions for different flame geometries. *P. Combust. Inst.*, 32(1):1391–1398, 2008. 124

J.D. Eldredge and A.P. Dowling. The absorption of axial acoustic waves by a perforated liner with bias flow. *J. Fluid Mech.*, 485:307–335, 2003. 10

Y.C. Fang and J.M. Chen. Experimental study of vortex shedding and subharmonic lock-on for a rotationally oscillating flat plate. *J. Wind Eng. Ind. Aerod.*, 84(2):163–180, 2000. 35

Z. Faragó and N.A. Chigier. Morphological classification of disintegration of round liquid jets in a coaxial air stream. *Atomization Spray*, 2(2):137–153, 1992. 9

T.H. Fay. The forced van der Pol equation. *Internat. J. Math. Ed. Sci. Tech.*, 40 (5):669–677, 2009. 30

R. Fitzhugh. Impulses and physiological states in theoretical models of nerve membranes. *Biophys. J.*, 1(6):445–466, 1961. 30

M. Füri, P. Papas, R.M. Rais, and P.A. Monkewitz. The effect of flame position on the Kelvin–Helmholtz instability in non-premixed jet flames. *P. Combust. Inst.*, 29(2):1653–1661, 2002. 49

N.L. Garland and D.R. Crosley. On the collisional quenching of electronically excited OH, NH and CH in flames. *P. Combust. Inst.*, 21(1):1693–1702, 1988. 64

A.G. Gaydon. *Spectroscopy of Flames*. Chapman and Hall, London, England, 1974. 62

A.V. Getling. *Rayleigh–Bénard Convection: Structures and Dynamics*. Advanced Series in Nonlinear Dynamics. World Scientific Publishing Company, Hackensack, NJ, USA, 1997. 11

F. Giannetti and P. Luchini. Structural sensitivity of the first instability of the cylinder wake. *J. Fluid Mech.*, 581:167–197, 2007. 28

H. Gotoda and T. Ueda. Transition from periodic to non-periodic motion of a bunsen-type premixed flame tip with burner rotation. *P. Combust. Inst.*, 29 (1):1503–1509, 2002. 67

P. Grassberger and I. Procaccia. Characterization of strange attractors. *Phys. Rev. Lett.*, 50(5):346–349, 1983. 67

S.I. Green. Introduction to vorticity. In S.I. Green, editor, *Fluid Vortices*, Fluid Mechanics and its Applications, chapter 1. Kluwer Academic Publishers, Dordrecht, Netherlands, 1995. 21

E.J. Gutmark, K.C. Schadow, M.N.R. Nina, and G.P.A. Pita. Suppression of combustion instability by geometrical design of the bluff-body stabilizer. *J. Propul. Power*, 11(3):456–463, 1995. 10

D.L. Gysling, G.S. Copeland, D.C. McCormick, and W.M. Proscia. Combustion system damping augmentation with Helmholtz resonators. *J. Eng. Gas Turb. Power*, 122(2):269–274, 2000. 10

M.P. Hallberg and P.J. Strykowski. On the universality of global modes in low-density axisymmetric jets. *J. Fluid Mech.*, 569:493–507, 2006. 72

M.P. Hallberg and P.J. Strykowski. Open-loop control of fully nonlinear self-excited oscillations. *Phys. Fluids*, 20(4):041703–4, 2008. 35

M.P. Hallberg, V. Srinivasan, P. Gorse, and P.J. Strykowski. Suppression of global modes in low-density axisymmetric jets using coflow. *Phys. Fluids*, 19 (1):014102–10, 2007. 55

K. Hannemann and H. Oertel Jr. Numerical simulation of the absolutely and convectively unstable wake. *J. Fluid Mech.*, 199:55–88, 1989. 20, 142

Y. Hardalupas and A. Selbach. Imposed oscillations and non-premixed flames. *Prog. Energ. Combust.*, 28(1):75–104, 2002. 63

D.J. Harrje and F.H. Reardon. Liquid propellant rocket instability. Technical Report SP-194, NASA, 1972. 3

U. Hegde, L. Zhou, and M.Y. Bahadori. The transition to turbulence of microgravity gas jet diffusion flames. *Combust. Sci. Technol.*, 102:95–113, 1994. 26

H. Helmholtz. On the discontinuous movements of fluids. *Reports of the Royal Prussian Academy of Philosophy in Berlin*, 23:215–228, 1868. 8

B. Henry, N. Lovell, and F. Camacho. Nonlinear dynamics time series analysis. In M. Akay, editor, *Nonlinear Biomedical Signal Processing: Dynamic analysis and modeling*, IEEE Engineering in Medicine and Biology Society, chapter 1. Wiley–IEEE Press, New York, NY, USA, 2000. 67

B. Higgins. On the sound produced by a current of hydrogen gas passing through a tube. *J. Nat. Phil. Chem. and the Arts*, 1:129–131, 1802. 2

C.M. Ho and P. Huerre. Perturbed free shear layers. *Annu. Rev. Fluid Mech.*, 16:365–424, 1984. 109

M.S. Howe. *Acoustics of Fluid-Structure Interactions*, chapter 6. Cambridge University Press, Cambridge, England, 2008. 8

Y. Huang and V. Yang. Dynamics and stability of lean-premixed swirl-stabilized combustion. *Prog. Energ. Combust.*, 35(4):293–364, 2009. 3

P. Huerre. Open shear flow instabilities. In G.K. Batchelor, H.K. Moffatt, and M.G. Worster, editors, *Perspectives in Fluid Dynamics: A Collective Introduction to Current Research*, chapter 4. Cambridge University Press, Cambridge, England, 2000. 11

P. Huerre and P.A. Monkewitz. Local and global instabilities in spatially developing flows. *Annu. Rev. Fluid Mech.*, 22:473–537, 1990. 15, 25, 45, 110

P. Huerre and M. Rossi. Hydrodynamic instabilities in open flows. In C. Godréche and P. Manneville, editors, *Hydrodynamics and Nonlinear Instabilities*, chapter 2. Cambridge University Press, Cambridge, England, 1998. 24

I.R. Hurle, R.B. Price, T.M. Sugden, and A. Thomas. Sound emission from open turbulent premixed flames. *P. Roy. Soc. A - Math Phy.*, 303(1475):409–427, 1968. 63

A. Hurwitz. On the conditions under which an equation has only roots with negative real parts. In R.E. Bellman and R. Kalaba, editors, *Selected Papers on Mathematical Trends in Control Theory*, pages 72–82. Dover Publications, Mineola, NY, USA, 1964. Translated from German by H.G. Bergman. 41

A.K.M.F. Hussain and K.B.M.Q. Zaman. The free shear layer tone phenomenon and probe interference. *J. Fluid Mech.*, 87(2):349–383, 1978. 16

O. Inoue. A new approach to flow problems past a porous plate. *AIAA J.*, 23: 1916–1921, 1985. 19, 20

C.C. Jahnke and F.E.C. Culick. Application of dynamical systems theory to nonlinear combustion instabilities. *J. Propul. Power*, 10(4):508–517, 1994. 32

S. Jendoubi and P.J. Strykowski. Absolute and convective instability of axisymmetric jets with external flow. *Phys. Fluids*, 6(9):3000–3009, 1994. 25

A. Johnson, M. Uddin, and A. Pollard. Calibration of hot-wire probes using non-uniform mean velocity profiles. *Exp. Fluids*, 39(3):525–532, 2005. 55

D.W. Jordan and P. Smith. *Nonlinear Ordinary Differential Equations*. Oxford University Press, Oxford, England, 4th edition, 2007. 133

M.P. Juniper. Triggering in the horizontal Rijke tube: non-normality, transient growth and bypass transition. *J. Fluid Mech.*, 667:272–308, 2011. 32

M.P. Juniper, L.K.B. Li, and J.W. Nichols. Forcing of self-excited round jet diffusion flames. *P. Combust. Inst.*, 32(1):1191–1198, 2009. 90

L. Kabiraj, R.I. Sujith, and P. Wahi. Experimental studies of bifurcations leading to chaos in a laboratory scale thermoacoustic system. In *Proceedings of ASME Turbo Expo*, Vancouver, BC, Canada, June 2011. ASME International Gas Turbine Institute. GT2011-46149. 29, 65

H. Kantz and T. Schreiber. *Nonlinear Time Series Analysis*. Cambridge University Press, Cambridge, England, 2nd edition, 2003. 67

V.R. Katta and W.M. Roquemore. On the structure of a stretched/compressed laminar flamelet: influence of preferential diffusion. *Combust. Flame*, 100(1–2): 61–70, 1995. 27, 96

J.J. Keller. Thermoacoustic oscillations in combustion chambers of gas turbines. *AIAA J.*, 33(12):2280–2287, 1995. 3

L.W.T. Kelvin. Hydrokinetic solutions and observations. *Philos. Mag.*, 42:362–377, 1871. 8

W. Koch. Local instability characteristics and frequency determination of self-excited wake flows. *J. Sound Vib.*, 99(1):53–83, 1985. 16, 142, 143

G.H. Koopmann. The vortex wakes of vibrating cylinders at low Reynolds numbers. *J. Fluid Mech.*, 28(3):501–512, 1967. 35, 36

W. Krebs, S. Bethke, J. Lepers, P. Flohr, B. Prade, C. Johnson, and S. Sattinger. Thermoacoustic design tools and passive control: Siemens power generation approaches. In T.C. Lieuwen and V. Yang, editors, *Combustion Instabilities in Gas Turbine Engines: Operational Experience, Fundamental Mechanisms, and Modeling*, Progress in Astronautics and Aeronautics, chapter 5. American Institute of Aeronautics and Astronautics, Reston, VA, USA, 2005. 1

C. Külsheimer and H. Büchner. Combustion dynamics of turbulent swirling flames. *Combust. Flame*, 131(1–2):70–84, 2002. 121

D.M. Kyle and K.R. Sreenivasan. The instability and breakdown of a round variable-density jet. *J. Fluid Mech.*, 249:619–664, 1993. 22, 55, 72, 82

L.D. Landau and E.M. Lifshitz. *Fluid Mechanics*, volume 6 of *Course of Theoretical Physics*. Pergamon Press, Oxford, England, 2nd edition, 1959. 144

P.J. Langhorne. Reheat buzz: an acoustically coupled combustion instability, Part 1: experiment. *J. Fluid Mech.*, 193:417–443, 1988. 3, 63

J. Le Conte. Philosophical Magazine HP, 1858. 235. 2

A.H. Lefebvre. Airblast atomization. *Prog. Energ. Combust.*, 6(3):233–261, 1980. 9

A.H. Lefebvre. *Atomization and Sprays*. Hemisphere Publishing, New York, NY, USA, 1989. 9

S. Leibovich. The structure of vortex breakdown. *Annu. Rev. Fluid Mech.*, 10: 221–246, 1978. 8

I. Lekakis. Calibration and signal interpretation for single and multiple hot-wire/hot-film probes. *Meas. Sci. Technol.*, 7:1313–1333, 1996. 55

L. Lesshafft, P. Huerre, P. Sagaut, and M. Terracol. Nonlinear global modes in hot jets. *J. Fluid Mech.*, 554:393–409, 2006. 31

G.S. Lewis, B.J. Cantwell, U. Vandsburger, and C.T. Bowman. An investigation of the structure of a laminar non-premixed flame in an unsteady vortical flow. *P. Combust. Inst.*, 22(1):515–522, 1988. 27

L.K.B. Li, D.M. Dressler, S.I. Green, M.H. Davy, and D.T. Eadie. Experiments on air-blast atomization of viscoelastic liquids, part 1: quiescent conditions. *Atomization Spray*, 19(1):19–39, 2009. 9

T.C. Lieuwen. Experimental investigation of limit-cycle oscillations in an unstable gas turbine combustor. *J. Propul. Power*, 18(1):61–67, 2002. 66, 67

T.C. Lieuwen and K. McManus. That elusive hum. *Mech. Eng. Power*, pages 53–55, June 2002. ASME Publication. 31

T.C. Lieuwen and Y. Neumeier. Nonlinear pressure–heat release transfer function measurements in a premixed combustor. *P. Combust. Inst.*, 29(1):99–105, 2002. 39

T.C. Lieuwen and B.T. Zinn. The role of equivalence ratio oscillations in driving combustion instabilities in low NO_x gas turbines. *P. Combust. Inst.*, 27(2): 1809–1816, 1998. 9

T.C. Lieuwen, H. Torres, C. Johnson, and B.T. Zinn. A mechanism of combustion instability in lean premixed gas turbine combustors. *Trans. ASME*, 123:182–189, 2001. 3

A Lingens. *Instabitat von Diffusionsflammen.* PhD thesis, RWTH Aachen, 1995. 26

A. Lingens, K. Neemann, J. Meyer, and M. Schreiber. Instability of diffusion flames. *P. Combust. Inst.*, 26(1):1053–1061, 1996a. 26, 28

A. Lingens, M. Reeker, and M. Schreiber. Instability of buoyant diffusion flames. *Exp. Fluids*, 20:241–248, 1996b. 27, 28, 92, 96, 165

E.N. Lorenz. Deterministic nonperiodic flow. *J. Atmos. Sci.*, 20(2):130–148, 1963. 29

M.A. Macquisten and A.P. Dowling. Combustion oscillations in a twin-stream afterburner. *J. Sound Vib.*, 188(4):545–560, 1995. 3

C. Mathis, M. Provansal, and L. Boyer. The Bénard-von Kármán instability: an experimental study near the threshold. *J. Phys. Lett. - Paris*, 45:483–491, 1984. 48

K.I. Matveev and F.E.C. Culick. A model for combustion instability involving vortex shedding. *Combust. Sci. Technol.*, 175(6):1059–1083, 2003. 42, 43

T. Maxworthy. The flickering candle: transition to a global oscillation in a thermal plume. *J. Fluid Mech.*, 390:297–323, 1999. 27

K.R. McManus, T. Poinsot, and S.M. Candel. A review of active control of combustion instabilities. *Prog. Energ. Combust.*, 19(1):1–29, 1993. 10

K.R. McManus, B. Yip, and S.M. Candel. Emission and laser-induced fluorescence imaging methods in experimental combustion. *Exp. Therm. Fluid Sci.*, 10(4):486–502, 1995. 62

R.D. Mehta. Turbulent boundary layer perturbed by a screen. *AIAA J.*, 23(9): 1335–1342, 1985. 52

R.D. Mehta and P. Bradshaw. Design rules for small low speed wind tunnels. *Aeronaut. J.*, 83(827):443–449, 1979. 52

P. Meliga, D. Sipp, and J.M. Chomaz. Absolute instability in axisymmetric wakes: compressible and density variation effects. *J. Fluid Mech.*, 600:373–401, 2008. 25

M.N. Mikhail. Optimum design of wind tunnel contractions. *AIAA J.*, 17(5): 471–477, 1979. 51

P.A. Monkewitz. The absolute and convective nature of instability in two-dimensional wakes at low Reynolds numbers. *Phys. Fluids*, 31(5):999–1006, 1988. 17

P.A. Monkewitz and L.N. Nguyen. Absolute instability in the near-wake of two-dimensional bluff bodies. *J. Fluid Struct.*, 1:165–184, 1987. 142, 143

P.A. Monkewitz and K.D. Sohn. Absolute instability in hot jets and their control. In *10th AIAA Aeroacoustics Conference*, Seattle, WA, USA, July 1986. 70

P.A. Monkewitz and K.D. Sohn. Absolute instability in hot jets. *AIAA J.*, 26 (8):911–916, 1988. 21, 23, 70

P.A. Monkewitz, B. Lehmann, B. Barsikow, and D.W. Bechert. The spreading of self-excited hot jets by side jets. *Phys. Fluids A*, 1(3):446–448, 1989. 24

P.A. Monkewitz, D.W. Bechert, B. Barsikow, and B. Lehmann. Self-excited oscillations and mixing in a heated round jet. *J. Fluid Mech.*, 213:611–639, 1990. 22, 48, 77, 145

P.A. Monkewitz, P. Huerre, and J.M. Chomaz. Global linear stability analysis of weakly non-parallel shear flows. *J. Fluid Mech.*, 251:1–20, 1993. 23

T. Morel. Comprehensive design of axisymmetric wind tunnel contractions. *J. Fluid Eng. – T. ASME*, 97(2):225–233, 1975. 51

Y. Mori, K. Hijikata, and T. Nobuhara. A fundamental study of symmetrical vortex generation behind a cylinder by wake heating or by splitter plate or mesh. *Int. J. Heat Mass Tran.*, 29(8):1193–1201, 1986. 20

H.N. Najm, P.H. Paul, C.J. Mueller, and P.S. Wyckoff. On the adequacy of certain experimental observables as measurements of flame burning rate. *Combust. Flame*, 113(3):312–332, 1998. 63

A.H. Nayfeh and D.T. Mook. *Nonlinear Oscillations*. John Wiley & Sons, New York, NY, USA, 1995. 34

Y. Neumeier and B.T. Zinn. Experimental demonstration of active control of combustion instabilities using real time modes observation and secondary fuel injection. *P. Combust. Inst.*, 26(2):2811–2818, 1996. 10

J.W. Nichols, P.J. Schmid, and J.J. Riley. Self-sustained oscillations in variable-density round jets. *J. Fluid Mech.*, 582:341–376, 2007. 21

F. Nicoud and T. Poinsot. Thermoacoustic instabilities: should the Rayleigh criterion be extended to include entropy changes? *Combust. Flame*, 142(1–2): 153–159, 2005. 7

N. Noiray, D. Durox, T. Schuller, and S. Candel. Passive control of combustion instabilities involving premixed flames anchored on perforated plates. *P. Combust. Inst.*, 31(1):1283–1290, 2007. 10

E. Ott. *Chaos in Dynamical Systems*. Cambridge University Press, Cambridge, England, 2nd edition, 2002. 34

K.S. Pasumarthi and A.K. Agrawal. Schlieren measurements and analysis of concentration field in self-excited helium jets. *Phys. Fluids*, 15(12):3683–3692, 2003. 22

A.A. Peracchio and W.M. Proscia. Nonlinear heat-release/acoustic model for thermoacoustic instability in lean premixed combustors. *J. Eng. Gas Turb. Power*, 121(3):415–421, 1999. 3, 7

B. Pier. Open-loop control of absolutely unstable domains. *P. Roy. Soc. A - Math Phy.*, 459(2033):1105–1115, 2003. 15, 120

R. Pierrehumbert. Local and global baroclinic instability of zonally varying flow. *J. Atmos. Sci.*, 41(14):2141–2162, 1984. 142, 143

T. Poinsot and D. Veynante. *Theoretical and Numerical Combustion*. R.T. Edwards, Flourtown, PA, USA, 2nd edition, 2005. 7

T.J. Poinsot, A.C. Trouve, D.P. Veynante, S.M. Candel, and E.J. Esposito. Vortex-driven acoustically coupled combustion instabilities. *J. Fluid Mech.*, 177:265–292, 1987. 8

B.E. Poling, J.M. Prausnitz, and J.P. O'Connell. *The Properties of Gases and Liquids*. McGraw-Hill, New York, NY, USA, 5th edition, 2001. 92

S.B. Pope. *Turbulent Flows.* Cambridge University Press, Cambridge, England, 2000. 78

A. Powell. On the edgetone. *J. Acoust. Soc. Am.*, 33(4):395–409, 1961. 16

R.B. Price, I.R. Hurle, and T.M. Sugden. Optical studies of the generation of noise in turbulent flames. *P. Combust. Inst.*, 12(1):1093–1102, 1969. 63

M. Provansal, C. Mathis, and L. Boyer. Bénard-von Kármán instability: transient and forced regimes. *J. Fluid Mech.*, 182:1–22, 1987. 16, 34, 35, 36, 48, 144

A.A. Putnam. *Combustion-Driven Oscillations in Industry.* Elsevier, New York, NY, USA, 1971. 5

L. Rayleigh. The explanation of certain acoustical phenomena. *P. R. Inst. GB*, 8:536–542, 1878. 4

L. Rayleigh. On the stability, or instability, of certain fluid motions. *P. Lond. Math Soc.*, 11(1):57–72, 1879. 21

L. Raynal, J.L. Harion, M. Favre-Marinet, and G. Binder. The oscillatory instability of plane variable-density jets. *Phys. Fluids*, 8(4):993–1006, 1996. 22, 23

C.D. Richards, B.D. Breuel, R.P. Clark, and T.R. Troutt. Concentration measurements in a self-excited jet. *Exp. Fluids*, 21(2):103–109, 1996. 22

G.A. Richards and M.C. Janus. Characterization of oscillations during premix gas turbine combustion. *J. Eng. Gas Turb. Power*, 120(2):294–302, 1998. 10

D.E. Rogers and F.E. Marble. A mechanism for high-frequency oscillations in ramjet combustors and afterburners. *Jet Propulsion*, 26(6):456–462, 1956. 8

W.M. Roquemore, L.D. Chen, J.P. Seaba, P.S. Tschen, L.P. Goss, and D.D. Trump. Jet diffusion flame transition to turbulence. In M. Samimy, K.S. Breuer, L.G. Leal, and P.H. Steen, editors, *A Gallery of Fluid Motion*, chapter 8. Cambridge University Press, Cambridge, England, 2003. 26, 27

E.J. Routh. *A Treatise on the Stability of a Given State of Motion, Particularly Steady Motion*. Macmillan Publishers, London, England, 1877. 41

D. Ruelle and F. Takens. On the nature of turbulence. *Commun. Math Phys.*, 20(3):167–192, 1971. 67

H. Sato, K. Amagai, and M. Arai. Flickering frequencies of diffusion flames observed under various gravity fields. *P. Combust. Inst.*, 28(2):1981–1987, 2000. 28

S.S. Sattinger, Y. Neumeier, A. Nabi, B.T. Zinn, D.J. Amos, and D.D. Darling. Sub-scale demonstration of the active feedback control of gas-turbine combustion instabilities. *J. Eng. Gas Turb. Power*, 122(2):262–268, 2000. 10

K.C. Schadow, K.J. Wilson, and E. Gutmark. Characterization of large-scale structures in a forced ducted flow with dump. *AIAA J.*, 25(9):1164–1170, 1987. 3

K.C. Schadow, E. Gutmark, T.P. Parr, K.J. Wilson, and J.E. Crump. Large-scale coherent structures as drivers of combustion instability. *Combust. Sci. Technol.*, 64(4–6):167–186, 1989. 8

G.S. Settles. *Schlieren and Shadowgraph Techniques: Visualizing Phenomena in Transparent Media*. Springer–Verlag, New York, NY, USA, 2001. 69

A. Sevilla and C. Martínez-Bazán. A note on the stabilization of bluff-body wakes by low density base bleed. *Phys. Fluids*, 18(9):098102–4, 2006. 20

A.F. Seybert and D.F. Ross. Experimental determination of acoustic properties using a two-microphone random-excitation technique. *J. Acoust. Soc. Am.*, 61 (5):1362–1370, 1977. 55

A.F. Seybert and B. Soenarko. Error analysis of spectral estimates with application to the measurement of acoustic parameters using random sound fields in ducts. *J. Acoust. Soc. Am.*, 69(4):1190–1199, 1981. 57

C.P. Shao, J.M. Wang, and Q.D. Wei. Visualization study on suppression of vortex shedding from a cylinder. *J. Visual. Japan*, 10(1):57–64, 2007. 28

P.R. Solomon and P.E. Best. Fourier transform infrared emission/transmission spectroscopy in flames. In N.A. Chigier, editor, *Combustion Measurements*, chapter 11. Hemisphere Publishing, New York, NY, USA, 1991. 63

H.B. Squire. On the stability for three-dimensional disturbances of viscous fluid flow between parallel walls. *P. Roy. Soc. A - Math Phy.*, 142(193):621–628, 1933. 11

K.R. Sreenivasan, S. Raghu, and D. Kyle. Absolute instability in variable density round jets. *Exp. Fluids*, 7(5):309–317, 1989. 22, 25, 35, 37, 55, 82

P.K. Stansby. The locking-on of vortex shedding due to the cross-stream vibration of circular cylinders in uniform and shear flows. *J. Fluid Mech.*, 74(4):641–665, 1976. 35, 36

R.C. Steele, L.H. Cowell, S.M. Cannon, and C.E. Smith. Passive control of combustion instabilities in lean premixed combustors. *J. Eng. Gas Turb. Power*, 122(3):412–419, 2000. 10

D.L. Straub and G.A. Richards. Effect of fuel nozzle configuration on premix combustion dynamics. In *International Gas Turbine & Aeroengine Congress & Exhibition*, Stockholm, Sweden, June 1998. 10

S.H. Strogatz. *Nonlinear Dynamics and Chaos*. Perseus Books, New York, NY, USA, 1994. 29, 32

P.J. Strykowski. *The Control of Absolutely and Convectively Unstable Shear Flows*. PhD thesis, Yale University, New Haven, CT, USA, 1986. 16, 17, 28, 48

P.J. Strykowski and D.L. Niccum. The stability of countercurrent mixing layers in circular jets. *J. Fluid Mech.*, 227:309–343, 1991. 15, 47, 87

P.J. Strykowski and K.R. Sreenivasan. On the formation and suppression of vortex 'shedding' at low Reynolds numbers. *J. Fluid Mech.*, 218:71–107, 1990. 28

J.T. Stuart. On the non-linear mechanics of hydrodynamic stability. *J. Fluid Mech.*, 4(1):1–21, 1958. 144

J.T. Stuart. On the non-linear mechanics of wave disturbances in stable and unstable parallel flows. *J. Fluid Mech.*, 9(3):353–370, 1960. 144

G.I. Taylor. Stability of a viscous liquid contained between two rotating cylinders. *Philos. T. R. Soc. A*, 223:289–343, 1923. 11

A.Y. Tong and W.A. Sirignano. Multicomponent droplet vaporization in a high temperature gas. *Combust. Flame*, 66(3):221–235, 1986a. 9

A.Y. Tong and W.A. Sirignano. Multicomponent transient droplet vaporization with internal circulation: integral equation formulation and approximate solution. *Numer. Heat Tr. A - Appl.*, 10(3):253–278, 1986b. 9

A.Y. Tong and W.A. Sirignano. Vaporization response of fuel droplet in oscillatory field. In *ASME, AIChE, and ANS National Heat Transfer Conference and Exhibition*, Pittsburgh, PA, USA, August 1987. 9

T.Y. Toong, F.S. Richard, M.S. John, and Y.A. Griffin. Mechanisms of combustion instability. *P. Combust. Inst.*, 10(1):1301–1313, 1965. 28

M.H. Trauth. *Matlab Recipes for Earth Sciences*. Springer–Verlag, New York, NY, USA, 3rd edition, 2010. 67

H. Tsuji and I. Yamaoka. Structure analysis of counterflow diffusion flames in the forward stagnation region of a porous cylinder. *P. Combust. Inst.*, 13(1): 723–731, 1971. 92

B. van der Pol. On relaxation oscillations. *Phil. Mag.*, 2:978–992, 1926. 30, 31

B. van der Pol and J. van der Mark. Frequency demultiplication. *Nature*, 120: 363–364, 1927. 34

F.J. Weinberg. *Optics of Flames*. Butterworths, London, England, 1963. 68

P.D. Welch. The use of Fast Fourier Transform for the estimation of power spectra: a method based on time averaging over short modified periodograms. *IEEE T. Audio Electroacoust.*, 15:70–73, 1967. 54

S.E. Widnall, D.B. Bliss, and C.Y. Tsai. The instability of short waves on a vortex ring. *J. Fluid Mech.*, 66(1):35–47, 1974. 25

C.R. Wilke. A viscosity equation for gas mixtures. *J. Chem. Phys.*, 18(4):517–519, 1950. 92

C.H.K. Williamson. Vortex dynamics in the cylinder wake. *Annu. Rev. Fluid Mech.*, 28:477–539, 1996. 17

C.J. Wood. The effect of base bleed on a periodic wake. *J. R. Aeronaut. Soc.*, 68:477–482, 1964. 19

V. Yang and W. Anderson, editors. *Liquid Rocket Engine Combustion Instability*, volume 169 of *Progress in Astronautics and Aeronautics*. American Institute of Aeronautics and Astronautics, Reston, VA, USA, 1995. 4, 10

V. Yang and F.E.C. Culick. On the existence and stability of limit cycles for transverse acoustic oscillations in a cylindrical combustion chamber, 1: standing modes. *Combust. Sci. Technol.*, 72(1–3):37–65, 1990. 41

B.S. Yildirim and A.K. Agrawal. Full-field measurements of self-excited oscillations in momentum-dominated helium jets. *Exp. Fluids*, 38(2):161–173, 2005. 22

M.H. Yu and P.A. Monkewitz. The effect of nonuniform density on the absolute instability of two-dimensional inertial jets and wakes. *Phys. Fluids A*, 2(7): 1175–1181, 1990. 18, 20, 23

M.H. Yu and P.A. Monkewitz. Oscillations in the near field of a heated two-dimensional jet. *J. Fluid Mech.*, 255:323–347, 1993. 22, 23

M.H. Yu, T.K. Lin, and Y.Y. Hsieh. Influence of acoustic forcing on the near field development of a heated plane jet. *Exp. Therm. Fluid Sci.*, 25(1–2):13–22, 2001. 22

A. Zebib. Stability of viscous flow past a circular cylinder. *J. Eng. Math.*, 21(2): 155–165, 1987. 16, 17

Y.B. Zel'dovich, G.I. Barenblatt, V.B. Librovich, and G.M. Mikhviladze. *The Mathematical Theory of Combustion and Explosions.* Consultants Bureau (Plenum Press), New York, NY, USA, 1985. Translated from Russian by D.H. McNeill. 3

B.T. Zinn. Pulsed combustor applications: past, present and future. In F. Culick, M.V. Heitor, and J.H. Whitelaw, editors, *Unsteady Combustion*, NATO Science Series E, chapter 6. Springer, New York, NY, USA, 1996. 4, 7

B.T. Zinn and T.C. Lieuwen. Combustion instabilities: basic concepts. In T.C. Lieuwen and V. Yang, editors, *Combustion Instabilities in Gas Turbine Engines: Operational Experience, Fundamental Mechanisms, and Modeling*, Progress in Astronautics and Aeronautics, chapter 1. American Institute of Aeronautics and Astronautics, Reston, VA, USA, 2005. 3, 7, 9